# FUNDAMENTAL MECHANISMS OF ENERGY TRANSPORT IN LAYERED ELECTROMAGNETIC HEAT EXCHANGERS WITH COMPRESSIBLE AND INCOMPRESSIBLE FLUIDS

by

Ajit Ashokrao Mohekar

A Dissertation Submitted to the Faculty of

Worcester Polytechnic Institute

in Partial Fulfillment of the Requirements for the Degree of

Doctor of Philosophy

in

Mechanical and Materials Engineering

August 2022

APPROVED:

| | |
|---|---|
| Professor Burt S. Tilley<br>Advisor | Professor Vadim V. Yakovlev<br>Co-advisor |
| Professor Jamal Yagoobi<br>Committee Member | Professor John Sullivan<br>Committee Member |
| Professor Aswin Gnanaskandan<br>Graduate Committee Representative | Dr. Brad Hoff<br>External Mentor |

# ABSTRACT

Robust electromagnetic (EM) heat exchangers (HXs) that efficiently covert EM waves into heat or mechanical work can act as receivers in ground-to-ground power beaming applications where energy is transferred from one location to another through the atmosphere with a beam of electromagnetic (EM) waves. The design of EM HXs considered in this research consists of a lossy ceramic material heated by EM waves and a fluid flow is employed to transfer the power from the ceramic. A nonlinear phenomenon associated with EM heating of ceramics is *thermal runaway*, where a slight increase in the applied EM power results in a significant rise in the ceramic temperature. This research is focused on determining whether it is viable to utilize a thermal runway for efficient power generation from an EM HX. When a fluid flow is coupled with EM heating of a ceramic, energy is transferred by conduction, convection, and work of thermal expansion within the fluid. In this dissertation, the impact of each heat transfer mechanism is studied individually through numerical and asymptotic modeling approaches.

With a numerical study on a triple layer EM HX with the incompressible flow, it is shown that the most efficient operation of the EM HX occurs when elevated temperatures are achieved at low applied EM powers. When an EM HX with a variable-density fluid flow is considered, three distinct primary instability mechanisms are found to occur simultaneously. Firstly, the thermal runaway instability in the ceramic is due to the nonlinear nature of EM heating. Secondly, the fringe field instability occurs because of the coupling between the electric field and temperature perturbations. Lastly, the Rayleigh-Bénard (RB) convection occurs when buoyancy dominates the viscous stresses within the fluid. The fringe field instabilities and RB convection are significant for practical applications as their coupling is expected to improve the performance of the EM HX. Finally, when a gaseous flow of an ideal gas is coupled with EM heating of the ceramic, two additional effects are observed. Firstly, local *Joule-Thompson (JT)* cooling of the gas occurs when work of thermal expansion dominates the net heat added to the system. Secondly, thermal runaway causes a jump in the kinetic energy of the gas (about 10 times the initial value) and *thermal choking* occurs when the flow reaches the sonic state. Finally, to investigate how JT cooling affects the macroscale energy balances, a numerical model describing a compressible flow through a lossy porous ceramic heated by EM waves is developed. Results show that JT cooling persists at the macroscale and has a stronger impact near the outlet, even during thermal runaway.

# ACKNOWLEDGMENTS

Firstly, I would like to thank my advisors Professor Burt Tilley and Professor Vadim Yakovlev for their continuous support, guidance, and patience. I would have never finished the degree without their help. I am thankful to them for always being there for me, taking care of me, and having my back whenever I struggled not only in research but also in my personal life. I strongly feel that they have trained me to become a confident individual who can take on any challenges in the future. I also thank Dr. Brad Hoff of the Air Force Research Laboratory, Kirtland for his suggestions during my research and for steering me in the right direction whenever I struggled to see the big picture.

I sincerely thank Professor Jamal Yagoobi for being the second reader of the thesis. I am honored to have him on my defense committee. After all, he taught me all the heat transfer basics in his course back in the Spring 2017 semester and inspired me to do research in this area. I also take this opportunity to thank Professor John Sullivan and Professor Aswin Gnanaskandan for reading my work and providing guidance whenever I needed it. Their suggestions have certainly improved the quality of this work.

I am grateful for the support from the Air Force Office of Scientific Research (AFOSR); Award: FA9550-18-1-0528. I would also like to thank the office of Academic and Research Computing at WPI for providing me access to high-performance computers.

Finally, I would like to thank my family for their constant support, trust, and encouragement, especially my parents, whose unconditional love has been my greatest strength. Special thanks to this wonderful person in my life, Savita, for her help and support. I cannot thank her enough for being there for me and bringing the best out of me for the last 8 years.

# LIST OF ABBREVIATIONS

1. EM: Electromagnetic
2. HX: Heat Exchanger
3. MW: Microwaves
4. MMW: Millimeterwaves
5. MTLS: Millimeterwave Thermal Launch System
6. FEM: Finite Element Method
7. FD: Finite Difference Method
8. PDE: Partial Differential Equations
9. ODE: Ordinary Differential Equations
10. IMEX: Implicit-Explicit
11. BVP: Boundary Value Problem
12. IVP: Initial Value Problem
13. RB: Rayleigh-Bénard
14. JT: Joule-Thompson
15. LST: Linear Stability Theory
16. 1D: One Dimensional
17. 2D: Two Dimensional
18. 3D: Three Dimensional

# TABLE OF CONTENTS

# 1 INTRODUCTION

A heat exchanager (HX) is used to cool or heat a medium with the use of a fluid. Refrigeration and air conditioning systems mainly provide cooling of a desired region by extracting heat from it with the use of a coolant. Traditional water boilers, which are used in electric power generation plants, generate high pressure and temperature steam through transport of thermal energy from burning fuels to water. Electromagnetic (EM) HX convert EM energy into heat or mechanical work. A common example of an EM HX is a solar thermal panel, where solar radiation are utilized to heat up a fluid [1].

One recent technology under development is high-power beaming application [2–9] where high power EM waves are radiated towards a receiver which then converts the incoming EM energy into some other desired form. Another promising concept is the space-based solar power, which can help utilize solar power 24 hours a day to contribute in the energy production on earth. A satellite in low earth orbit collects and converts solar power into EM energy which is then beamed towards the earth. Here at the receiving end, the incident power is then converted into any other energy form. In both of these technologies, EM HXs operating at high powers can be critical components when desired output from the receiver system is the heat or mechanical work.

Along the similar line, beamed energy propulsion, where EM waves are utilized to produce thrust, may provide a viable alternative to current propulsion technologies [10]. For example, microwave (MW) thermal thrusters utilize MW energy to propel a rocket. Since such rockets eliminate the need on-board fuel supply, they can provide a high thrust to weight ratio. Moreover, the EM power supply may be reusable for multiple rocket launches making this technology cost effective in the long-term. NASA carried out an experiment on Millimeter Wave Thermal Launch System (MTLS) in 2015 to demonstrate how EM waves can be utilized to propel a small-scale

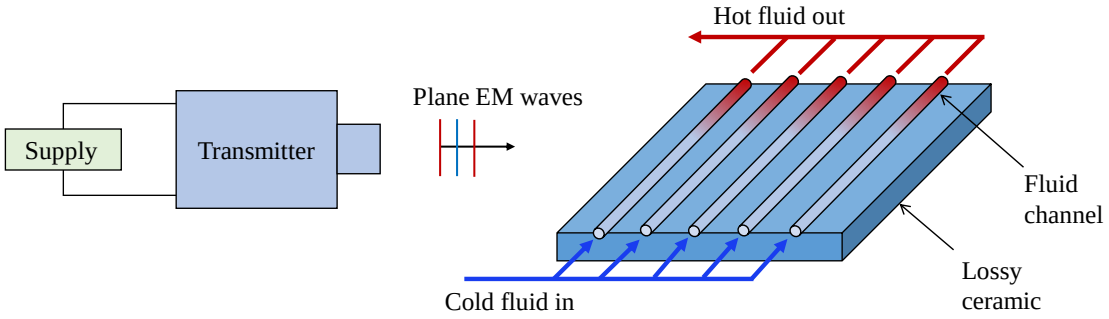


Figure 1.1: Simple block diagram of a continuous power beaming system. EM HX acts as a receiver in such systems, and convert EM energy into heat or mechanical work.

rocket [11]. A 100 kW beam of millimeter waves (MMW) at 95 GHz is used to heat up an array of uniform diameter ceramic tubes made up of silicon carbide. When sufficiently high temperatures are achieved (around 1400 K), pressurized hydrogen is expanded through the tubes. Because of heat transfer from the heated ceramic, gas does work of thermal expansion and accelerates as it moves through ceramic channels. Thrust is generated as a result of this change in linear momentum of the gas as it leaves the system. In the interest of development of this technology, it is required to investigate impact of the coupling between fluid dynamics and EM heating of ceramic.

In this research, we investigate EM HXs that are useful in power beaming applications. A simple block diagram of such a system is shown in Figure 1.1. A transmitter converts input energy into EM waves and beams towards an EM HX at the receiving end where conversion of EM energy to heat or mechanical work takes place. When it comes to operating frequency of EM radiations, MW and MMW are promising choices in continuous power-beaming applications as they are readily available at high power. While MMW may have advantages over MW in terms of dimensions of transmitting antennas, they may not efficiently propagate through the atmosphere [2,4]. Depending on efficiency of transmission, MMW may be preferable at high altitudes or in space, and MW or near MMW may be convenient for ground-to-ground power beaming [3]. In this work, we focus our attention at EM HXs that are useful in ground-to-ground high power beaming applications (i.e., frequency of operation is in the MW regime).

A common thread between all of these application is the conversion of EM energy into heat or

mechanical work. The operation of EM HXs considered here involves heating of a ceramic material by high frequency EM waves and a fluid flow is employed to collect dissipated thermal energy. Generally speaking, the mechanisms for heat transfer between the ceramic and an incompressible coolants are conduction and convection. As a result, such an EM HX convert EM waves into internal energy. Compressible coolants transfer heat from the ceramic through conduction and convection along with work of thermal expansion. EM HXs with compressible coolants can, therefore, convert EM waves into mechanial work in addition to internal energy (an example that operates on the similar principle is beamed energy propulsion or NASA MTLS rocket). *The overall goal of this work is to determine, through numerical and analytical multiphysics modeling, whether such EM HXs are a viable choice for heat or mechanical power generation.*

In this chapter we first describe physical processes involved in operation of an EM HX with the help of conservation laws. Then we present a brief literature review of research that is directly applicable to EM HXs. Based on this literature review, we draw some important questions that motivate this work.

## 1.1 Operational Principles of an EM HX

Heat generation in lossy materials irradiated by EM waves is due to two sources. In the presence of alternating EM field, polar molecules oscillate as they try to align themselves with the time-varying electric field according to the Lorentz phenomenon. The increased kinetic energy of molecules causes a volumetric heating. This is called *dielectric heating*. The second mode of heat generation is when an alternating magnetic field causes free charges to rotate causing generation of eddy currents. Volumetric heated caused by this current flow is known as *inductive heating*. Many typical ceramics such as zirconia, silicon carbide, and aluminum nitride undergo both dielectric and inductive heating when irradiated by an alternating EM field. To consider the contribution due to both modes, typically effective electrical conductivity (also called as the effective loss factor), $\sigma_{eff}$, is defined such that volumetric heat source, $\dot{q}$, in a lossy material takes into account heating

due to both mechanisms. The expression for $\dot{q}$ in lossy regions is given as

$$\dot{q}_j = \frac{1}{2}\sigma_{eff_j}|\mathbf{E}_j|^2, \tag{1.1}$$

where $|\mathbf{E}|_j$ is the magnitude of the electric field, and subscript $j$ is the region of solution (either fluid or ceramic). In the context of an EM HX here we consider, $j = 1$ is fluid region and $j = 2$ is ceramic region. Effective electrical conductivity $\sigma_{eff_j}$ is defined such that it takes into account both inductive and dielectric heating.

EM waves are generated as a result of coupling between electric and magnetic fields. Time-varying electric field gives rise to a magnetic field, and vice versa. Dependence between the time-harmonic electric and magnetic fields in a nonmagnetic medium is described by Faraday's and Ampere's laws as

$$\nabla \times \mathbf{E}_j = i\omega\mu_0\mathbf{H}_j, \tag{1.2a}$$

$$\nabla \times \mathbf{H}_j = -i\omega\epsilon_0(\epsilon_{r_j} + i\epsilon''_j)\mathbf{E}_j + \sigma_j\mathbf{E}_j, \tag{1.2b}$$

where $\omega$ is the angular frequency of EM waves, $\mathbf{H}_j$ is the magnetic field, $\mu_0$ is permeability of the free space, $\epsilon_0$ is permittivity of the free space, $\epsilon_r$ and $\epsilon''$ are real and imaginary parts of the dielectric constant, respectively, and $\sigma_j$ is the electrical conductivity. A typical curl-curl form of Maxwell's equations is obtained by taking curl of (1.2a), and magnetic fields are eliminated using (1.2b). Resulting curl-curl Maxwell's equations are [12]

$$\nabla \cdot (\epsilon_j\mathbf{E}_j) = 0, \tag{1.3a}$$

$$\nabla^2\mathbf{E}_j - \nabla\left(\nabla \cdot \mathbf{E}_j\right) + {k_0}^2\epsilon_j\mathbf{E}_j = 0, \tag{1.3b}$$

where $k_0 = \frac{2\pi}{\lambda_0}$, $\lambda_0$ is the wavelength of EM waves in free space, and $\epsilon_j$ is defined as

$$\epsilon_j = \left(\epsilon_{r_j} + i\left[\frac{\sigma_j + \omega\epsilon_0\epsilon''_j}{\omega\epsilon_0}\right]\right), \tag{1.4a}$$

$$\epsilon_j = \left(\epsilon_{r_j} + i\frac{\sigma_{eff_j}}{\omega\epsilon_0}\right). \tag{1.4b}$$

Here, $\sigma$ contributes in inductive heating and $\epsilon''$ is responsible for dielectric heating of the medium. Combining $\sigma$ and $\epsilon''$ into $\sigma_{eff}$ allows us to include both inductive and dielectric heating in the thermal energy balance.

By expanding terms in (1.3a), we can write $\nabla\epsilon_j \cdot \mathbf{E}_j + \epsilon_j \nabla \cdot \mathbf{E}_j = 0$. This suggests that when the permittivity gradients are perpendicular to electric fields within the fluid and the ceramic regions (i.e., $\nabla\epsilon_j \cdot \mathbf{E}_j = 0$), the electric field becomes divergence free, i.e., $\nabla \cdot \mathbf{E}_j = 0$, and the Maxwell's curl-curl equation (1.3b) reduces to vector Helmholtz equations. As the first step towards modeling EM HXs, this dissertation only considers 2D geometries. This is done to identify the impact of dominant heat transfer mechanisms while keeping relatively low computational costs. To further simplify the problem, we assume that the incident plane EM waves are monochromatic in nature and are polarized in the direction perpendicular to the 2D geometry plane of an EM HX. If permittivities of fluid and ceramic regions are temperature dependent then $\nabla\epsilon_j$ vector is parallel to the 2D EM HX geometry plane and the electric field vector is perpendicular to this plane. Gauss' law for this special scenario reduces to $\nabla \cdot \mathbf{E}_j = 0$ even when $\nabla\epsilon_j \neq 0$, and the electric field intensities within the fluid and the ceramic regions are given by scalar Helmholtz equations.

Flow of a compressible fluid is governed by Navier-Stokes equations. Mass, momentum, and energy conservation laws explained below are taken from [13]. The conservation of mass of the fluid is given as

$$\frac{\partial \rho_1}{\partial t} + \nabla \cdot (\rho_1 \mathbf{u}) = 0, \tag{1.5}$$

where $\rho_1$ is density of the fluid and $\mathbf{u}$ is the fluid velocity. A flow said to be incompressible when $\nabla \cdot \mathbf{u} = 0$, i.e., the flow is divergence free. Which suggests that for an incompressible flow $\rho_1$ can vary in space and time but $\frac{\partial \rho_1}{\partial t} + \mathbf{u} \cdot \nabla \rho_1 = 0$.

Conservation of linear momentum, i.e., Newton's second law, applied to a differential element of a compressible fluid with constant viscosity is given by

$$\rho_1 \left[ \frac{\partial \mathbf{u}}{\partial t} + (\mathbf{u} \cdot \nabla)\mathbf{u} \right] = -\nabla p + \mu \nabla^2 \mathbf{u} + \frac{\mu}{3} \nabla(\nabla \cdot \mathbf{u}) + \mathbf{F}, \tag{1.6}$$

where $p$ is the absolute fluid pressure, $\mu$ is dynamic viscosity which is assumed constant, and $\mathbf{F}$

is the body force experienced by the fluid. The left hand side of (1.6) is net force experienced by the fluid per unit volume due to instantaneous and convective accelerations which is balanced by normal forces due to pressure gradient, shear forces due to viscosity of the fluid, and external forces such as buoyancy, electrohydrodynamic forces, etc. acting on a fluid element.

Conservation of energy per unit volume applied to a differential fluid element is given by

$$\rho_1 \left[ \frac{\partial e_1}{\partial t} + (\mathbf{u} \cdot \nabla) e_1 \right] - \frac{p}{\rho_1} \left[ \frac{\partial \rho_1}{\partial t} + (\mathbf{u} \cdot \nabla) \rho_1 \right] = \nabla \cdot (k_1 \nabla T_1) + \Phi + \dot{q}_1,$$

where $e_1 = c_{v_1} T_1$ is the internal energy, $c_{v_1}$ is the specific heat at constant volume, $T_1$ is the temperature, $k_1$ is the thermal conductivity, $\Phi$ is the heat generation due to viscous dissipation, and $\dot{q}_1$ is volumetric heat source in the fluid element. For constant $c_{v_1}$ and $k_1$, negligible $\Phi$, and $\dot{q}_1$ due to EM heating, the energy equation reduces to

$$\rho_1 c_{v_1} \left[ \frac{\partial T_1}{\partial t} + \mathbf{u} \cdot \nabla T_1 \right] + p \nabla \cdot \mathbf{u} = k_1 \nabla^2 T_1 + \frac{1}{2} \sigma_{eff_1} |E_1|^2. \tag{1.7}$$

The term $p(\nabla \cdot \mathbf{u})$ in (1.7) is derived by utilizing the mass conservation (1.5). In the models described in this work, we assume that fluids are lossless, i.e., $\sigma_{eff_1} = 0$. On the left hand side, the first and second terms represent the rate of change of internal energy, the term $p \nabla \cdot \mathbf{u}$ represents the work done by the differential element through thermal expansion, and the terms on the right hand side are heat added to (or rejected from) the differential fluid element through conduction and volumetric heat sources. If the flow is incompressible then $\nabla \cdot \mathbf{u} = 0$ and the work of thermal expansion is absent and coolant only transfer heat from the ceramic through conduction and convection.

Application of the first law of thermodynamics to a differential element of the ceramic region with constant density, specific heat, and thermal conductivity undergoing EM heating is given as

$$\rho_2 c_{p_2} \frac{\partial T_2}{\partial t} = k_2 \nabla^2 T_2 + \frac{1}{2} \sigma_{eff_2} |E_2|^2. \tag{1.8}$$

Density of compressible fluids typically depend on both absolute pressure and temperature. Therefore, to close the system of equation, we need a relation between $p$, $\rho_1$, and $T_1$. In our studies,

we assume that the equation of state of the compressible gas is given by the ideal gas law as

$$p = \rho_1 R_g T_1, \tag{1.9}$$

where $R_g$ is the gas constant, $T_1$ is temperature of the gas.

### 1.1.1 Boundary Conditions

At the plane interface between two media, a pillbox argument can be applied to integral form of Maxwell's equations to derive continuity of tangential electric and magnetic fields [14] conditions. Assuming that electric field propagates from nonmagnetic medium 1 to medium 2, the interface conditions are given by

$$\hat{n} \times \nabla \times \mathbf{E}_1 = \hat{n} \times \nabla \times \mathbf{E}_2, \tag{1.10a}$$

$$\hat{n} \times \mathbf{E}_1 = \hat{n} \times \mathbf{E}_2, \tag{1.10b}$$

where $\hat{n}$ is the outward unit normal at the interface pointing from media 2 to 1. These boundary conditions are imposed at all the interfaces to satisfy Ampere's and Faraday's laws in the neighborhood of the interface. Depending on geometries of EM HXs considered in upcoming chapters of the dissertation, the boundary conditions on the electric field are derived from (1.10).

Similarly, when solving for $T$, we apply the perfect thermal contact boundary condition (i.e., heat flux and temperature are continuous across the interface) at the interfaces between different media EM HXs. At the interface between media 1 and 2, the boundary condition is

$$\hat{n} \cdot \mathbf{q}_1'' = \hat{n} \cdot \mathbf{q}_2'', \tag{1.11a}$$

$$T_1 = T_2, \tag{1.11b}$$

where $\mathbf{q}_j'' = -k_j \nabla T_j$ is the heat flux vector in respective medium $j$. At the interface between free space and the EM HX, heat transfer with the environment occurs through convection and radiation.

Boundary condition at such interface, $j$, is given by

$$\hat{n} \cdot (-k_j \nabla T_j) = h(T_j - T_A) + \xi s_r (T_j^4 - T_A^4), \tag{1.12}$$

where $h$ is the convective heat transfer coefficient, $T_A$ is the ambient temperature which is assumed to be constant, $\xi$ is the radiation emissivity of the surface, and $s_r$ is Stefan-Boltzmann radiation constant. If convective heat transfer occurs through natural convection with the surrounding air, the value of $h$ can be found from the Nusselt number correlations that are determined experimentally [15]. Typically, the values of $h$ and $\xi$ are functions of surface temperature, characteristics length scale, and material properties of ambient air. For simplicity we assume that both $h$ and $\xi$ do not change with $T$ and the thermal boundary conditions are linear and homogeneous. In this work, typical values of $h$ are determined from Nussel number correlations for natural convection at the vertical wall, and values of $\xi$ are taken from [15] for typical ceramic surfaces.

When solving the viscous Navier-Stokes equations, no slip and no penetration boundary conditions are imposed on the fluid velocity at the walls of the fluid channel. These conditions are

$$\mathbf{u} = 0, \text{ (no slip) and } \hat{n} \cdot \mathbf{u} = 0 \text{ (no penetration).} \tag{1.13}$$

In addition, since the fluid flow is driven by the imposed pressure drop, the values of gauge pressures are specified at the inlet and outlet of the fluid channel.

## 1.2 EM Heating of Layered Structures

EM HXs which we consider in this work are required to operate at high incident powers. One peculiar phenomenon associated with EM thermal processing of ceramic materials at such powers is *thermal runaway*, a nonlinear phenomenon in which a small increase in the applied EM power invokes a sharp temporal increase in temperature. For many ceramic materials, including zirconia or silicon carbide, the loss factor, $\sigma_{eff}$, can be represented through an exponential fit, increasing with temperature [16,17]. Because of this coupling, electric field strength and dielectric heat source

within the ceramic become temperature dependent, and the ceramic heats up efficiently at higher temperatures. When the rate of volumetric heat addition is much larger than the energy removal rate from the ceramic, thermal runaway occurs causing drastic rise of ceramic temperatures (e.g., 2,000 K for silicon carbide). Thermal runaway is studied experimentally [18, 19] and computationally [17], and it is shown that thermal runaway occurs when the maximum temperature in processed material reaches a critical value. Temperatures during thermal runaway are high enough to cause material damage through melting or cracking.

Due to such a rapid temperature growth, the phenomena of thermal runaway is considered as one of the challenges in the development of applications such as MW assisted sintering of ceramics [20, 21], chemical vapor infiltration [22], etc. When designing such applications, a robust mechanisms of controlling thermal runaway must be employed to ensure reliability of the product. In the work of [23], the frequency of EM waves is adaptively altered with temperature to ensure efficient and controlled heating of polymer nano composites. Since the dielectric heat source is proportional to the frequency of the EM waves, this approach allows to control temperature growth by managing the average volumetric heat source. Another approach is to design an automatic temperature feedback controller based on the applied EM power [24]. The role of the controller is to periodically switch on and off the applied powers depending on the temperature of the sample which is being heated by the EM waves. Such control systems are effective when maintaining ceramic temperatures below the critical value, but thermal runaway is highly sensitive to applied power which makes design of such controller practically difficult for high temperature applications. In the work of [19], the size of the MW resonating cavity is adaptively modified to alter EM field absorption and reflection characteristics within the sample being heated by EM waves. Although all of the ideas above are promising in controlling thermal runaway in closed systems (such as resonating cavities), new approaches are required to ensure temperature control in open systems such as EM HXs useful in power beaming applications and beamed energy propulsion.

Analytical models of heating of a single dielectric slab [25, 26] (Figure 1.2) and a three-layer structure (Figure 1.3) [27] by symmetric irradiation of plane monochromatic EM waves describe thermal runway. These models assume that electric field is polarized along the $y$-direction, wave-

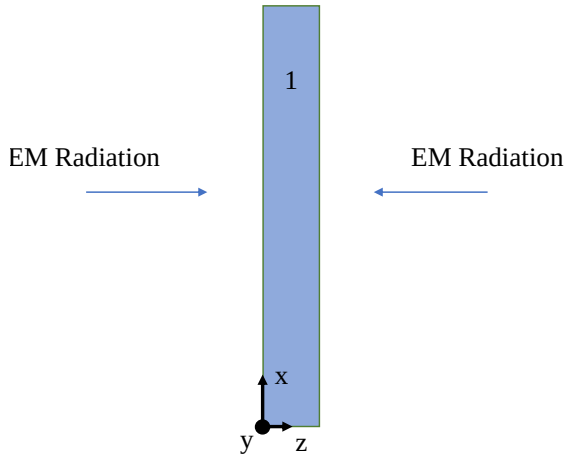


Figure 1.2: Single-layer ceramic dielectric slab undergoing heating by symmetric irradiation by plane, monochromatic EM waves. This geometry is considered by [25, 26].

length of incident EM waves is much larger than the layer thickness, and thermal losses to the surrounding through convection (Newton's law of cooling) and radiation are negligible. Under these approximations, the leading-order temperature in the ceramic region turns out to be uniform and electric field is only $z$-dependent. The equilibrium of EM heating in these cases is described by [25, 26]

$$P = \frac{L\left(T^{(0)}\right)}{\sigma_{eff}\left(T^{(0)}\right)||E^{(0)}||^2}, \tag{1.14}$$

where $L\left(T^{(0)}\right)$ is the total energy lost to the surrounding though radiation and convection, $T^{(0)}$ is the leading order temperature which is constant in all regions, and $E^{(0)}$ is the leading order electric field which is $z$-dependent, and $||E^{(0)}||^2 = \int_0^l |E^{(0)}|^2 dz$. Terms in numerator and denominator represent external thermal losses and the total heat added to the system, respectively.

Using (1.14), a parametric plot of average steady temperatures as a function of applied power can be graphed, which is known as a *power response curve*. The resulting power response considered in [25–27] is an S-curve as shown in Figure 1.4. A branch of the power response curve is stable (or unstable) when its slope is positive (or negative) [27]. Generally speaking, an S-shaped power response curve has two stable branches. On the lower branch, the temperatures are low ($\sim 400\ K$),

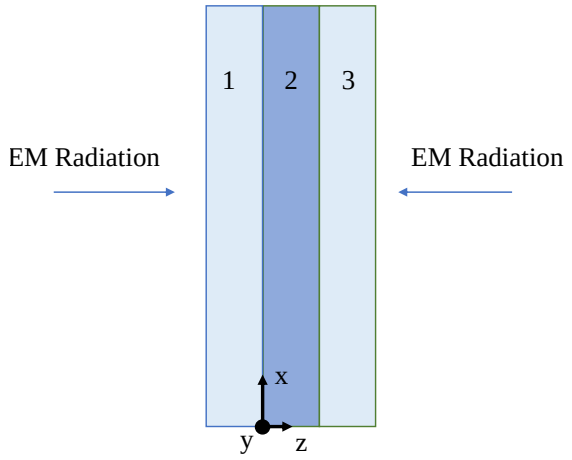


Figure 1.3: Triple-layer laminate system undergoing heating by symmetric irradiation by plane, monochromatic EM waves. This structure is considered in [27].

and $\sigma_{eff}$ is small, as a result, electric field does not attenuate much and volumetric heat source is small. The external losses $L(T)$ are able to balance the rate of internal heat generation. On the upper stable branch, the temperatures are high ($\sim 2,000\ K$), and $\sigma_{eff}$ is also large. As a result, electric field drastically attenuates near the surface of the ceramic layer and negligible EM energy penetrates into the ceramic. This phenomenon is known the *skin effect*. In this case, the equilibrium is mainly achieved by a balance between increased $\sigma_{eff}$ and less available EM energy due to attenuated electric field at the surface. EM HXs operating on the lower stable temperature branch may not operate efficiently. On the other hand, high stable temperatures may damage the ceramic material itself. An important feature of an S-curve is that there exits a hysteresis between the applied power and the temperature. Physically, it means that if the initial temperature of the ceramic region is high enough (i.e., closer to the upper branch), then a very small amount of EM power is needed to be supplied in order to maintain such high temperatures.

Recently, an analytical model [28,29] studying EM heating of thin triple layer laminate (lossless-lossy-lossless, Figure 1.3) suggests an innovative electric-field-resonance based approach to control temperature during thermal runway. This model considers heating of a thin triple layer structure by symmetric normal plane wave irradiation. Unlike [25–27], this model assumes that the wavelength

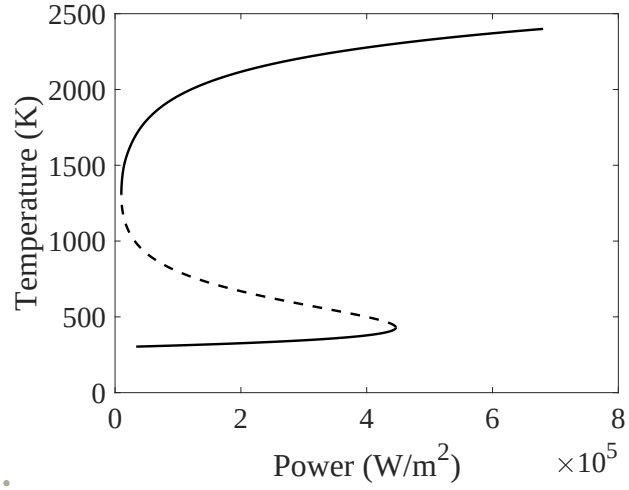


Figure 1.4: S-shaped power response curve reported in [25–27]. When wavelength of incident radiation is larger than layer thickness, S-curve is observed. Solid and dashed lines represent stable and unstable solutions, respectively.

of the incident wave is comparable to the layer's thickness (i.e., they consider heating by high frequency EM waves). Because of this assumption, alterations in layer's thicknesses lead to an electric field resonance in the central lossy layer. The model applies thin-domain asymptotics and shows a similar relation between applied power and leading-order steady-state temperature as given by (1.14). Due to the electric field resonance in the lossy region, the response curve in this case acquires a middle stable branch and becomes a double S-curve as shown in Figure 1.5. On this newly found middle branch, the temperatures are large ($\sim 1,000\ K$) but below values that are seen on the upper branch ($\sim 2,000\ K$). As a result, $\sigma_{eff}$ is large such that electric field region attenuates but the skin effect (drastic attenuation of the field on the surface as seen in case of the upper branch) is not observed. A net combination of increased $\sigma_{eff}$ and attenuated electric field in the ceramic region are then balanced by $L(T)$ at the equilibrium. A computational model presented in [7] numerically verifies the existence of the double S-curve. The model [28] first proved the existence of the double S-curve and extended model [29] confirmed that the field resonance in the lossy layer causes the response curve to have a middle stable branch. The implication from these models showing existence of double S-curve is that when an EM HX operates on the middle branch, stable temperatures are elevated, but remain below values where mechanical damage to the material can occur.

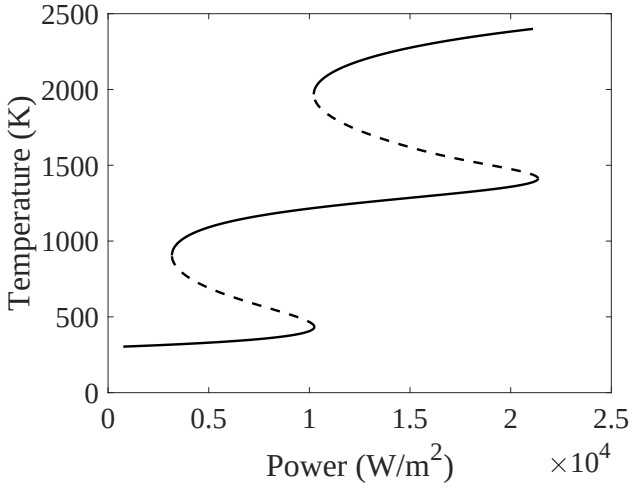


Figure 1.5: Double S-curve reported in [28, 29]. When wavelength of incident EM waves on a triple-layer structure (lossless-lossy-lossless, as shown in Figure 1.3) is comparable to layer thicknesses, double S-curve is observed. Solid and dashed lines represent stable and unstable solutions, respectively.

The EM HXs considered in this work rely on the coupling between a fluid flow and EM heating of a ceramic. Since EM HXs that are useful in ground-to-ground power beaming applications are required to operate at high EM powers and temperature, it is of interest to understand the impact of coupling between the phenomenon of thermal runaway and fluid dynamics. When a single-phase incompressible fluid is considered in an EM HX which operates on the lower stable branch of the response curve (low temperatures and applied powers), hot fluid is delivered at the outlet (an example of such an EM HX is a solar water heater). But, when the operation on the middle or upper branches of a response curve is considered, liquids change their phase into gases under standard atmospheric conditions, and a superheated steam is expected at the outlet. From a transient simulation of thermal runaway without any fluid flow, heat flux entering the fluid region rises from 1 to 100 kW/m$^2$ and the wall temperature rises from 350 to 2000 K in a short amount of time of 5-10 seconds. When this data is compared with typical pool boiling curve [15], almost all liquid coolants are expected to undergo phase-change due to boiling during thermal runway. It is known that boiling causes improvement in the total heat transfer coefficient within the fluid, and experimentally, we expect a competition between rapid rise of temperature (due to thermal runaway) and improved heat transfer between fluid and the ceramic due to boiling heat transfer. But for simplicity, we do not include phase change heat transfer in our modeling efforts.

Another phenomena that may occur in an EM HX is the higher order harmonic generation. Since the dielectric properties of ceramic materials are temperature dependent, nonlinear interaction between the material and the EM wave may result in the higher order harmonic generation. The frequency of EM wave in this work is fixed to 2.45 GHz. The time-scale at which EM field oscillates is on the order of nanoseconds whereas the temperature evolution occurs on the order of seconds. This disparity in time scales suggests that temperature (and thus dielectric properties) can be treated as linear on the time-scales at which EM field oscillates. Therefore, higher order harmonic generation is not considered in this work.

## 1.3 Research Questions and Goals

As discussed in the previous section, thermal runaway in ceramics can be described as a balance between amount of heat generated during EM heating and amount of heat lost to the surroundings. When heat generated in a ceramic region is larger than that it is losing to the surrounding, thermal runaway initiates, leading to a significant rise of internal energy of the ceramic. The EM HXs that we consider in this work rely on heating of ceramic region by EM waves, and a coolant is employed to extract the dissipated thermal energy. The hysteresis between applied power and steady-state temperatures seen in the double S-curves raises some intriguing possibilities for efficient energy transfer between ceramic and fluid at low input EM power at safer operating temperature. In the models of [28, 29], the electric field resonance required by the double S-curve is achieved due to symmetric irradiation by EM waves. However, from power beaming applications' point of view, symmetric irradiation may not be practical as it requires two different EM power sources. The fundamental research question motivated by this discussion is

1. *Is it possible to have a double S-curve with asymmetric irradiation from one side by EM waves on ceramic laminates?*

In chapter 2 of this dissertation we answer this research question. We analyze a more practical case, where the plane wave is applied to a two-layer long and thin laminate (lossless-lossy) structure. One side of the lossy ceramic layer maintains a perfect thermal contact with the layer of lossless

dielectric. The other side of the ceramic is grounded (i.e., electric field amplitude is zero at this end). A plane monochromatic EM wave is incident of the lossless layer. Only the ceramic layer is heated by the incident EM wave and lossless dielectric heats up due to conduction heat transfer at the interface. The grounded end of the lossy layer causes internal reflection of the EM waves. We show that the resonance producing a double S-curve can be achieved in the lossy layer by choosing its thickness such that a constructive interference between the incident and reflected waves is achieved. This demonstrates a practical way of achieving the middle stable branch for the operation of an EM HX. But the question is what happens when we include fluid flow? The devices we are looking at are required to work in high power and temperature regimes (specifically on the middle and upper stable branch), and they rely on transferring energy from the ceramic to the fluid during the event of thermal runaway. To determine viability of this energy harnessing approach, some additional research questions that are needed to be answered are

2. *How does a fluid flow affect the phenomenon of thermal runaway in the ceramic and vice versa?*

3. *How effectively can we extract the elevated internal energy of ceramic region during thermal runaway with the help of a fluid flow?*

Depending on whether the coolant is in liquid or gaseous phase, energy can be transferred by conduction, convection, and the work of thermal expansion. Convection occurs as result of fluid motion, and it is present regardless of whether fluid is compressible or incompressible. For gaseous coolants, density varies as a function of absolute pressure and temperature. In the presence of gravity, the density gradients within the fluid give rise to natural convection (Rayleigh-Bénard convection) when buoyancy dominates over the viscous stresses within the fluid. Another mode of heat transfer that arises due to the fluid density gradients is the acceleration or deceleration of the gas. In order to satisfy the mass conservation, the flow field cannot be divergence free if the density gradients are nonzero. Because of additional modes of heat losses through convection and work of thermal expansion, onset characteristics of thermal runway are affected by the fluid flow as we need to supply more EM power to compensate for the additional modes of heat losses.

To provide an answer to the research question 3, it is required to define a metric that can measure the effectiveness of the energy conversion. One way of determining the effectiveness can be to evaluate the thermal efficiency of the energy conversion. In case of incompressible fluids, where the goal of an EM HX is to convert EM energy into internal energy and deliver a hot fluid at the outlet, efficiency can be defined as

$$\text{Efficiency}(\%) = \frac{\text{Heat transport through convection}}{\text{EM heat supplied}} \times 100.$$

In case of EM HX with compressible gases, density gradients produce acceleration of the gas. Beamed energy propulsion technologies rely on this working principle where the net gain in gas kinetic energy per unit volume is utilized to generate thrust. But, from ground-to-ground power beaming applications' point of view, we are interested in investigating how much mechanical power can be generated from the gas acceleration when coupled with EM heating of the ceramics. Therefore, in case of such EM HX, effectiveness can be determined by

$$\text{Efficiency}(\%) = \frac{\text{Work of thermal expansion (mechanical power generation)}}{\text{EM heat supplied}} \times 100.$$

Developing multiphysics models that can provide answers to the second and third research questions is complicated due to nonlinear nature of fluid dynamical effects, thermal runway, and their bidirectional coupling. To answer research questions 2 and 3, we break down the full problem into three different simplified and tractable multiphysics models where we focus on investigating each mode of heat transfer, i.e., forced convection, buoyancy driven convection, and gas acceleration and their impact on the energy conversion.

As the first step in multiphysics modeling efforts, in chapter 3, we investigate the coupling between thermal runaway and forced convection by looking at an EM HX with a single-phase incompressible fluid flow at slow flow speeds. We develop a 2D numerical model mimicking the operation of a layered EM HX in COMSOL Multiphysics. A triple-layer geometry of the EM HX represents a lossy ceramic slab surrounded by two channels with a plane Poiseuille flow of a single-phase lossless coolant (Figure 1.3, channels 1 and 3 contain a pressure driven plane Poiseuille flow

along the $x$-direction). Layer thicknesses are chosen such that the electric field resonance necessary for a double S-curve is achieved in the lossy layer [28, 29]. The model is then solved using two different numerical techniques; one with an implicit-explicit finite difference scheme, and second with finite element method in COMSOL Multiphysics modeling software. Results suggests that the EM HX is more efficient (about 25%) when operated on middle or upper branches compared to operation on the lower branches (about 4%). To answer the research question 2, we generate power response curves for different coolant flow rates. We find that as flow rate increases, power at which thermal runway initiates also increases as we need to compensate for heat losses through convection within the fluid. We also find that the convective heat transfer causes a drastic drop in average steady-state temperatures of the upper branch when flow speed is increased. The model described here is purely of theoretical interest. As discussed earlier, under experimental conditions boiling heat transfer will occur and single-phase approximation is no longer valid. But, this model gives insights into the impact of convective heat transfer on thermal runway and vice versa. Moreover, results presented here demonstrate how hysteresis on the double S-curve can be used for efficient energy conversion along with safer operating temperature.

Models of EM HX that couple the compressible gas dynamics with EM heating of a ceramic may provide insights into what we could observe experimentally. In such HXs, we have two additional mechanisms of energy transport; natural convection and gas acceleration (or work of expansion). In chapter 4, we focus on identifying the impact of buoyancy driven natural convection on heat transfer between the fluid and the ceramic, and chapter 5 is focused on investigating impact of gas acceleration (or work of expansion). Before we explore the impact of natural convection on the effectiveness of the energy conversion in such an EM HX, we first need to identify onset characteristics of different fluid dynamical and thermal instabilities that are simultaneously occurring in such an EM HX. When a laminar flow of a variable density fluid is coupled with EM heating of a ceramic, we have two primary instabilities that can occur simultaneously

- Natural convection in the fluid region which occurs when buoyancy dominates over viscous stresses within the fluid. These are also known as Rayleigh Bénard (RB) instabilities.
- Thermal runaway in the ceramic region which is inherent due to nonlinear nature of EM

heating of ceramics with exponentially temperature dependent loss factor.

In chapter 4, we identify onset characteristics of both the instabilities. We consider a horizontal plane Poiseuille flow of a lossless coolant which obeys the Boussinesq approximation (i.e., fluid density drops linearly with temperature) is situated on top of a lossy ceramic layer in presence of the gravity acting downward. Plane EM waves are irradiated normally on the fluid layer such that EM waves are polarized in the direction of the flow. As the ceramic heats up, fluid near the ceramic becomes less dense than fluid on the opposite channel walls. When buoyancy dominates over viscous stresses in the fluid layer, convection rolls (also known as Bénard cells) develop [30,31]. The parameter which characterizes this instability is the Rayleigh number, $\bar{Ra}$, which is a measure of importance of buoyancy relative to viscous stresses within the fluid, and is dependent on fluid properties and temperature drop across the channel. When $\bar{Ra} > \bar{Ra}_c$, where $\bar{Ra}_c$ is some critical value, buoyancy dominates and we observe instability in the form convection rolls. In our model, heat supplied to the coolant increases nonlinearly with applied power of the EM waves due to temperature dependent loss factor of the ceramic, and therefore, $\bar{Ra}$ nonlinearly depends on applied power of the EM waves. Since the thermal runaway instability occurs regardless of fluid flow, we first carry out linear stability analysis on the EM-thermal problem without fluid flow (i.e., buoyancy is absent), and identify applied powers of incident waves where such EM-thermal instabilities are present and mark them on the power response curve. After that, we carry out linear stability on the stable regions of the power response curves (i.e., applied powers where EM-thermal instabilities are absent), and find the critical Rayleigh number at which RB convection takes place. We then carry out parametric studies to identify other factors that affect the onset characteristics of RB convection. In this chapter, we describe the onset characteristics of RB convection, and results suggest that full 3D numerical simulation are required to identify how thermal runaway and RB convection instabilities interact with each other, and how this coupling affects the effectiveness of energy conversion in such EM HXs.

Another possible design of an EM HX consists of a porous ceramic which is heated by EM waves and a compressible gas flowing through the pores then delivers power at the outlet. Porous ceramics are of interest here because the heat transfer between the coolant and the ceramic is expected to

increase in a porous channel due to increased contact area for heat transfer. Before we can design such a device, we first need to first identify the compressible gas dynamics taking place at the pore-scale. Since we know that thermal runaway is a local phenomenon and can occur at the pore scale, our goal is to investigate the impact of coupling between work of expansion (gas acceleration) and thermal runaway. In chapter 5, we study the pore-scale gas dynamics when coupled with EM heating of ceramics and identify the dominant energy balance. For this, we make an idealization of the pore scale model with a very thin and long double layer laminate structure. A thin layer of a ceramic is kept in the perfect thermal contact with a thin channel carrying a compressible flow. Other end of the ceramic is grounded and thermally insulated. Depending on the fluid channel thickness we can identify following fluid flow effects (when operating pressure is of $o(1)$ atm)

- When pore-scale thicknesses are $o(10^{-6})$ m, Reynolds number, which gives the relative importance of flow inertia compared to viscous stresses within the fluid, is small. Fluid inertia terms can ignored in the fluid momentum conservation equations. Gas is expanding from high to low pressure through a very thin and long channel.

- When pore-scale thicknesses are $o(10^{-2})$ m, as considered in the MTLS experiment, flow speeds are high such that the Reynolds number is large and the viscous stresses can be ignored in the momentum conservation. Gas enters the channel at subsonic Mach number conditions and exits at near sonic flow conditions. This situation is favorable from mechanical power generation point of view.

We consider both the cases and develop two different analytical models of EM HX investigating pore-scale gas dynamics. In both of these models, we assume that the aspect ratio of the double layer EM HX is small. This allows us to expand all the unknown variables in a perturbation series in terms of the small aspect ratio. At the leading order, the cross-sectional averaged conservation laws and the equation of state are derived. In both the models, the resulting systems of nonlinear ordinary differential equations (ODEs) are then solved using ODE solver packages in MATLAB.

We first derive the lubrication model for the cases when $l_1$ is of $o(10^{-6})$ m, and identify that the gas begins to cool down locally near the outlet when work of thermal expansion dominates the heat

addition into the system. This phenomenon is known in the literature as Joule-Thompson (JT) cooling. After determining onset conditions for the JT cooling, we investigate the coupling between thermal runaway and JT cooling. We find that work of expansion (or cooling of the gas) has a little impact during thermal runaway, but it causes temperatures to drop down near the outlet. Apart from the competition between JT cooling and thermal runaway phenomena, the lubrication model may not be practical for mechanical power generation as the flow speeds are slow. To address this, we couple a high-speed compressible gaseous flow with thermal runaway in the ceramic. It is assumed that the flow Reynolds number is large and viscous stresses within the fluid are neglected. With these assumption, the compressible gas-dynamics can be described with Rayleigh flow (a frictionless flow of a gas through thin channels of uniform cross section with heat addition). This model is limited by the phenomenon of *thermal choking*. When flow velocity and temperatures are such that we reach sonic state within the channel, thermal choking occur and further heat addition is not possible without altering the inlet flow conditions. By carrying out a linear stability analysis, we determine critical EM power at which thermal choking occurs. The maximum practical Mach number that can be achieved in this model is $\frac{1}{\gamma}$, where $\gamma$ is the ratio of specific heats. Finally, we determine effectiveness of the mechanical power generation from this EM HX, and discuss how we can improve the efficiency of the operation.

In chapter 5, we show that when a compressible gas flows through a lossy porous ceramic heated by EM waves JT cooling and thermal choking occur at the pore-scale. This motivates a research question: do these heat transfer mechanisms persist at the macroscale? In chapter 6 of this dissertation, we investigate the impact of JT cooling at the macroscale. Since JT phenomenon occur at low Reynolds number, the macroscale mass and momentum conservation laws are represented by compressible Darcy's law coupled to the volume-averaged macroscale energy conservation [32]. We find that the JT cooling persist at the macroscale and causes temperature to cool down near the outlet, even when thermal runaway occurs in the ceramic. This suggests that when a high-speed compressible flow through a lossy porous media is considered, macroscale model describing mass, momentum, and energy conservation must be derived to capture pore-scale thermal choking. This can be done as a future extension of this work.

# 2 ASYMMETRIC HEATING OF A DOUBLE LAYER LAMINATE BY PLANE ELECTROMAGNETIC WAVES

One challenge in the development of EM HXs, that are expected to operate at high EM powers and temperatures, is the phenomenon of thermal runaway. The rapid rise of ceramic temperature (up to 2,000 K for silicon carbide), that occurs during the event of thermal runaway, poses a challenge toward maintaining continuous operation of an EM HX without mechanical failure of ceramic materials. To address this, the recent work of Gaone et. al in [28, 29] demonstrates an approach of resonance based control of thermal runaway which suggests that it may be possible for EM HXs to operate at elevated temperatures (up to 1,500 K for zirconia). These models consider heating of a triple layer geometry (lossless-lossy-lossless) due to a symmetric irradiation by plane EM waves. When layer thicknesses are comparable to incident wavelength, an electric field resonance is achieved in the middle lossy layer. As a result, the lossy ceramic heats up efficiently and power response curve is a double S-curve, and there exists a stable middle branch on which EM HX may operate safely and efficiently. However, from an experimental point of view, it may not be feasible to maintain symmetric illumination by EM waves as it requires to different power sources.

To tackle this experimental challenge, instead of considering symmetric irradiation of EM waves, we analyze a more practical case, where the plane wave is applied to a two-layer (lossless-lossy) structure. One end of the ceramic maintains perfect thermal contact with the lossless dielectric layer, and the other end of the ceramic is grounded (i.e., electric field vanishes at this boundary). As the EM waves are expected reflect from the grounded end, we want to investigate whether it would be possible to achieve an electric field resonance in the lossy layer. In this chapter, we show

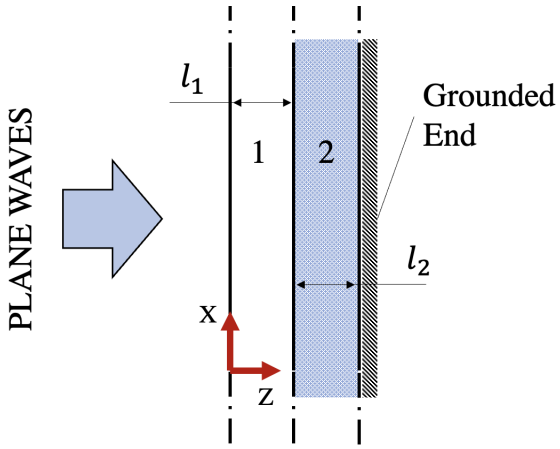


Figure 2.1: Layout of the layered structure: region 1 is a lossless dielectric material, and region 2 is a lossy ceramic.

that resonance producing a double S-curve can be achieved by choosing layer thickness such that a constructive interference between the incident and reflected waves is achieved in the lossy layer.

As done in [28, 29], we consider a long and thin geometry of the laminates, and the aspect ratio of the geometry is small. We then expand all the unknown variables in a perturbation series in term of the small aspect ratio, and determine cross-sectional averaged thermal energy conservation law at the leading order. It turns out that the ceramic temperature is uniform in space and electric field is dependent only on one spatial coordinate. This allows us to analytically solve the system of equations governing leading order electric field and ceramic temperature. Power response curves demonstrating existence of the middle stable branch are generated from the analytical model. This model is verified by comparing a power response curve generated by a numerical COMSOL model. Finally, a parametric study is carried out to identify how other parameters such as ceramic loss factor and thermal losses affect the shape of the double S-curve.

## 2.1 Problem Formulation

We consider a layered structure shown in Figure 2.1. Region 1 is a lossless dielectric layer and region 2 is a lossy ceramic. A plane EM wave, polarized in the $y$-direction and traveling in the $z$-direction, is incident on the lossless layer. Only region 2 (ceramic) is heated by EM waves, and region 1 heats up due to conduction heat transfer at the interface between 1 and 2. The frequency

of the incident EM waves is 2.45 GHz below, but the model presented here can take into account wide frequency range if the dielectric loss factor data is available.

As the dielectric loss factor of the ceramic is temperature dependent, the permittivity gradients are in the $xz$-plane, and the incident EM field is polarized in the $y$-direction, the Gauss' law (1.3a) for this scenario reduces to $\nabla \cdot \mathbf{E}_j = 0$, and the Maxwell's equation (1.3b) is reduced to the Helmholtz equation. As the incident electric field vector has only one component polarized in the $y$-direction, the strength of the electric field in regions 1 and 2 can be found by solving scalar Helmholtz equation

$$\frac{\partial^2 E_j}{\partial z^2} + k_0^2 \mu_{r_j} \left[ \epsilon'_{r_j} + i \frac{\sigma_{eff_j}(T_j)}{\omega \epsilon_0} \right] E_j = 0, \tag{2.1}$$

where subscript $j$ represents the region of the solution ($j = 1$ and $j = 2$ are lossless dielectric and ceramic regions, respectively), $E = \bar{E}/E_0$, $\bar{E}$ is the dimensional form of the electric field amplitude, $E_0$ is the strength of the plane wave, $z = \bar{z}/L_z$, $\bar{z}$ is the dimensional length along $z$, $L_z$ is the length scale in $z$, $k_0 = 2\pi L_z/\lambda_0$ is the non-dimensional wave number, $\mu_r$ is the relative permeability, $\epsilon'_r$ is the relative permittivity of the medium, $\sigma_{eff}$ is the effective electrical conductivity which increases exponentially with temperature, $T$ is temperature, $\omega$ is the angular frequency, and $\epsilon_0$ is permittivity of free space. Since region 1 is a lossless dielectric, $\sigma_{eff_1} = 0$.

We introduce non-dimensional form $T = (\bar{T} - T_A)/T_A$, where $\bar{T}$ is the dimensional temperature and $T_A$ is the ambient temperature, dimensionless time is scaled with the conduction time scale in region 2 which is defined as $L_x^2/\alpha_2$, where $\alpha_2$ is the thermal diffusivity of region 2 and $L_x$ is the length scale along the $x$-direction. Since the incident electric field is uniform in the $x$-direction, variation of $T$ along the $x$-direction can be ignored for a long and thin laminate structure. With these assumptions, the 1D time-dependent non-dimensional energy equations become

$$\eta^2 \frac{\partial T_1}{\partial t} = \alpha \frac{\partial^2 T_1}{\partial z^2}, \tag{2.2a}$$

$$\eta^2 \frac{\partial T_2}{\partial t} = \frac{\partial^2 T_2}{\partial z^2} + \eta^2 P \sigma_2(T_2) |E_2(T_2)|^2, \tag{2.2b}$$

where $\eta = L_z/L_x$ is the aspect ratio of the geometry, $T_1$ and $T_2$ are non-dimensional temperatures in regions 1 and 2, respectively, $\alpha = \alpha_1/\alpha_2$ is the ratio of thermal diffusivities of regions 1 and 2,

respectively, $P = (L_x^2 \sigma_0 E_0^2)/(2k_2 T_A)$ is non-dimensional power, $k_2$ is thermal conductivity of region 2, $\sigma_2 = \sigma_{eff_2}(T_2)/\sigma_0$ is nondimensional electrical conductivity, and $\sigma_0 = \omega\epsilon_0$. The length scale in the $z$-direction, i.e., $L_z$, is chosen to be $l_2$.

As region given by $z < 0$ is free space plane wave solution to Helmholtz equation is given by

$$E_a(x) = e^{ik_0 z} + \Gamma e^{-ik_0 z}, \tag{2.3}$$

where $E_a$ is the electric field in region 1, $\Gamma$ is the reflection coefficient between the free space and region 1. At the left boundary between the free space and 1, $\Gamma$ can be eliminated by applying tangential continuity of the electric and magnetic fields (1.10) [26]. The boundary condition on the EM fields are

$$\frac{\partial E_1}{\partial z} + ik_0 E_1 = 2ik_0, \text{ at } z = 0, \tag{2.4a}$$

$$E_1 = E_2, \ \frac{\partial E_1}{\partial z} = \frac{\partial E_2}{\partial z} \text{ at } z = \frac{l_1}{l_2} = l, \tag{2.4b}$$

$$E_2 = 0, \text{ at } z = 1 + l, \tag{2.4c}$$

and the thermal boundary conditions are

$$k\frac{\partial T_1}{\partial z} = \eta^2 Bi T_1 + \eta^2 R\left[(T+1)^4 - 1\right], \text{ at } z = 0, \tag{2.5a}$$

$$k\frac{\partial T_1}{\partial z} = \frac{\partial T_2}{\partial z}, T_1 = T_2 \text{ at } z = l, \tag{2.5b}$$

$$\frac{\partial T_2}{\partial z} = 0, \text{ at } z = 1 + l, \tag{2.5c}$$

where $\eta^2 Bi = \frac{hl_2}{k_2}$ is scaled Biot number, $h$ is the heat transfer coefficient at $z = 0$, $k = \frac{k_1}{k_2}$ is the ratio of thermal conductivities of regions 1 and 2, respectively, $\eta^2 R = \frac{\xi s_r l_2 T_A^3}{k_2}$ is the scaled radiation parameter, $s_r$ is the Stefan–Boltzmann radiation heat constant, and $\xi$ is the emissivity of the surface at $z = 0$. Boundary conditions (2.4a) and (2.4b) describe continuity of the tangential electric and magnetic fields at the interfaces between the regions, (2.4c) suggests that the layered structure is attached to the ground/metal plate at $z = 1 + l$. We assume that thermal lossless to

| Region | $\epsilon_{r_j}$ | $\sigma_j(T)[\frac{S}{m}]$ | $\rho_j[\frac{kg}{m^3}]$ | $c_{p_j}[\frac{J}{kgK}]$ | $k_j[\frac{W}{mK}]$ |
|---|---|---|---|---|---|
| $j=1$ | 6.69-133.8 | 0 | 2848 | 217 | 0.2 |
| $j=2$ | 6.69 | $0.0004e^{2.28T}$ | 2848 | 217 | 0.2 |

Table 2.1: Dielectric and thermal properties of the materials considered in the double layer laminate structure.

the surrounding are scaled with $\eta^2$; since $\eta$ is assumed to be small, thermal losses are also small. Condition (2.5a) describes the thermal losses to the surrounding by Newton's law of cooling and through radiation heat transfer, (2.5b) states that the interfaces between the regions are in perfect thermal contact, i.e., heat flux and temperature are continuous, and (2.5c) is adiabatic boundary condition at the grounded end. We first solve the coupled system (2.1) and (2.2) asymptotically using a thin domain approximation ($\eta \ll 1$) and compute the power response curve. Then we solve the system in COMSOL Multiphysics and compare the power response curves produced by both the models.

Since the main objective of this chapter is demonstration of a principle possibility of the control over thermal runaway in the structure in Figure 2.1, we do not consider here practical materials leaving that for future consideration. Thermal properties as well as $\epsilon_r$ are assumed to be temperature independent, and all the materials are non-magnetic ($\mu_r = 1$). Since another objective of this study is to find desirable permittivity of region 2, we consider a wide range of values for $\epsilon_{r_2}$. As it is shown below, the power response curves are independent of density, $\rho$, and specific heat, $c_p$, of regions 2 and 3, so we choose the same values for $\rho$ and $c_p$ in all regions. The material properties used in computations are listed in Table 2.1. For computation of power response curves, we take $\eta = 0.1$. The relation between $\sigma_2$ and $T$ is determined by curve fitting using the least squares. The 1D Helmholtz equation (2.1) can be solved exactly in terms of $T$ and the general solution has the form

$$E_j(z) = a_j e^{i\zeta_j z} + b_j e^{-i\zeta_j z}, \tag{2.6}$$

where $\zeta_j = \sqrt{k_0^2 \mu_{r_j} \left[\epsilon'_{r_j} + i\frac{\sigma_{eff_j}(T_j)}{\omega\epsilon_0}\right]}$, and the coefficients $a_j$ and $b_j$ depend on the boundary conditions (2.4). Under the thin-domain approximation $\eta \ll 1$ we can expand temperatures in the form of an asymptotic series

$$T_j = T_j^{(0)} + \eta T_j^{(1)} + \eta^2 T_j^{(2)} + o(\eta^3).$$

Substituting $T_j$ in (2.2), we get zeroth and first order terms as

$$\frac{\partial^2 T_j^{(0)}}{\partial z^2} = 0, \ \frac{\partial^2 T_j^{(1)}}{\partial z^2} = 0.$$

Applying boundary conditions (2.5), we see that both zeroth and first order solutions are independent of $z$, and the leading order solution can be written as

$$T_j^{(0)} = T^{(0)}(t).$$

The second-order correction term results in the system of equations

$$\alpha \frac{\partial^2 T_1^{(2)}}{\partial z^2} = \frac{\partial T^{(0)}}{\partial t}, \tag{2.7a}$$

$$\frac{\partial^2 T_2^{(2)}}{\partial z^2} = \frac{\partial T^{(0)}}{\partial t} - P\sigma_2(T^{(0)})|E_2(T^{(0)})|^2. \tag{2.7b}$$

Integrating (2.7a) over $(0, l)$ and (2.7b) over $(l, 1+l)$, and applying boundary conditions (2.5), we get an ordinary differential governing equation for the average temperature

$$\left(\frac{kl}{\alpha} + 1\right) \frac{\partial T}{\partial t} = P\sigma_2(T)||E_3(T)||^2 - BiT - R[(T+1)^4 - 1], \tag{2.8}$$

where $||E_2(T)||^2 = \int_l^{1+l} |E_2(z)|^2 dz$, $|E_2|^2 = E_2 E_2^*$, and $E_2^*$ is the complex conjugate of $E_2$. At steady state, the solution to (2.8) can be written as

$$P = \frac{BiT + R[(T+1)^4 - 1]}{\sigma_2(T)||E_2||^2}. \tag{2.9}$$

To find the power response curve from (2.9), we solve for $P$ for a given $T$ range, and plot $T$ as a function of $P$.

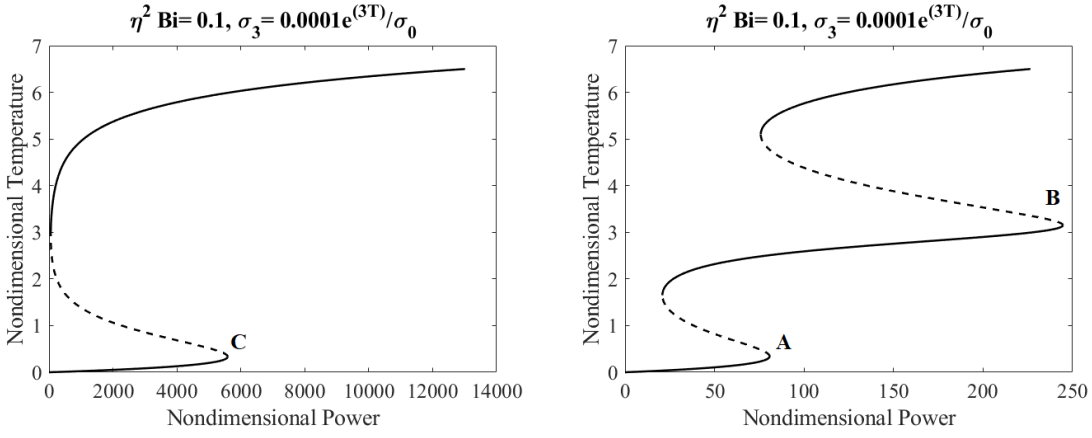


(a) (b)

Figure 2.2: Power response curves without (a) and with (b) an electric field resonance in region 3 for $\epsilon_{r_1} = 71$ and $R = 0$, stable (solid curves) and unstable solutions (dashed curves).

## 2.2 Results

### 2.2.1 Effect of Electric Field Resonance

Gaone et. al in [28,29] studied the effect of the electric field resonance on the power response curve of a layered structure. For a triple layer (lossless-lossy-lossless), a power response curve becomes a double S-curve if electric field resonance is achieved in the lossy layer. The resonance criteria considered in [28,29] are given for any odd multiple $n_1$, $n_2$ as

$$l_1 = \frac{n_1\lambda_1}{4}, \text{ and } l_2 = \frac{n_2\lambda_2}{2}, \tag{2.10}$$

where $\lambda_1$ and $\lambda_2$ are the wavelengths of EM wave in regions 1 and 2, respectively. For the geometry considered in this chapter, we follow the criteria (2.10) and choose $n_1 = 1$ and $n_2 = 3$. The ground/metal plate boundary acts as a perfect reflector of the EM waves in region 2. The total reflection causes constructive interference between incident and reflected waves, and resonance builds up in the lossy layer. From Figure 2.2, we see that as we achieve electric field resonance in the lossy layer, S-curve transitions into a double S-curve. A branch of a power response curve is stable (or unstable) if it has a positive (or negative) slope [27]. It can be seen from Figure 2.2(a)

that, when the incident power of the EM wave is higher than critical power at point C, thermal runaway is triggered there, but stabilized at the upper stable branch ($\sim 2,000\ K$). However, from Figure 2.2(b), we see that the double S-curve has a new stable (middle) branch between lower and upper branch. When incident power is above critical power at A but less than power at B, thermal runway may stabilize at the middle branch ($\sim 1,000\ K$). We also notice that because of the electric field resonance, more EM energy is trapped inside the lossy layer as compared to a non-resonant case. Therefore, critical power levels (powers corresponding to points C and A) are significantly lowered.

### 2.2.2 Comparison with COMSOL Model

We now solve the 1D system of equations (2.1)-(2.5) numerically in COMSOL Multiphysics using the finite element method. The geometry shown in Figure 2.1 is discretized using quadratic Lagrange elements. As done in [7, 33, 34], the maximum element size is chosen such that we have at least 25 elements per wavelength in both regions 1 and 2.

As the problem is nonlinear due to temperature dependent electrical conductivity, COMSOL's steady-state solver (Newton-Raphson method) may not converge if the initial guess is not close to the true solution. Therefore, we solve heat equations using COMSOL's time-dependent solver along

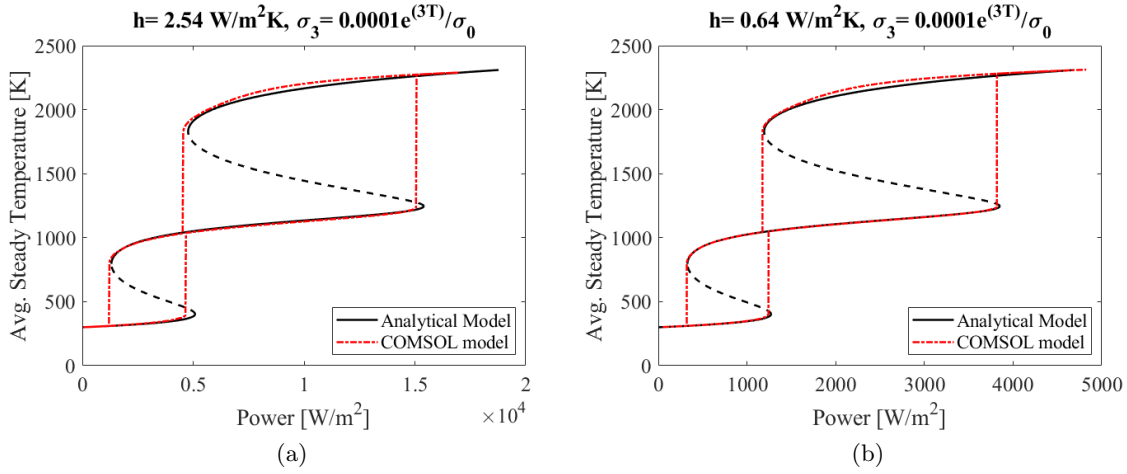


Figure 2.3: Power response curves obtained by the analytical and COMSOL models for $\eta^2 Bi = 0.1$, (a) and $\eta^2 Bi = 0.025$ (b). In both the situations, we maintain $\epsilon_{r_1} = 71$ and $R = 0$.

with an adaptive time-stepping algorithm provided in COMSOL package. The solver discretizes time derivatives using the second-order implicit backward-difference formula. The time step taken by the solver is adjusted depending on temporal gradients of the fields. Finally, the steady state is assumed to be reached when absolute difference between average temperatures at previous and current time steps falls below $10^{-6}$.

To generate power response curve, we run parametric sweeps on the applied incident powers of EM waves using the COMSOL model. Hysteresis on the double S-curve is captured by running two parametric sweeps: (i) for increasing power (ii) for decreasing powers. In both the cases, solution from the previous parameter is utilized as initial guess for the next parameter to reduce computational cost and time. With this setup, COMSOL model takes about 2 hours to generate a power response curve, whereas analytical model takes about 2 seconds to get the response curve.

As a verification, we now compare power response curves generated by both the analytical and COMSOL models. From Figure 2.3(a), we see that, for $h = 2.54\ \frac{W}{m^2K}$, the curves do not match with each other. This disagreement is due to the differences in assumptions made by corresponding models. The analytical model approximates the solution for a very thin and long ceramic channel assuming uniform temperatures in the $z$-direction. On the other hand, COMSOL model considers spatial variation of temperature in $z$. We have discussed the effect of spatially varying temperature on the power response curve in more details in [7]. We now maintain $h = 0.64\ \frac{W}{m^2K}$, and further limit thermal lossless to the surrounding making spatial variation of temperatures more uniform. We expect that as $h \to 0$, the response curves given by both models get closer. From Figure 2.3, we observe that the power response curves are in satisfactory agreement.

### 2.2.3 Parametric Studies

In this section we discuss how $\sigma_2$, $Bi$, $R$, and $\epsilon_{r_1}$ affect the shape of the power response curve. Throughout this parametric study, thermal properties are the same as in Table 1. For many typical ceramics, the loss factor increases exponentially with temperature, therefore, we assume $\sigma_2$ to have a form of $\bar{\sigma}e^{\beta T}$ [28, 29, 35].

First, we hold $\beta$ constant and vary $\bar{\sigma}$. From Figure 2.4 (a) it is seen that when $\bar{\sigma}$ is increased,

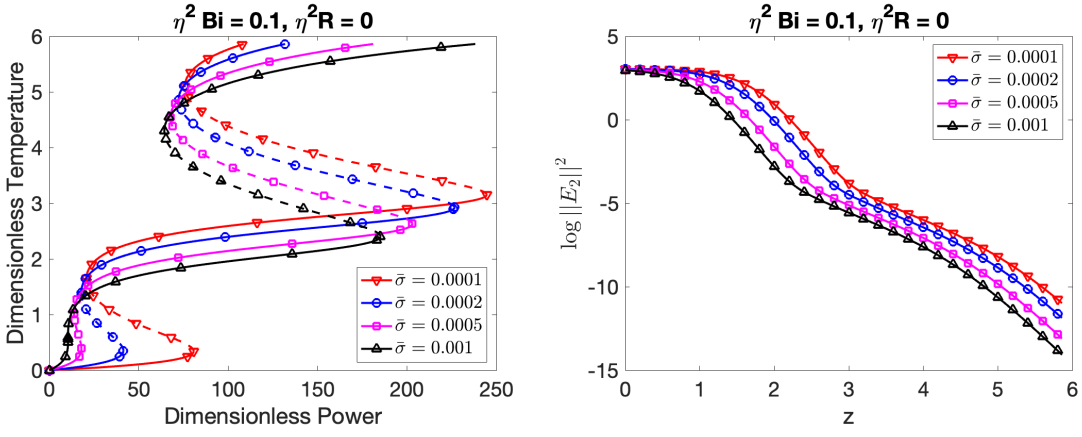


Figure 2.4: Power response curves (a), and $\log ||E_2||^2$ as a function of dimensionless temperature (b) with varying $\bar{\sigma}$ for $\beta = 3$ and $\epsilon_{r_1} = 71$.

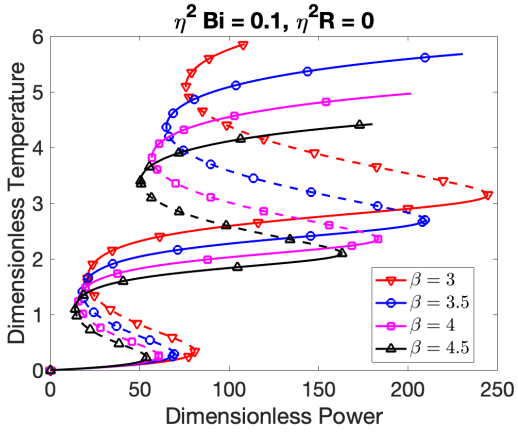


Figure 2.5: Power response curves with varying $\beta$ values for $\epsilon_{r_1} = 71$ and $\bar{\sigma} = 0.0001$.

the region of unstable solution diminishes, and for $\bar{\sigma} = 0.001$ the only stable solution is found in the low power region. To understand why an unstable solution disappears in low power region with increasing $\bar{\sigma}$, we take natural logarithm of both sides of (2.9) and take its derivative with respect to temperature for $R = 0$

$$\frac{d}{dT}\left(\log P\right) = \frac{1}{T} - \beta - \frac{d}{dT}\left(\log ||E_2||^2\right).$$

A branch of a response curve is stable (or unstable) when $\frac{dP}{dT}$ is positive (or negative). Since

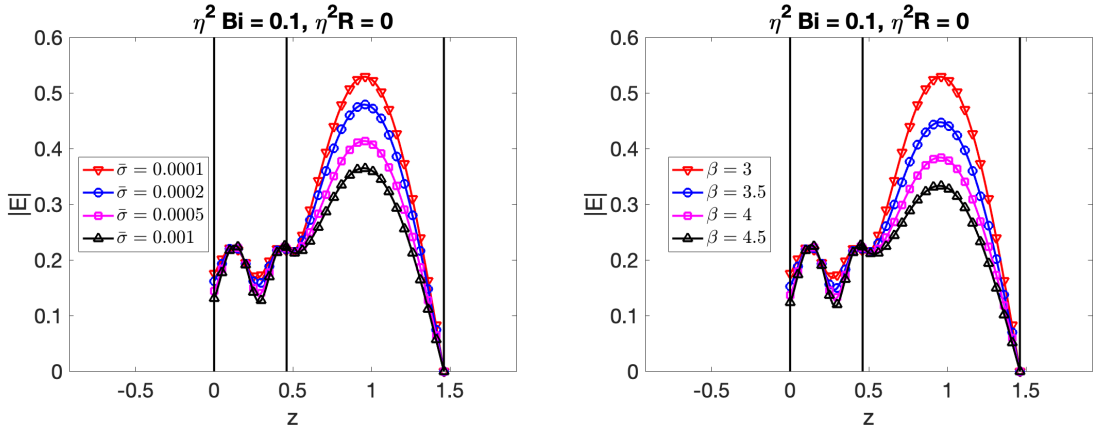


(a) (b)

Figure 2.6: Magnitude of the non-dimensional electric field as a function of $z$ for $\beta = 3$ and varying $\bar{\sigma}$, and for varying $\beta$ and $\bar{\sigma} = 0.0001$. In both the cases $\epsilon_{r_1} = 71$.

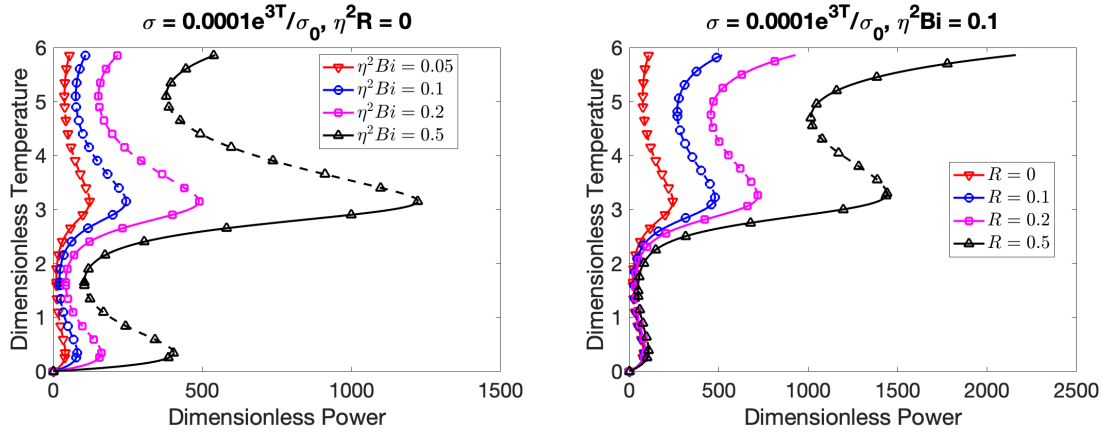


(a) (b)

Figure 2.7: Power response curves for varying $Bi$ (a) and $R$ (b) for $\bar{\sigma} = 0.0001$, $\beta = 3$, and $\epsilon_{r_1} = 71$.

$T > 0$ we satisfy

$$\frac{1}{T} > \beta + \frac{d}{dT}\left(\log ||E_2||^2\right), \tag{2.11}$$

on the stable branch. From Figure 2.4(b), we notice that in the lower unstable temperature range $-\frac{d}{dT}\left(\log ||E_2||^2\right)$ is larger when $\bar{\sigma} = 0.001$ compared to other cases. This makes combined contribution of $\beta$ and $\frac{d}{dT}\left(\log ||E_2||^2\right)$ in (2.11) smaller than $\frac{1}{T}$; as a result, only a stable solution exits in the lower temperature region. From (2.11), we observe that the range of stable temperatures

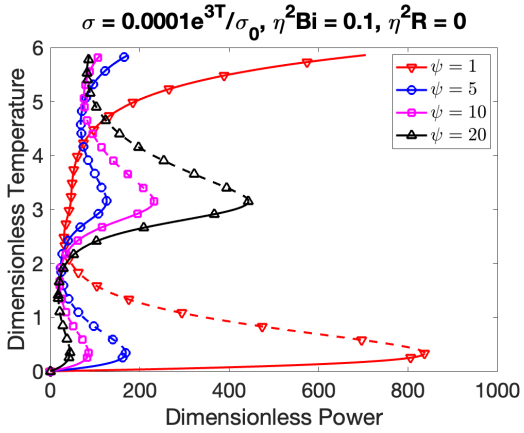


Figure 2.8: Power response curves with variations in $\psi$, where $\psi = \frac{\epsilon_{r_1}}{\epsilon_{r_2}}$. Note that for double S curve to appear we need $\psi > 1$.

may increase if $\beta$ is increased. We confirm this in Figure 2.5, where the length of the stable branch increases with increasing $\beta$. It can be also seen that with increasing $\bar{\sigma}$ or $\beta$, the EM losses also increase, which causes $|E_2|$ to decrease, as seen in Figure 2.6. Since less EM energy is available for the source of thermal energy, temperatures of the middle and top branches keep dropping down, as seen in Figures 2.4 (a) and 2.5.

In the model (2.9), two different heat removal mechanisms are included. One mode of cooling is due to convective heat transfer taking place with the surroundings at the boundary at $z = 0$. Second is radiation heat exchange between surface and the ambient. Newton's and radiation cooling are characterized by $Bi$ and $R$, respectively. Figure 2.7 (a) shows that the length of the middle branch increases as $Bi$ goes up. Moreover, critical temperature at which thermal runaway takes place remains constant, but power needed for this transition increases with $Bi$. This is expected as $P$ is proportional to $Bi$ as seen from (2.9). Since $Bi$ is a measure of convective heat losses taking place with the surroundings, experimentally it is possible to alter the values of $Bi$ by modifying surrounding conditions. In Figure 2.7 (b), we plot power responses as a function of increasing $R$. As expected, the radiation heat losses act as a strong cooling mechanism at higher temperatures, and the length of the middle branch increases with $R$. Practically, improvements in $R$ can be achieved by applying high emissivity coatings at the interface between the environment and region 1 [36]. For example, in the work of [37], surface emissivities of 0.9 are achieved at 1273 K with a double

layer coating of silicon di-oxide and aluminum oxide.

Simple cooling mechanisms, such as air or liquid cooled heat sinks may be attached to the boundary at $z = 0$ to ensure that the operating temperature values are safer for the EM HX. A critical review of different types of air cooled heat sinks along with the Nusselt number correlations can be found in [38]. By manipulating the fin structure and the external air flow rate (with the help of a fan) it is possible to achieve improvements in the heat transfer coefficient values, and thus $Bi$. Referring to Figure 2.7, by attaching heat sinks and applying high-emissivity coatings on the interface at $z = 0$, it would be practically possible to control temperatures on the middle and upper branches. In addition, the length of the middle stable branch can be altered depending on the experimental power levels of the EM radiations.

To identify the impact of dielectric constant of the region 1 on the shape of a double S-curve, we define the ratio of permittivities of regions 1 and 2 as $\psi = \frac{\epsilon_{r_1}}{\epsilon_{r_2}}$. Keeping $\epsilon_{r_2}$ constant, we change $\epsilon_{r_1}$ by varying $\psi$. When $\epsilon_{r_1}$ changes, the thickness of region 1 also changes according to the resonance criteria. From Figure 2.8, we see that when $\psi = 1$, the electric field resonance breaks, and an S-curve emerges. We also observe that the length of the middle branch increases with $\psi$. This is expected because the strength of the resonance in region 2 is greatest when $\epsilon_{r_1}$ is large and $\epsilon_{r_2}$ is small [28, 29]. Thus for a double S-curve to have a shape such that thermal runaway could be stabilized at the middle branch, having higher permittivity of the outer layer is preferable.

## 2.3 Conclusions

We describe two (analytical and numerical) models of a grounded two-layer system undergoing EM heating by plane waves. We find that the resonance producing a double S-curve can be achieved with a one-sided irradiation. Because of the electric field resonance, thermal runaway initiates at lower power levels, but may stabilize at the middle branch of the double S-curve. We apply a thin-domain asymptotic approximation and reduce the system of equations into a time-dependent ordinary differential equation. Its steady-state solution gives the power response curve. A numerical model has been also developed in COMSOL Multiphysics. Double S-curves generated by both the models are found to be in satisfactory agreement. We have shown that temperatures of the middle

and upper branches may be decreased by increasing the electrical conductivity of the lossy layer as less EM energy is available for heat generation. We show that the length of the middle branch increases with thermal losses to the surrounding. Thus the resonance-based control is, in principle, possible for the considered structure (with the ground/metal surface on the back of region 3), but it depends on the relation between dielectric constants of regions 1 and 2. For example, when a double-layer geometry consists of air in the lossless region and zirconia as the lossy ceramic, it is not possible to achieve a double S-curve because the dielectric constant of air is always going to be smaller than that of zirconia's. But, in such cases, the research question that needs to be addressed in future is whether it is possible achieve a double S-curve with different combinations of geometries and materials (e.g., air-lossless ceramic-lossy ceramic triple layer structure).

The results presented here may be significant for the development of EM HX as it has been demonstrated a practical way of achieving resonance based control over thermal runaway. While doing this, we have made several assumptions, such as uniform temperatures or constant permittivity of region 1, that may be challenging to maintain in the experiments. Additionally, we are interested to explore what happens to the middle branch when fluid flow is coupled with EM heating of ceramics. We continue this discussion in the next chapter, where we extend models of [7, 28, 29] by including a pressure-driven flow of single-phase incompressible fluids with EM heating of ceramics.

# 3 A TRIPLE LAYER ELECTROMAGNETIC HEAT EXCHANGER WITH A PLANE POISEUILLE FLOW

The working principle of a high-power EM HX considered in this work is based on interactions between a moving fluid and EM heating of a ceramic. Existence of the middle branch of the power response curves, demonstrated in [28,29] and chapter 2, suggests that it may be possible to achieve continuous operation of EM HX at a safer operating temperature. Numerical or analytical models are required to investigate viability of this energy conversion approach. In the fluid region, heat can be transferred by conduction, convection, and work of thermal expansion. As the first step towards modeling of EM HXs, in this chapter we focus on investigating coupling between nonlinear EM heating of a ceramic and convective heat transport in a fluid, and its impact on energy conversion. We consider a single-phase incompressible fluid flow, driven by an imposed pressure drop, is coupled with EM heating of a ceramic (zirconia) whose loss factor increases exponentially with temperature. Research questions that we want to address in this chapter are

1. *How does convective heat transport affect the onset of thermal runaway in the ceramic and vice versa?*

2. *What is the effectiveness of EM energy to heat conversion in such EM HX when operated on respective branches of the power power response curves?*

Results presented in this chapter are purely of theoretical interests as the single phase approximation will not be valid experimentally during thermal runaway due to boiling heat transfer. However, answers to these research questions help to provide insight into what to expect when compressible gas coolants are considered. We consider a triple-layered structure (Figure 3.1) in

which a lossy ceramic (region 3) is surrounded by lossless coolant channels (regions 2 and 4). Thicknesses of the fluid channels and the ceramic layer are $l_1$ and $l_2$, respectively, and fetch length of the EM HX is $L$. Ceramic region is heated by EM waves and coolant extracts energy from the heated region through conduction and convection. We describe a model developed in COMSOL Multiphysics and incorporate coupling between electromagnetic, fluid flow, and heat transfer phenomena by introducing a fully developed plane Poiseuille fluid flow in regions 2 and 4 along the positive $x$-axis. In order to validate the COMSOL model, we compare the results with the results from another numerical model developed using a two-step implicit-explicit (IMEX) finite difference scheme. We first consider the case with no fluid flow and visualize steady-state profiles of temperature and electric field. Then we introduce fluid flow in regions 2 and 4 by maintaining a nonzero pressure drop across the inlet and outlet. The amount of heat carried away by the fluid is characterized by the Péclet number, which is the ratio of thermal energy convected to the fluid to the thermal energy conducted within the fluid. To answer the research question 1, we generate power response curves with increasing Péclet numbers to explain how convection heat transport affects the onset characteristics of thermal runaway. To further strengthen the answer to the first question, we perform transient simulations in COMSOL multiphysics to understand temperature evolution during thermal runaway. We find that when the local maximum temperature reaches a

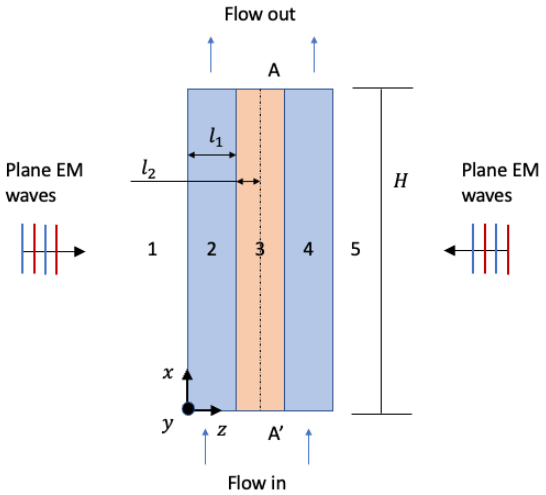


Figure 3.1: Geometry of the three layered system subjected to EM heating (symmetric about $AA'$). Media 1 and 5 are free space, layers 2 and 4 are lossless fluid and layer 3 is a lossy dielectric.

| Region | $\epsilon_{r_j}$ | $\sigma_{eff_j}(T)[\frac{S}{m}]$ | $\rho_j[\frac{kg}{m^3}]$ | $c_{p_j}[\frac{J}{kgK}]$ | $\mu_j[\frac{Ns}{m^2}]$ | $k_j[\frac{W}{mK}]$ |
|---|---|---|---|---|---|---|
| $j = 1, 5$ | 1 | 0 | - | - | - | - |
| $j = 2, 4$ [39, 40] | 45 | 0 | 1248 | 2405 | 0.004 | 0.4 |
| $j = 3$ [17] | 6.69 | $0.0004e^{2.32T}$ | 2848 | 217 | - | 0.2 |

Table 3.1: Considered Material Properties for Simulations

critical value, thermal runaway is triggered locally resulting in generation of hotspots. To answer the research question 2, we determine effectiveness of the energy absorption by the fluid by calculating the overall thermal efficiency of the considered EM HX and show how higher efficiencies can be achieved along with having control over thermal runaway. Since this chapter is motivated solely by theoretical interests, for simplicity, we consider Péclet numbers values such that conduction and convection heat transfer within the fluid are comparable. But, in upcoming chapters we consider high flow speeds whenever modeling efforts are aimed towards gaining experimental insights.

In the previous chapter, we discussed an experimental challenge behind maintaining electric field resonance required for the double S-curve, which is temperature dependent dielectric constant of the fluid region. As the fluid's permittivity changes with temperature, wavelength of EM waves within the fluid also changes. Because of this, maintaining electric field resonance required for the double S-curve is difficult for continuous operation of an EM HX. This raises another question

3. *How sensitive is the double S-curve to permittivity variations within the fluid region?*

To answer this question, we carry out a parametric study on fluid permittivity. We break the electric field resonance in the lossy layer by increasing fluid's dielectric constant and look at how length of the middle branch changes with the permittivity ratio.

## 3.1 Development of Numerical Models

We consider plane EM waves incident from both sides with the assumption that incoming waves are polarized along the $y$-direction and traveling in the $z$-direction. The time-averaged power density of the incident plane wave is

$$P_{av} = \frac{E_0^2}{2\Upsilon}, \tag{3.1}$$

where $E_0$ is the strength of incident electric field, and $\Upsilon$ is characteristic impedance of free space. In order to achieve an electric field resonance necessary to produce the double S-curve, we need to satisfy following conditions [28]

$$l_1 = \frac{n_1 \lambda_2}{4}, \text{ and } l_2 = \frac{n_2 \lambda_3}{4}, \tag{3.2}$$

where $l_1$ and $l_2$ are thicknesses of regions 2 and 3. $n_1$ and $n_2$ are any odd integers, and $\lambda_2$ and $\lambda_3$ are wavelengths in regions 2 and 3, respectively. In all of our simulations presented in the paper, we take $n_1 = 1$, $n_2 = 3$, and $L = 20l_2$.

An incompressible and lossless viscous fluid in region 2 is composed of equal parts glycerin and water (as this fluid may be characterized as a low-loss liquid [39] in microwave (MW) regime). The frequency $f$ of incident EM waves is assumed to be 2.45 GHz. Dielectric and thermal properties of glycerin are taken from [39] and [40], respectively. Region 3 is a lossy zirconia; its material properties are given in [17]. A full exploration of the temperature-dependent material properties is left for the future development. However, the electric field resonance, which is essential for the existence of the middle branch, is particularly sensitive to temperature variations in the permittivity. As a leading-order approximation, we determine intervals about the reference permittivity over which the double S curve would exist. We think this gives insights on the impact of variable permittivity on this phenomenon, while providing a tractable problem to address. All the materials used are assumed non-magnetic ($\mu_r = 1$). In addition, only the material in the middle layer (region 3) absorbs MW energy, and the outer layers (regions 1, 2, 4, and 5) are considered lossless. The material properties used in this modeling work are summarized in Table 3.1.

Since the plane waves are polarized along the $y$-direction, Maxwell's equations governing electric field in both regions reduce to Helmholtz's equations. We scale the electric field with $E_0$. Lengths along the $z$-direction in regions 2 and 3 shown in Figure 3.1 are scaled with $l_1$. Lengths along the $x$-direction in both regions are scaled on $L$. The nondimensional temperature is given as $T_j = \frac{\bar{T}_j - T_A}{T_A}$, where $T_j$ and $\bar{T}_j$ are the scaled deviation temperatures from ambient and the dimensional temperatures in regions $j = 2, 3$, respectively, and $T_A$ is the ambient temperature. In our models, $T_A$ is set at 300 K. Time is scaled on the conduction time scale in region 3 as $\frac{l_1^2}{\alpha_3}$, where $\alpha_j = \frac{k_j}{\rho_j c_{p_j}}$ is

thermal diffusivity, $k_j$ is thermal conductivity, $\rho_j$ is density, and $c_{p_j}$ is specific heat of the respective regions 2 and 3. Finally, the velocity of fluid is scaled on $\bar{V}$, where $\bar{V} = \frac{|P_g|l_1^2}{2\mu}$, $|P_g|$ is the magnitude of pressure gradient maintained across the inlet and outlet. The resulting set of nondimensional governing equations for the electric field amplitude and the energy balances in regions 2 and 3 is

$$\frac{\partial^2 E_2}{\partial z^2} + \eta^2 \frac{\partial^2 E_2}{\partial x^2} + \zeta_2^2 E_2 \quad = 0, \tag{3.3}$$

$$\frac{\partial^2 E_3}{\partial z^2} + \eta^2 \frac{\partial^2 E_3}{\partial x^2} + \zeta_3^2 E_3 \quad = 0, \tag{3.4}$$

$$\frac{\partial T_2}{\partial t} + \eta \alpha Pe \left( u \frac{\partial T_2}{\partial x} \right) = \alpha \left[ \frac{\partial^2 T_2}{\partial z^2} + \eta^2 \frac{\partial^2 T_2}{\partial x^2} \right], \tag{3.5}$$

$$\frac{\partial T_3}{\partial t} = \frac{\partial^2 T_3}{\partial z^2} + \eta^2 \frac{\partial^2 T_3}{\partial x^2} + P|E_3|^2 \sigma_3(T_3), \tag{3.6}$$

where $E_2$ and $E_3$ are nondimensional electric field strengths in region 2 and 3, respectively, $\eta = \frac{l_1}{H}$, $\zeta_2^2 = k_0^2 \epsilon_{r_2}$, and $\zeta_3^2 = k_0^2 \left[ \epsilon_{r_3} + i \frac{\sigma_{eff_3}(T_3)}{\omega \epsilon_0} \right]$ are nondimensional wavenumbers of EM waves in regions 2 and 3, respectively, $k_0 = \frac{\omega}{c} l_1$ is the nondimensional wavenumber of EM waves in free space, $\omega$ is angular frequency, $c$ is the speed of EM wave in free space, $\epsilon_0$ is permittivity of free space, $\epsilon_{r_2}$ and $\epsilon_{r_3}$ are relative permittivities of regions 2 and 3, respectively, $T$ is temperature, $\sigma_3(T) = \frac{\sigma_{eff_3}(T_3)}{\omega \epsilon_0}$ is temperature dependent dimensionless effective electrical conductivity, $\alpha = \frac{\alpha_2}{\alpha_3}$, $Pe = \frac{l_1 \bar{V}}{\alpha_2}$ is the Péclet number, $v$ is the nondimensional fluid velocity along the positive $x$-direction, and nondimensional power $P = \frac{1}{2} \frac{E_0^2 \omega \epsilon_0 l_1^2}{k_3 T_A}$.

Since our focus in this work is on the coupling between the electric field strength and temperature, we chose an exact laminar solution to the Navier-Stokes equations, fully-developed plane Poiseuille fluid flow is given by the equation

$$u(z) = -(z^2 - z), \tag{3.7}$$

Although this assumption is limited in terms of the Reynolds number of the flow, our formulation is amenable for larger Reynolds numbers if we include Taylor dispersion for sufficiently long channels [41].

As region 1 is free space, for $z < 0$,

$$E_1(x) = e^{ik_0 z} + \Gamma e^{-ik_0 z}, \tag{3.8}$$

where $E_1$ is the electric field in region 1, $\Gamma$ is the reflection coefficient between regions 1 and 2. At the left boundary between regions 1 and 2, $\Gamma$ can be eliminated by applying tangential continuity of the electric and magnetic fields [26]; that yields

$$\frac{\partial E_2}{\partial z} + ik_0 E_2 = 2ik_0. \tag{3.9}$$

Similarly, at the interface between regions 2 and 3, tangential continuity of the electric and magnetic fields can be written as

$$\begin{aligned} E_2 &= E_3, \\ \frac{\partial E_2}{\partial z} &= \frac{\partial E_3}{\partial z}. \end{aligned} \tag{3.10}$$

Since the problem is symmetric along $AA'$, we have,

$$\frac{\partial E_3}{\partial z} = 0. \tag{3.11}$$

At the top and bottom boundaries, we apply

$$\frac{\partial E_2}{\partial x} = \frac{\partial E_3}{\partial x} = 0. \tag{3.12}$$

For the energy equations (4) and (5), at the left boundary between regions 1 and 2 we have convective losses to the surroundings characterized by Newton's law of cooling as

$$k\frac{\partial T_2}{\partial z} = BiT_2 + R[(T_2 + 1)^4 - 1], \tag{3.13}$$

where $k = \frac{k_2}{k_3}$, $Bi = \frac{hl_1}{k_3}$ is the Biot number, $h$ is the heat transfer coefficient, $k_j$ is the thermal conductivity of region $j$, $R = \frac{\xi s_r l_2 T_A^3}{k_3}$ is the radiation parameter, $s_r$ is the Stefan–Boltzmann

radiation heat constant, and $\xi$ is the emissivity of the surface at $z = 0$. In our simulations presented in this chapter, we specify $h = 5$ W/m$^2$K and $\xi = 0.1$ which are taken from [15] for natural convection with the surrounding air and black-body radiation for ceramic surfaces. At the interface between regions 2 and 3, we assume perfect thermal contact

$$\begin{aligned} T_2 &= T_3, \\ k\frac{\partial T_2}{\partial z} &= \frac{\partial T_3}{\partial z}. \end{aligned} \tag{3.14}$$

At the line of symmetry $AA'$,

$$\frac{\partial T_3}{\partial z} = 0. \tag{3.15}$$

Along the top boundaries of regions 2 and 3 we prescribe no diffusive heat flux condition

$$\frac{\partial T_2}{\partial x} = \frac{\partial T_3}{\partial x} = 0. \tag{3.16}$$

The lower boundary at $y = 0$ is maintained at the fixed ambient temperature in regions 2 and 3,

$$T_2 = T_3 = 0. \tag{3.17}$$

We develop two models to solve the system (3.3)-(3.7): the one with a finite difference scheme implemented in MATLAB, the other is with finite element method (FEM) in COMSOL Multiphysics. We consider two different cases: the first is with no fluid flow, i.e, $Pe = 0$, and the second with fluid flow $Pe \neq 0$. In both cases, we compare steady-state temperature profiles produced by both the numerical models.

### 3.1.1 Finite Difference Model

The finite difference scheme presented here is second order both in time and space. Spatial derivatives of electric field in (3.3) and (3.4) are discretized using second-order central difference scheme. The final pentagonal linear system of equations is solved using the GMRES solver [42]. Energy equations in both regions are then solved using a two-step alternating-direction implicit-explicit

method [43]. The nonlinear heat source in region 3 is treated explicitly and the rest of the terms are treated implicitly. At each step we solve the system of linear equations using a standard tridiagonal solver [44]. The external boundary and interface conditions involving derivatives are discretized with central-differencing with the ghost points method [45].

Due to explicit treatment of the nonlinear heat source, the method is unstable for larger time steps. After carrying out numerical experiments, we find temporal step size 0.1 is sufficient when there is no thermal runaway, and when it is expected, we choose 0.01 as step size when discretizing time derivatives. Section of spatial step size is based on Nyquist criterion [46]:

$$S_j < \frac{\lambda_j}{2}, \tag{3.18}$$

where $S_j$ is the maximum size of the cells. According to (3.18), the step size in both the $z$- and $x$-directions should be such that we have at least 2 cells per wavelength in both regions. As a general rule for solving Helmholtz equations, 10 to 12 grid points per wavelength are sufficient for producing reasonable accuracy at smaller wavenumbers [47]. With this consideration, we discretize each region such that we have 61 uniformly distributed grid points along the $z$ and $x$-directions. In other words, we choose approximately 66 and 10 cells per wavelength along the $z$ and $x$-directions. In addition, convergence tests are carried to determine number of grid points in each region. We find that change in average and maximum $T$ and $|E|$ is below $10^{-2}$ when grid points in each region increased from 51 to 61.

### 3.1.2 COMSOL Multiphysics Model

The set up for setting up the COMSOL model is similar to the one discussed in the last chapter. The geometry is discretized using Lagrange triangular elements. In [7, 33, 34], the maximum element size is chosen such that we have at least 15 elements per wavelength throughout the computational domain. To determine the mesh size, we again carried out converge tests and throughout the computations below, we discretize both the domains with approximately 25 elements per wavelength.

As the problem is highly nonlinear due to the temperature dependent electrical conductivity in the zirconia, we solve energy equations using COMSOL's time-dependent solver along with the

proprietary adaptive time-stepping algorithm provided in COMSOL package. The solver discretizes time using the second-order implicit backward-difference formula. The time step taken by the solver is adjusted depending on temporal gradients of the fields. Finally, the steady state is assumed to be reached when absolute difference between average temperatures at previous and current time steps falls below $10^{-6}$. COMSOL Multiphysics 5.3a package runs on a server which has two Intel(R) Xeon(R) CPU E5-2643 processors and 128 GB of installed RAM. Typical time taken for a simulation to perform is about 10 minutes. In comparison, the IMEX model takes about 25 minutes to reach the steady-state. This expected as the IMEX model is developed for a fixed time step, and the COMSOL model utilizes an adaptive time stepping algorithm.

To generate a complete power response curve (stable branches), we conduct two parametric studies on the applied power values using the COMSOL model. First, we run a parametric sweep for increasing applied powers, and then for decreasing incident powers. In both the cases, we use the final solution from the previous parameter as an initial guess for the next parameter to save computational costs. With this continuation approach, we can use Newton-Raphson steady-state solver for the parametric studies. With this approach total time taken to generate one power response curve is about 3 hours.

## 3.2 Results

Firstly, we verify the COMSOL model by comparing electric field and temperature profiles with the ones produced by the finite difference model model. The agreement between them is presented in Appendix A and also published in [48].

The results discussed below are produced using the COMSOL model. We now introduce fluid flow along the positive $x$-direction in region 2 by keeping nonzero $Pe$ in the model. In addition to conduction, heat is now transferred by convection due to the fluid motion in region 2. The rate at which fluid delivers the energy at the outlet (per unit cross-section area of the channel in $\mathrm{W/m^2}$) is given by

$$P_{abs} = \frac{k_2 T_A}{l_1} Pe \int_0^1 T_o v_o dx, \tag{3.19}$$

where $T_o$ and $v_o$ are temperature and fluid velocity profiles at the outlet, respectively. For $Pe \neq 0$, the EM losses in the ceramic are balanced by $P_{abs}$ and thermal losses to the surrounding. Overall efficiency of thermal energy production can be defined as the ratio of thermal power delivered by the fluid at the outlet to incident power of EM waves. Using the expression above, we calculate the overall thermal efficiency of the power absorption $\chi_{\text{total}}$ as

$$\chi_{\text{total}} = \frac{P_{abs} l_1}{P_{in} L} \times 100 \ (\%). \tag{3.20}$$

The results from the computational model are organized as described below.

- For $Pe \neq 0$ we increase the applied power, $P_{av}$, until we achieve the onset of thermal runaway. At the steady-state, we observe a hotspot in the ceramic region when transition from lower to middle stable branches take place. By looking at transient temperature profiles during this transition, we explain the mechanisms behind the hotspot.

- To understand how onset characteristics of thermal runaway are affected by convective heat transfer, we generate power response curves for increasing $Pe$. By calculating thermal efficiencies using (3.20), we then quantify effectiveness of the energy exchange when operated on respective branches of the response curve. We also investigate the impact of radiation heat transfer on onset characteristics of thermal runaway by producing power response curves with increasing radiation heat losses.

- Finally, to quantify how sensitive a double S-curve is to the electric field resonance in the lossy layer, we carry out a parametric study on $\epsilon_{r_2}$ while keeping $\epsilon_{r_2} = 6.69$.

### 3.2.1 Local Onset of Thermal Runaway

Firstly we set $Pe = 8.6$ and keep increasing the applied powers, and steady-state $T$ and $|E|$ profiles for this scenario are plotted in Figure 3.2. When $P_{av} = 8,000$ W/m$^2$, the EM HX operates on the lower branch of the response curve, and overall temperatures are low as expected. But, when incident power is $P_{av} = 15,000$ W/m$^2$, the EM HX operates on the middle stable branch of the

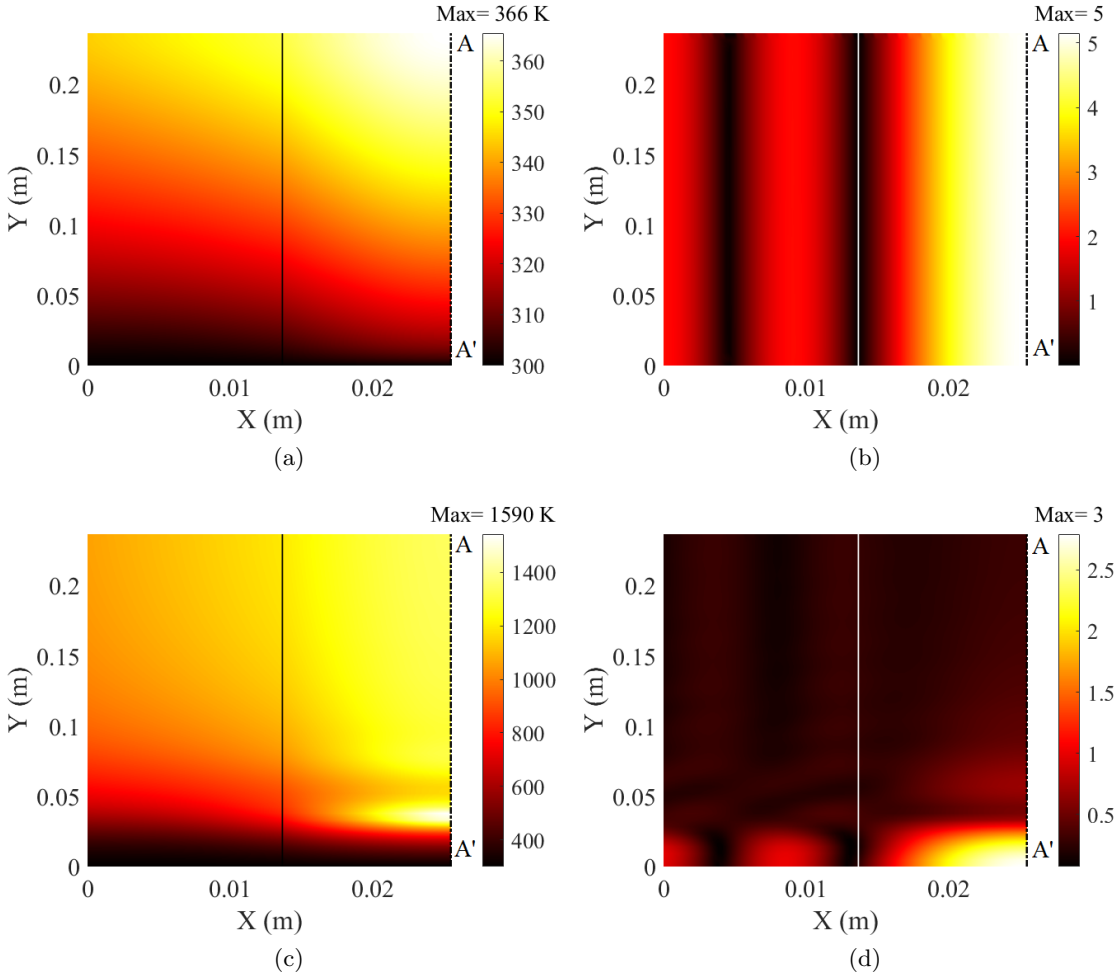


Figure 3.2: Steady-state dimensional $T$ profile when $P_{av} = 8,000$ W/m$^2$ (a) and $P_{av} = 15,000$ W/m$^2$ (b), and dimensionless $|E|$ profiles at the steady-state for $P_{av} = 8,000$ W/m$^2$ (c) and $P_{av} = 15,000$ W/m$^2$ (d). In these simulations $Pe = 8.6$ and $\eta = 0.06$. The solid line represents the interface between regions 2 and 3 and AA' is the axis of symmetry.

double S-curve (this can be confirmed by looking at power response curves shown in Figure 3.3). As a result of this transition from the lower to middle stable branch, a hotspot is generated in the ceramic region indicating localized EM heating. This observation is consistent regardless of whether a fluid flow is present or absent (see Figure A.2 and Figure A.4). This raises another research question

- Which mechanisms are responsible for hotspot generation in the ceramic region?

To answer this question we look at the transient behavior of temperatures in the ceramic when

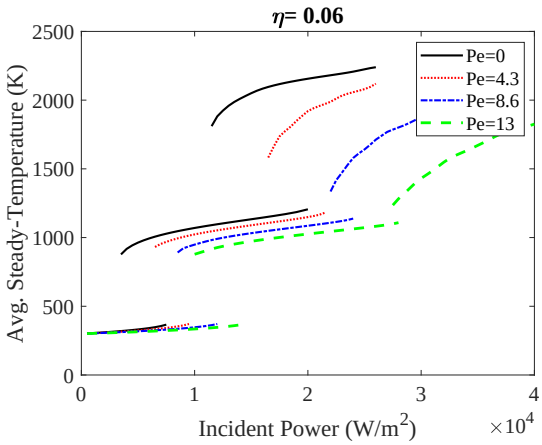


Figure 3.3: Stable branches of power response curves for $\eta = 0.06$ and different Péclet numbers produced using COMSOL Multiphysics model.

the EM HX operates on the middle stable branch. In Figure 3.4, we plot snapshots of transient temperature profiles when a hotspot appears in the ceramic region for $P_{av} = 12,000$ W/m$^2$, $Pe = 4.3$. In Figure 3.5 evolution of maximum and average temperatures, $T_{max}$ and $T_{avg}$, with time is plotted for different $P_{av}$ and $Pe$. To produce both figures, $P_{av}$ and $Pe$ are chosen such that steady-state solutions are on middle stable branch when initial temperature is maintained at 300 K.

We explain the transient behavior in three stages.

STAGE $I$: This region is before initiation of thermal runaway. Temperatures in region 3 are small and $\sigma_3 \approx 0.0004$. In that case $|E_3|^2$ is large, but $\sigma_3$ is small such that the heat source $P|E_3|^2\sigma_3(T)$ is balanced by $P_{abs}$, thermal losses at the boundaries, and a small instantaneous temperature rise.

STAGE $II$: In this region thermal runaway is observed. Instantaneous temperature profiles during this stage are shown in Figure 3.4 for $P_{av} = 12,000$ W/m$^2$ and $Pe = 4.3$. Transient $T_{max}$ and $T_{avg}$ for this case are shown in Figure 3.5 (b). We observe that when $t = 64$ in Figure 3.4 (a), maximum temperature reaches a critical value and thermal runaway is about to instigate. When $t = 66$, a significant rise in maximum temperature (from 649 K to 1,651 K) takes place indicating the initiation of thermal runaway, and a local hot spot is observed as seen in Figure 3.4 (b). At this critical moment, the EM losses in region 3, where the temperature is maximum, are large enough

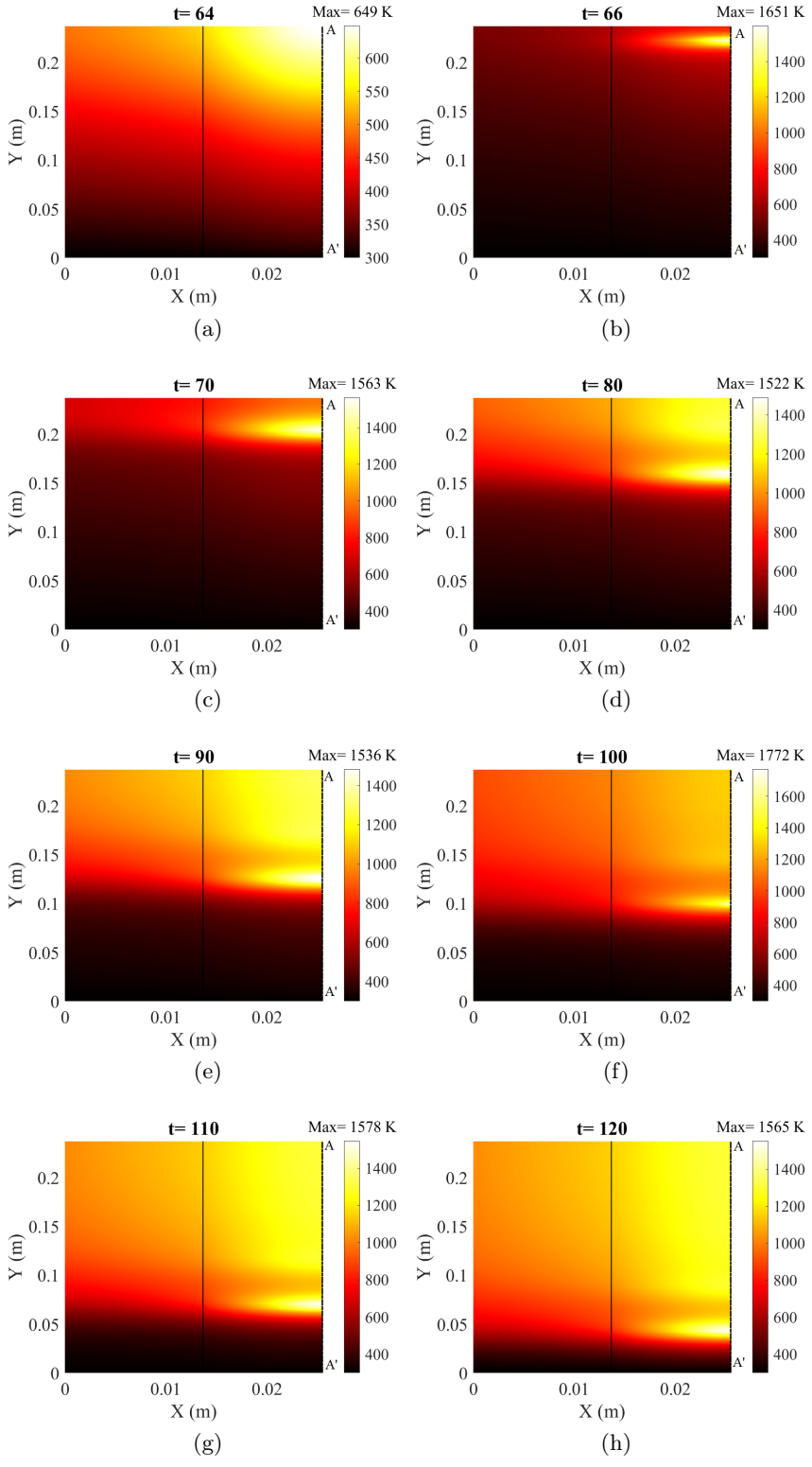


Figure 3.4: Transient evolution of the hotspot observed in STAGE *II* for $P_{av} = 12,000$ W/m$^2$, $Pe = 4.3$. The solid line represents the interface between regions 2 and 3 and AA' is the axis of symmetry.

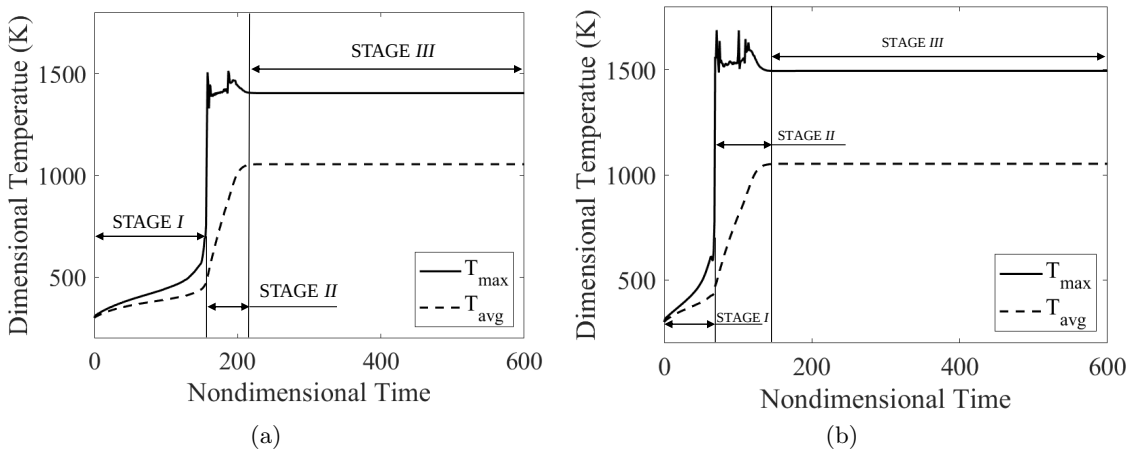


Figure 3.5: Transient evolution of maximum and average temperatures $T_{max}$ and $T_{avg}$ given by COMSOL model when $P_{av} = 9,000$ W/m$^2$, $Pe = 0$ (a) and $P_{av} = 12,000$ W/m$^2$, $Pe = 4.3$ (b). Parameters $P_{av}$ and $Pe$ are chosen such that EM HX operates on the middle branch when initial temperature is 300 K. STAGE *I* is heating when there is no thermal runaway, STAGE *II* is stabilization of thermal runaway on the middle branch, and STAGE *III* is when steady-state is achieved.

such that thermal losses at the boundaries and $P_{abs}$ cannot balance the local heat source, which results in the large instantaneous temperature rise and a local hotspot. Oscillations are seen in the transient $T_{max}$ (in Figure 3.5) during STAGE *II* indicate that mechanisms of heat generation (EM losses) and combined thermal losses ($P_{abs}$ and losses at the boundaries) instantaneously compete with each other. Since the maximum temperature is expected to occur near the outlet (due to the insulated boundary condition), the hotspot first appears neat the outlet. As time progresses, thermal energy in the hotspot is conducted towards the colder region, and some energy is transferred by the fluid along with heat losses to the environment. As a results, the hotspot travels towards the negative $x$-direction as seen from Figure 3.4 (b)-(g). As the hotspot moves down, $P_{abs}$ increases, as more time is available for the fluid to collect heat from the ceramic as it moves from inlet to outlet. Finally, the combined thermal losses begin to dominate heat generation and the thermal runaway stabilizes when $t = 120$ in Figure 3.4 (h).

STAGE *III*: During this stage, combined thermal losses balance the heat generation and the equilibrium is achieved.

The key observation from this study is that the thermal runaway is governed by the local temperatures. The slope of $T_{max}$ at the critical point is much larger than the slope of $T_{avg}$. In

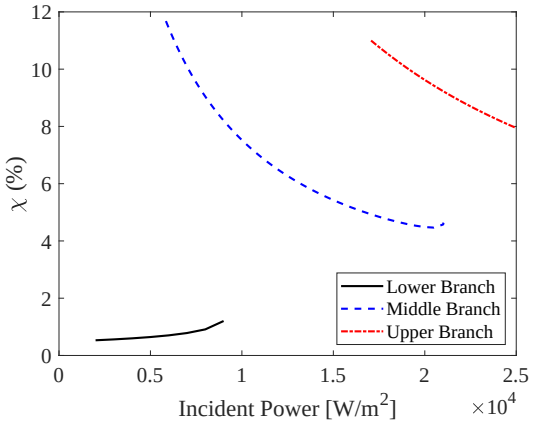


Figure 3.6: Overall thermal efficiency of the device operating on respective branches of power response curves for $Pe = 4$.

other words, a rapid rise in local maximum results in a rise of average temperature during thermal runaway. This observation is consistent with results in [7, 17]; as soon as the local maximum temperature reaches a critical value, thermal runaway initiates resulting in appearance of the hot spot. In our simulation for $Pe = 0$ and $Pe \neq 0$, we observe critical $T_{max} \approx 650$ K. This result is significant for practical applications because it gives us insight on the dynamic nature of thermal runaway phenomena. The mechanism we uncovered from the transient simulation is expected to persist regardless of whether a fluid is in gaseous or liquid state. When experimental trials are to be conducted on an EM HX, local hotspots are going to occur when we operate on the middle stable branch. Thermal safety of an EM HX during continuous operation at such power levels may be determined by investigating whether the ceramic material can dissipate the local heat source without compromising its mechanical structure.

### 3.2.2 Power Response Curves and Effectiveness Calculations

To understand how onset characteristics of thermal runaway are affected by the fluid flow, we generate power response curves for increasing $Pe$ values. We first choose velocity scales such that $Pe \sim o(1)$ for $\eta = 0.06$. When we have a fluid flow in region 2, we introduce additional mode of heat transfer through forced convection which is expected to increase with $Pe$. From (3.19), as $P_{abs}$ increases with $Pe$, we expect that $P_{av}$ required to achieve transition from the lower to

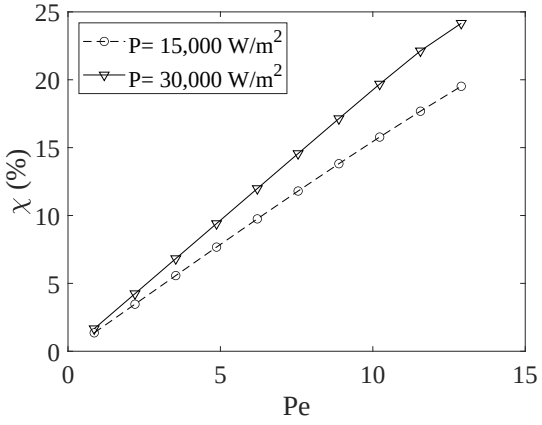


Figure 3.7: Efficiency of the considered EM HX as a function of $Pe$ when operated on the upper and middle branch for $\eta = 0.06$.

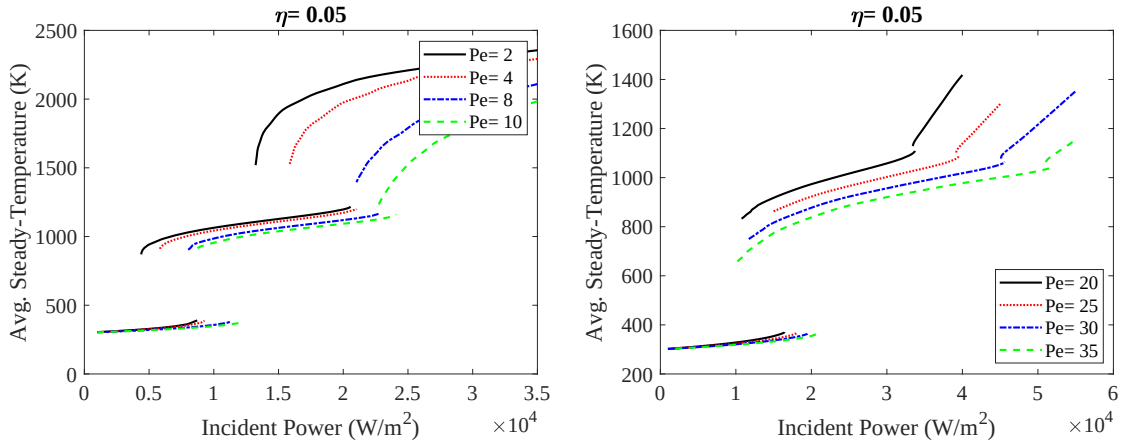


(a) (b)

Figure 3.8: Stable branches of power response curves for different Péclet numbers produced using COMSOL Multiphysics model.

middle branch would increase with $Pe$ as we need to compensate for additional heat losses through convection. This can be confirmed by looking at Figure 3.3: $P_{av}$ at which transition from lower to middle stable branches occurs increases with $Pe$.

The temperature profiles plotted in Figure 3.2 and the transient nature of the hotspot generation suggest that the EM HX may be able to operate efficiently when operated on the middle stable branch in comparison with operation on the lower stable branch. To quantify that we calculate $\chi$

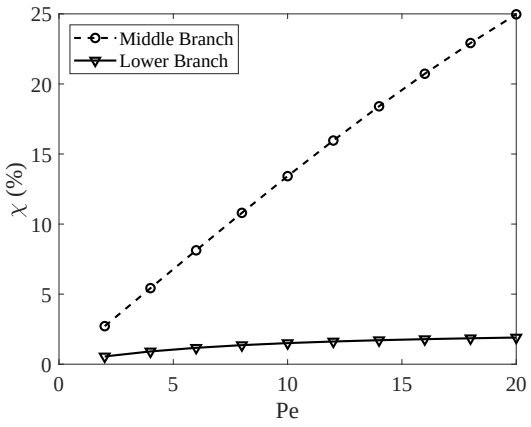


Figure 3.9: Overall thermal efficiency as a function of $Pe$ when device is operated on lower and middle branches. Efficiencies for lower and middle branches are calculated for $P_{av} = 7,000\ W/m^2$ and $P_{av} = 15,000\ W/m^2$, respectively.

when the EM HX is operated on lower, middle, and upper branches for $Pe = 4$, and plot $\chi$ as a function of $P_{av}$ in Figure 3.6. Although, for $Pe = 4$, average fluid temperatures when the device operates on the upper branch are much higher ($\sim 2,500$ K) compared to cases when it operates on the middle branch ($\sim 1,000$ K), the middle branch is found to be more efficient for $P_{av}$ between $5,800 - 6,300$ W/m$^2$. This plot demonstrates how the devices operated on the middle branch can operate efficiently even when average temperatures are moderate ($\sim 1,000$ K). Although the model we consider here does not replicate practical conditions, we can infer from this result that the most efficient operation of an EM HX may be achieved when high ceramic temperatures are achieved at low applied powers (e.g., leftmost turning point on the double S-curve) regardless of whether a fluid is in gaseous or liquid state. The electric field resonance in the lossy region causes efficient heating of the ceramic and the middle stable branch allows the EM HX to operate at higher temperatures but at relatively low applied powers. As a result, highest efficiency is observed near the leftmost turning points of the response curve.

Another observation we make from Figure 3.3 that average temperatures of upper and middle stable branches keep dropping as $Pe$ is increased. Especially, the upper branches undergo drastic reduction in temperatures compared to the middle and lower branches. This behavior seems plausible because at higher $Pe$ the rate at which fluid extracts heat from the heated ceramic increases as seen from (3.19). In general, the amount of heat transfer through convection between coolant and

a heated region depends on the temperature difference between them. Convection is large when temperature difference is large. When EM HX operates on the upper branch, there naturally exists a large temperature difference between the coolant and ceramic compared to when EM HX is on middle or lower branch. As a result, the convection heat transfer between the coolant and ceramic is large. In Figure 3.7, we plot $\chi$ as a function of $Pe$ for $P_{av} = 15,000$ W/m$^2$ and $P_{av} = 30,000$ W/m$^2$. Parameter $P_{av}$ is chosen such that steady-state solution is on the middle or upper branches for all considered values of $Pe$ in this parametric study. From Figure 3.7, slopes of the respective curves suggest that the rate at which $P_{abs}$ increases with $Pe$ is larger for the upper branch compared to the middle one. In other words, the rate at which convection heat transfer increases with $Pe$ is larger on the upper branch. This explains why the upper branches undergo drastic temperature drop off with increasing $Pe$.

We now generate power response curves for $Pe \sim o(1)$ and $Pe \sim o(\frac{1}{\eta})$ for $\eta = 0.05$. Response curves for this case are shown in Figure 3.8. As found previously, the convective heat transport within the fluid region causes reduction in temperature of middle and upper branches with $Pe$. As a result, hysteresis on the upper branch keep on diminishing with $Pe$ as seen in Figure 3.8(a). When Péclet numbers are moderate, i.e., $Pe = o(\frac{1}{\eta})$, from Figure 3.8(b) we see that hysteresis is minimal, and transition between middle and upper branches is not as abrupt as compared to cases when $Pe \sim o(1)$. Next, we plot $\chi$ as a function of $Pe$ in Figure 3.9, when the steady-state solutions are on middle and lower branches. To generate the plot, $P_{av}$ is chosen such for $o(1) \leq Pe \leq o(\frac{1}{\eta})$, the steady-state solution are on the lower and middle branches when initial temperature is maintained at 300 K and 1,000 K, respectively. We observe that the operation on the middle branch is more efficient (about 20%) compared to operation on the lower branch (about 1%). Another observation is that $\chi$ increases almost linearly with $Pe$ when $o(1) \leq Pe \leq o(\frac{1}{\eta})$.

Another heat loss mechanism that may affect the shape of a double S-curve is the radiation heat transfer at the boundaries. When an EM HX operates on the middle or upper stable branches, convective heat transfer (described by the Newton's law of cooling) is small compared to radiation heat losses. In Figure 3.10, we plot power response curves with increasing radiation emissivity, $\xi$, at $z = 0$. We observe that as the radiation losses improve, the length of the middle branch increases,

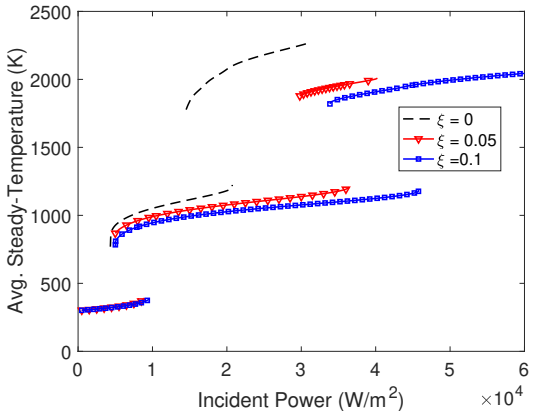


Figure 3.10: Power response curves with increasing radiation heat transfer at $z = 0$. As expected the impact of radiation losses is stronger on the middle and upper branch.

and radiation has stronger impact at high temperatures compared to when EM HX operates on the lower branch. This observation is consistent with what we found in chapter 2 (see Figure 2.7b).

The results presented in this section motivate an interesting optimization problem for a future study. From Figure 3.6 we see that operating in the hysteresis region of the response curve may lead to the highest possible thermal efficiencies. But, with increasing $Pe$, although we deliver thermal power at larger rates at the outlet, hysteresis keeps on diminishing. This suggests that there exists an inherent competition between flow velocities and the hysteresis of the response curve and an optimum $Pe$ may exist where the highest efficiencies are possible. The model presented here serves the purpose of highlighting the most important design characteristics of an EM HX (e.g., the electric field resonance producing the double S-curve), but optimization studies should be carried out on a model which closely resembles experimental conditions (i.e., model with gaseous flows). But first we need to understand how compressible gas dynamics affect the onset of thermal runaway and vice versa. This will be explored in upcoming chapters.

### 3.2.3 Effect of Fluid Permittivity

Until now we discussed results when resonance criteria given by (3.2) is followed exactly. From earlier discussions, we identified that the most efficient operation of an EM HX is achieved on the middle stable branch, but experimentally it is difficult to continuously maintain electric field

resonance in the lossy layer (which is required for the double S-curve). Material parameters $\epsilon_{r_1}$ and $\epsilon_{r_2}$ are expected to vary with $T$ (and so the EM wavelengths). To satisfy the resonance criteria given by (3.2) when EM wavelengths vary with $T$ may not be possible as it requires layer thicknesses to change with $T$. This poses a research question

- How sensitive is the double S-curve to the resonance criteria given by (3.2)? The answer to this research question may help determine the experimental viability of a double S-curve.

To answer this question, we break the resonance criteria by varying fluid permittivity and keeping all other parameters constant. We define permittivity ratio as

$$\psi = \frac{\epsilon_{r_2}}{\epsilon_{r_3}}.$$

We keep $\epsilon_{r_3}$ constant and vary $\psi$. The perfect electric field resonance is achieved when $\psi = 6.76$. Our goal here is to explore how shape of the response curve changes in the neighborhood of $\psi = 6.76$.

For $Pe = 0$ and $Pe = 2$, power response curves for $\psi = 6$, $\psi = 6.76$, $\psi = 7.6$ and $\psi = 8.6$ are shown in Figure 3.11 and Figure 3.12, respectively. Although, we do not follow resonance criteria exactly, we still observe existence of middle branch in the neighborhood of $\psi = 6.76$. To understand how the middle branch behaves with permittivity ratio, we simulate response curves for different $\psi$ and $Pe$. We define length of the middle branch as the difference between powers at extreme points. Plot of the length of middle branches with $\psi$ for different $Pe$ is shown in Figure 3.13. We see that the length of the middle branches slowly starts to increase we approach the reference $\psi = 6.76$, and keeps on increasing until it reaches to maximum at $\psi = 7.4$. The plot in Figure 3.13 gives an estimate on the ranges of $\psi$ within which we have three distinct stable branches. As we start to move away from the ranges shown in the plot, the middle branch merges into the upper branch as seen from Figure 3.11(d) and Figure 3.12(d), and eventually acquires a typical S shaped power response curve if the permittivity ratio is increased even further. In that case, only two stable branches exists; the lower branch ($\sim 300$ K) and the upper branch ($\sim 2,500$ K). These observations are consistent with results discussed in [28, 29]. These papers, for no flow case, report

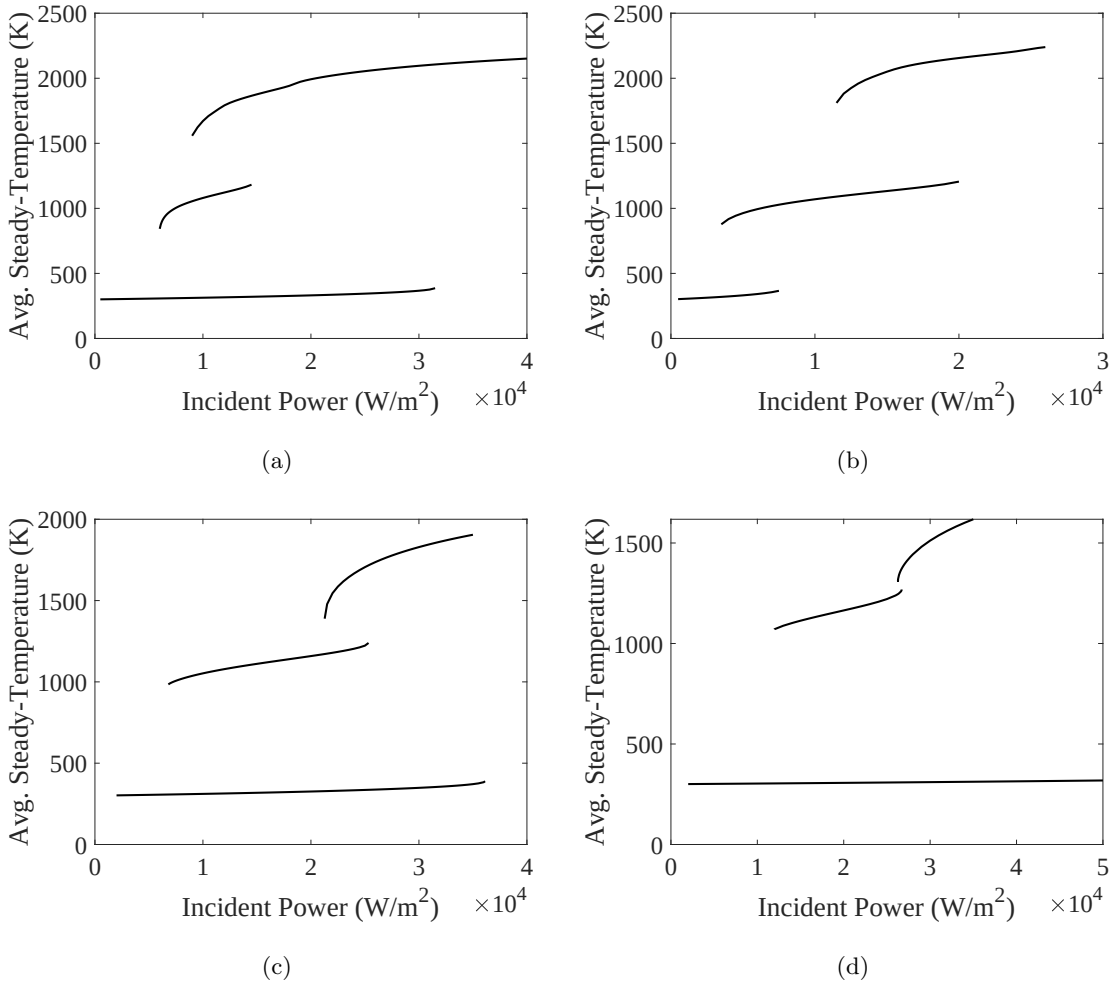


Figure 3.11: Stable branches of power response curves for $Pe = 0$ and permittivity ratio of $\psi = 6$ (a), $\psi = 6.76$ (perfect resonance) (b), $\psi = 7.6$ (c), and $\psi = 8.6$ (d).

that the length of the middle branch first increases and then decreases with permittivity ratio. We have demonstrated that the middle branch exists, as long as permittivity variation is within roughly 10% of the reference $\psi = 6.76$ as seen in Figure 3.13 for $Pe \sim o(1)$.

## 3.3 Conclusions

In this chapter, we have presented a numerical model produced in COMSOL Multiphysics which describes the operation of a triple layer EM HX with plane Poiseuille flow of liquids. The model is validated by comparing steady-state electric field and temperature profiles with the ones produced

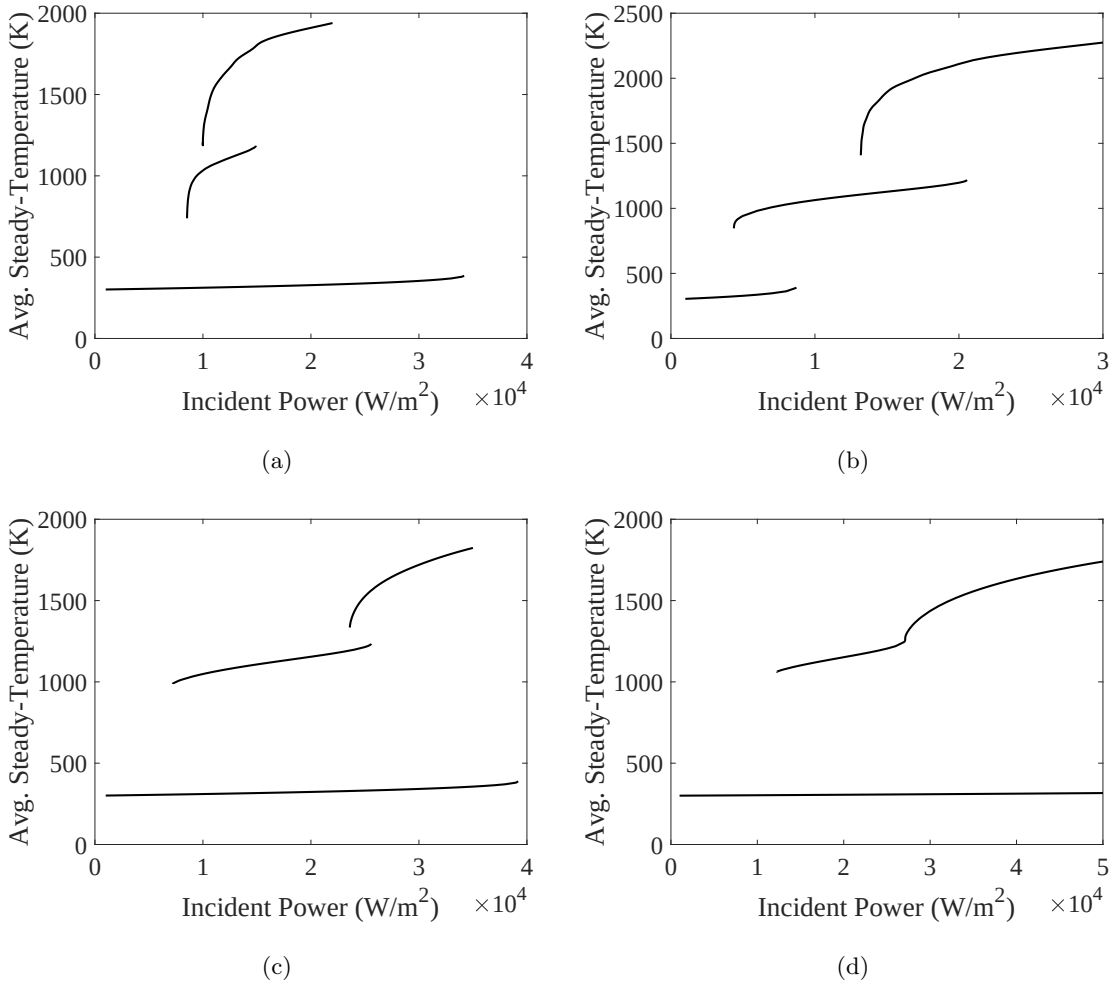


Figure 3.12: Stable branches of power response curves for $Pe = 2$ and permittivity ratio of $\psi = 6$ (a), $\psi = 6.76$ (perfect resonance) (b), $\psi = 7.6$ (c), and $\psi = 8.6$ (d).

by another model using an IMEX finite difference scheme. Because of the electric field resonance in the lossy region we found that power response curve is a double S-curve when $Pe \sim o(1)$ and $Pe \sim o(\frac{1}{\eta})$. We have found that EM HX operating on the middle branch are more efficient (about 20%) compared to the ones operating on the lower branch (about 1.5%) when $Pe \sim o(\frac{1}{\eta})$.

From the comparison of power response curves for different $Pe$, we observe that the onset of thermal runaway is delayed and average temperatures of upper and middle stable branches keep dropping as $Pe$ is increased. Large convection heat transfer between the fluid and the ceramic causes the upper branches undergo drastic reduction in temperatures compared to the middle and

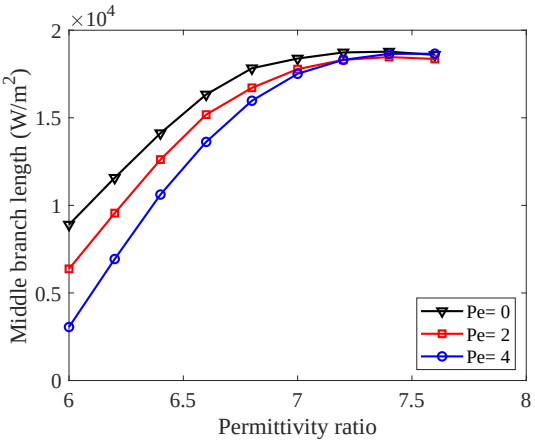


Figure 3.13: Length of the middle branch as a function of permittivity ratio $\psi$.

lower branches. When $Pe$ is sufficiently large around $o(\frac{1}{\eta})$, we observe hysteresis on the upper branch diminishes.

We have described the transient behavior of the thermal runaway in the considered triple layer EM HX. Results confirm that thermal runaway instigates as soon as the local maximum temperature reaches a critical value. The EM losses in region 3, at the point where the temperature is maximum, are large enough such that thermal losses at the boundaries and convection between coolant and the ceramic cannot balance the local heat source, which results in large instantaneous temperature rise and a local hotspot. As the time progresses, the hotspot travels towards the bottom boundary allowing fluid to collect thermal energy from the local heat source. The hotspot in ceramic region causes an EM HX to operate more efficient on the middle branch. When thermal losses at the boundaries and power absorbed by fluid balance the local heat source, steady-state is achieved and thermal runaway stabilizes on the middle branch.

We have also investigated cases where we vary permittivity of the fluid region, keeping all other parameters fixed. We have found that middle branch exists for $Pe \sim o(1)$ when the variations in fluid permittivity are roughly within 10% of the reference value.

Results presented here are theoretical, and suggest that models of EM HX with compressible gases, considered in upcoming chapters, more closely align with experimental conditions. But following are some of the conclusions that may hold true regardless of the single-phase approximation

- Including additional modes of heat transfer (convection and work of expansion) in the fluid region delays the onset of thermal runaway. This is expected as we need to supply more power to compensate for additional heat loss mechanisms.

- Thermal runaway occurs locally in the ceramic resulting in generation of local hotspots. If an EM HX consists of a lossy porous ceramic with a fluid flow through the pores, thermal runaway is expected to occur at the pore scale. This result motivates chapter 5 where we investigate coupling between gas dynamics and thermal runaway at the pore scale.

- Highest possible efficiencies are achieved when high temperatures are obtained at relatively low powers. In the model presented in this chapter, electric field resonance in the lossy layer causes efficient heating of the ceramic, and a result, the EM HX is the most efficient when operated near the leftmost turning point of the middle stable branch. But experimentally it is difficult to maintain electric field resonance criteria and achieve a double S-curve. This motivates exploration of new techniques of efficient heating of the ceramics.

# 4 RAYLEIGH-BÉNARD CONVECTION IN AN ELECTROMAGNETIC HEAT EXCHANGER UNDER LAMINAR FLOW CONDITIONS

As discussed in the previous chapter, models of EM HXs with compressible coolants can provide insights into what we could observe experimentally. In the case of such EM HXs, we need to consider two additional modes of heat transfer. One is natural (or Rayleigh-Bénard) convection which occurs when buoyancy acting on the fluid dominates over the viscous stresses, and the second is the acceleration of the gas that occurs to satisfy the mass conservation in the presence of density gradients.

In this chapter, we study the impact of heat transfer through natural convection, and the next chapter is focused on investigating design-impact of work of thermal expansion on such EM HX. As a simplification, we consider an EM HX with weakly compressible fluids whose density drops linearly with increase in temperature (Boussinesq approximation). Although the work of expansion is negligible in our model, density gradients within the fluid layer give rise to buoyancy-driven flow under the action of gravity, leading to onset of natural convection between the coolant and ceramic. Many typical liquids undergo thermal expansion when they are heated, and their density drops with temperature. The parameter which measures sensitivity of volume change of liquids with increasing temperature is the coefficient of thermal expansion, denoted by $\beta$, which is the ratio of net change in volume when temperature is varied by 1 K to the initial volume. For example, water and glycerin have $\beta$ values of $2 \times 10^{-4}$ 1/K and $5 \times 10^{-4}$ 1/K, respectively at the room temperature. This chapter is focused on investigating how natural convection between a weakly

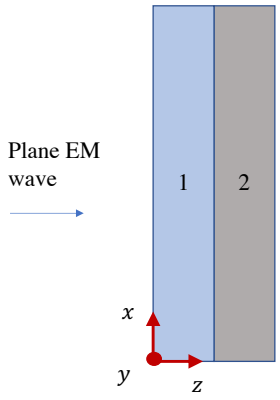


Figure 4.1: Geometry of the layered system considered in the COMSOL simulation. An ideal gas which initially stationary is enclosed in region 1, and region 2 is a lossy dielectric heated by EM waves.

compressible coolant and the ceramic affects the performance of the device.

To demonstrate why consideration of buoyancy forces in an EM HX are important, we consider a COMSOL model of a buoyant coolant in a closed cavity subject to EM heating. We consider geometry as shown in Figure 4.1. Plane EM waves polarized in the $y$-direction and traveling in the positive $z$-direction are incident on the structure. We assume that a lossless ideal gas initially at rest is enclosed in region 1 (i.e., flow is initially stationary with no slip condition along the boundaries of region 1), and region 2 is a lossy ceramic which is heated by EM waves. Figure 4.2 shows steady-state results when gravity is acting in the negative $x$-direction. We observe one convection roll and thermal runaway instability occurs in the ceramic region when incident power increased from $5,100$ W/m$^2$ to $5,200$ W/m$^2$. The scenario depicted in Figure 4.3 considers gravity acting in the positive $z$-direction; this orientation is similar to when the fluid is heated from below. Since density of the fluid drops with temperature, the fluid near the ceramic is less dense compared to the fluid near the opposite wall. This density gradient in the fluid give rise to buoyancy-driven flow (i.e., natural convection) when buoyancy dominates over the viscous stresses with the fluid. Such instability is called Rayleigh-Bénard (RB) convection [30, 31]. Looking at Figure 4.3, even though incident power is increased to $6,000$ W/m$^2$, we do not see thermal runway at this power

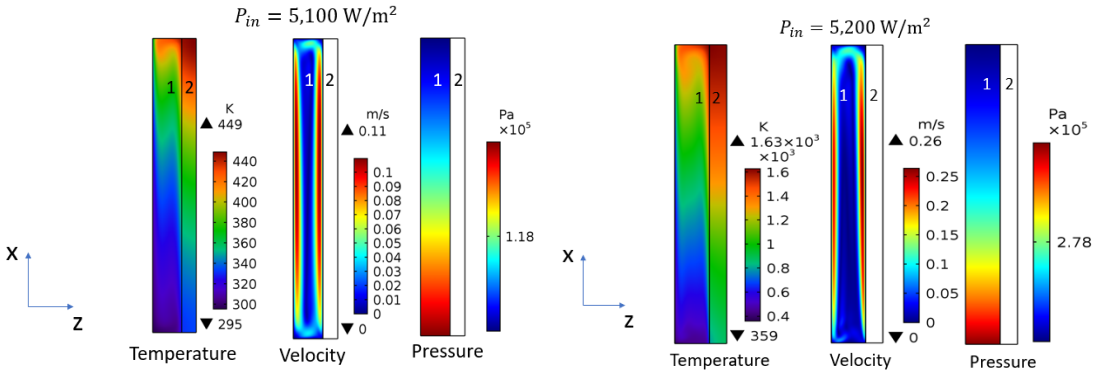


Figure 4.2: Results from direct numerical simulations in COMSOL Multiphysics as shown in Figure 4.1. In region 1 ideal gas is enclosed in a cavity, and region 2 is a lossy ceramic layer. EM waves polarized along the $y$-axis and traveling in the $z$-direction are incident on region 1. Buoyancy is acting in the negative $x$-direction. No thermal runaway case (a) and thermal runaway case (b). Increasing incient power just by 100 W/m$^2$, we observed thermal runaway.

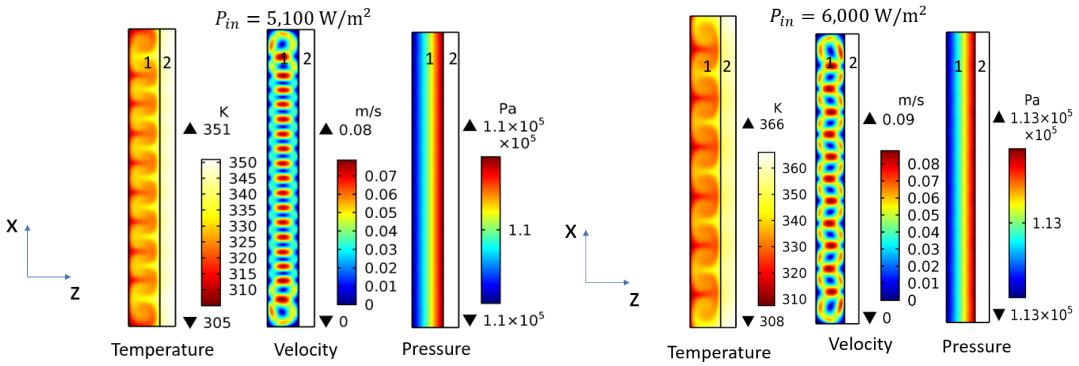


Figure 4.3: Preliminary results from direct numerical simulations in COMSOL Multiphysics as shown in Figure 4.1. In region 1 ideal gas is enclosed in a cavity, and region 2 is a lossy ceramic layer. EM waves polarized along the $y$-axis and traveling in the $z$-direction are incident on region 1. Buoyancy is acting in the positive $z$-direction. With this configuration we achieve heating from below and RB convection is observed. Even if we increase incident power by 900 W/m$^2$, we do not observe thermal runaway. This indicated enhancement of heat transfer between fluid and ceramic due to RB convection.

level because of enhanced heat transfer due to RB convection.

This simulation also highlights conjugate nature of the RB convection problem. From the classical theory, it is known that the impact of buoyancy acting on the fluid improves as the temperature gradient across the fluid layer (along the $z$-direction) increases [31]. Enhancements in the fluid velocity in the fluid region causes convective heat transfer to increase which then affects the temperature profiles in the ceramic region. In fact, as the impact of buoyancy increases Nusselt number (i.e., the convective heat transfer coefficient within the fluid) is expected to increase exponentially with the buoyancy [31]. In the EM HX, it is expected to see improvements in the convective heat transfer with applied EM power, which would affect the performance of the device, but this analysis requires full 3D number numerical simulation of the RB convection coupled to EM heating for the ceramic. But first, it is required to identify the onset characteristics of instability mechanisms within the EM HX.

The research question motivated by this discussion is

1. *What is the critical power at which Rayleigh-Bénard convection initiates?*

In the classical RB convection problem, a stationary horizontal fluid layer is heated from below by specifying temperature at the bottom and top boundaries [30, 31]. Typically, the RB instability is characterized by the Rayleigh number $\bar{Ra}$, which is dependent on temperature gradient across the channels and gives relative importance of buoyancy and viscous stresses within the fluid layer. When $\bar{Ra} > \bar{Ra}_c$, where $\bar{Ra}_c$ is some critical value, convection rolls are observed. In the classical RB problem, it is assumed that fluids obey Boussinesq approximation, i.e., density drops linearly with temperature, and its variations are included only in body force term in the momentum conservation equations. The fluid is treated as incompressible in the mass and energy conservation equations. This approximation is valid typically for liquids as their density variation with temperature is small, and is not dependent on pressure. To determine the value of $\bar{Ra}_c$, a linear stability analysis is carried out. Initially, it is assumed that the fluid is stationary given the temperature gradient across the channel (i.e., for a given $\bar{Ra}$). This state is known as the base-state and is derived by solving Navier-Stokes and thermal energy equations by assuming that fluid velocity is zero and heat transfer is due to conduction only. Infinitesimal perturbations, which are represented as linear

combination of 3D time-dependent normal-modes, are then introduced in the base-state solution. The goal of a linear stability analysis is to find out how the normal modes evolve in time. The base-state is unstable if at least one mode grows in time resulting into a state other then the original state, i.e., RB convection occurs. The base-state solution is stable if the amplitude of all the normal-modes decay in time.

RB convection can be observed in a plane Poiseuille flow of a coolant which is heated from below. There are two distinct instabilities that can be observed in a plane Poiseuille flow in the presence of adverse thermal gradients. Firstly, hydrodynamic instabilities (i.e., transition to turbulence) can occur when fluid inertia dominates over viscous stresses. Local shear stresses acting within the fluid depend on velocity gradients across thickness of the channel. For example, in case of a fully developed plane Poiseuille flow in the $x$-direction, shear stresses are proportional to $du/dz$, where $u$ is the flow velocity in the $x$ direction, and $z$ is the direction normal to $x$. With increasing Reynolds number, $Re$, which gives relative importance of inertia to viscous forces, shear stresses increase monotonically as the term $du/dz$ is expected to increase with $Re$. When $Re > Re_c$, where $Re_c$ is some critical value, large shear is induced due to sharp changes in velocity causing flow to become unstable against infinitesimal disturbances [31, 49], and instabilities are developed in the form of Tollmien-Schlichting waves [50]. These are known as shear-induced instabilities, and can be characterized solely by the Reynolds number. Second, RB convection can occur when $Re < Re_c$ and buoyancy acting on the fluid dominates the viscous stresses (i.e., $\bar{Ra}$ larger than some critical value) within the fluid [50]. Regardless of buoyancy, shear-induced (hydrodynamic) instabilities are always observed when $Re > Re_c$, and in case of a laminar plane Poiseuille flow, the most dominant mode of instability is RB convection.

Along with hydrodynamic and convective instabilities taking place within the fluid, the thermal runaway instability can occur in the ceramic due to the nonlinear nature of EM heating. When loss factor of a ceramic increases exponentially with temperature, the volumetric EM heat source in the energy equation also increases as it is proportional to the loss factor. When the rate of heat removal from the ceramic (via heat transfer with environment or any other heat loss mechanism) is small compared to volumetric heat addition, thermal runaway takes place leading to rapid rise

of ceramic temperature. This leads to the following research questions:

2. *Can thermal runway in the ceramic drive the RB instability within the fluid? If yes, then under which conditions does this instability occur?*

Onset of RB convection in a stationary absorbing fluid layer undergoing heating due to one sided irradiation by plane EM waves is considered by Gilchrist and Kriegsmann in [51]. Their model assumes a constant effective electrical conductivity of the fluid layer and onset of convection is due to nonuniform EM heating of the fluid layer. This model is extended considering plane wave irradiation from both sides of the fluid layer by Bhattacharya and Basak in [52] considering water as the fluid, and in [53] with oil as the fluid region. A common theme between these models is the constant effective conductivity of fluids, and onset of convection is due to nonlinear density gradients in the fluid layer that occur due to EM heating of the fluid itself. The difference between our model and previous works is that we consider a lossless Boussinesq fluid which is heated from below as a result of heat generation in the lossy layer. As these previous models consider constant electrical conductivity, thermal runaway instability is absent. To provide answers to the research questions, our work is focused on carrying out linear stability analysis that can capture onset of both thermal runaway (i.e., we consider temperature dependent ceramic loss factor) and RB convection instabilities.

In this chapter, we consider a horizontal double layered EM HX as shown in Figure 4.4. Region 1 contains a Poiseuille flow of a lossless weakly-compressible fluid in the $\hat{y}$-direction along with presence of gravity acting downwards, and region 2 is a ceramic material with a temperature dependent loss factor. Layer thicknesses are chosen according to electric field resonance criteria given in [28, 29]. We assume that the geometry is infinite in the $x$ and $y$-directions. With this configuration, we achieve a typical heating of a fluid layer from below. Since our focus is to study Bénard convection in the considered EM HX, we maintain flow speeds such that $Re < Re_c$, and hydrodynamic instabilities are not present. As in [50] and the classical RB problem [31], the base-state represents energy transfer only due to the conduction within the fluid region. The system of nonlinear equations governing the base-state is then solved using a second-order central finite difference scheme, and resulting nonlinear system of equation is solved using the Newton-Raphson

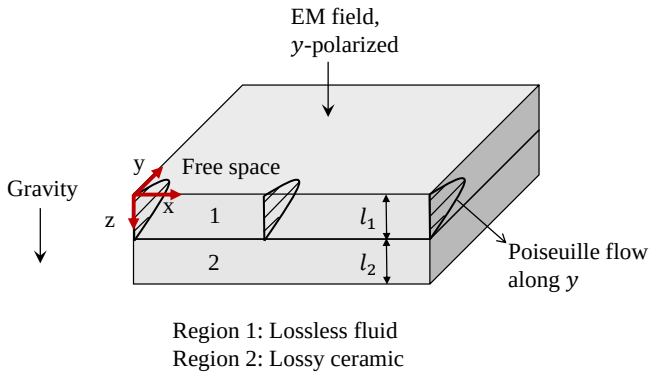


Figure 4.4: Geometry of the layered system subjected to EM heating. Layer 1 is lossless fluid and layer 2 is a lossy dielectric. Plane Poiseuille Flow is oriented along the $y$-direction.

solver. Also, a numerical continuation algorithm is utilized to generate power response curves from the base-state solution.

To provide answers to the research questions, we take the following approach.

- To answer question 1, we carry out a 2D normal-mode linear-stability analysis to determine the critical power at which RB convection initiates. We find that due to temperature dependent loss factor of the ceramic region, a 3D electric (fringe) field propagating outwards originates in the ceramic region. As the heat source is dependent on the field strength, the fringe field feeds back into the system, and therefore affects the stability of the problem. In the models of [51–53] the loss factor of the fluid is assumed constant, and the fringe field is absent. But, we later show that the fringe field promotes RB instability in a 2D limiting case.

To answer the research question 2, we take following steps.

- We consider stability of the system assuming that buoyancy is absent (only EM heating in the absence of RB convection). This problem has been studied by Pelesko and Kriegsmann in [27]. They carried out linear stability analysis against 1D infinitesimal perturbations and found that a branch of an S-curve is stable (or unstable) when its slope is positive (or negative).

However, we introduce 2D perturbations (as it is required due to 2D nature of RB convection) and find that some of the solutions that are stable against 1D perturbations become unstable when 2D disturbances are introduced.

- Full nonlinear 2D COMSOL simulations are presented to explain how transient evolution of temperature takes place when we operate in the newly found unstable region of the power response curve.

- For verification, we provide comparison of growth-rates and eigenfunctions given by both COMSOL and linear stability models.

- We then allow for buoyancy, and carry out linear stability analysis to determine the critical Rayleigh number required for onset of RB convection when operated on stable branches of the power response curve.

## 4.1 Governing Equations

In this chapter, we assume the frequency of incident EM waves to be 2.45 GHz. In order to achieve electric field resonance necessary to produce the double S-curve, we need to satisfy following conditions [8]

$$l_1 = \frac{n_1 \lambda_1}{4}, \text{ and } l_2 = \frac{n_2 \lambda_2}{2}, \tag{4.1}$$

where $n_1$ and $n_2$ can be any odd number, i.e., $1, 3, 5, ...$, $\lambda_1$ and $\lambda_2$ are wavelength in regions 1 and 2, respectively. Until otherwise noted we take $n_1 = 3$ and $n_2 = 1$.

We introduce nondimensional variables as

$$\mathbf{x} = \frac{\mathbf{x}'}{l_1}, \mathbf{u} = \frac{\mathbf{u}' l_1}{\alpha_1}, t = \frac{t' \alpha_1}{l_1^2}, p = \frac{p' l_1^2}{\mu \alpha_1},$$
$$\mathbf{E}_j = \frac{\mathbf{E}'_j}{E_0}, T_j = \frac{T'_j - T_A}{T_A}, k_0 = k'_0 l_1,$$

where primed quantities represent respective dimensional variables, $\mathbf{x}$ is the position vector with components $(x, y, z)$, $l_1$ is the thickness of region 1, $\mathbf{u}$ is the fluid velocity vector which has com-

ponents $(u, v, w)$ in $x$, $y$, and $z$ directions, respectively, $\alpha_1 = \frac{k_1}{\rho_1 C_{p_1}}$ is the fluid thermal diffusivity, $k_1$ is the fluid thermal conductivity, $\rho_1$ is the fluid density, $c_{p_1}$ is the fluid specific heat, $p$ is the fluid gauge pressure, $\mu$ is the dynamic viscosity, $\mathbf{E}_j$ is the electric field vector with components $(E_{j_x}, E_{j_y}, E_{j_z})$, subscript $j$ represents the region of the solution (i.e., $j = 1, 2$ represent regions 1 and 2, respectively), $E_0$ is the intensity of incident electric field, $T_j$ is the temperature, $T_A$ is the ambient temperature, $k_0$ is the wavenumber of EM waves in free space.

The thermal energy balance for the geometry shown in Figure 4.4 can be represented by

$$\frac{\partial T_1}{\partial t} + \mathbf{u} \cdot \nabla T_1 = \nabla^2 T_1, \ 0 < z < 1, \tag{4.2a}$$

$$\rho c_p \frac{\partial T_2}{\partial t} = k \nabla^2 T_2 + P |E_2|^2 \epsilon_2''(T_2), \ 1 < z < 1 + l, \tag{4.2b}$$

where $\rho = \frac{\rho_2}{\rho_1}$, $\rho_2$ is the ceramic density, $c_p = \frac{c_{p_2}}{c_{p_1}}$, $c_{p_2}$ is the ceramic specific heat, $k = \frac{k_2}{k_1}$, $k_2$ is the ceramic thermal conductivity, $P = \frac{E_0^2 \omega \epsilon_0 {l_1}^2}{2 k_1 T_A}$ is the dimensionless power of EM waves, and $l = l_2/l_1$.

Electric field propagation through free space, regions 1 and 2 is governed by the Maxwell's equations

$$\nabla \cdot (\epsilon_j \mathbf{E}_j) = 0, \tag{4.3a}$$

$$\nabla^2 \mathbf{E}_j - \nabla (\nabla \cdot \mathbf{E}_j) + k_0^2 \epsilon_j \mathbf{E}_j = 0. \tag{4.3b}$$

Since the volume charge and current density sources in (4.3) are absent, the strength of the electric field depends on the power of incident EM waves. Dielectric constants of free space and region 1 are assumed to be constant, and electric fields in free space and region 1 become divergence free. Finally, the motion fluid obeying Boussinesq approximation is governed by the Navier-Stokes equations [30]

$$\nabla \cdot \mathbf{u} = 0, \tag{4.4a}$$

$$\frac{1}{Pr} \left[ \frac{\partial \mathbf{u}}{\partial t} + (\mathbf{u} \cdot \nabla) \mathbf{u} \right] = -\nabla p + \nabla^2 \mathbf{u} - Ra^2 T_1 \hat{z}, \tag{4.4b}$$

where $Pr = \frac{\mu c_{p_1}}{k_1}$ and $Ra^2 = \frac{\rho_1 g {l_1}^3 \beta T_A}{\mu \alpha_1}$ are Prandtl and Rayleigh numbers, respectively.

At the interface between free-space and region 1 (at $z' = 0$), thermal losses to the surrounding are characterized by Newton's law of cooling with a fixed heat transfer coefficient. At the interface between regions 1 and 2, a perfect thermal contact is maintained, i.e., heat flux and temperature are continuous, and boundary at $z' = l_1 + l_2$ is thermally insulated. Tangential components of the electric and magnetic fields are continuous at the interfaces, and the boundary at $z' = l_1 + l_2$ is electrically grounded, i.e., a metal plane boundary condition (perfect electrical conductor) [46]. The geometry is uniform in the $x$- and $y$-directions. The perturbations introduced in the base-state solution are periodic with period $L$. Mathematically, these conditions are written as

$$\left.\begin{array}{c} \mathbf{u} = 0, \frac{\partial T_1}{\partial z} = BiT_1 + R[(T_1+1)^4 - 1] \\ \hat{n} \times \nabla \times \mathbf{E}_a = \hat{n} \times \nabla \times \mathbf{E}_1, \\ \hat{n} \times \mathbf{E}_a = \hat{n} \times \mathbf{E}_1, \end{array}\right\} \text{ at } z = 0, \tag{4.5}$$

$$\left.\begin{array}{c} \mathbf{u} = 0, T_1 = T_2, \frac{\partial T_1}{\partial z} = k\frac{\partial T_2}{\partial z} \\ \hat{n} \times \nabla \times \mathbf{E}_1 = \hat{n} \times \nabla \times \mathbf{E}_2, \\ \hat{n} \times \mathbf{E}_1 = \hat{n} \times \mathbf{E}_2, \end{array}\right\} \text{ at } z = 1, \tag{4.6}$$

$$\hat{n} \times \mathbf{E}_2 = 0, \frac{\partial T_2}{\partial z} = 0, \text{at } z = 1 + l, \tag{4.7}$$

where $Bi = \frac{hl_1}{k_1}$, $h$ is specified heat transfer coefficient, $R = \frac{\xi s_r l_1 T_A^3}{k_1}$ is the radiation parameter, $s_r$ is the Stefan–Boltzmann radiation heat constant, and $\xi$ is the emissivity of the surface at $z' = 0$, $l = \frac{l_2}{l_1}$, $l_2$ is thickness of region 2.

## 4.2 Base-State Solution

At steady state, it is assumed that convection is absent within the fluid layer. We are looking for solutions independent of the $x$- and $y$-directions, and temperature depends on $z$ only. As $\epsilon_2$ depends only on temperature and incident plane wave is polarized in the $y$-direction, the electric field vector becomes divergence free (Gauss's law), and Maxwell's equations (4.3b) reduce to Helmholtz equation.

The plane-wave electric field solution in free space at the steady-state is given by

$$\mathbf{E}_a^{ss} = \left[e^{ik_0 z} + \Gamma e^{-ik_0 z}\right] \hat{y}, \tag{4.8}$$

where $\Gamma$ is the reflection coefficient between free space and fluid region 1, and $\hat{y}$ is unit vector along the $y$-direction. Electric fields penetrating and interacting with regions 1 and 2 are given by $\mathbf{E}_1^{ss} = \left[E_{1_y}^{ss}(z)\right] \hat{y}$ and $\mathbf{E}_2^{ss} = \left[E_{2_y}^{ss}(z)\right] \hat{y}$, where $E_{1_y}^{ss}$ and $E_{2_y}^{ss}$ satisfy Helmholtz equation as

$$\frac{d^2 E_{1_y}^{ss}}{dz^2} + k_0^2 \epsilon_1' E_{1_y}^{ss} = 0, \tag{4.9a}$$

$$\frac{d^2 E_{2_y}^{ss}}{dz^2} + k_0^2 \left[\epsilon_2' + i\epsilon_2''(T_2^{ss})\right] E_{2_y}^{ss} = 0, \tag{4.9b}$$

along with energy equations

$$\frac{d^2 T_1^{ss}}{dz^2} = 0, \tag{4.10a}$$

$$k\frac{d^2 T_2^{ss}}{dz^2} = -P|E_{2_y}^{ss}|^2 \epsilon_2''(T_2^{ss}). \tag{4.10b}$$

When we apply (4.5) -(4.7) to the base-state problem, and utilize solution (4.8), boundary conditions become

$$\left.\begin{array}{c} \mathbf{u}^{ss} = 0, \frac{dT_1^{ss}}{dz} = BiT_1^{ss} + R\left[(T_1^{ss}+1)^4 - 1\right] \\ \frac{dE_{1_y}^{ss}}{dz} + ik_0 E_{1_y}^{ss} = 2ik_0, \end{array}\right\} \text{ at } z = 0, \tag{4.11}$$

$$\left.\begin{array}{c} \mathbf{u}^{ss} = 0, T_1^{ss} = T_2^{ss}, \frac{dT_1^{ss}}{dz} = k\frac{dT_2^{ss}}{dz} \\ E_{1_y}^{ss} = E_{2_y}^{ss}, \frac{dE_{1_y}^{ss}}{dz} = \frac{dE_{2_y}^{ss}}{dz} \end{array}\right\} \text{ at } z = 1, \tag{4.12}$$

$$E_{2_y}^{ss} = 0, \frac{dT_2^{ss}}{\partial z} = 0, \text{at } z = 1 + l, \tag{4.13}$$

The system (4.9)-(4.13) is nonlinear due to the temperature dependent loss factor of the ceramic region. Approximations to the analytical solution of the above system are presented in [8] using thin-domain asymptotics, where the leading-order temperature is spatially uniform in the limit of small thermal losses to the surroundings. In our problem, consideration of spatial varia-

tion of the temperature within the fluid is necessary to produce density gradients, therefore, we solve (4.9)-(4.13) numerically using a second-order central finite difference scheme in conjunction with Newton-Raphson method to solve the nonlinear algebraic system. In our numerical model, we split $E_{1_y}^{ss}$ and $E_{2_y}^{ss}$ into their real and imaginary components and the heat source term then becomes $P\left[\left(\mathrm{Re}\{E_{2_y}^{ss}\}\right)^2+\left(\mathrm{Im}\{E_{2_y}^{ss}\}\right)^2\right]\epsilon_2''(T_2^{ss})$, where Re and Im are operators that extract real and imaginary parts of a variable, respectively. We discretize the 1D computational domain with 400 data points.

Since the convection is absent at the base-state, fluid mass and momentum conservation equations can be solved independently. Under the assumption of fully-developed parallel flow in laminar regime, flow profiles can be described by a plane Poiseuille flow in the $y$-direction. To get an expression of velocity profiles, we impose a constraint on the base-state flow in terms of dimensionless average velocity

$$Pe=\int_0^1(\mathbf{u}^{ss}\cdot\hat{y})\,dz, \tag{4.14}$$

where $\mathbf{u}^{ss}$ is the parabolic profile of fluid velocity which is directed in the $y$-direction, $Pe=\frac{\bar{V}l_1}{\alpha_1}$, where $\bar{V}$ is the dimensional average velocity of the flow. Plane Poiseuille flow satisfying (4.14) and no slip boundary conditions is given by $\mathbf{u}^{ss}=[PeF(z)]\,\hat{y}$, where $F(z)=-6(z^2-z)$. Resolving $\mathbf{u}^{ss}$ into component form, we get

$$u^{ss}(z)=0,$$
$$v^{ss}(z)=PeF(z),$$
$$w^{ss}(z)=0.$$

Since fluid flow profiles at the base state are not affected by temperature solutions, we can extend the numerical solution of the base-state EM-thermal problem to generate power response curves by using a numerical continuation algorithm. A power response curve produced with the numerical continuation approach is shown in Figure 4.5. We get a double S-curve because channel thicknesses are chosen according to resonance criteria [8, 28, 29].

Branches of the response curve shown in Figure 4.5 with negative slope are inherently unstable

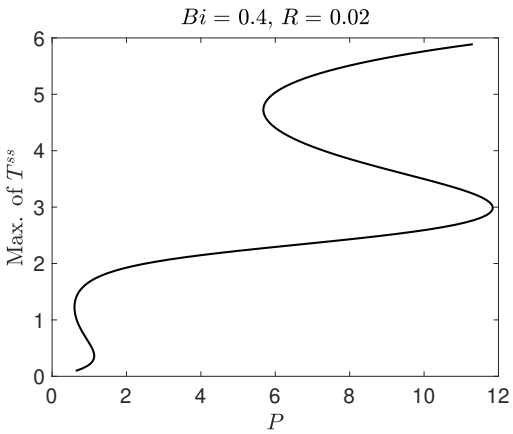


Figure 4.5: Double S-curve we get by solving (4.9), (4.10) along with the numerical continuation approach.

due to thermal runaway instability [26]. But on the stable regions of the response curve, RB convection initiates when buoyancy dominates over the viscous stresses within the fluid. Looking at the classical RB convection problem (where a stationary fluid layer is heated from below by a specified temperature gradient at the base state), instability occurs when $\bar{Ra} > \bar{Ra}_{\text{crit}}$, where

$$\bar{Ra} = \frac{\rho_1 g {l_1}^3 \beta T_A \Delta T_1^{ss}}{\mu \alpha_1} = Ra^2 \Delta T_1^{ss}, \tag{4.15}$$

where $\Delta T_1^{ss} = T_1^{ss}(z = 1) - T_1^{ss}(z = 0)$ is the dimensionless temperature drop across the fluid layer. In our problem, $\Delta T_1^{ss}$ increases nonlinearly with applied power (as seen from the response curve Figure 4.5), and there are two ways RB instability can be promoted. The first way is to keep $Ra^2$ constant, and increase the applied power $P$; when $P > P_{\text{crit}}$, convection initiates (i.e., here we are increasing $\Delta T_1^{ss}$). The second way is to keep $P$ constant and convection initiates when $Ra^2 > Ra^2_{\text{crit}}$ (i.e., $\Delta T_1^{ss}$ is fixed but importance of buoyancy is increased by manipulating other material properties). In this chapter we investigate both the approaches.

In order to demonstrate how a base-state power response curve may be useful to determine onset characteristics of the RB convection, in Figure 4.6, we plot $\Delta T_1^{ss}$ as a function of $P$ when the value of the radiation parameter $R$ is varied. From this figure, we can identify following effects:

- When lower branches of these plots are compared when $R$ is varied, we can see that $\Delta T_1^{ss}$ is slightly larger when $R = 0$. From (4.15), we can then say that $Ra_{\text{crit}}$ required for the onset

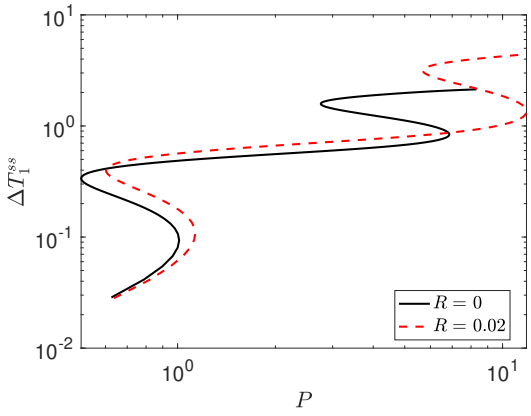


Figure 4.6: Temperature drop across the fluid layer from the base-state solution, $\Delta T_1^{ss}$, plotted against the applied EM power. Note that the plot is in logarithmic scale to demonstrate the differences between the curves.

of RB convection would be smaller when $R = 0$ (compared to when $R = 0.02$), when the base-state is on the lower branch.

- Similarly, when middle and upper branches are compared, we can expect that $Ra_{\text{crit}}$ would drop down when $R = 0.02$, as $\Delta T_1^{ss}$ is larger on the middle and upper branches.

In the section 4.4.3, we continue this discussion to confirm the above effects.

## 4.3 Linear Stability Theory

In our problem, at the base state, we assume that convection between fluid and the ceramic is absent, and heat transfer takes place only due to conduction. If buoyancy is absent (i.e., $Ra^2 = 0$), the base-state represents scenario of 1D EM heating of ceramic laminates (as considered in [26–29]). In the base-state solution, we then introduce infinitesimal perturbations, and our goal is to determine, through linear stability analysis, whether these disturbances are growing (unstable) or decaying (stable) with time. Perturbations are introduced in the basic solutions as follows

$$\mathbf{u} = \mathbf{u}^{ss} + \tilde{\mathbf{u}},$$

$$p = p^{ss} + \tilde{p},$$

$$T_j = T_j^{ss} + \tilde{T}_j,$$

$$\mathbf{E}_j = \mathbf{E}_j^{ss} + \tilde{\mathbf{E}}_j,$$

where the tilde quantities are infinitesimal perturbations. To determine equations governing evolution of these tilde quantities in space and time, we substitute above relations into the system (4.2)-(4.7). Since it is assumed that the amplitudes of perturbations are infinitesimal, stability characteristics may be investigated by retaining only the linear terms (and ignoring higher order terms) with respect to tilde quantities [31].

Linearizing the Navier-Stokes equation (4.4) yields

$$\frac{\partial \tilde{u}}{\partial x} + \frac{\partial \tilde{v}}{\partial y} + \frac{\partial \tilde{w}}{\partial z} = 0, \tag{4.16a}$$

$$\frac{1}{Pr}\left[\frac{\partial \tilde{u}}{\partial t} + PeF(z)\frac{\partial \tilde{u}}{\partial y}\right] = -\frac{\partial \tilde{p}}{\partial x} + \nabla^2 \tilde{u}, \tag{4.16b}$$

$$\frac{1}{Pr}\left[\frac{\partial \tilde{v}}{\partial t} + PeF(z)\frac{\partial \tilde{v}}{\partial y} + \tilde{w}PeF'(z)\right] = -\frac{\partial \tilde{p}}{\partial y} + \nabla^2 \tilde{v}, \tag{4.16c}$$

$$\frac{1}{Pr}\left[\frac{\partial \tilde{w}}{\partial t} + PeF(z)\frac{\partial \tilde{w}}{\partial y}\right] = -\frac{\partial \tilde{p}}{\partial z} + \nabla^2 \tilde{w} - Ra^2\tilde{T}_1. \tag{4.16d}$$

Energy equations in regions 1 and 2 reduce to

$$\frac{\partial \tilde{T}_1}{\partial t} + PeF(z)\frac{\partial \tilde{T}_1}{\partial y} + \tilde{w}\frac{dT_1^{ss}}{dz} = \nabla^2 \tilde{T}_1, \tag{4.17a}$$

$$\rho c_p \frac{\partial \tilde{T}_2}{\partial t} = k\nabla^2 \tilde{T}_2 + P|E_2^{ss}|^2 \left(\frac{\partial \epsilon''}{\partial T}\right)_{T_2^{ss}} \tilde{T}_2 + 2P\left[\mathrm{Re}(E_{2_y}^{ss})\,\mathrm{Re}(\tilde{E}_{2_y}) + \mathrm{Im}(E_{2_y}^{ss})\,\mathrm{Im}(\tilde{E}_{2_y})\right]\epsilon''(T_2^{ss}), \tag{4.17b}$$

Linearized electric field equations are given by

$$\nabla \cdot \tilde{\mathbf{E}}_a = 0, \tag{4.18a}$$

$$\nabla^2 \tilde{\mathbf{E}}_1 + k_0^2 \tilde{\mathbf{E}}_a = 0, \tag{4.18b}$$

$$\nabla \cdot \tilde{\mathbf{E}}_1 = 0, \tag{4.18c}$$

$$\nabla^2 \tilde{\mathbf{E}}_1 + k_0^2 \epsilon_{r_1} \tilde{\mathbf{E}}_1 = 0, \tag{4.18d}$$

$$\nabla \cdot \left(\epsilon_2^{ss} \tilde{\mathbf{E}}_2\right) = -\left[\left(\frac{\partial \epsilon_2}{\partial T}\right)_{T_2^{ss}} E_{2_y}^{ss}\right] \frac{\partial \tilde{T}_2}{\partial y}, \tag{4.18e}$$

$$\nabla^2\tilde{\mathbf{E}}_2 - \nabla(\nabla\cdot\tilde{\mathbf{E}}_2) + k_0^2\epsilon_2^{ss}\tilde{\mathbf{E}}_2 = -\left[k_0^2\left(\frac{\partial\epsilon_2}{\partial T}\right)_{T_2^{ss}}\mathbf{E}_2^{ss}\right]\tilde{T}_2. \tag{4.18f}$$

The linearized boundary conditions are

$$\left.\begin{aligned} \tfrac{\partial\tilde{T}_1}{\partial z} &= Bi^*\tilde{T}_1 \\ \tilde{\mathbf{u}} &= 0, \\ \hat{n}\times\nabla\times\tilde{\mathbf{E}}_a &= \hat{n}\times\nabla\times\tilde{\mathbf{E}}_1, \\ \hat{n}\times\tilde{\mathbf{E}}_a &= \hat{n}\times\tilde{\mathbf{E}}_1, \end{aligned}\right\} \text{ at } z=0, \tag{4.19}$$

$$\left.\begin{aligned} \tfrac{\partial\tilde{T}_1}{\partial z} &= k\tfrac{\partial\tilde{T}_2}{\partial z}, \\ \tilde{T}_1 &= \tilde{T}_2, \\ \tilde{\mathbf{u}} &= 0 \\ \hat{n}\times\nabla\times\tilde{\mathbf{E}}_1 &= \hat{n}\times\nabla\times\tilde{\mathbf{E}}_2, \\ \hat{n}\times\tilde{\mathbf{E}}_1 &= \hat{n}\times\tilde{\mathbf{E}}_2, \end{aligned}\right\} \text{ at } z=1, \tag{4.20}$$

$$\left.\begin{aligned} \tfrac{\partial\tilde{T}_2}{\partial z} &= 0, \\ \hat{n}\times\tilde{\mathbf{E}}_2 &= 0, \end{aligned}\right\} \text{ at } z=1+l, \tag{4.21}$$

where $Bi^* = Bi + 4R[T_1^{ss}(z=0)+1]^3$.

When $\epsilon_2$ is temperature dependent $\left(\text{i.e., } \frac{\partial\epsilon_2}{\partial T}\neq 0\right)$, perturbed temperature $\tilde{T}_2$ appears in (4.18e) and (4.18f) similar that of volume charge and current density sources in typical Maxwell's equations. Let $\frac{q}{\epsilon_0} = -\left[\left(\frac{\partial\epsilon_2}{\partial T}\right)_{T_2^{ss}}E_{2_y}^{ss}\right]\frac{\partial\tilde{T}_2}{\partial y}$ and $i\omega\mu_0\mathbf{J} = \left[k_0^2\left(\frac{\partial\epsilon_2}{\partial T}\right)_{T_2^{(0)}}\mathbf{E}_2^{ss}\right]\tilde{T}_2$, and then (4.18e) and (4.18f) can be written as

$$\nabla\cdot\left(\epsilon_2^{ss}\tilde{\mathbf{E}}_2\right) = \frac{q}{\epsilon_0}, \tag{4.22a}$$

$$\nabla^2\tilde{\mathbf{E}}_2 - \nabla(\nabla\cdot\tilde{\mathbf{E}}_2) + k_0^2\epsilon_2^{ss}\tilde{\mathbf{E}}_2 = -i\omega\mu_0\mathbf{J}, \tag{4.22b}$$

where $q$ and $\mathbf{J}$ can be volume charge and current densities. Now (4.22) are analogous to that of Maxwell's equations (time harmonic with $e^{-i\omega t}$) governing electric field $\tilde{\mathbf{E}}_2$ which is generated as a result of nonzero sources $q$ and $\mathbf{J}$ in a nonmagnetic medium with spatially varying permittivity.

Moreover, both $q$ and $\mathbf{J}$ satisfy the time-harmonic (with $e^{-i\omega t}$) charge continuity equation which is given as

$$-i\omega q + \nabla \cdot \mathbf{J} = 0. \tag{4.23}$$

With this analogy between (4.18e) and (4.18f) and (4.22), we can, therefore, say that $\tilde{T}_2$ act as sources of 3D perturbed electric (fringe) field $\left(\text{i.e., } \tilde{\mathbf{E}}_2\right)$ which originates in region 2 and propagates outwards. In addition, $\tilde{T}_2$ depends on the $y$ component of $\tilde{\mathbf{E}}_2$ as seen in (4.17b), and the fringe field feeds back into the systems and affects the stability of the system. On the other hand, when $\epsilon_2$ is independent of temperature, regardless of perturbations in temperature, the source terms in linearized Maxwell's equations (4.18e) and (4.18f) are absent, and no fringe field is generated.

### 4.3.1 Normal-Mode Analysis

Since the system (4.16)-(4.21) is linear and homogeneous, we can separate the spatial and time dependence of perturbations so that the general solution is a superposition of normal modes in the form

$$\begin{aligned}
\tilde{\mathbf{u}} &= \mathbf{u}^{(1)}(z)e^{[i(\mathbf{a}\cdot\mathbf{d})+st]} + cc, \\
\tilde{p} &= p^{(1)}(z)e^{[i(\mathbf{a}\cdot\mathbf{d})+st]} + cc, \\
\tilde{T}_j &= T_j{}^{(1)}(z)e^{[i(\mathbf{a}\cdot\mathbf{d})+st]} + cc, \\
\mathrm{Re}\left(\tilde{\mathbf{E}}_j\right) &= \mathrm{Re}\left(\mathbf{E}_j^{(1)}(z)\right)e^{[i(\mathbf{a}\cdot\mathbf{d})+st]} + cc,, \\
\mathrm{Im}\left(\tilde{\mathbf{E}}_j\right) &= \mathrm{Im}\left(\mathbf{E}_j^{(1)}(z)\right)e^{[i(\mathbf{a}\cdot\mathbf{d})+st]} + cc,
\end{aligned}$$

where $\mathbf{a} = (a_1, a_2, 0)$ is the wave-vector of perturbations, $\mathbf{d} = (x, y, 0)$, and $s$ is the growth rate of the perturbations. By representing disturbances as a superposition of normal modes, we determine the stability of the base-state solution by substituting the above forms into the linearized system and then solving for the eigenvalue $s$ for given $\mathbf{a}$. In general, $s$ is complex valued, which means that growth of disturbances over time can be in the form of traveling waves such that the real part of $s$, $\mathrm{Re}(s)$, corresponds to exponential variation of amplitudes over time and the imaginary part of $s$, $\mathrm{Im}\,(s)$, represents angular speed of the disturbances. When $s$ is real, disturbances exhibit

a standing-wave pattern, and their amplitude grows or decays exponentially with time. When $\mathrm{Re}(s) < 0$ for all $\mathbf{a}$, then amplitudes of disturbances decay over time, and the base-state is linearly stable against infinitesimal disturbances. When $\mathrm{Re}(s) > 0$ for at least one value of $\mathbf{a}$, then the normal-mode associated with that wavenumber grows exponentially with time, and acts as the dominant mode of instability showing that the base-state solution is unstable. When $\mathrm{Re}(s) = 0$ for a given $\mathbf{a}$, then the base-state is neither stable nor unstable, but is a neutrally stable state.

With the above formulation, we make transformations $\frac{\partial}{\partial t} \to s$, $\frac{\partial}{\partial x} \to ia_1$, $\frac{\partial}{\partial y} \to ia_2$, and $\frac{\partial}{\partial z} \to D$. The linearized Navier-Stokes equations (4.16) reduce to

$$\begin{aligned}
ia_1 u^{(1)} + ia_2 v^{(1)} + Dw^{(1)} &= 0, \\
\left\{(D^2 - a^2) - \left[\frac{s}{Pr} + iReF(z)(\mathbf{a}\cdot\hat{u})\right]\right\} u^{(1)} &= ia_1 p^{(1)}, \\
\left\{(D^2 - a^2) - \left[\frac{s}{Pr} + iReF(z)(\mathbf{a}\cdot\hat{u})\right]\right\} v^{(1)} &= ia_2 p^{(1)} + ReF'(z)w^{(1)}, \\
\left\{(D^2 - a^2) - \left[\frac{s}{Pr} + iReF(z)(\mathbf{a}\cdot\hat{u})\right]\right\} w^{(1)} - Ra^2 T_1^{(1)} &= Dp^{(1)},
\end{aligned}$$

where $Re = \frac{Pe}{Pr}$, $\hat{u} = (0, \hat{y}, 0)$ is unit vector oriented in the direction of Poiseuille flow at the the base state, and $a^2 = a_1^2 + a_2^2$. Multiplying $x$ momentum equation by $ia_1$ and $y$ momentum equation by $ia_2$ and making use of continuity equation, we get

$$\begin{aligned}
L_2\left[Dw^{(1)}\right] + iReF'(z)(\mathbf{a}\cdot\hat{u})\left[w^{(1)}\right] &= a^2 p^{(1)}, \\
L_2\left[w^{(1)}\right] - Ra^2\left[T_1^{(1)}\right] &= Dp^{(1)},
\end{aligned}$$

where $L_2 = \left\{(D^2 - a^2) - \left[\frac{s}{Pr} + iReF(z)(\mathbf{a}\cdot\hat{u})\right]\right\}$. Analogous to the classical RB problem, we can eliminate pressure from the $z$ momentum equations as

$$\left\{\left(D^2 - a^2\right)^2 + iRe(\mathbf{a}\cdot\hat{u})\left[F''(z) - F(z)(D^2 - a^2)\right]\right\} w^{(1)} + a^2 Ra^2 T_1^{(1)} = \frac{s}{Pr}(D^2 - a^2)w^{(1)}. \quad (4.24)$$

Energy equations reduce to

$$\left[(D^2 - a^2) - iPeF(z)(\mathbf{a}\cdot\hat{u})\right] T_1^{(1)} - w^{(1)}\left(\frac{dT_1^{ss}}{dz}\right) = sT_1^{(1)}, \quad (4.25a)$$

$$\left[k(D^2-a^2)+P|E_2^{ss}|^2\left(\frac{\partial\epsilon''}{\partial T}\right)_{T_2^{ss}}\right]T_2^{(1)}+P\left[E_{2_y}^{ss}\left(\mathbf{E}^{*(1)}_2\cdot\hat{y}\right)+E_{2_y}^{*ss}\left(\mathbf{E}_2^{(1)}\cdot\hat{y}\right)\right]\epsilon''(T_2^{ss})=s(\rho c_p)T_2^{(1)}. \tag{4.25b}$$

Similarly, Maxwell's equations are reduced as

$$ia_1E_{a_x}^{(1)}+ia_2E_{a_y}^{(1)}+DE_{a_z}^{(1)}=0, \tag{4.26a}$$

$$\left[(D^2-a^2)+k_0^2\right]\mathbf{E}_a^{(1)}=0, \tag{4.26b}$$

$$ia_1E_{1_x}^{(1)}+ia_2E_{1_y}^{(1)}+DE_{1_z}^{(1)}=0, \tag{4.26c}$$

$$\left[(D^2-a^2)+k_0^2\epsilon_{r_1}\right]\mathbf{E}_1^{(1)}=0, \tag{4.26d}$$

$$\frac{d\epsilon_2^{ss}}{dz}E_{2_z}^{(1)}+\epsilon_2^{ss}\left(ia_1E_{2_x}^{(1)}+ia_2E_{2_y}^{(1)}+DE_{2_z}^{(1)}\right)=-\left[\left(\frac{\partial\epsilon_2}{\partial T}\right)_{T_2^{ss}}E_{2_y}^{ss}\right]ia_2T_2^{(1)}, \tag{4.26e}$$

$$\left[(D^2-a^2+k_0^2\epsilon_2^{ss})\right]\mathbf{E}_2^{(1)}-\mathbf{\Psi}\left(ia_1E_{2_x}^{(1)}+ia_2E_{2_y}^{(1)}+DE_{2_z}^{(1)}\right)=-\left[k_0^2\left(\frac{\partial\epsilon_2}{\partial T}\right)_{T_2^{ss}}\mathbf{E}_2^{ss}\right]T_2^{(1)}, \tag{4.26f}$$

where the vector operator $\mathbf{\Psi}=(ia_1,ia_2,D)$. The perturbed boundary conditions are given by

$$\left.\begin{aligned} DT_1^{(1)}&=BiT_1^{(1)},\\ w^{(1)}&=Dw^{(1)}=0,\\ DE_{a_y}^{(1)}-ia_2E_{a_z}^{(1)}&=DE_{1_y}^{(1)}-ia_2E_{1_z}^{(1)},\\ DE_{a_x}^{(1)}-ia_1E_{a_z}^{(1)}&=DE_{1_x}^{(1)}-ia_1E_{1_z}^{(1)},\\ E_{a_x}^{(1)}&=E_{1_x}^{(1)},\\ E_{a_y}^{(1)}&=E_{1_y}^{(1)}, \end{aligned}\right\}\ \text{at } z=0, \tag{4.27}$$

$$\left.\begin{aligned} DT_1^{(1)} &= kDT_2^{(1)}, \\ T_1^{(1)} &= T_2^{(1)}, \\ w^{(1)} &= Dw^{(1)} = 0, \\ DE_{1_y}^{(1)} - ia_2 E_{1_z}^{(1)} &= DE_{2_y}^{(1)} - ia_2 E_{2_z}^{(1)}, \\ DE_{1_x}^{(1)} - ia_1 E_{1_z}^{(1)} &= DE_{2_x}^{(1)} - ia_1 E_{2_z}^{(1)}, \\ E_{1_x}^{(1)} &= E_{2_x}^{(1)}, \\ E_{1_y}^{(1)} &= E_{2_y}^{(1)}, \end{aligned}\right\} \text{ at } z = 1, \tag{4.28}$$

$$\left.\begin{aligned} DT_2^{(1)} &= 0, \\ DE_{2_x}^{(1)} - ia_1 E_{2_z}^{(1)} &= 0, \\ DE_{2_y}^{(1)} - ia_2 E_{2_z}^{(1)} &= 0, \end{aligned}\right\} \text{ at } z = 1 + l. \tag{4.29}$$

In addition to conditions (4.27)-(4.29), we impose a constraint on the fringe field such that $\mathbf{E}_a^{(1)}$ is transmitted into the free space, i.e., $\mathbf{E}_a^{(1)}$ is always propagating form $z = 0$ towards $-\infty$ and nothing is reflected back from $-\infty$ to $z = 0$. The general solution satisfying the constraint and (4.26b) is

$$\mathbf{E}_a^{(1)} = \begin{cases} \mathbf{c}_a e^{-i\left(\sqrt{k_0^2 - a^2}\right)z}, & \text{for } k_0^2 \geq a^2, \\ \mathbf{c}_a e^{\left(\sqrt{a^2 - k_0^2}\right)z}, & \text{for } k_0^2 < a^2, \end{cases} \tag{4.30}$$

where $\mathbf{c}_a = (c_{a_x}, c_{a_y}, c_{a_z})$ are unknowns to be determined from (4.26a) and (4.27).

Gage and Reid in 1968 [50] carried out 3D linear stability analysis on a plane Poiseuille flow heated from below due to a specified adverse temperature gradient across the flow. They found that the primary mode of Bénard instability is when flow direction and wave-vector of perturbations are perpendicular to each other (i.e., when $\mathbf{a} \cdot \hat{u} = 0$). When $\mathbf{a} \cdot \hat{u} = 0$, flow inertia does not affect the stability characteristics as terms containing $Re$ drop out (see (4.24)). Physically, this means that onset of RB convection in the fluid is a result of competition between buoyancy and shear stresses within the fluid. But when $\mathbf{a} \cdot \hat{u} \neq 0$, buoyancy must dominate over viscous stresses as well as flow inertia (which is characterized by $Re$). Therefore, when a Poiseuille flow is in the $y$-direction, primary instabilities (or the first convection rolls that are observed experimentally) are going to be convection rolls whose amplitude varies in the $xz$-plane. In our problem, the plane Poiseuille

flow, which is in the $y$-direction, is heated from below due to heat transfer from electromagnetically heated ceramic. Primary instability is going to occur when buoyancy dominates over viscous stresses within the fluid, i.e., $xz$-dependent perturbations are the dominant mode of instability. Thus, from now onward we assume that the wavevector of perturbations is oriented in the $x$-direction, i.e., $\mathbf{a} = (a, 0, 0)$.

## 4.4 Results

To solve the eigenvalue problem, we approximate spatial derivatives with second-order central difference scheme such that the descretized system of linear equations can be represented as $\mathbf{Mx} = s\mathbf{Rx}$, where $\mathbf{M}$ and $\mathbf{R}$ are square coefficient matrices, and $\mathbf{x}$ is the column vector of unknowns. The eigenvalue problem is solved for given a base-state solution and $a$ using in-built linear algebra package in MATLAB R2021a (using `eigs` function), and the largest real part of eigenvalue then determines stability of the system.

In case of the RB convection instability, we find that all eigenvalues are real-valued, which is expected because the system (4.24)-(4.29) is analogous to when flow is initially stationary (i.e., the classical Rayleigh-Bénard problem), and the principle of exchange of instabilities holds [51–53]. Finally, neutral stability curves are generated by utilizing Newton's root finding algorithm which returns base-state solutions that have $\mathrm{Re}\{s\} = 0$ for a given $a$.

In our problem, there are two possible mechanisms that can promote instability–thermal runaway in the ceramic and RB convection in the fluid region. Then the question becomes:

- *How do we determine which mechanism is causing the base-state to become linearly unstable against infinitesimal perturbations?*

To answer this question we look at these instabilities individually. Organization of this section is as follows.

1. We first consider stability of the base-state solution when the buoyancy is absent (i.e., $Ra^2 = 0$). This way RB convection is absent, and thermal runaway in the ceramic is the only primary instability. We carry out linear stability analysis to determine which of the base-state solutions

are inherently unstable due to the nature of nonlinear EM heating of ceramics. We use the power response curve shown in Figure 4.5 to represent stable and unstable base-states for this EM-thermal scenario. As a verification, we compare our results with the finding of Pelesko and Kriegsmann [27] for 1D linear stability analysis. For 2D scenario, we compare growth rates given by both COMSOL and linear stability models.

2. Once we identify which states are stable on the power response curve, we then focus on these stable regions and determine $Ra^2_{\text{crit}}$ at which onset of RB instability takes place by carrying out a linear stability analysis.

### 4.4.1 Thermal Runaway Instabilities (No flow and $Ra^2 = 0$)

The temperature response of a ceramic layer during thermal runaway has been studied previously by Kriegsmann in [26]. This work introduced S-shaped power response (or S-) curves that are plots of steady-state temperature as a function of applied EM power. Pelesko and Kriegsmann in [27] considered heating of ceramic laminates and carried out a linear stability analysis, and found out that a branch of a response curve is stable (or unstable) when its slope is positive (or negative). However, stability analysis of Pelesko and Kriegsmann is limited to 1D perturbations (i.e., disturbances introduced in the base-state are not sinusoidal normal-modes and have wavenumber to be zero). Since our problem requires consideration of $xz$-dependent perturbations due to the 2D nature of RB convection, we extend stability analysis done by Pelesko and Kriegsmann [27] to include nonzero wavenumbers.

To verify the linear stability model, we recreate the analysis done by Kriegsmann and Pelesko [27], i.e., we set wavenumber to be zero and solve the eigenvalue problem to determine the growth rate Re{s}. In Figure 4.7, we mark base-state solutions by red asterisks that have positive values of Re{s}, and we arrive at the same conclusion that branches of power response curves with negative (or positive) slope are linearly unstable (or stable) against 1D infinitesimal perturbations. These unstable solutions represent onset of thermal runaway, i.e., any infinitesimal perturbations in the base-state are going to grow exponentially in time resulting in a different state [26]. Direction of arrows shown in the zoomed portion of the plot in Figure 4.7 shows how perturbations evolve

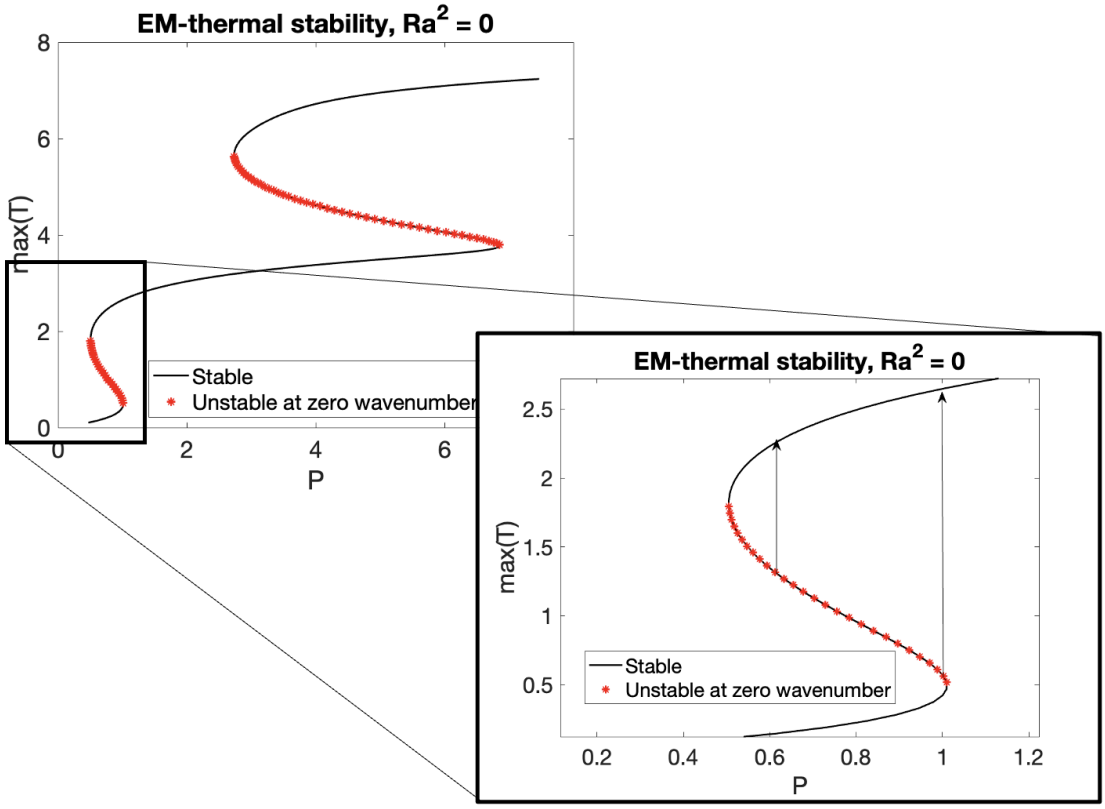


Figure 4.7: Stability of solutions on the power response curve against 1D perturbations ($a = 0$); branches with negative slope are unstable which is consistent with [27]. Direction of arrow in zoomed in portion of the figure indicate that perturbations grow with time and stabilize on the middle stable branch [27].

with time and stabilize on the middle stable branch. Such exponential transient evolution of $T$ during thermal runaway has been reported in the previous chapter and in [7, 48]. As an additional verification, we compare growth rates from linear stability model with a transient model solved in COMSOL Multiphysics. These results are discussed in Appendix B.

### 4.4.2 Fringe Field Instability

Next, we introduce 2D $xz$-dependent perturbations ($a \neq 0$) and solve for the growth rate for wavenumbers within $0 < a < 2$. We limit the range of wavenumber to 2 because growth rates monotonically drop when $a > 2$. If the growth rate is positive at least for one value of wavenumber, we mark the solution to be unstable. Stability characteristics of base-state solutions are shown in Figure 4.8. Data points marked by blue squares in Figure 4.8 (a) are solutions that are stable against

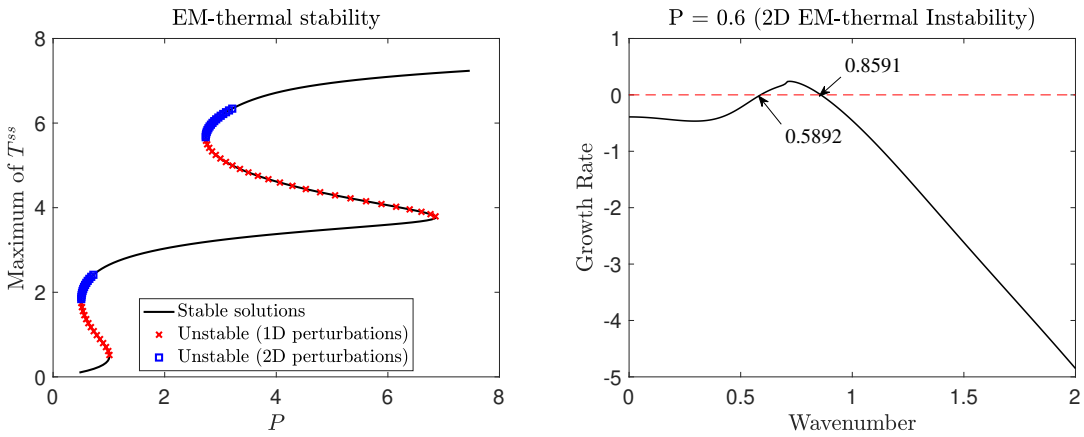


Figure 4.8: Stability of solutions on the power response curve against 1D ($a = 0$) and 2D ($a \neq 0$) perturbations; highlighted by blue markers are solutions that are stable when $a = 0$ but unstable at different wavenumbers (a). Growth rate vs. wavenumber response when $P = 0.6$ on the middle branch (highlighted with blue markers in (a)); it can be seen that this solution is stable at zero wavenumber but become unstable against 2D perturbations whose wavenumber is between 0.59 and 0.86.

1D perturbations but they become unstable when $xz$-dependent disturbances are considered. To demonstrate such stability characteristics, we plot the most dangerous growth rate as a function of wavenumber in Figure 4.8 (b) when 2D perturbations are introduced in the base-state solution at $P = 0.6$ on the middle branch (highlighted by blue squares in Figure 4.8 (a)). We can see that growth rate is positive when wavenumbers are roughly within 0.59 and 0.86. It means that, normal modes whose wavenumber is within this range are going to grow exponentially with time. To verify this finding, we show an agreement between growth rates given by linear stability and COMSOL models (for nonzero wavenumber) in Appendix B. This new mechanism of 2D EM-thermal instability motivates another research question:

- *How does transient evolution of $T$ look like when we introduce perturbations in the unstable states marked by blue squares in Figure 4.8 (a)? Do perturbations keep on growing exponentially to a different steady-state?*

To answer this question, we carry out direct numerical simulations on a full nonlinear 2D COMSOL model which solves the 2D system of equations (4.2) and (4.3) along with boundary conditions (4.5)-(4.7) with no fluid flow. To make sure that both linear stability and COMSOL models are

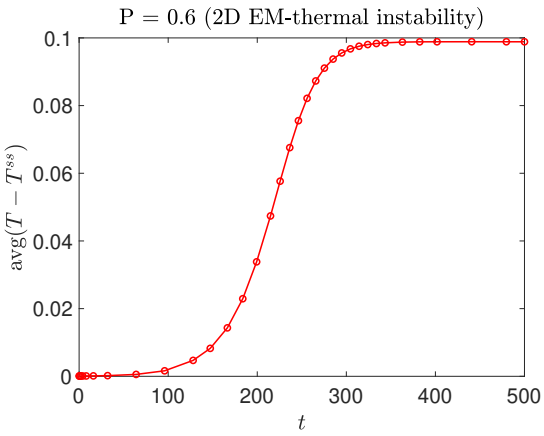


(a) Transient growth of avg($\tilde{T}$)

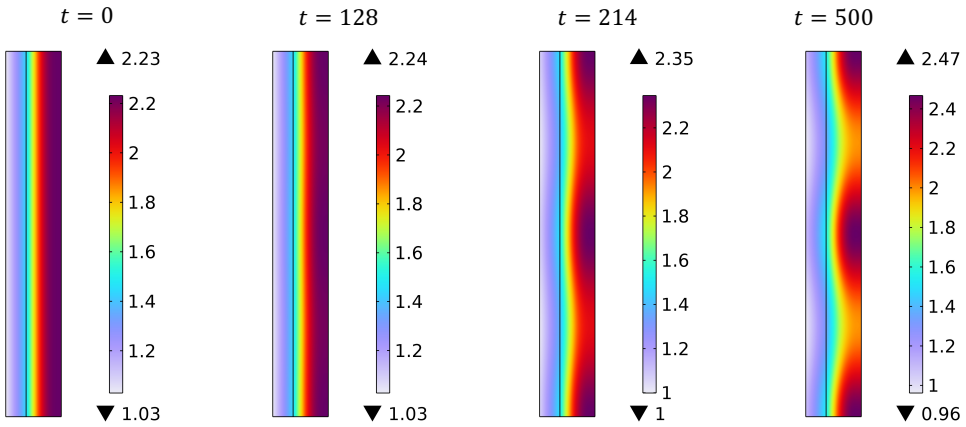


(b) Transient snapshots of 2D $T$-profiles

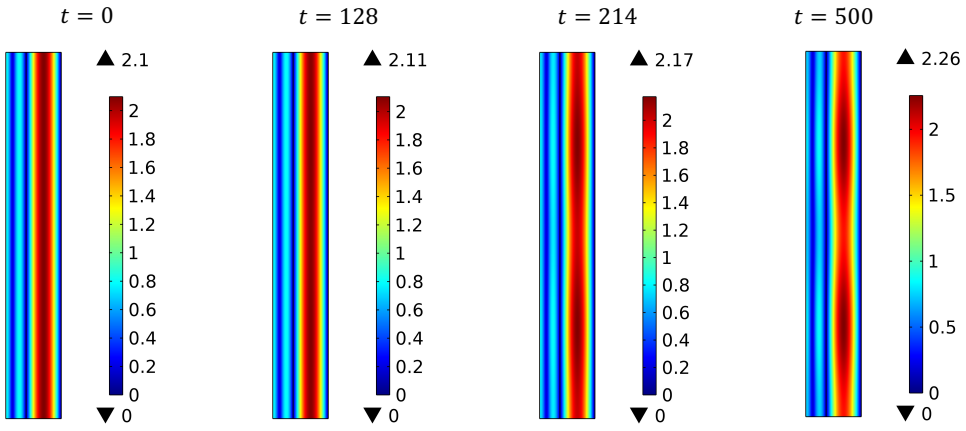


(c) Transient snapshots of 2D $|E|$-profiles

Figure 4.9: Direct numerical simulations using COMSOL Multiphysics demonstrating 2D EM-thermal instabilities (also known as fringe field instabilities in this chapter). Transient growth of avg($\tilde{T}$) is plotted in (a), steady-state $T$ and $|E|$ profiles are plotted in (b) and (c), respectively. The COMSOL model is simulated for $P = 0.6$ and the initial guess is provided such that the model simulates instabilities highlighted by blue square markers in Figure 4.8.

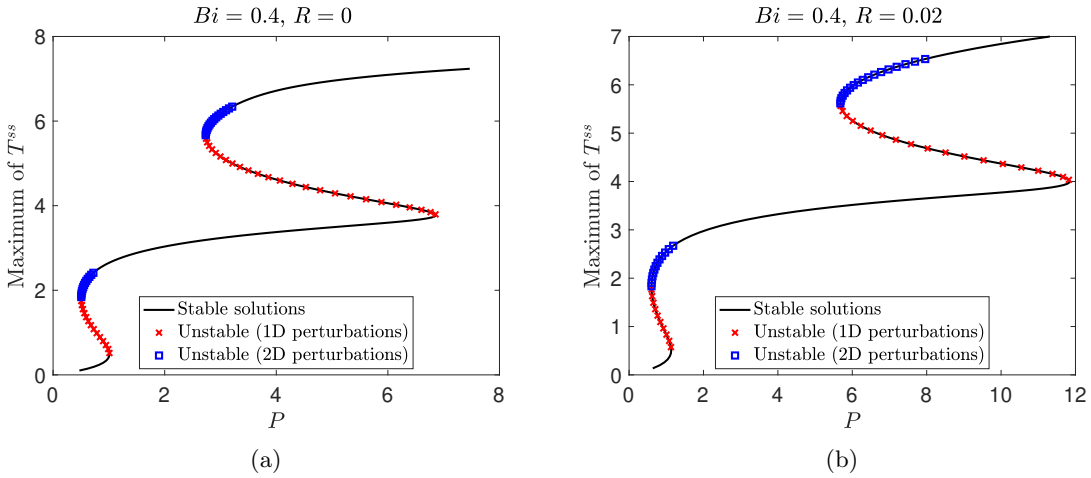


Figure 4.10: Impact of the environmental heat losses on the fringe field instability when $R = 0$ (a) and $R = 0.02$ (b). In both of these cases $Bi = 0.4$. Here $R$ is varied as heat loss by thermal radiation is the dominant mode of heat transfer with the environment.

consistent, we extract eigenfunctions from the linear stability model and use them in the initial guess setting in the COMSOL simulation (i.e., initial guess in the COMSOL model is $T_{\text{in}}(x,z) = T^{ss}(z) + \bar{T}(x,z)$, where $\bar{T}$ is derived from eignefunction from the linear stability analysis). Since we are after determining transient evolution of $\tilde{T}$ from the COMSOL model, we define a new variable, $\tilde{T}$, in the model to store the value of $T(x,z,t) - T^{ss}(z)$ as a function of $t$. We then take the surface average of $\tilde{T}$ and plot how the average $\tilde{T}$ is varying with $t$ in Figure 4.9 (a). To understand how sinusoidal perturbations are evolving with time, we plot snapshots of $T$ and $|E|$ profiles at different times steps in Figure 4.9 (b) and (c), respectively. We see that $\tilde{T}$ keep on growing exponentially until it reaches a new steady-state as seen in Figure 4.9 (b) and (c) when $t = 500$. These 2D EM-thermal instabilities are a result of the fringe field coupling described by (4.22) and (4.23)– that's why we call them as fringe field instabilities. The research question that is motivated by this discussion is

- *Which mechanisms are promoting the fringe field instabilities?*

First, we explore how environmental heat losses affect the fringe field instability. Since these instabilities are occurring on the middle and upper branches, we increase the radiative heat losses at the boundaries by increasing the radiation parameter $R$. The stability characteristics from

this parametric study are plotted in Figure 4.10. We can see that the fringe field instabilities are promoted with environmental heat losses through radiation. To understand the impact of electric field resonance producing double S-curve on the fringe field instabilities we carry out linear stability on the EM-thermal problem by choosing channel thicknesses such that (4.1) is not satisfied (by keeping $n_1 = 4$ and $n_2 = 1$). In this scenario, we now have a typical S-shaped power response curve at the base-state. Results from the stability analysis are plotted in Figure 4.11. We notice that the stability characteristics, even with 2D perturbations, are the same as that of [27]. Fringe field instabilities are absent in case of an S-curve and a branch of an S-curve with negative slope is unstable. This suggests that electric field resonance achieved by satisfying (4.1) may be one of the driving mechanisms behind the fringe-field instability. This suggests that a separate detailed study is required to identify other factors that may be responsible for the this instability mechanism. Future extension of work will be focused on addressing this.

The implications from this instability mechanism may be significant from practical applications' point of view. In chapter 3, we have identified that the most efficient operation of an EM HX may occur on the middle stable branch, especially near the turning point where high ceramic temperature can be maintained at lower applied powers. The 2D fringe field instabilities described in Figure 4.9 lie in the most efficient region of the middle branch. This motivates additional research questions such as: how do these 2D EM-thermal instabilities affect the performance of the device? What happens to the hotspot that we saw in Figure 3.4 when the fringe field instabilities are coupled with fluid dynamics? How does fringe field and RB convection instabilities interact with each other? To answer these questions, 3D numerical studies that couple fluid dynamics and EM heating of ceramics are required. These research questions will be addressed in future extension of this work.

### 4.4.3 Rayleigh Bénard Instability in the Fluid Region

First we start with physical explanation of different instabilities that can occur in our problem when there is fluid flow and $Ra^2 \neq 0$.

1. On the stable branches of the response curve (solutions marked by solid lines in Figure 4.8(a)) thermal runway and fringe field instabilities are absent, and the primary mechanism of

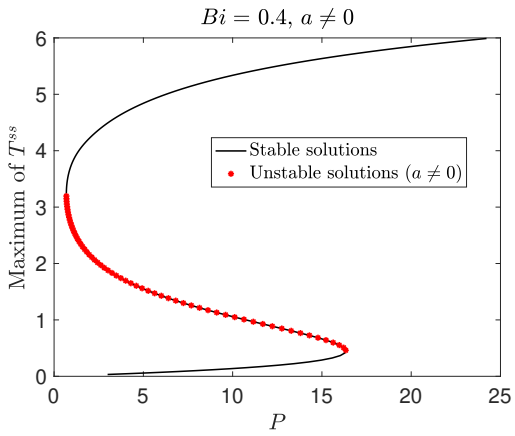


Figure 4.11: Stability characterestics of an S-curve. To get this plot, we carry out 2D linear stability analysis on the EM thermal problem, and channel thickness are such that we do not satisfy the resonance criteria 4.1.

instability is the RB convection which occurs when buoyancy dominates over viscous stresses within the fluid (i.e., when $Ra^2 > Ra^2_{\text{crit}}$ for a given $P$).

2. Looking at unstable regions marked by red cross and blue square in Figure 4.8(a), there are three different primary instabilities that can occur simultaneously (RB convection, thermal runway, and fringe field instabilities), and experimentally we may observe nonlinear interaction between them which would affect the transient growth of perturbations. Linear stability analysis can answer whether a base-state solution is stable or unstable but cannot capture interactions between these instabilities.

To address these points, this subsection is organized in the following way.

1. For a given $P$ on stable branches in Figure 4.8, we first generate neutral stability curves that are plots of $Ra^2$ vs. $a$ when $\text{Re}\{s\} = 0$. The smallest value of $Ra^2$ on these curves is $Ra^2_{\text{crit}}$, and the wavenumber corresponding to this point is $a_{\text{crit}}$.

2. By utilizing the numerical continuation method discussed earlier in conjunction with the Brent's algorithm, we find out $Ra^2_{\text{crit}}$ as a function of $P$ on stable branches in Figure 4.8 (a).

To generate neutral stability curves from 2D linear analysis we set $\text{Re}\{s\} = 0$ in (4.24)-(4.30), and since primary instability is $xz$-dependent perturbations we have $\mathbf{a} = (a, 0, 0)$ and $\mathbf{a} \cdot \hat{u} = 0$. To

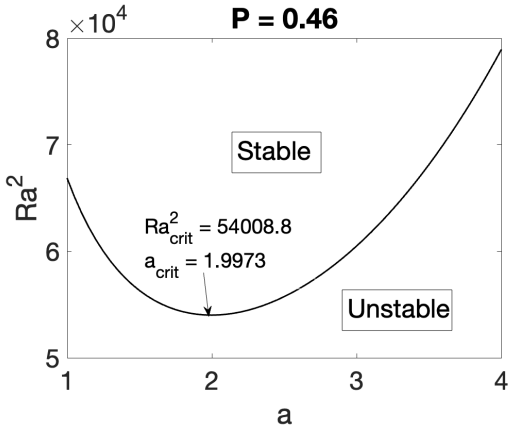


Figure 4.12: Neutral curves generated using linear stability analysis in conjunction with a root finding algorithm when incident $P = 0.46$ on the lower stable branch of the response curve shown in Figure 4.8(a). Smallest value of $Ra^2$ on this curve is the $Ra^2_{\text{crit}}$ which determines the onset of RB instability in the fluid region.

generate neutral stability curves, we utilize Newton's root finding algorithm with the linear stability code such that for a given $a$ and $P$, root finder returns a value of $Ra^2$ such that $\text{Re}\{s\} = 0$. A neutral stability curve is shown in Figure 4.12 when applied power of $P = 0.46$ on the lower stable branch in Figure 4.8 (a). This curve represents the marginal stability state, which means that region above (or below) this curve is unstable (or stable). Lowest value of $Ra^2$ on this curve gives us $Ra^2_{\text{crit}}$, i.e., when we have $Ra^2 < Ra^2_{\text{crit}}$, all normal-mode disturbances decay in time, and RB convection is not observed. Critical wavenumber associates with $Ra^2_{\text{crit}}$ is $a_{\text{crit}}$ which relates to the wavelength (or size) of the most dominant convection roll that we first observe experimentally. Such parabola-like shape of the neutral curve allows us to utilize Brent's algorithm to determine $Ra^2_{\text{crit}}$ (MATLAB's `fminbnd` function in the optimization toolbox). A limiting case of the complete 2D linear stability analysis can be derived by assuming that linearized heat source is absent, and the equations governing the neutral stability state can be given by,

$$\left(D^2 - a^2\right)^2 w^{(1)} + a^2 Ra^2 T_1^{(1)} = 0, \tag{4.31a}$$

$$(D^2 - a^2) T_1^{(1)} - w^{(1)} \left(\frac{dT_1^{ss}}{dz}\right) = 0, \tag{4.31b}$$

$$(D^2 - a^2) T_2^{(1)} = 0. \tag{4.31c}$$

This way equations of fluid motion and thermal energy conservation in the fluid region are the same

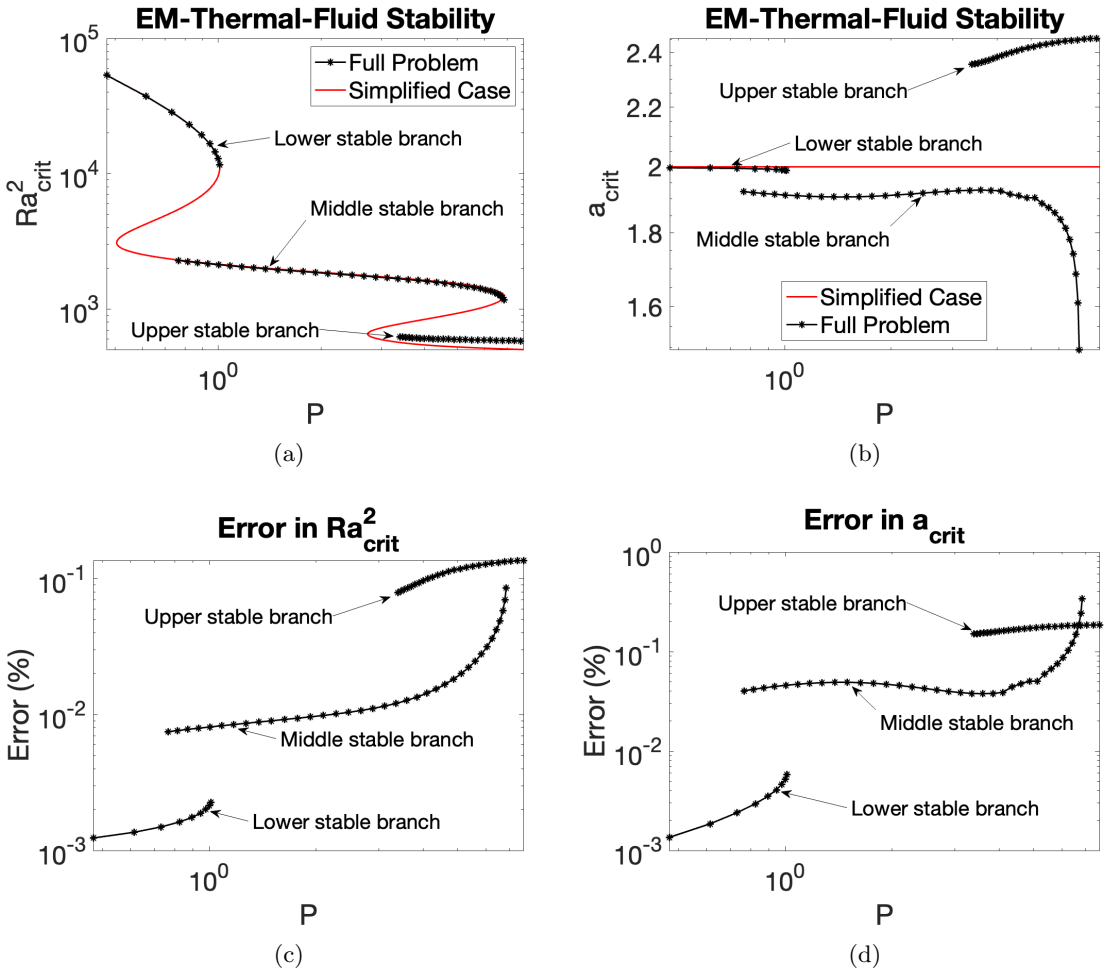


Figure 4.13: Comparison between $Ra^2_{\text{crit}}$ and $a_{\text{crit}}$ given by the full 2D linear stability analysis and simplified models is shown in (a) and (b), respectively. Relative errors ( in %) between the the comparisons shown in (a) and (b) are plotted in (c) and (d), respectively. Here simplified model does not account for fringe field coupling, maximum values of errors in (c) and (d) are 13.63% and 33.82%, respectively.

as that of classical RB convection problem and can be solved analytically. To do that (4.31c) is solved exactly and $T_1^{(1)}$ from (4.31a) is eliminated using (4.31b) to get a sixth order ODE in terms of $w^{(1)}$. Physically this problem is analogous to when loss factor of the ceramic is independent of temperature (i.e., $\frac{\partial \epsilon_2''}{\partial T} = 0$ as assumed in [51–53]), and impact of the fringe field is neglected.

In Figure 4.13 (a) and (b) we show comparison between $Ra^2_{\text{crit}}$ and $a_{\text{crit}}$ values given by the full 2D linear stability analysis and the simplified problem given by (4.31). Relative error between

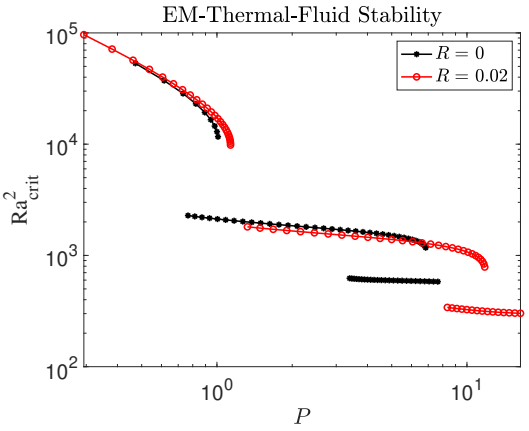


Figure 4.14: Impact of radiation heat losses on $Ra^2_{\mathrm{crit}}$.

these models is calculated as

$$\text{Error}(\%) = \left| \frac{\text{Full Problem - Simplified Problem}}{\text{Full Problem}} \right| \times 100,$$

and is plotted in Figure 4.13 (c) and (d). As the simplified model (4.31) ignores the impact of the fringe field coupling (i.e., coupling between $\tilde{T}$ and $\tilde{E}$), errors plots can be a measure of how important the impact of fringe field is. Looking at Figure 4.13 (c), maximum error in $Ra^2_{\mathrm{crit}}$ predicted by the simplified model is 13.63%, and is observed on the upper branch. This suggests that the impact of fringe field coupling cannot be ignored when RB convection is expected to take place on the upper branch. Now we investigate how environmental heat losses affect the onset of RB convection by generating $Ra^2_{\mathrm{crit}}$ vs. $P$ plot with increasing $R$. This comparison is plotted in Figure 4.14. This result confirms our prediction discussed at the end of section 4.2. By looking at how $\Delta T_1^{ss}$ varies as a function of $P$, it may be possible to predict how environmental heat losses affect the onset characteristics of the RB convection.

We now provide some sample calculations for 50% water-glycerin region 1 and zirconia in region 2 (lossy ceramic with temperature dependent loss factor). This fluid medium is chosen for the sample calculations because it satisfies the Boussinesq approximation and can be considered as a low loss fluid at lower temperatures [39]. Thermal and dielectric properties of the fluid are taken from [40] and [39], respectively, and properties of zirconia are taken from [17]. Values of

dimensionless numbers are $\epsilon_1' = 45$, $\epsilon_2' = 6.69$, $Ra = 4.21 \times 10^2$ (this suggests that the onset of RB convection is expected to occur on the lower stable branch of the response curve), $Pr = 24.5$, $\rho = 2.28$, $c_p = 0.09$, $k = 0.5$, and temperature dependent electrical conductivity of zirconia is $\sigma_2 = \omega\epsilon_0\epsilon_2'' = 0.0004e^{2.32T}$. From (4.15), for this scenario, the value of $Ra^2$ known, but onset of convection takes place when the applied EM power $P > P_{\text{crit}}$.

**Effect of the Fringe Field**

To understand how the fringe field affects the stability problem, we consider two cases: one with a constant loss factor and another with a temperature dependent loss factor of the ceramic region. When the loss factor is constant, the source terms in Maxwell's equations (4.26) are absent, no fringe field is generated, and the problem is equivalent to the one that represents stability of a stationary fluid layer heated from below with a constant heat flux applied at the bottom. Since the growth rate $s$ for this case is real-valued, neutral stability states can be represented by setting $s = 0$ in (4.24) and (4.25). We can eliminate temperature and represent neutral stability states with a $6^{\text{th}}$ order ordinary differential equation as done in [51–53]. We analytically solve the eigenvalue problem and generate stability plots for constant $\epsilon_2''$ case.

We now introduce a temperature dependent loss factor and generate a stability plot using the

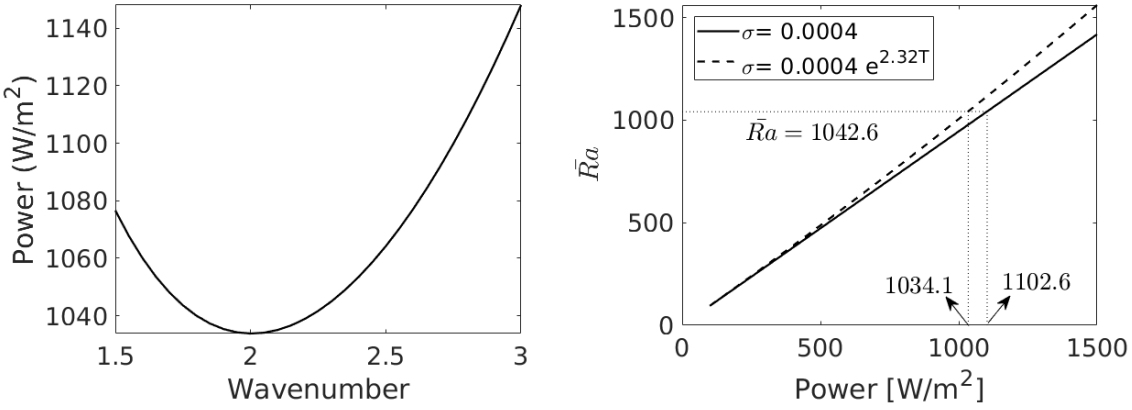


(a) (b)

Figure 4.15: Stability plot given by finite difference solution when temperature dependence of ceramic loss factor is included, $P_{crit} = 1033.5$ W/m$^2$, $a_{crit} = 2.02$ (a). Comparison of $\bar{Ra}$ given by (4.15)with constant and temperature dependent ceramic loss factors (b). Average interpolation error in (b) is 0.5%.

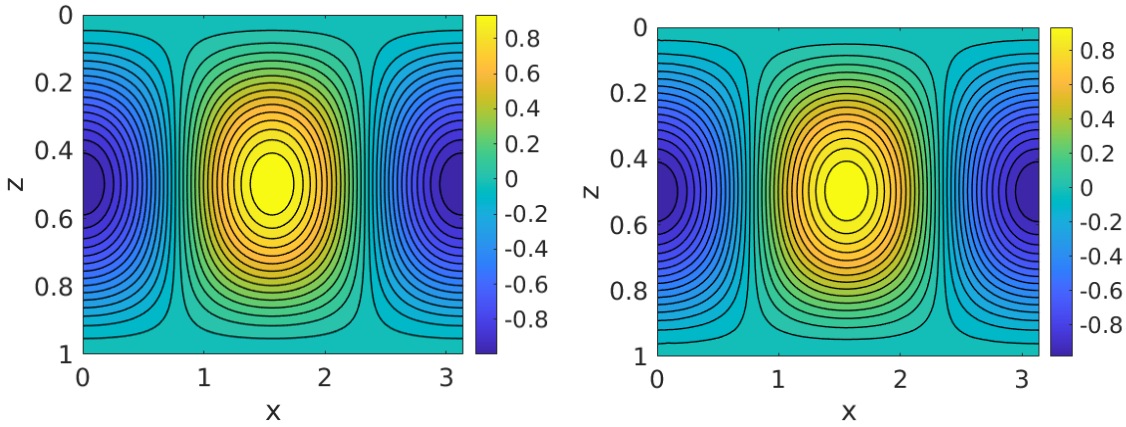


Figure 4.16: Normalized vertical component of velocity from linear stability analysis (a) and COMSOL mode (b) and the difference between (a) and (b) is plotted in (c) at incident power of $1,040$ W/m$^2$ when $\sigma_2 = 0.0004e^{2.32T}$

finite difference model. We expect that when the temperature dependence of the loss factor is included, the perturbed fringe field feeds back into the system and affects the overall stability. Neutral curve for this scenario is described in Figure 4.15(a). We find that that the critical power at which RB convection initiates drops from 1102.6 W/m$^2$ to 1033.5 W/m$^2$ when temperature dependence is included, which means that the fringe field promotes the Bénard convection. To justify the drop in critical power, we evaluate the classical Rayleigh number, $\bar{Ra}$, which is given by (4.15). We then plot $\bar{Ra}$ when $\epsilon_2$ is constant and temperature dependent in Figure 4.15(b). As expected, $\bar{Ra}$ increases nonlinearly with applied power when the temperature dependent loss factor is considered. As a first-order estimate, we assume that instabilities occur in both of these cases at the same $\bar{Ra}$. From the analytical solution, $\bar{Ra}$ corresponding to the critical power is 1042.6, and $\bar{Ra} = 1042.6$ corresponds to expected critical power of 1034.1 W/m$^2$ in case of temperature dependent $\epsilon_2$. From Figure 4.15, observed $P_{crit}$ is 1033.8 W/m$^2$ which is within 0.03% of expected estimate value.

We carry out direct numerical simulations in COMSOL Multiphysics of the system (4.4)-(4.7) for temperature dependent ceramic loss factor. We observe Bénard convection in COMSOL simulations when critical power is $1,040$ W/m$^2$, which is within 0.6% of the critical value given by the linear stability theory. A comparison of vertical component of velocity normalized about the maximum

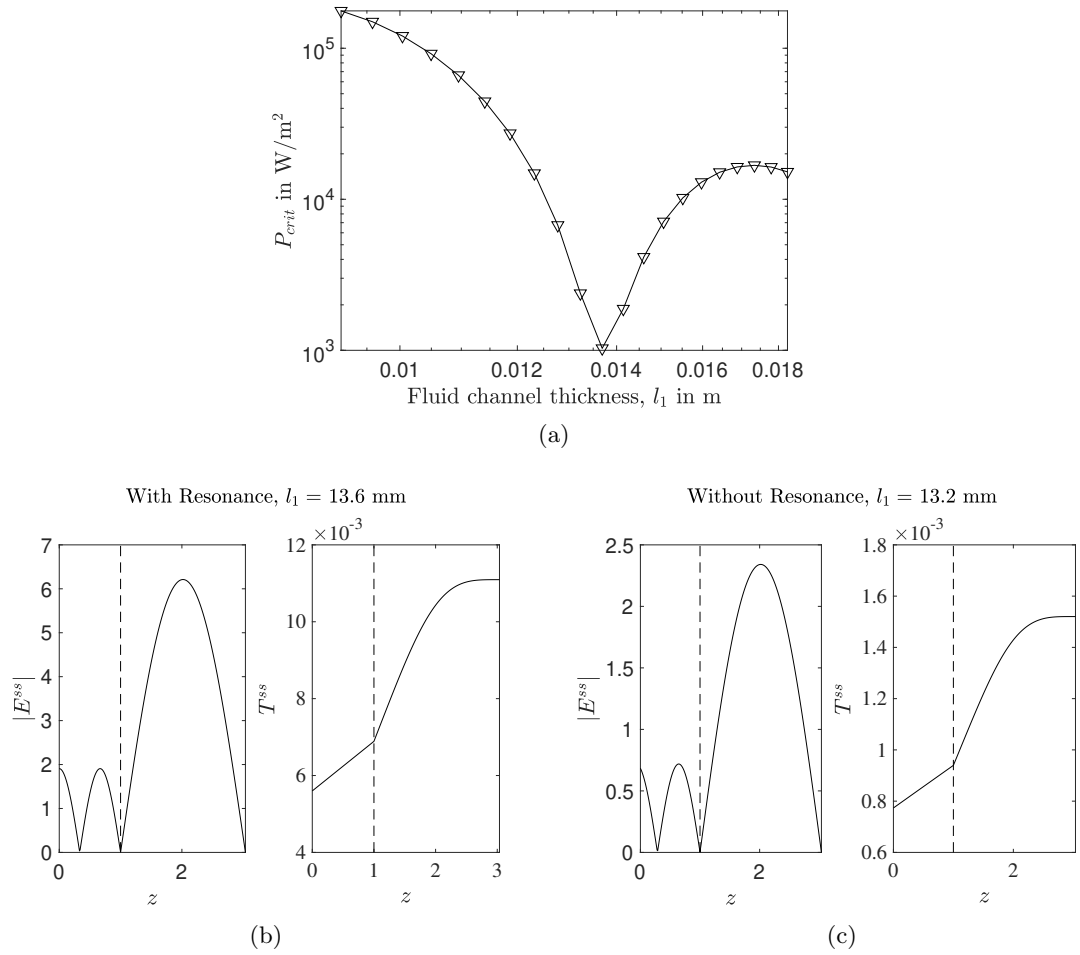


Figure 4.17: Critical power as a function of thickness of the fluid channel; sharp drop in critical power at $l_1 = 13.6$ mm corresponds to the case of Bragg resonance in region 2 (a). Base state $|E|$ and $T$ with (b) and without (c) Bragg resonance.

value, i.e., $w/w_{\max}$ from both models is shown in Figure 4.16. We see that wavelengths of convection rolls and normalized velocity are in satisfactory agreement. In the COMSOL model we use second-order quadratic Lagrange triangular elements for discretization. Maximum length of the element is such that there are $N$ elements per wavelength of EM waves in the fluid region. The required mesh density for the full coupled problem is determined with a convergence test on $N$. For $N = 30$ used in the model variations in numerical results are under 0.002%.

**Parametric Studies**

In the results shown up to this point we kept the channel thicknesses such that we satisfy Bragg resonance criteria (4.1). In this study, we keep rest of the parameters to be the same and vary the channel thickness to break the Bragg resonance conditions. Variation of critical power as a function of channel thickness is shown in Figure 4.17(a). The sharp drop in critical power corresponds to the case when Bragg resonance conditions are satisfied. We can, therefore, conclude that field resonance in lossy ceramic region is a strong destabilizing mechanism. To explain the sudden drop in critical power, we look at the base state $|E|$ and $T$ solutions with and without resonating conditions. We can see that from Figure 4.17(b) and (c) maximum field strength $|E|$ in region 2 is increased when we satisfy resonance conditions, and lead to efficient heating of the ceramic region. As a result, ceramic temperatures in resonating case are order of magnitude larger compared to non-resonating case, and we need to supply more EM power to initiate Bénard convection in the non-resonating cases.

Material property which is responsible for fringe field generation is the temperature dependent ceramic permittivity. To understand how the loss factor affects the stability, we consider a parametric study where we assume that $\sigma_2 = Ae^{BT}$ and vary $A$ and $B$ with rest of the parameters kept as the same as before. In this study, we keep the channels thickness such that Bragg resonance conditions (4.1) are satisfied with $n_1 = 3$ and $n_2 = 1$.

First, we keep $A = 0.001$ and vary $B$, critical power as a function of $B$ is shown in Figure 4.18(a). We see that critical power is not as sensitive to the variations in $B$ as it drops by only 100 $W/m^2$ when $B$ is increased from 0 to 10. In the next study, we keep $B = 3$ and vary $A$, critical power as a function of $A$ is shown in Figure 4.18(b). We explain the dramatic variation of critical powers with respect to $A$ in three stages: **Stage (*I*)** consists of $A$ values between $10^{-4} - 0.05$; **Stage (*II*)** is comprised of $A$ values between $0.05 - 1$; and **Stage (*III*)** corresponds to $A$ between $1 - 20$. Additional results required to support the explanation are shown in Figure 4.19. In Figure 4.19(a), we plot norm of the absolute field strength, which is defined as $norm(|E|) = \int_0^{1+l} |E| dz$, as a function $A$. In Figure 4.19(b), the volumetric heat source $q$ plotted as a function of $A$, where $q = \int_1^{1+l} |E_2^{ss}|^2 \sigma_2(T_2^{ss}) dz$.

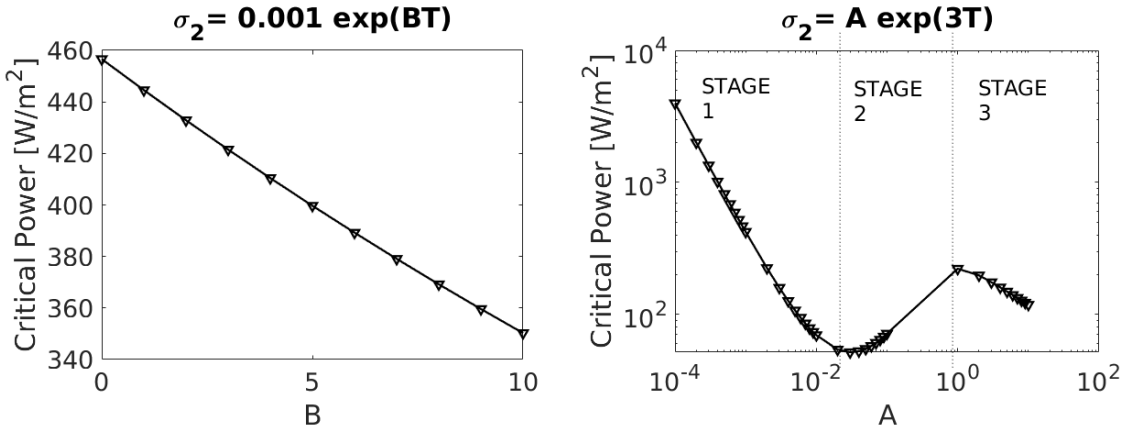


(a) (b)

Figure 4.18: Critical power variation with loss factor $\sigma_2 = Ae^{BT}$. When $B$ is varied keeping $A = 0.001$ (a) and $A$ is varied keeping $B = 3$ (b).

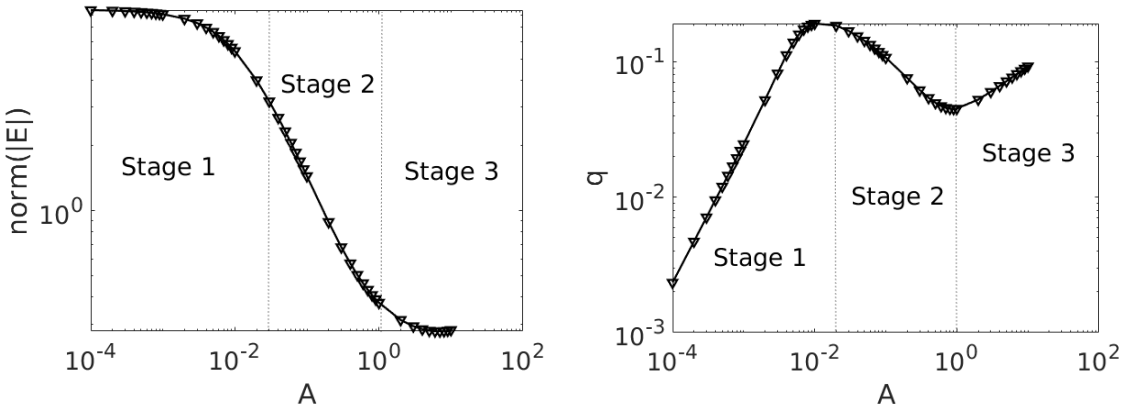


(a) (b)

Figure 4.19: Average field strength (a) and heat source (b) variation with loss factor $\sigma_2 = Ae^{BT}$ when $A$ is varied keeping $B = 3$.

**Stage (*I*)** During this stage, loss factor $\sigma_2$ increases with $A$ and electric field gradually attenuates as seen in Figure 4.19(a). As a result, $q$, which depends on both $\sigma_2$ and $|E_2|$, is dominated by increases in $\sigma_2$ as seen in Figure 4.19(b). Since amount of heat generated in lossy region increases, we need to supply less power to achieve Bénard convection; critical power drops with $A$.

**Stage (*II*)** As $A$ is increased even further, $\sigma_2$ increases, but it causes field strength to drop significantly as seen in Figure 4.19(a). During this stage the heat source $q$ is dominated by drastic attenuation of the field strength as seen from Figure 4.19(b). We need to supply more power to

compensate for drop in the heat source. Therefore, critical power increases with $A$.

**Stage (*III*)** During this stage, $\sigma_2$ is large enough such that skin effect becomes noticeable and electric field rapidly drops near the surface, and localized heating at the ceramic surface is observed. Within the range of $A$ values, surface heating is dominated by the loss factor, and the heat source starts to increase with $A$, and thus critical power drops.

## 4.5 Conclusions

When EM HXs with compressible gases are considered, we have two new mechanisms of heat transfer: natural convection which occurs under the action of gravity and gas accelerates to accommodate density variations in the fluid region. In this chapter, we have investigated onset characteristics of natural convection within the fluid. We have considered stability of laminar plane Poiseuille flow of a lossless coolant obeying Boussinesq approximation in a horizontal double layer EM HX where fluid flow is situated above a lossy ceramic. Since the fluid is lossless, only the ceramic material undergoes EM heating and the plane Poiseuille flow is heated from below due to the thermal contact with the ceramic layer. It is known that the most dominating mode of Bénard instability is when flow direction and wave-vector of disturbances are perpendicular to each other. Therefore, through normal mode linear stability analysis, we determine the critical power at which the plane Poiseuille flow along the $y$-direction is unstable to normal modes of disturbances whose wave-vector is parallel to the $x$-direction. We solve the eigenvalue problem characterizing the stability of the system using a second-order central difference scheme. The model is then validated against an analytical solution which is a limiting case with the constant ceramic loss factor.

In our problem, we have three different primary instability mechanisms that can occur simultaneously: thermal runaway and fringe field instabilities occur within the ceramic and RB convection instability takes place in the fluid region. Linear stability analysis can tell us whether a base-state is stable or unstable, but may not identify which mechanism is causing this instability. To address this we first set $Ra^2 = 0$ (i.e., RB convection is absent) and carry out a 2D linear stability analysis on the EM thermal problem. Newly found fringe field instabilities occur near the leftmost turning point (low power high temperature regions) of the middle and upper branches of double S-curve

when wavenumber of the perturbations is nonzero. One of the primary mechanisms responsible for this instability is the electric field resonance required for the double S-curve and environmental heat losses. But, further investigation is required to fully explain mechanisms behind the fringe field instability.

Once we have identified stable region of the response curve where thermal runaway and fringe field instabilities are absent, we then determined critical Rayleigh number, $Ra^2_{\text{crit}}$. When $Ra^2 > Ra^2_{\text{crit}}$, buoyancy dominates over the viscous stresses within the fluid and RB convection initiates. Through parametric studies, we have then determined several mechanisms that promote RB convection. When the ceramic loss factor is temperature dependent, perturbations introduced in steady-state temperature act as a source of perturbed electric (fringe) field which originates in the ceramic region and propagates outwards. Since the EM heat source is dependent on the electric field strength, the fringe field feeds back into the system and promotes the RB instability. For 50% glycerin-water solution as the fluid and zirconia as the ceramic material, we find that critical EM power at which convection initiates drops from 1102.6 W/m$^2$ to 1033.8 W/m$^2$ when temperature dependent loss factor is included. We have also found out that the electric field resonance is a strong mechanism that promotes RB convection.

In this chapter, we have determined the onset characteristics of RB convection in a double layer EM HX under laminar flow conditions through linear stability analysis. But, full 3D numerical models are required to understand how RB convection affects the performance of the device. Moreover, such models can help understand the interaction between the fringe field instability, thermal runaway, and RB convection. Development of such models is left for future developments. In the next chapter, we focus on a different mode of heat transfer which the acceleration of the gas, and explore how it can be utilized to generate mechanical power from EM HXs.

# 5 COMPRESSIBLE COOLANTS IN ELECTROMAGNETIC HEAT EXCHANGERS

From a practical point of view, it is of experimental interest to consider EM HXs which rely on coupling between EM heating of ceramics and compressible gas dynamics. When density gradients are present within a fluid, heat can be transferred by natural convection in the presence of gravity and gas may accelerate to high speeds in order to satisfy the mass conservation (i.e., velocity field is not divergence free). In the previous chapter, we investigated the onset characterestics of natural convection in an EM HX, and in this chapter we focus on coupling between EM heating of ceramics and the acceleration of the gas due to work of thermal expansion. The working principle of beamed energy propulsion technology relies on the acceleration of the gas. In the NASA's millimeter wave thermal launch system (MTLS) experiment [54], an array of ceramic tubes is heated by high-power EM waves. When a sufficiently high temperature is achieved, the gas is expanded through the channel array. Net gain in the kinetic energy of the gas due to EM heat addition in the ceramic tubes is then utilized to produce thrust at the outlet. To develop the ground-to-ground power beaming technology, we are interested in investigating how much mechanical power can be generated at the outlet when compressible gas dynamics is coupled with nonlinear EM heating of ceramics.

The MTLS experiment considered a high-pressure gaseous flow through an array of thin and long ceramic channels heated by EM waves. This structure may be considered as an ideal porous media which obeys the capillary tubes model of porosity and permeability [32]. This motivates another possible design of an EM HX which consists of a lossy porous ceramic material heated by EM waves and when a compressible gas flowing through the pores delivers the power at the

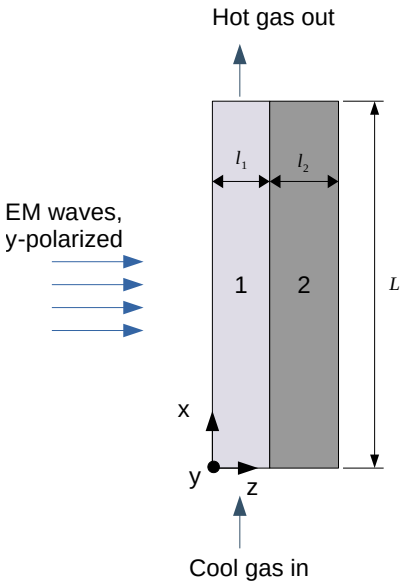


Figure 5.1: Structure of the considered EM HX. Region 1 is a pressure-driven flow of an ideal gas and region 2 is a lossy ceramic material.

outlet. It is expected that due to larger contact area between the fluid and the ceramic, heat exchange between them would be improved. In order to design such an EM HX, we first need to understand the impact of compressible gas dynamics taking place at the pore scale when coupled with the phenomenon of thermal runaway in the ceramic. At the pore scale, thicknesses are small, and natural convection can be ignored as the Rayleigh number is small (e.g., $Ra^2$ in of $o(10^{-2})$ when pore-scale lengths are $o(10^2)$ $\mu$m, where $Ra^2$ is defined in chapter 4. As shown in chapter 3, thermal runaway is a local phenomenon expected to occur at the pore-scale. Therefore, it is of interest to identify the impact of coupling between thermal runaway and work of expansion taking place at the pore-scale. The research questions we want to address in this chapter are

1. *Which mode of heat transfer is dominant at the pore scale?*

2. *How does compressible gas dynamics affect the onset of thermal runaway in the ceramic and vice versa?*

To answer these questions, we make an idealization of the pore scale model with a 2D thin and long double-layer EM HX such that a channel carrying a compressible flow of an ideal gas (in region 1)

is in perfect thermal contact with a thin ceramic (in region 2) heated by incident plane EM waves, as shown in Figure 5.1. Plane EM waves polarized in the $y$-direction are incident on the structure; only the ceramic is heated by EM waves, and the fluid heats up and does work of thermal expansion due to the thermal contact with the heated ceramic. Although existence of the new stable solution in a double S-curve shows promise towards keeping thermal runaway under control, our model [8] suggests that middle branch is possible when $\epsilon_1' > \epsilon_2'$, where $\epsilon_1'$ and $\epsilon_2'$ are real components of dielectric constants of regions 1 and 2, respectively. With gases ($\epsilon_r = 1$) as fluids in region 1, a double S-curve is not possible as $\epsilon'$ of typical ceramics is greater than 1. On the other hand, compressible gases may cool down as a result of work done by thermal expansion. Thus, we are interested to find out how work of thermal expansion done by the gas affects the phenomenon of thermal runaway in ceramics. The objective of this chapter is to derive analytical models capturing thermal energy transport done by gas in region 1 when coupled with the phenomenon of thermal runway in the ceramic in region 2.

Compressible gas dynamics taking place at the pore-scale depends on the Mach number, $\bar{M}^2$, which is the ratio of characteristic flow velocity to the speed of sound in the gas, and the Reynolds number, $Re$, which gives us the importance of the flow inertia with respect to viscous stresses within the fluid. If channel thickness are of $o(10^{-6})$ m, both $Re$ and $\bar{M}^2$ are small, and the viscous stresses are more important compared the flow inertia. The impact of the compressible gas dynamics at these pore-scale lengths is then determined by the Bearing number, $\Lambda$, which is the ratio of viscous pressure scale to the ambient atmospheric pressure. When work of expansion dominates the net heat added to the system, we may observe Joule-Thompson (JT) cooling of the gas. The phenomenon of classical JT cooling occurs when a compressible gas undergoes insenthalpic expansion from high to low pressures through a small orifice or a porous plug; when the gas does work of thermal expansion, its internal energy drops to maintain constant enthalpy (assuming that there is no entropy generation) [55]. In our model, the gas flows through a thin channel (thickness of $o(10^2)$ $\mu$m) from high to low pressure conditions (similar to the classical JT cooling problem), but the process in no longer isenthalpic as the heat is added to the system through volumetric EM heating, and some heat interaction takes place with the environment. Cooling of the gas is

expected when the work done by the gas becomes larger than the net heat added to the system. One question that arises from this discussion is:

3. *How does JT cooling affects the onset of thermal runaway in the ceramic?*

We develop an analytical model based on lubrication theory to answer this question. By carrying out parametric studies we then determine critical conditions for JT cooling to take place. Finally, by looking at competition between different modes of heat transfer, we show that JT cooling causes temperatures to drop down near the outlet even during thermal runaway.

Although the lubrication model can help identify the coupling between JT cooling and thermal runaway, the mechanical power generated under such conditions is expected to be small because of slow flow speeds. To address this, we consider a high-speed compressible flow through a thin channel with thickness of $o(10^{-2})$ m and length of $o(1)$ m (these dimensions are comparable to the NASA MTLS experiment [54]). The flow speeds in this model are such that $Re \gg 1$, and $\bar{M}^2$ is of $o(1)$. Under these conditions, we can ignore the contribution due to viscous stresses within the flow (as the inertia is dominating), and the gas dynamics is in the regime of *Rayleigh flow*, which describes the frictionless compressible flow through thin channels of uniform cross section with heat addition [56, 57]. Since viscous stresses are negligible, $\Lambda = 0$, but the impact of the compressible gas dynamics depends on the values of $\bar{M}^2$. We look at flow speeds such that the EM HX operates under subsonic conditions (i.e., $0 < \bar{M}^2 < 1$). The Rayleigh flow model derived here is limited by the phenomenon of *thermal choking* [56, 57]; when $\bar{M}^2 = 1$ (sonic state) anywhere within the fluid channel, it is not possible to add heat into the system without altering the inlet flow conditions. With the help of linear stability analysis and parametric studies we determine operating conditions to avoid thermal choking. Finally, we calculate mechanical power efficiency to determine the effectiveness of this energy conversion.

In both of these models, we assume that the aspect ratio of the 2D geometry is small. This allows us to expand all the unknown variables in a perturbation series in terms of the small aspect ratio. At the leading order, the cross-sectional averaged conservation laws and the equation of state are derived. In both the models, the resulting systems of nonlinear ordinary differential equations (ODEs) are then solved using the ODE solvers in MATLAB (`ode15s` and `bvp4c` functions).

## 5.1 Model with Viscous Effects: Lubrication Theory

Steady-state compressible Navier-Stokes equations governing the fluid flow in region 1 are given by

$$\nabla \cdot \left(\rho_1' \mathbf{u}'\right) = 0, \tag{5.1a}$$

$$\rho_1'(\mathbf{u}' \cdot \nabla)\mathbf{u}' = -\nabla p' + \mu \nabla^2 \mathbf{u}' + \frac{\mu}{3}\nabla(\nabla \cdot \mathbf{u}'), \tag{5.1b}$$

where $\rho_1'$ is the density of the gas in kg/m$^3$, $\mathbf{u}' = (u', w', 0)$ is the flow velocity vector in m/s which has components $u'$ and $w'$ along the $x$ and $z$-directions, respectively, $p'$ is the fluid gauge pressure in Pa, $\mu$ is the dynamic viscosity of the fluid in Ns/m$^2$.

The time-averaged dimensional power density of the incident plane wave can be calculated using the Poynting theorem as

$$P_{av} = \frac{E_0^2}{2\Upsilon}, \tag{5.2}$$

where $E_0$ is strength of the incident electric field in V/m, and $\Upsilon$ is the characteristic impedance of free space [12] in ohm. We assume the frequency ($f$) of incident EM waves to be 2.45 GHz in the microwave regime. When the plane waves, polarized in the $y$-direction, are incident on the system (Figure 5.1), Maxwell's equations governing propagation of the EM field vector are reduced to scalar Helmholtz equations governing $y$-component of EM waves as

$$\nabla^2 E_j' + {k_0'}^2 \left[\epsilon_{r_j} + i\epsilon_j''(T)\right] E_j' = 0, \tag{5.3}$$

where subscript $j$ is the region of solution ($j = 1$ corresponds to fluid channel and $j = 2$ is the ceramic region shown in Figure 5.1), $E$ is the electric field amplitude in V/m, $k_0' = 2\pi/\lambda_0$ is the wavenumber of EM waves in free-space in 1/m, $\lambda_0$ is the EM wavelength in m, $\epsilon_r$ is the dielectric constant, and $\epsilon''$ is the temperature dependent dielectric loss factor. In our problem, $\epsilon_1'' = 0$ as air is lossless.

Thermal energy conservation in regions 1 and 2 at the steady-state is given by

$$(\rho_1' c_{v_1}) \left[\mathbf{u}' \cdot \nabla T_1'\right] + p' \nabla \cdot \mathbf{u}' = k_1 \nabla^2 T_1', \tag{5.4a}$$

$$0 = k_2 \nabla^2 T_2' + \frac{1}{2} \omega \epsilon_0 |E_2'|^2 \epsilon_2''(T_2'), \tag{5.4b}$$

where $T'$ is the temperature in K, $c_v$ and $c_p$ are specific heat in J/kgK at constant volume and pressure, respectively, $k$ is the thermal conductivity in W/mK, $\omega$ is the angular frequency of the EM waves, and $\epsilon_0$ is the permittivity of the free space. In addition, the compressible gas in region 1 is assumed to obey the ideal gas law

$$p_{\text{atm}} + p' = \rho_1' R_g T_1', \tag{5.5}$$

where $p_{\text{atm}}$ is the atmospheric pressure in Pa, and $R_g$ is the ideal gas constant which has the value of 287 J/kgK.

We now introduce dimensionless variables as

$$z = \frac{z'}{l_1},\ x = \frac{x'}{L},\ u = \frac{u'}{U},\ w = \frac{w'}{W},\ p = \frac{p' l_1^2}{12 L \mu U},\ E_j = \frac{E_j'}{E_0},\ T_j = \frac{T_j'}{T_A},\ k_0 = k_0' l_1, \tag{5.6}$$

where primed quantities represent respective dimensional variables, $x$ is the position vector along the $x$-axis, $z$ is the position vector along the $z$-axis, $l_1$ is the thickness of region 1, $L$ is the length of the layers (as shown in Figure 5.1), $U$ and $W$ are the velocity scales in $x$- and $z$-directions, respectively, and $T_A$ is the ambient temperature.

Dimensionless Helmholtz equations derived from (5.3) are given by

$$\frac{\partial^2 E_1}{\partial z^2} + \eta^2 \frac{\partial^2 E_1}{\partial x^2} + k_0^2 \epsilon_1' E_1 = 0, \tag{5.7a}$$

$$\frac{\partial^2 E_2}{\partial z^2} + \eta^2 \frac{\partial^2 E_2}{\partial x^2} + k_0^2 \left[\epsilon_2' + i\epsilon_2''(T_2)\right] E_2 = 0, \tag{5.7b}$$

where $\eta = \frac{l_1}{L}$ is the aspect ratio of the structure, $\epsilon'$ is the real part dielectric constant, and $\epsilon''$ is the loss factor. In our model, we keep $\epsilon_1' = 1$ and $\epsilon_2 = \epsilon_2' + i\epsilon''(T_2) = 6.69 + i\left[\frac{0.0004 e^{2.32T}}{\omega \epsilon_0}\right]$ for

zirconia [17]. In addition to (5.7), a $y$-polarized plane wave solution in the free space can be given by

$$E_a = e^{ik_0 z} + \Gamma e^{-ik_0 z}, \tag{5.8}$$

where $\Gamma$ is the reflection coefficient. Boundary conditions on the EM problem are

$$\frac{\partial E_1}{\partial z} + ik_0 E_1 = 2ik_0 \text{ at } (z = 0), \tag{5.9a}$$

$$\left.\begin{aligned} \tfrac{\partial E_1}{\partial z} &= \tfrac{\partial E_2}{\partial z} \\ E_1 &= E_2 \end{aligned}\right\} \text{ at } (z = 1), \tag{5.9b}$$

$$E_2 = 0 \text{ at } (z = 1 + l), \tag{5.9c}$$

where the condition (5.9a) is derived by making use of (5.8) and continuity of tangential components of electric and magnetic fields at the interface between the free space and the region 1 [26].

From the fluid mass conservation equation (5.1), the relation between velocity scales can be derived as $W \sim \eta U$. Steady-state Navier-Stokes equations governing the mass and momentum conservation of the fluid region 1 are given as

$$\frac{\partial}{\partial x}(\rho_1 u) + \frac{\partial}{\partial z}(\rho_1 w) = 0, \tag{5.10a}$$

$$\eta Re \rho_1 \left[u\frac{\partial u}{\partial x} + w\frac{\partial u}{\partial z}\right] = -12\frac{\partial p}{\partial x} + \eta^2\frac{\partial^2 u}{\partial x^2} + \frac{\partial^2 u}{\partial z^2} + \frac{\eta^2}{3}\frac{\partial}{\partial x}\left(\frac{\partial u}{\partial x} + \frac{\partial w}{\partial z}\right), \tag{5.10b}$$

$$\eta^3 Re \rho_1 \left[u\frac{\partial w}{\partial x} + w\frac{\partial w}{\partial z}\right] = -12\frac{\partial p}{\partial z} + \eta^2\left[\eta^2\frac{\partial^2 w}{\partial x^2} + \frac{\partial^2 w}{\partial z^2}\right] + \frac{\eta^2}{3}\frac{\partial}{\partial z}\left(\frac{\partial u}{\partial x} + \frac{\partial w}{\partial z}\right), \tag{5.10c}$$

where $Re = \frac{\rho_0 U l_1}{\mu}$ is the Reynolds number. Factor 12 appears in the pressure gradient terms because of how we defined dimensionless $p$ in (5.6). This is done for mathematical convenience as it allows simplification in the leading-order momentum equation that we discuss in upcoming sections.

Thermal energy conservation laws (5.4) with dimensionless variables are given by

$$\eta Pe \rho_1 \left[u\frac{\partial T_1}{\partial x} + w\frac{\partial T_1}{\partial z}\right] + \eta(\gamma - 1)Pe(1 + \Lambda p)\left[\frac{\partial u}{\partial x} + \frac{\partial w}{\partial z}\right] = \eta^2\frac{\partial^2 T_1}{\partial x^2} + \frac{\partial^2 T_1}{\partial z^2}, \tag{5.11a}$$

$$0 = \eta^2\frac{\partial^2 T_2}{\partial x^2} + \frac{\partial^2 T_2}{\partial z^2} + \frac{\eta}{l}P|E_2|^2\epsilon_2''(T_2), \tag{5.11b}$$

where $Pe = \frac{l_1 U}{\alpha_1}$ is the Péclet number, $\alpha_1 = \frac{k_1}{\rho_0 c_{v_1}}$, $\gamma = \frac{c_{p_1}}{c_{v_1}}$, $(\gamma - 1)Pe$ characterizes work of thermal expansion, $\Lambda = \frac{12LU\mu}{l_1^2 \rho_0 R T_A}$ is the Bearing number, $l = \frac{l_2}{l_1}$ is the ratio of thicknesses of regions 2 and 1, and $P = \frac{E_0^2 \omega \epsilon_0 l_2 L}{2 T_A k_2}$ is dimensionless power of the incident EM waves. Finally, the equation of state of the gas in region 1 is given as

$$\rho_1 = \frac{1}{T_1}[1 + \Lambda p] \tag{5.12}$$

Boundary conditions on fluid velocity and temperature in dimensionless form are

$$\left.\begin{aligned} \tfrac{\partial T_1}{\partial z} &= \eta Bi(T_1 - 1) - \eta R(T_1^4 - 1) \\ u &= w = 0 \end{aligned}\right\} \text{ at } (z = 0), \tag{5.13a}$$

$$\left.\begin{aligned} \tfrac{\partial T_1}{\partial z} &= k \tfrac{\partial T_2}{\partial z}, \\ T_1 &= T_2, \end{aligned}\right\} \text{ at } (z = 1), \tag{5.13b}$$

$$\frac{\partial T_2}{\partial z} = 0 \text{ at } (z = 1 + l) \tag{5.13c}$$

where $Bi = \frac{hL}{k_1}$ is the Biot number, $R = \frac{\xi s_r T_A^2 L}{k_1}$, $\xi$ is the emissivity of the surface, and $s_r$ is the Stefan-Boltzmann radiation parameter. $Bi$ and $R$ together characterize heat losses taking place with the surroundings.

### 5.1.1 Asymptotic Model without Thermal Diffusion

With $\eta \ll 1$ and $Re$, $Pe$, $Bi$, and $\Lambda$ to be of $O(1)$, we can expand the unknown variables as

$$\rho_1 = \rho_1^{(0)} + \eta \rho_1^{(1)} + \ldots, \; p = p^{(0)} + \eta p^{(1)} + \ldots,$$
$$u = u^{(0)} + \eta u^{(1)} + \ldots, \; w = w^{(0)} + \eta w^{(1)} + \ldots,$$
$$E_1 = E_1^{(0)} + \eta E_1^{(1)} + \ldots, \; E_2 = T_2^{(0)} + \eta E_2^{(1)} + \ldots,$$
$$T_1 = T_1^{(0)} + \eta T_1^{(1)} + \ldots, \; T_2 = T_2^{(0)} + \eta T_2^{(1)} + \ldots.$$

Substituting above approximations into the governing equations and collecting leading-order terms, we find

$$\frac{\partial}{\partial x}\left(\rho_1^{(0)}u^{(0)}\right)+\frac{\partial}{\partial z}\left(\rho_1^{(0)}w^{(0)}\right)=0, \tag{5.14a}$$

$$\frac{\partial p^{(0)}}{\partial z}=0, \tag{5.14b}$$

$$12\frac{\partial p^{(0)}}{\partial x}=\frac{\partial^2 u^{(0)}}{\partial z^2}, \tag{5.14c}$$

$$\frac{\partial^2 T_1^{(0)}}{\partial z^2}=0, \tag{5.14d}$$

$$\frac{\partial^2 T_2^{(0)}}{\partial z^2}=0, \tag{5.14e}$$

$$\rho_1^{(0)}=\frac{1}{T_1^{(0)}}\left(1+\Lambda p^{(0)}\right), \tag{5.14f}$$

along with leading-order boundary conditions from (5.13)

$$\left.\begin{array}{c}\frac{\partial T_1^{(0)}}{\partial z}=0\\ u^{(0)}=w^{(0)}=0\end{array}\right\}\ \text{at } (z=0), \tag{5.15a}$$

$$\left.\begin{array}{c}\frac{\partial T_1^{(0)}}{\partial z}=k\frac{\partial T_2^{(0)}}{\partial z},\\ T_1^{(0)}=T_2^{(0)},\end{array}\right\}\ \text{at } (z=1), \tag{5.15b}$$

$$\frac{\partial T_2^{(0)}}{\partial z}=0 \text{ at } (z=1+l). \tag{5.15c}$$

From (5.14d), (5.14e) and boundary conditions (5.15), we can say that both $T_1^{(0)}$ and $T_2^{(0)}$ are independent of $z$. Because of the perfect thermal contact between regions 1 and 2 we have

$$T_1^{(0)}(x)=T_2^{(0)}(x)=T^{(0)}(x).$$

From (5.14b), $p^{(0)}$ depends only on $x$. As the pressure is independent of $z$, leading-order $x$-momentum equation (5.14c) can be integrated twice to get an expression of $u^{(0)}$. After applying

no slip conditions, the integral yields

$$u^{(0)}(x,z) = 6\frac{\partial p^{(0)}}{\partial x}(z^2 - z). \tag{5.16}$$

From (5.14f), we can then conclude that $\rho_1^{(0)}$ is $z$ independent. Finally, electric field at the leading-order then governed by

$$\frac{\partial^2 E_1^{(0)}}{\partial z^2} + k_0^2 \epsilon_1' E_1^{(0)} = 0, \tag{5.17a}$$

$$\frac{\partial^2 E_2^{(0)}}{\partial z^2} + k_0^2 \left[\epsilon_2' + i\epsilon_2'' \left(T^{(0)}\right)\right] E_2^{(0)} = 0, \tag{5.17b}$$

along with boundary conditions from (5.9)

$$\frac{\partial E_1^{(0)}}{\partial z} + ik_0 E_1^{(0)} = 2ik_0 \text{ at } (z = 0), \tag{5.18a}$$

$$\left.\begin{array}{c} \frac{\partial E_1^{(0)}}{\partial z} = \frac{\partial E_2^{(0)}}{\partial z}, \\ E_1^{(0)} = E_2^{(0)}, \end{array}\right\} \text{ at } (z = 1), \tag{5.18b}$$

$$E_2^{(0)} = 0 \text{ at } (z = 1 + l). \tag{5.18c}$$

Closure problem in terms of $T^{(0)}$ can be obtained by looking at first-order correction terms in energy equations as

$$Pe\rho_1^{(0)} u^{(0)} \frac{dT^{(0)}}{dx} + (\gamma - 1)Pe\left(1 + \Lambda p^{(0)}\right)\left[\frac{\partial u^{(0)}}{\partial x} + \frac{\partial w^{(0)}}{\partial z}\right] = \frac{\partial^2 T_1^{(1)}}{\partial z^2}, \tag{5.19a}$$

$$0 = \frac{\partial^2 T_2^{(1)}}{\partial z^2} + P|E_2^{(0)}|^2 \epsilon_2''(T^{(0)}), \tag{5.19b}$$

with boundary conditions

$$\frac{\partial T_1^{(1)}}{\partial z} = Bi\left(T^{(0)} - 1\right) + R\left(T^{(0)^4} - 1\right), \text{ at } z = 0 \tag{5.20a}$$

$$\frac{\partial T_1^{(1)}}{\partial z} = k\frac{\partial T_2^{(1)}}{\partial z},\ T_1^{(1)} = T_2^{(1)}, \text{ at } z = 1, \tag{5.20b}$$

$$\frac{\partial T_2^{(1)}}{\partial z} = 0, \text{ at } z = 1 + l. \tag{5.20c}$$

Now integrating (5.14a) and (5.19a) over $0 < z < 1$ and (5.19b) over $1 < z < (1 + l)$, applying boundary conditions (5.20), and making use of (5.16), we get averaged leading-order governing equations (superscripts are dropped) as

$$-Pe\rho_1 \frac{dp}{dx}\frac{dT}{dx} - (\gamma - 1)Pe(1 + \Lambda p)\frac{d^2p}{dx^2} + Bi(T - 1) + R(T^4 - 1) - q(T) = 0, \tag{5.21a}$$

$$\frac{d}{dx}\left(\rho_1 \frac{dp}{dx}\right) = 0, \tag{5.21b}$$

$$\rho_1 = \frac{1}{T}\left(1 + \Lambda p\right). \tag{5.21c}$$

where $q(T) = kP||E_2||^2\epsilon_2''(T)$ and $||E_2||^2 = \frac{1}{l}\int_1^{1+l} |E_2|^2 dz$. From (5.21b) we can write $\rho_1 \frac{dp}{dx} = -m$, where $m$ is a nonzero arbitrary positive constant which represents the average mass flow rate through the channel, and the system (5.21) becomes

$$Pe\ m\frac{dT}{dx} - (\gamma - 1)Pe(1 + \Lambda p)\frac{d^2p}{dx^2} + Bi(T - 1) + R(T^4 - 1) - q(T) = 0, \tag{5.22a}$$

$$m = -\frac{1}{T}\frac{dp}{dx}(1 + \Lambda p), \tag{5.22b}$$

$$\rho_1 \frac{dp}{dx} = -m. \tag{5.22c}$$

Eliminating the second term on the left hand side of (5.22a) using (5.22b) we get

$$m\gamma Pe\frac{dT}{dx} + \Lambda(\gamma - 1)Pe\left(\frac{dp}{dx}\right)^2 + Bi(T - 1) + R(T^4 - 1) - q(T) = 0, \tag{5.23a}$$

$$\frac{dp}{dx} = -\frac{mT}{1 + \Lambda p}. \tag{5.23b}$$

Additionally, $p$ and $\rho_1$ must satisfy the mass conservation constraint (5.22c).

As we have a pressure-driven flow in region 1, we specify $p$ at the inlet, and outlet is open to atmospheric condition ($p = 0$). We also consider that the cool gas is entering the system at the fixed temperature. The boundary conditions are

$$p(x = 0) = p_0,\ p(x = 1) = 0, \tag{5.24a}$$

$$T(x=0) = T_0. \tag{5.24b}$$

In addition to (5.23)-(5.24), we need to solve (5.17) and (5.18) to get a complete solution.

### 5.1.2 Asymptotic Model with Thermal Diffusion

The asymptotic model discussed in the last subsection ignores the diffusive heat transport along the $x$-direction at the leading-order. This is justified when spatial temperature gradients seen in the model are $O(1)$ (i.e., when operated on the lower power region of the S-curve). In [48] we have shown that thermal runaway is initiated locally when maximum temperature in the ceramic reaches a critical value. Such nonuniform heating results in local hotspots (a very sharp temperature gradients concentrated locally) in the regions where onset of thermal runaway takes place. As a result, diffusion may be comparable to heat transport via convection and thermal expansion. If the heat diffusion along the $x$-direction is included at the first-order correction in previous asymptotic analysis, we get

$$m\gamma Pe\frac{dT}{dx} + m^2\Lambda(\gamma-1)Pe\left[\frac{T^2}{(1+\Lambda p)^2}\right] - \eta(1+kl)\frac{d^2T}{dx^2} + Bi(T-1) + R(T^4-1) - q(T) = 0, \tag{5.25}$$

along with (5.23b) and (5.22c). Since (5.25) requires an additional boundary condition on $T$, we assume that fluid leaving the system at the outlet does not exchange heat with the surroundings, i.e., we have

$$p(x=0) = p_0,\ p(x=1) = 0, \tag{5.26a}$$

$$T(x=0) = T_0, \frac{dT}{dx}(x=1) = 0. \tag{5.26b}$$

Effect of heat diffusion on temperature profiles during thermal runaway will be highlighted in Section 5.2.

### 5.1.3 Numerical Solution

The general solution to EM problem (5.17) can be given as (with superscripts dropped)

$$E_1 = c_1 e^{ik_0\sqrt{\epsilon_1}z} + c_2 e^{-ik_0\sqrt{\epsilon_1}z}, \tag{5.27a}$$

$$E_2 = d_1 e^{ik_0\sqrt{\epsilon_2(T)}z} + d_2 e^{-ik_0\sqrt{\epsilon_2(T)}z}, \tag{5.27b}$$

where $\sqrt{\epsilon_1} = \sqrt{\epsilon_1'} = 1$ and $\sqrt{\epsilon_2} = \sqrt{\epsilon_2' + i\epsilon_2''\,(T(x))}$. Unknown coefficients $c_1, c_2, d_1$ and $d_2$ are determined from boundary conditions (5.18).

We solve the system (5.25)-(5.26) along with (5.27) and (5.18) using the MATLAB's boundary value problem (BVP) suite (`bvp4c` function) [58] in conjunction with the secant root finding method. The numerical solution has the following steps:

1. As the system (5.25) is second order in $T$ and first order in $p$, we solve (5.25) subject to (5.26b) and outlet boundary condition on $p$ in (5.26a) for given a guessed value of $m = m_{\text{guess}}$.

2. To get a complete solution to the problem, we need to find $m_{\text{guess}}$ such that mass conservation constraint (5.22c) and the inlet condition on $p$ are satisfied. As $m$ is an arbitrary nonzero constant, its value must be uniform across the domain; we can write (5.22c) at the inlet as

$$\rho_{1\text{at } x=0}\left(\frac{dp}{dx}\right)_{\text{at } x=0} + m = 0, \tag{5.28}$$

   where $\rho_{1\text{at } x=0}$ is determined from the inlet boundary conditions on $p$, $T$ in (5.26), and using the equation of state (5.21c). Note that we do not satisfy the mass conservation constraint unless true value of $\rho_{1\text{at } x=0}$ matches with its guessed value we get from step 1 for a given $m_{\text{guess}}$. In other words, we satisfy the mass conservation constraint (5.22c) when guessed $p$ we get in the step 1 matches the inlet condition (5.26a).

3. Iterative secant root finding algorithm is utilized to find $m_{\text{guess}}$ such that solution to the system of BVP satisfies the mass conservation constraint at the inlet. The root finding algorithm converges when the magnitude of the left hand side of (5.28) drops below $10^{-12}$.

Finally, we use a similar approach to solve the model without diffusion (5.23)-(5.24), except we use MATLAB's initial value problem (IVP) suite (`ode15s` function) [59] to solve the system of first-order differential equations for a given $m_{\text{guess}}$ subject to inlet boundary conditions in (5.24). Appropriate $m$ is then determined by the secant root finding method such that $p$ satisfies the outlet boundary condition in (5.24).

### 5.1.4 Results

We first verify the two numerical models described in the previous subsection by comparing results with an exact solution for $\Lambda = 0$ and constant $\epsilon_2''$. For temperature dependent $\epsilon_2''$, we compare the two numerical solutions with another computational model simulated in COMSOL Multiphysics for thermal runaway scenario. Results of this verification can be found in Appendix C. We then demonstrate how gas cools down when work of thermal expansion dominates over net heat added to the system (i.e., JT cooling). With the help of parametric studies we then determine conditions under which JT cooling initiates. Finally, by looking at local competition between different modes of heat transfer, we describe how JT cooling affects the onset of thermal runaway.

In the simulations below we consider air and zirconia in regions 1 and 2, respectively. Thermal and dielectric properties of zirconia are taken from [17]. Material parameters used in the following simulations are: $\epsilon_1' = 1, \epsilon_2' = 6.69, \epsilon_1'' = 0, \epsilon_2''(T) = \frac{0.0004e^{2.32T}}{\omega\epsilon_0}$, $\rho_2 = 2,848$ kg/m$^2$, $R_g = 287$ J/kgK, $c_{p_1} = 1,000$ J/kgK, $c_{p_2} = 217$ J/kgK, $c_{v_1} = 713$ J/kgK, $k_1 = 0.02$ W/mK, and $k_2 = 0.2$ W/mK. Some dimensionless parameters that are kept constant throughout this chapter are $p_0 = 1$ and $T_0 = 1$.

#### Importance of Heat Diffusion

When temperature dependent loss factor of the ceramic is included, (5.17)-(5.18) is coupled with (5.23)-(5.24); the nonlinear problem cannot be solved exactly even for $\Lambda = 0$. When $\epsilon_2''$ is temperature dependent, we compare results from the two numerical models with another one simulated in COMSOL Multiphysics which solves the system (5.7)-(5.13). We find that when the incident EM power is $P_{av} = 5,000$ W/m$^2$, thermal runaway initiates in the ceramic region resulting in

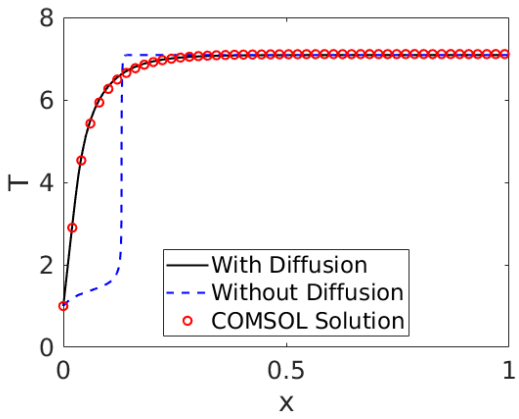


Figure 5.2: Comparison between two numerical models (with and without diffusion) and COMSOL simulation for incident EM power $P_{av} = 5,000$ W/m$^2$ when $L = 1$ m, $l_2 = 0.02$ m and $\eta = 0.01$. Average relative errors between COMSOL solution and the model with diffusion are 0.014 and errors between COMSOL solution and the model without diffusion are 0.149. Here we have $\lim_{\eta\to 0} \eta(1 + kl) = \lim_{\eta\to 0}(\eta + \bar{k}) = \bar{k} = \frac{kl_2}{L} = O(1)$.

sharp local temperature gradients. In Figure 5.2, when the COMSOL solution (which accounts for thermal diffusion) is compared against the thin-domain model without thermal diffusion, we see that temperature profiles produce the largest errors in the regions where local onset of thermal runaway takes place. On the other hand, when heat diffusion is included in the thin domain model, error between the solutions given by the COMSOL and numerical models drops to 0.014 which is expected as the thin-domain model is $O(\eta)$ accurate.

Looking at (5.25) we can see that dimensionless parameter $\eta(1 + kl)$ gives us the order of magnitude of heat transport through thermal diffusion. Since we assume $\eta \ll 1$, $\lim_{\eta\to 0} \eta(1+kl) = \lim_{\eta\to 0}(\eta+\bar{k}) = \bar{k}$, where $\bar{k} = \frac{kl_2}{L}$ governs the thermal diffusion along the $x$-direction. We can then expect that when $\bar{k} \to 0$, diffusion becomes negligible and temperature profiles produced by the model with diffusion should converge to the ones produced by the model without thermal diffusion (even for thermal runaway scenario). We now vary $\bar{k}$ from 0.1 to 0.05 by keeping $l_1 = 10^{-4}$ m, $l_2 = 0.02$ m, $k = 10$ and varying $L$ from 2 to 4 m (here small $l_1$ is chosen to satisfy $\eta \ll 1$). Looking at Figures 5.2 and 5.3, we see that errors between the two solutions keep dropping as $\bar{k}$ gets smaller. We can, therefore, conclude that heat transfer via thermal diffusion at the microscale is governed by the term $\bar{k}$ when $\eta \ll 1$ and should be ignored only when $\bar{k} \ll 1$ is satisfied.

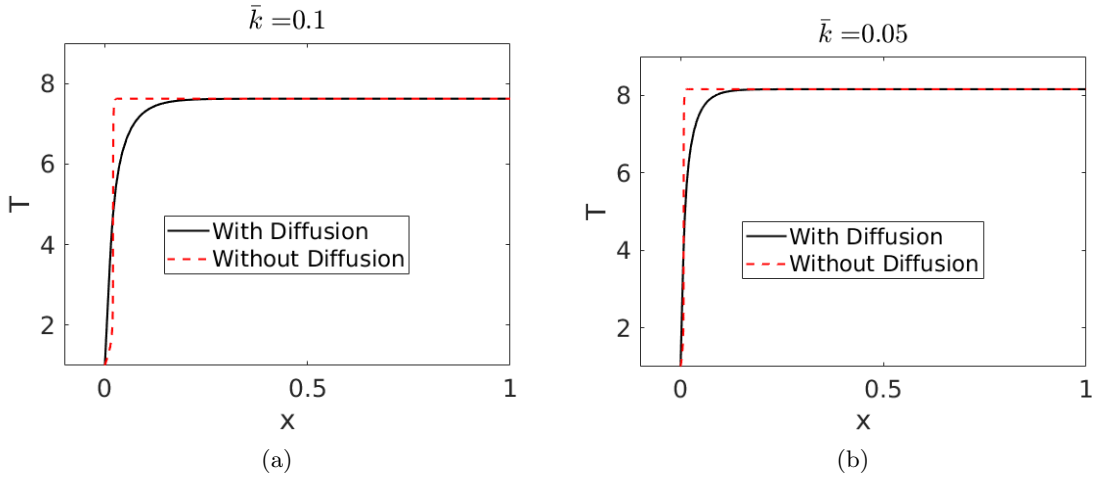


Figure 5.3: Comparison between the models with and without diffusion for different $\bar{k} = k\frac{l_2}{L}$ values when incident EM power $P_{av} = 5,000$ W/m$^2$. Here $\bar{k}$ is varied by keeping $l_1 = 10^{-4}$ m, $l_2 = 0.02$ m, $k = 10$ and varying $L$ from 2 to 4 m. Average relative errors seen in (a) and (b) are 0.0406 and 0.0249, respectively.

### Joule-Thompson Cooling of the Gas

Assuming that $\eta \ll 1$ and $\bar{k} \ll 1$ (i.e., heat diffusion is small), the net energy balance of the system can be represented as

$$\Delta e + \Delta w = Q, \tag{5.29}$$

where $\Delta e$, $\Delta w$ and $Q$ are local change in gas internal energy, work done by the gas and heat added to the system. Referring to (5.22a), local work of thermal expansion done by the gas and heat added to the system are given by

$$\Delta w = -(\gamma - 1)Pe(1 + \Lambda p)\frac{d^2p}{dx^2} \text{ and } Q = q(T) - Bi(T - 1) - R(T^4 - 1).$$

Dividing (5.29) by $Q$ and rearranging we get

$$\frac{\Delta e}{Q} = 1 - \frac{\Delta w}{Q}. \tag{5.30}$$

When $\frac{\Delta w}{Q} > 1$, we see that the change in internal energy becomes negative and the gas cools. Dimensionless parameters that govern the work of thermal expansion are $(\gamma - 1)Pe$ and $\Lambda$. Here,

we keep $Pe$ constant and vary $\Lambda$ to identify how $\Delta e$ is affected by $\Lambda$. Variations in $\Lambda$ are achieved by changing $l_1$ and keeping $l_2 = 0.02$ m, $L = 4$ m, and the incident EM power to be $P_{av} = 1,000$ W/m$^2$. Looking at Figure 5.4(a) when $\Lambda = 0.04$, term $\frac{\Delta w}{Q}$ is always less than 1 resulting in a positive term on the right hand side of (5.30), which means that the heat added in the system is large compared to the work of thermal expansion done by the gas; $\Delta e > 0$ and the gas keeps on heating up as it moves from the inlet to the outlet. In Figure 5.4(b) and (c), when $\Lambda$ is large, cooling of the gas initiates locally, where $\frac{\Delta W}{Q} > 1$, i.e., when work of thermal expansion is greater than the net heat added into the system. This suggests that when channel thicknesses are such that $\Lambda$ is large, there exists a competition between local onset of thermal runaway and JT cooling in the pore; thermal runaway acts as a volumetric heat source, and JT cooling phenomenon behaves like a heat sink. This raises an interesting research question

- *How does JT cooling affect the onset characteristics of thermal runaway?*

We first investigate conditions under which JT cooling initiates, and then provide the answer to the research question by looking at local competition between JT cooling and thermal runaway in the ceramic. We now set $\Lambda = 0$, which physically means that density is a function of temperature only, and ignore the acceleration of the gas that occurs due to density variations with pressure. The thin domain model for this case becomes

$$Pe\ m\frac{dT}{dx} - (\gamma - 1)Pe\frac{d^2p}{dx^2} = \left[q(T) - Bi(T-1) - R(T^4 - 1)\right], \tag{5.31a}$$

$$m = -\frac{1}{T}\frac{dp}{dx}, \tag{5.31b}$$

$$\rho_1\frac{dp}{dx} = -m. \tag{5.31c}$$

Now, the term $\Delta w$ is written as

$$\Delta w = -(\gamma - 1)Pe\frac{d^2p}{dx^2}.$$

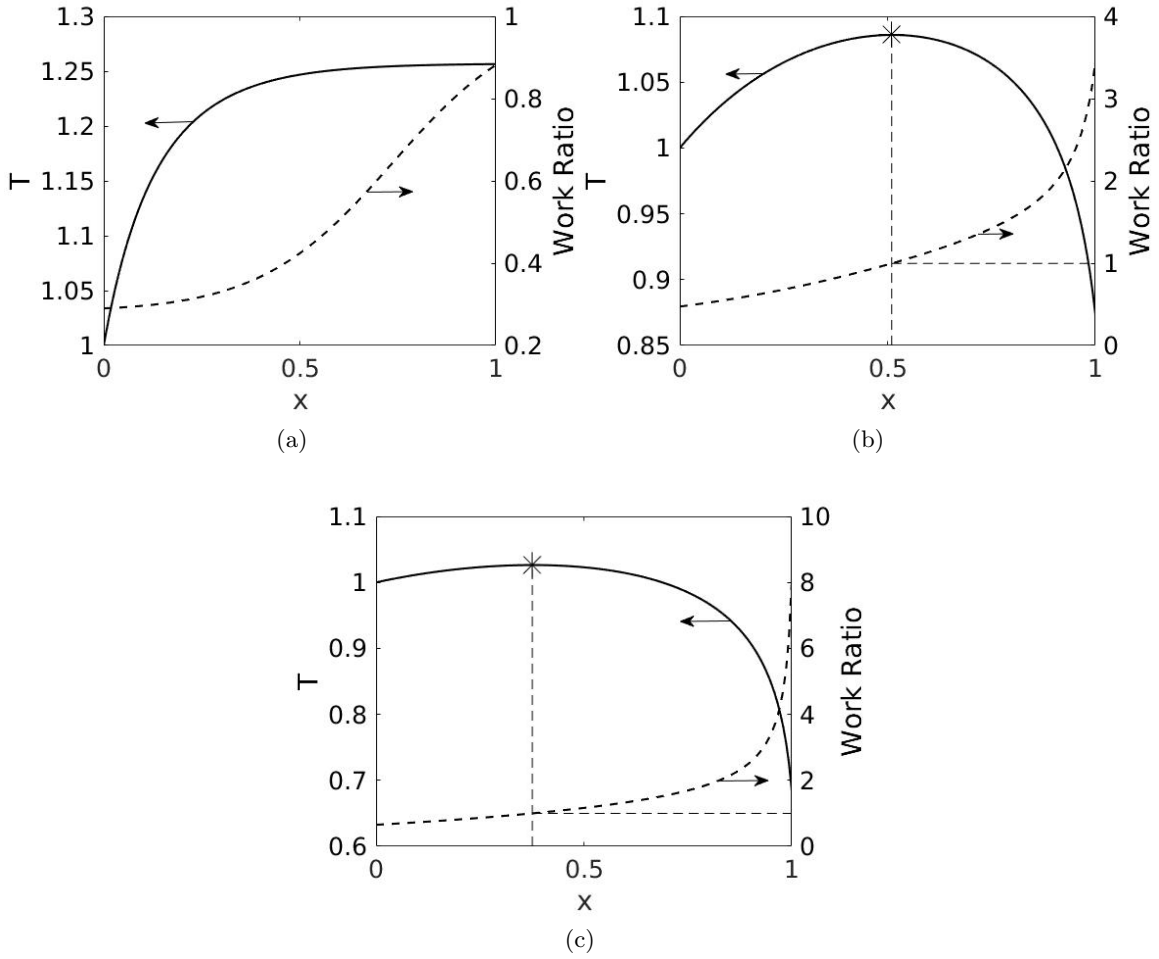


Figure 5.4: $T$ and work ratio defined as $\frac{\Delta w}{Q}$ as a function of $x$ for $\Lambda = 0.04$ (a), $\Lambda = 5$ (b) and $\Lambda = 10$ (c). In this simulation $\Lambda$ is varied by changing $l_1$ and keeping $l_2 = 0.02$ m, $L = 4$ m, and incident EM power is $P_{av} = 1,000$ W/m$^2$. Points marked by asterisk represent where temperature starts dropping as $\frac{\Delta w}{Q} > 1$.

Eliminating $p$ in the above equation using (5.31b) leads to

$$\Delta w = m(\gamma - 1) Pe \frac{dT}{dx}. \tag{5.32}$$

Also, we eliminate $p$ from (5.31a) using (5.31b), we get

$$Pe\gamma m \frac{dT}{dx} = Q. \tag{5.33}$$

According to the first law of thermodynamics, (5.33) means that the net change in the gas enthalpy is balanced by the net heat added to the system. Now substituting (5.33) into (5.32) we get

$$\frac{\Delta w}{Q} = \frac{\gamma - 1}{\gamma}. \tag{5.34}$$

From (5.34), since $\gamma \approx 1.4$ for ideal gases, $\frac{\Delta w}{Q}$ has a constant value of 0.285 which is less that 1. Therefore, we can conclude that JT cooling will not be observed for gases when $\Lambda = 0$. Physically, it means that net fraction of total heat added into the system that is converted into work of expansion is always constant for $\Lambda = 0$ and depends only on $\gamma$ irrespective of other dimensionless parameters.

Physically speaking, when $\Lambda = 0$, gas may begin to cool down locally when $q(T) \ll 1$ (i.e., very small incident powers so that EM heating is negligible) and inlet temperature of the gas is higher than the ambient temperature. When this is true, heat will be lost to the surrounding from the system through convection and radiation, $Q < 0$, and gas would begin to cool down as it is losing energy to the environment (not because of JT cooling).

When $\Lambda \neq 0$ is true in the gas (i.e., when density of the gas varies strongly with pressure) we need to identify how $\Lambda$ affects the JT cooling. For this case, $\Delta w$ is given as

$$\Delta w = -(\gamma - 1)Pe(1 + \Lambda p)\frac{d^2 p}{dx^2},$$

eliminating $p$ using (5.23b), we get

$$\Delta w = (\gamma - 1)Pe\left[m\frac{dT}{dx} + \Lambda\left(\frac{dp}{dx}\right)^2\right]. \tag{5.35}$$

Now we rewrite the energy equation (5.22a) as

$$mPe\frac{dT}{dx} = Q - \Delta w. \tag{5.36}$$

Substitution of (5.36) into (5.35) yields

$$\frac{\Delta w}{Q} = \frac{(\gamma - 1)}{\gamma}\left[1 + \Lambda Pe\left\{\frac{1}{Q}\left(\frac{dp}{dx}\right)^2\right\}\right].$$

We can then conclude that JT cooling occurs at a location $x$ where

$$\max\left\{(\Lambda Pe)\left[\frac{1}{Q}\left(\frac{dp}{dx}\right)^2\right]\right\} > \frac{1}{\gamma-1},$$

which further simplifies to

$$\max\left\{(\Lambda Pe)\left[\frac{1}{Q}\left(\frac{dp}{dx}\right)^2\right] - \left(\frac{1}{\gamma-1}\right)\right\} > 0. \tag{5.37}$$

Also as a verification, when $\Lambda = 0$ condition (5.37) can never be satisfied for $\gamma > 1$ which is consistent with what we have found through (5.34). Further simplification of (5.37) cannot be possible because $\frac{dp}{dx}$ is coupled with $T$ and $\Lambda$ through the equation of state. To check whether or not the condition (5.37) is satisfied for a given $\Lambda$ and $Pe$, we are required to solve the complete problem for $p$ and $T$, which suggests that a parametric study is required on $\Lambda$ and $Pe$ to find whether we have JT cooling.

We use the following approach to carry out parametric study on $\Lambda$ and $Pe$. Let us define

$$f(\Lambda, Pe) = \max\left\{(\Lambda Pe)\left[\frac{1}{Q}\left(\frac{dp}{dx}\right)^2\right] - \left(\frac{1}{\gamma-1}\right)\right\}. \tag{5.38}$$

Since both $Q$ and $\frac{dp}{dx}$ are a function of $x$, JT cooling of the gas begins locally where $f(\Lambda, Pe) > 0$. We now take following steps in this parametric study:

1. Fix the incident EM power, $Bi$, and $R$.
2. For a given $Pe$ value, find $\Lambda$ such that the $f(\Lambda, Pe) = 0$ using a root finding algorithm.
3. By repeating the step 2 for increasing values of $Pe$, we can generate a parametric curve with $\Lambda$ on the $y$-axis and $Pe$ on the $x$-axis. Using this curve, we can find out minimum value of $\Lambda$ such that we observe JT cooling for a given incident power and $Bi$.
4. Finally, we repeat steps 1-3 for different incident power with fixed $Bi$ and vice versa.

In Figure 5.5, we plot parametric curves with $\Lambda$ as a function of $Pe$ such that $f(\Lambda, Pe) = 0$ in (5.38). With these curves, the parameter space $(\Lambda, Pe)$ is divided into two region: when parameter

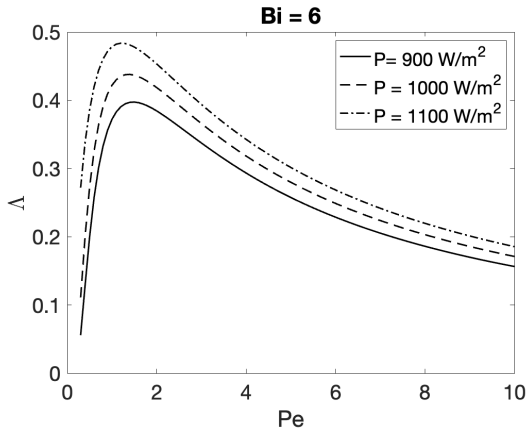


Figure 5.5: Parametric curves characterizing Joule-Thompson cooling as a function of $\Lambda$ and $Pe$: region above (or below) the curve corresponds to Joule-Thompson cooling (or heating) of the gas

values lie below the curve, $\frac{\Delta W}{Q} < 1$ everywhere and gas temperature increases as it moves from inlet to outlet because of a positive $\Delta e$ at all locations. When parameter values lie above the curve, $\frac{\Delta W}{Q} > 1$ locally and gas begins to cool down. When parameters values lie on the neutral curve, $\frac{\Delta W}{Q} = 1$ meaning that work of thermal expansion done by the gas is balanced by the net heat added to the system, as a result, we have $\Delta e = 0$ locally and gas will neither heat up not cool down, but will maintain its temperature.

The maximum value of $\Lambda$ on the neutral curve is the $\Lambda_{\text{crit}}$. When $\Lambda > \Lambda_{\text{crit}}$, we have local JT cooling of the gas irrespective of $Pe$. Figure 5.5 shows neutral curves with increasing applied EM powers; we see that $\Lambda_{\text{crit}}$ increases with the applied power. This is expected because with the incident power, EM heating source within the ceramic increases, leading to rise of $Q$. More work of thermal expansion is needed to be done by the gas to satisfy $\frac{\Delta W}{Q} > 1$; as a result $\Lambda_{\text{crit}}$ increases with the incident power. From (5.37), the work of thermal expansion done by the gas is dependent both on $\Lambda$ and $Pe$. To understand the behavior of the neutral curves in Figure 5.5, we plot maximum value of $\frac{\Delta W}{Q}$ as functions of $Pe$ and $\Lambda$ in Figure 5.6 for $P = 1000$ W/m$^2$ and $Bi = 6$. From Figure 5.6(b), we notice that $\max\left\{\frac{\Delta W}{Q}\right\}$ monotonically increases with $\Lambda$ when $Pe$ is held fixed; which suggests that the gas does more work of expansion as $\Lambda$ increases. Now in Figure 5.6(a), value of $\max\left\{\frac{\Delta W}{Q}\right\}$ drops in the region $Pe \leq 1.75$, thus the required value of $\Lambda$ to satisfy $\frac{\Delta W}{Q} > 1$ increases with $Pe$ as seen in Figure 5.5 for $P = 1000$ W/m$^2$. In the region $Pe > 1.75$,

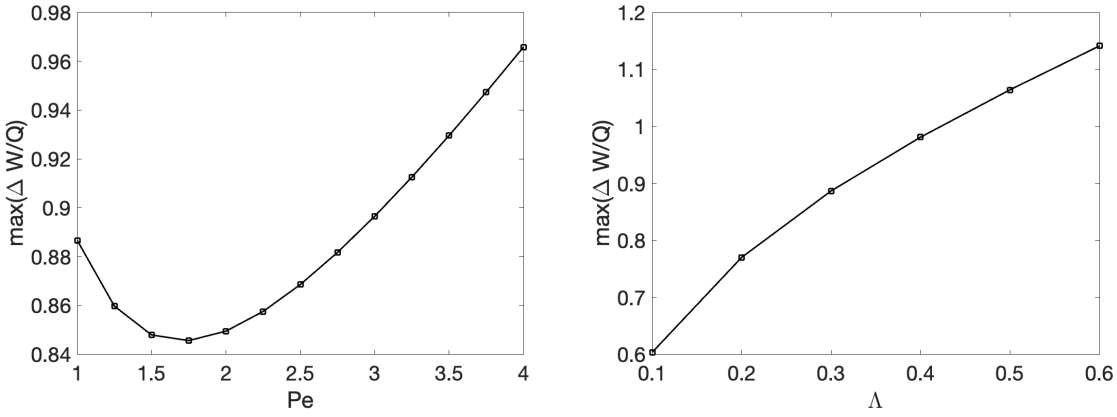


(a) (b)

Figure 5.6: Maximum value of $\frac{\Delta W}{Q}$ in the gas region as a function of $Pe$ when $\Lambda = 0.3$(a), and $\Lambda$ when $Pe = 1$(b). Common parameters in both of these simulation are $P = 1000\ W/m^2$, $Bi = 6$, and $R = 0$.

$\max\left\{\frac{\Delta W}{Q}\right\}$ monotonically increases with $Pe$, and thus required $\Lambda$ to satisfy $\frac{\Delta W}{Q} > 1$ keeps on dropping.

### Thermal Runaway vs. Joule-Thompson Cooling

In this section, we explain the competition between these two volumetric heating/cooling mechanisms. In order to explain the impact of the work of expansion on the onset of thermal runaway in the ceramic, we first rewrite energy equation in the following form

$$\underbrace{\frac{m\gamma\frac{dT}{dx}}{k||E_2||^2\epsilon_2''(T)}}_{\text{Term A}} + \underbrace{\frac{\bar{B}i(T-1)+\bar{R}(T^4-1)}{k||E_2||^2\epsilon_2''(T)}}_{\text{Term B}} + \underbrace{\frac{(\gamma-1)\Lambda\left(\frac{dp}{dx}\right)^2}{k||E_2||^2\epsilon_2''(T)}}_{\text{Term C}} = \underbrace{\bar{P},}_{\text{Power parameter}} \tag{5.39}$$

where Terms A, B and C are fractions of the applied power parameter that are being transferred by convection, environmental heat losses, and work of thermal expansion, respectively, $\bar{B}i = \frac{Bi}{Pe}$, $\bar{R} = \frac{R}{Pe}$, and $\bar{P} = \frac{P}{Pe}$. To derive (5.39), we utilize $q(T) = kP||E_2||^2\epsilon_2''(T)$, divide (5.23a) by $Pe$ so that $m$ becomes dependent only on $\Lambda$, and we can identify the impact of $\Lambda$ on the local thermal energy balances.

We plot $T$ profiles for thermal runaway scenario with increasing $\Lambda$ in Figure 5.7. To produce

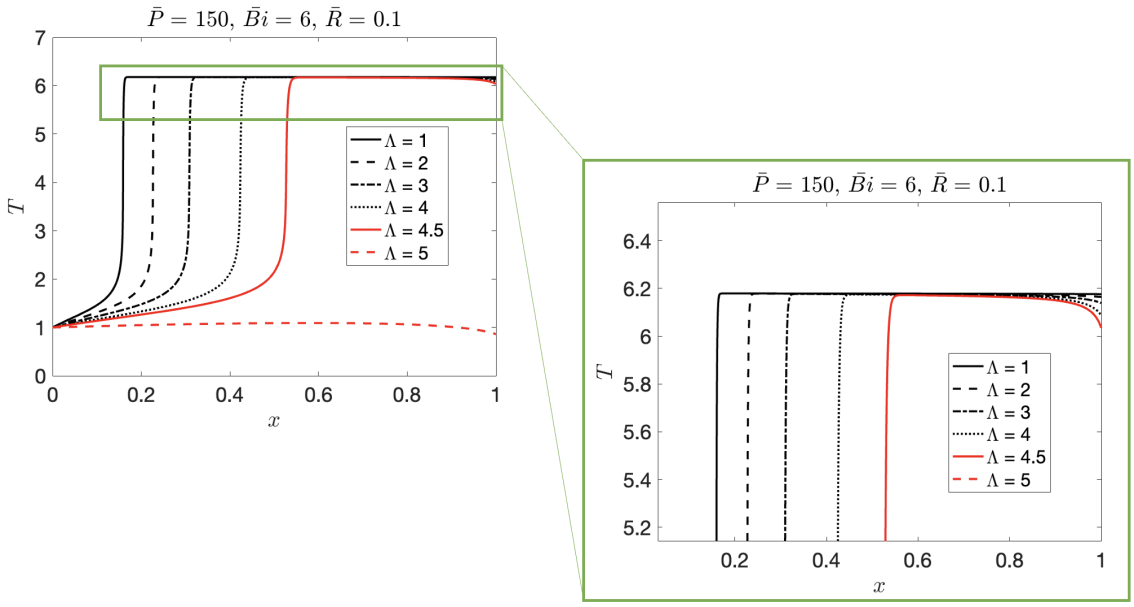


Figure 5.7: Temperature profiles with increasing $\Lambda$ for thermal runaway scenario. To generate these plots we set $\bar{P} = 150$, $\bar{Bi} = 6$, and $\bar{R} = 0.1$ in (5.39) and solve for the $T$ profiles.

these results, we solve (5.39) for $\bar{P} = 150$, $\bar{Bi} = 6$, and $\bar{R} = 0.1$. Here we make two observations:

- Firstly, spatial onset of thermal runaway is delayed as we increase $\Lambda$. This occurs because $m$ increases with $\Lambda$ leading to improvement in the convective heat transfer, i.e., Term A in (5.39) improves. This observation can be made for incompressible fluids as well [8].

- Secondly, $T$ near the outlet starts to drop down, and this suggests that something interesting is occurring at the outlet because of compressible gas dynamics.

In order to understand why we observe drop in $T$ near the outlet, we look at local competition between terms A, B and C when $\Lambda = 0$ and $\Lambda \neq 0$. In Figures 5.8 (a) and (b) we plot $T$ and $\rho$ profiles for thermal runaway scenario when $\Lambda = 0$. Physically, this means that density of the gas is a function of $T$ only, and is independent of $p$. We explain these plots in 3 different stages: Stage I captures the inlet, Stage II consists of onset of thermal runaway in the ceramic, and Stage III includes the outlet. Local competition between convection (Term A), environmental heat losses (Term B) and work of expansion (Term C) in respective stages is plotted in Figure 5.8 (c). Similarly, the normalized electric field amplitude $||E_2||^2$ and the EM heat source $q_{dot} = k||E_2||^2\epsilon''(T)$ in these

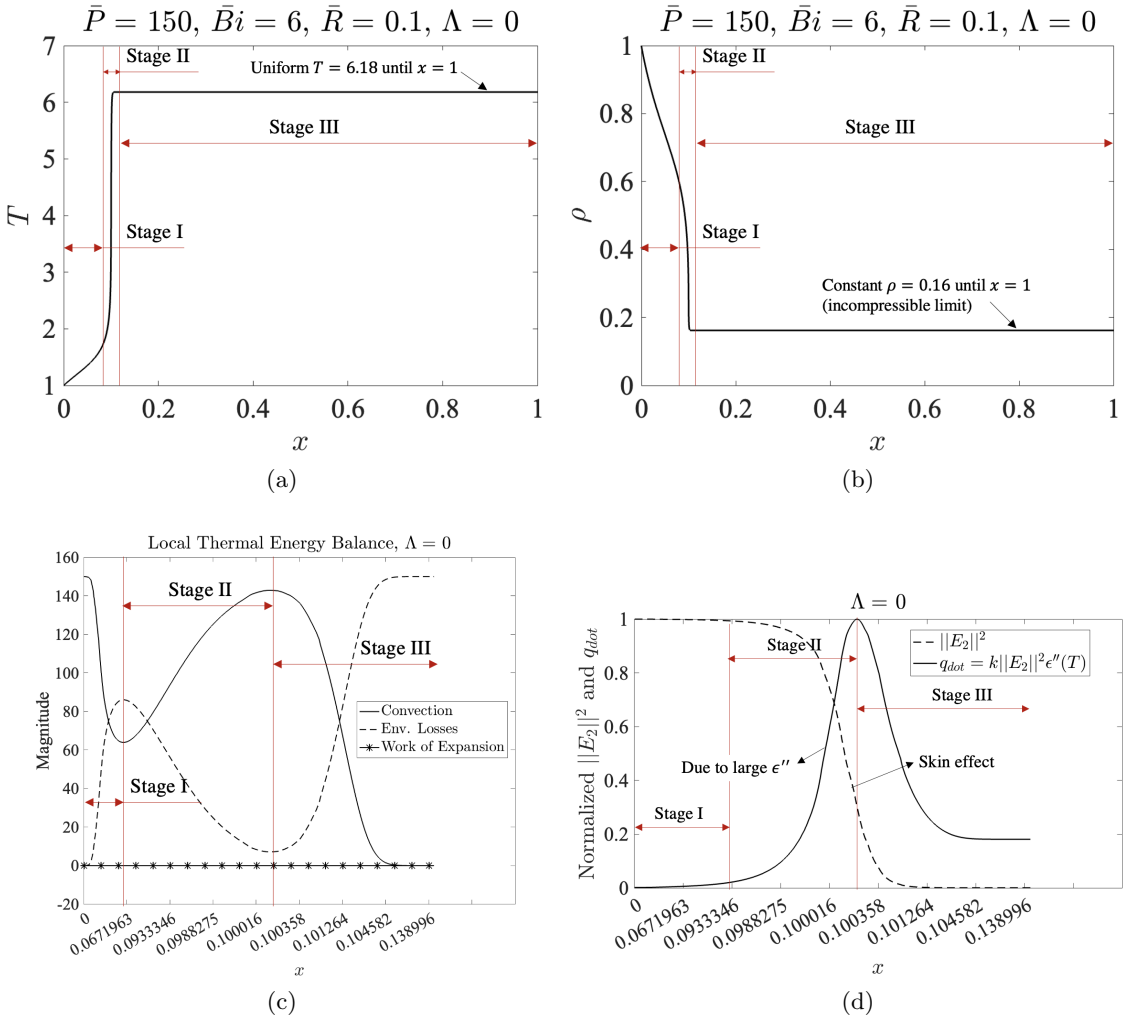


Figure 5.8: Temperature and density profiles are plotted in (a) and (b) for thermal runaway scenario when $\bar{P} = 150$, $\bar{B}i = 6$, $\bar{R} = 0.1$, and $\Lambda = 0$. Local competition between different modes of heat transfer shown in (5.39) is plotted in (c), and normalized $||E_2||^2$ and EM heat source $q_{dot} = k||E_2||^2\epsilon''(T)$ is plotted in (d). We explain these results in three stages: Stage I captures the inlet, Stage II consists of onset of thermal runaway in the ceramic, and Stage III includes the outlet.

stages are plotted in Figure 5.8 (d) (here normalization is done by dividing the maximum values of respective variables).

In Stage I, the temperature of the gas starts to increase as we are adding heat into the ceramic as seen in Figure 5.8 (a). Looking at Stage I in Figure 5.8 (c) we observe increase in environmental heat losses as they are proportion to $T$. In Stage II shown in Figure 5.8 (d) we see a rapid rise of $q_{dot}$, and this occurs because of large $\epsilon''$ eventually leading to onset of thermal runaway in the ceramic region and sharp temperature gradients observed in Stage II in Figure 5.8 (a). Since convective heat losses are proportional to temperature gradients they increase in Stage II seen in Figure 5.8 (c).

Finally, looking Stage III in Figure 5.8 (d), we observe a sharp drop in electric field amplitude $||E_2||^2$, and this phenomenon is known as the *skin effect*, i.e., when $\epsilon''$ is large, most of the EM power is absorbed near the surface of the ceramic and negligible energy penetrates the ceramic. Since there is less EM power available for heating, EM heat source also drops down in Stage III. When environmental losses balance the EM heat source, we observe equilibrium and $T$ becomes uniform near the outlet. Since, $\rho$ is dependent only on $T$, it reaches a constant value and gas behaves like an incompressible fluid near the outlet. This observation is consistent with what we found in earlier that JT cooling of the gas is not possible when $\Lambda = 0$. The key observation here is that in Stage II onset of thermal runaway is a result of competition between convection, environmental heat losses, and EM heat source.

Now we set $\Lambda = 4$, and plot the same results in Figure 5.9 for thermal runaway scenario. First observation we make here is that the work of thermal expansion is small compared to convection and environmental losses in Stage II as seen in Figure 5.9 (c), but in Stage III expansion work starts to increase when total contribution of work done and environmental heat losses (i.e., Term B + Term C) is greater than the applied power parameter $\bar{P}$, Term A becomes negative and temperature starts to drop down near the outlet. From this result, we confirm that work of thermal expansion done by the gas has a little impact on onset of thermal runaway, but it causes temperature to drop down near the outlet.

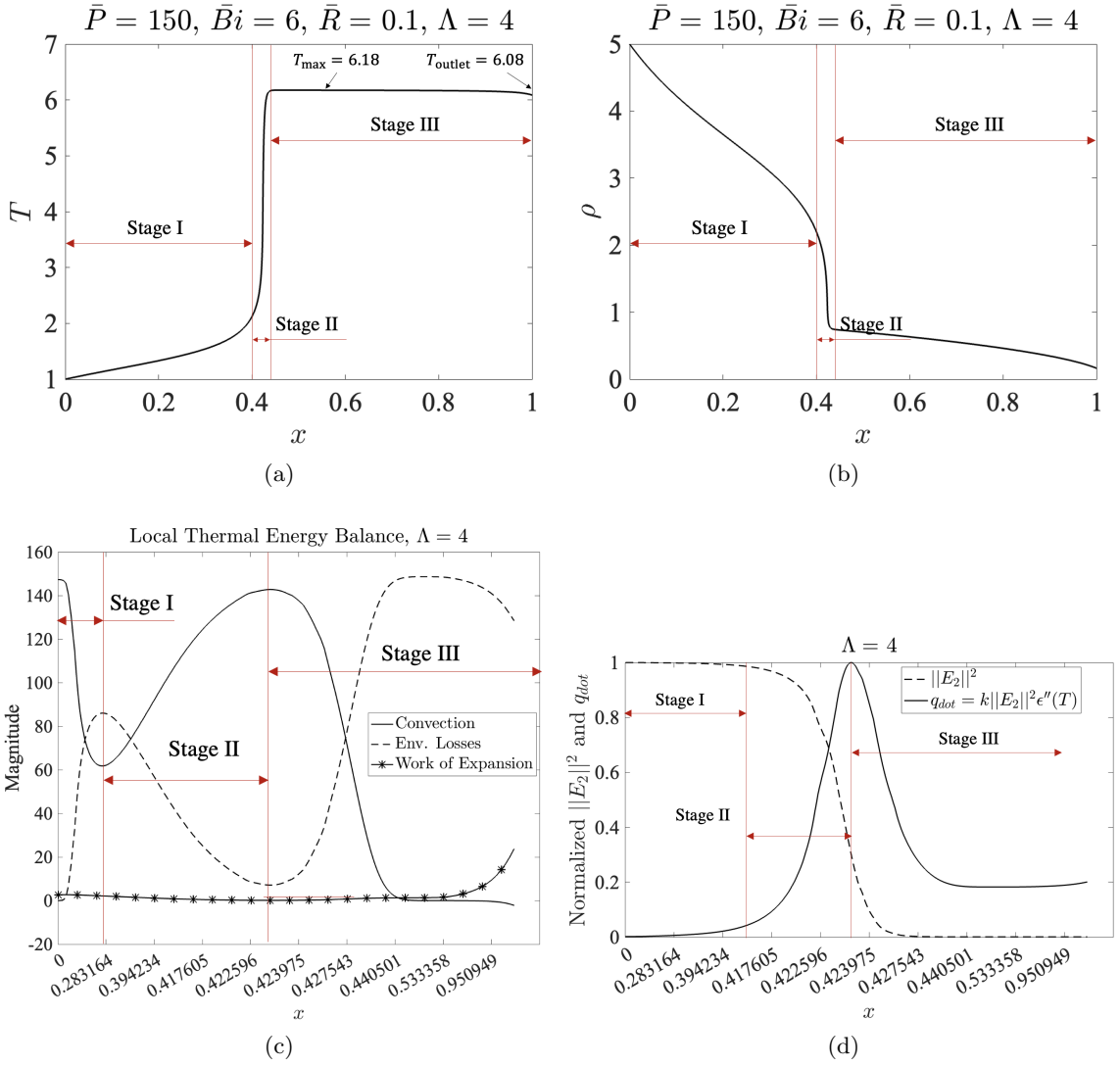


Figure 5.9: Temperature and density profiles are plotted in (a) and (b) for thermal runaway scenario when $\bar{P} = 150$, $\bar{B}i = 6$, $\bar{R} = 0.1$, and $\Lambda = 4$. Local competition between different modes of heat transfer shown in (5.39) is plotted in (c), and normalized $||E_2||^2$ and EM heat source $q_{dot} = k||E_2||^2\epsilon''(T)$ is plotted in (d). We explain these results in three stages: Stage I captures the inlet, Stage II consists of onset of thermal runaway in the ceramic, and Stage III includes the outlet.

## 5.2 High-Speed Gas Flows Through Thin Channels

Until now, we looked at the cases when channel thicknesses are small and are of $o(10^{-6})$ m such that $Re \sim o(1)$. From a practical application point of view, this configuration produces negligible mechanical power from the gas acceleration due to slow flow speeds. In this section, we consider another limiting case of when $Re \gg 1$ (i.e, flow inertia dominates and viscous stresses are negligible). Although $\Lambda = 0$ here, the compressible gas dynamics is governed by the dynamic Mach number $\bar{M}^2$, which is of $o(1)$ in our model. In the considered structure of this EM HX (Figure 5.1), we assume that the gas enters the channel with known temperature, pressure, density, and flow velocity such that gas is at a subsonic state at the inlet. Because of heat addition into the gas due to EM heating of the ceramic, gas undergoes thermal expansion, and accelerates as it moves from the inlet to the outlet. Beamed energy propulsion technologies operate on this working principle; when sufficiently high ceramic temperatures are achieved, a pressurized gas is expanded over the heated region. Net gain in the kinetic energy of the gas then indicates how much thrust can be achieved. Another way of harnessing power from such an EM HX is to utilize hot and accelerated gas the outlet to drive a turbine. The kinetic energy of the gas can be converted into rotation of a turbine producing electricity. The purpose of this model is to quantify the mechanical power output from such an EM HX. Research question of interest is

- *How much mechanical power can be generated from EM heating of the ceramic and thermal runaway?*

Because of the choice of high-speed flows through channels, we assume that fluid momentum conservation is given by Euler's equations [13] as

$$\nabla \cdot (\rho_1' \mathbf{u}') = 0,$$
$$\rho_1' (\mathbf{u}' \cdot \nabla)\mathbf{u}' + \nabla p' = 0,$$

along with thermal energy conservation given by (5.4). Dimensionless variables are the same as

defined in (5.6) except we now introduce velocity and gauge pressure scales as below

$$u = \frac{u'}{U_{in}},\ p = \frac{p'}{\rho_0 U_{in}^2},$$

where $U_{in}$ is the flow velocity at the inlet in m/s, and $\rho_0$ is the density of the gas at the ambient conditions (here $p'$ is the fluid gauge pressure). With these dimensionless variables, the system of governing equations becomes

$$\frac{\partial}{\partial x}(\rho_1 u) + \frac{\partial}{\partial z}(\rho_1 w) = 0, \tag{5.41a}$$

$$\rho_1 \left[ u\frac{\partial u}{\partial x} + w\frac{\partial u}{\partial z} \right] = -\frac{\partial p}{\partial x}, \tag{5.41b}$$

$$\eta^2 \rho_1 \left[ u\frac{\partial w}{\partial x} + w\frac{\partial w}{\partial z} \right] = -\frac{\partial p}{\partial z}, \tag{5.41c}$$

$$\eta Pe \rho_1 \left[ u\frac{\partial T_1}{\partial x} + w\frac{\partial T_1}{\partial z} \right] + \eta(\gamma - 1)Pe(1 + M^2 p) \left[ \frac{\partial u}{\partial x} + \frac{\partial w}{\partial z} \right] = \eta^2 \frac{\partial^2 T_1}{\partial x^2} + \frac{\partial^2 T_1}{\partial z^2}, \tag{5.41d}$$

$$0 = \eta^2 \frac{\partial^2 T_2}{\partial x^2} + \frac{\partial^2 T_2}{\partial z^2} + \frac{\eta}{l} P |E_2|^2 \epsilon_2''(T_2), \tag{5.41e}$$

$$\rho_1 = \frac{1}{T_1}\left(1 + M^2 p\right), \tag{5.41f}$$

where $Pe = \frac{l_1 U_{in}}{\alpha_1}$, and $M^2 = \frac{U_{in}^2}{RT_A}$ with the rest of the dimensionless groups as defined earlier in this chapter. Electric field strength is governed by (5.7) and boundary conditions are the same as that of (5.9a) and (5.13).

As the first step towards modeling the full problem, we apply the thin-domain asymptotic method to the system of equations (5.41). We show that the fluid flow in the channel is described by the law of *Rayleigh flow* (i.e., a frictionless flow through a duct with uniform cross sectional area with heat addition) at the leading-order. Traditionally, Rayleigh flow model is used to determine first-order estimates of key design-parameters of external combustion engines used in aerospace applications [56, 57]. Assumptions in the Rayleigh flow limit are as follows

- Flow is frictionless, i.e., property changes due to viscous stresses at the channel walls are ignored. It is possible to include the impact of friction at the walls along with heat addition

into the flows through friction factor correlations (also known as Fanno-Rayleigh type flows [56, 57]), but this is left for future work.

- Flow velocity is uniform along the $z$-direction and only varies in the $x$-direction (i.e., $\frac{\partial u}{\partial z} = 0$). This assumption is valid when inlet flow velocity is uniform along the $z$-direction, viscous stresses at the walls are absent, and the channel cross-section does not vary along the direction of the flow.

- Entropy of the flow increases due to the addition of heat. In our problem, heat is added to the gas due to conduction heat transfer at the interface between the fluid channel and the ceramic.

With these assumptions, we carry out the thin domain asymptotic analysis of the system (5.41) as done previously in this chapter. Cross-sectional averaged conservation laws at the leading-order are

$$\rho_1 u = m, \text{ and } m \text{ is a positive constant,} \tag{5.42}$$

$$m\frac{du}{dx} = -\frac{dp}{dx}, \tag{5.43}$$

$$m\frac{dT}{dx} + (\gamma - 1)(1 + M^2 p)\frac{du}{dx} = Q(T), \tag{5.44}$$

$$\rho_1 = \frac{1}{T}\left(1 + M^2 p\right), \tag{5.45}$$

where $Q(T) = k\bar{P}||E_2||^2\epsilon''(T) - \bar{B}i(T-1) - \bar{R}(T^4 - 1)$, $\bar{P} = \frac{P}{Pe}$, $\bar{B}i = \frac{Bi}{Pe}$, and $\bar{R} = \frac{R}{Pe}$. The heat source term is required to be proportional to $Pe$ so that heat transferred by convection and work of expansion are of the same orders of magnitude of the heat added to the system (since $Pe$ has a large value, the coupling between convection, expansion work, and EM heating is apparent only when the heat source is of the same orders of magnitude of other heat transfer modes), i.e., incident powers required to achieve thermal runaway in the ceramic scale with $Pe$.

From (5.42) and (5.45) we can write

$$u = \frac{mT}{1 + M^2 p}. \tag{5.46}$$

Now taking derivative of (5.46), and utilizing the momentum equation (5.43) we get

$$\frac{du}{dx} = \left(\frac{u^2}{T}\right) M^2 \frac{du}{dx} + \left(\frac{u}{T}\right) \frac{dT}{dx},$$

which can be further simplified as

$$\left(1 - \frac{M^2 u^2}{T}\right) \frac{du}{dx} = \left(\frac{u}{T}\right) \frac{dT}{dx}.$$

Let us now define the dynamic Mach number as $\bar{M}^2 = \frac{u'^2}{\gamma R T'} = \frac{M^2 u^2}{\gamma T}$, and we can write $\gamma \bar{M}^2 = \frac{M^2 u^2}{T}$. Substituting this relation in the above equation we get

$$(1 - \gamma \bar{M}^2) \frac{du}{dx} = \frac{u}{T} \frac{dT}{dx}. \tag{5.47}$$

Substituting (5.46) and (5.47) into thermal energy conservation (5.44) we get

$$m \frac{dT}{dx} \left[1 + \left(\frac{\gamma - 1}{1 - \gamma \bar{M}^2}\right)\right] = Q(T).$$

After rearrangement of the terms, we get

$$\frac{dT}{dx} = \frac{Q(T)}{m} \left[\frac{1 - \gamma \bar{M}^2}{\gamma(1 - \bar{M}^2)}\right]. \tag{5.48}$$

Substituting (5.48) into (5.47) we get

$$\frac{du}{dx} = \left[\frac{uQ(T)}{mT}\right] \left[\frac{1}{(1 - \gamma \bar{M}^2)}\right] \left[\frac{1 - \gamma \bar{M}^2}{\gamma(1 - \bar{M}^2)}\right]. \tag{5.49}$$

We can solve the system of nonlinear first-order ODEs (5.48) and (5.49) for given inlet conditions on temperature and flow velocities.

From (5.48) and (5.49) we can write following differential identities

$$\frac{dT}{T} = \frac{Q(T)}{mT} \left[\frac{1 - \gamma \bar{M}^2}{\gamma(1 - \bar{M}^2)}\right] dx, \tag{5.50a}$$

$$\frac{du}{u} = \left[\frac{Q(T)}{mT}\right]\left[\frac{1}{\left(1-\gamma\bar{M}^2\right)}\right]\left[\frac{1-\gamma\bar{M}^2}{\gamma(1-\bar{M}^2)}\right]dx = \left[\frac{1}{\left(1-\gamma\bar{M}^2\right)}\right]\frac{dT}{T}. \tag{5.50b}$$

Using the expression of dynamic Mach number as $\bar{M}^2 = \frac{M^2u^2}{\gamma T}$, we can write

$$\frac{d(\bar{M}^2)}{\bar{M}^2} = 2\frac{du}{u} - \frac{dT}{T}. \tag{5.51}$$

Substituting (5.50) into (5.51), we get

$$\frac{d(\bar{M}^2)}{\bar{M}^2} = \left[\frac{1+\gamma\bar{M}^2}{1-\gamma\bar{M}^2}\right]\frac{dT}{T} \tag{5.52}$$

Equation (5.52) exactly describes the classical Rayleigh flow. To simplify even further, we can separate the variables and integrate both sides of (5.52) from inlet to outlet conditions. Upon integration, we get

$$\frac{T}{T_0} = \left(\frac{\bar{M}^2}{\bar{M}_0^2}\right)\left(\frac{1+\gamma\bar{M}^2}{1+\gamma\bar{M}_0^2}\right)^{-2}, \tag{5.53}$$

where $T_0$ is the inlet temperature, and $\bar{M}_0^2$ is the dynamic Mach number at the inlet which is given as $\bar{M}_0^2 = \frac{M^2}{\gamma T_0}$ (as $u = 1$ at the inlet). To solve the system of differential algebraic equations (5.48) and (5.53), we utilize MATLAB's ODE solver (MATLAB function `ode15s`) for given inlet conditions of $T_0$ and $\bar{M}_0^2$.

Before we discuss results from this model, let us first look at the algebraic constrain (5.53) separately to get some insights into numerical solution of the full problem. As the (5.53) is quadratic in nature, for a given $\frac{T}{T_0}$, there are two possible solutions for the Mach number. These two roots are given by

$$\bar{M}_1^2 = \frac{-b-\sqrt{b^2-4ac}}{2a}, \bar{M}_2^2 = \frac{-b+\sqrt{b^2-4ac}}{2a}, \tag{5.54}$$

where $a = \gamma^2$, $b = 2\gamma - \frac{T_0}{\bar{M}_0^2 T}(1+\gamma\bar{M}_0^2)^2$, and $c = 1$.

Roots of the algebraic constraint (5.53) are plotted in Figure 5.10 assuming that inlet Mach number is such that flow is subsonic with $\bar{M}_0 = 0.0298$ (which corresponds to inlet velocity and temperature of 60 m/s and 300 K). For this inlet condition following observations can be made from (5.54) and (5.48):

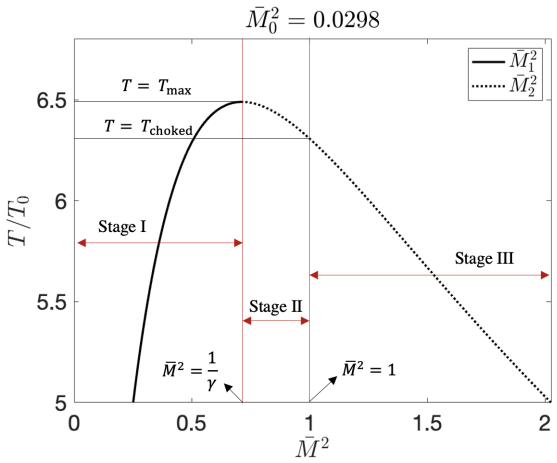


Figure 5.10: Two roots of the algebraic constraint given by (5.54) as a function of $\frac{T}{T_0}$ for $\bar{M_0}^2 = 0.0298$, i.e., inlet velocity and temperatures are $u_{\text{in}} = 60$ m/s and 300 K, respectively.

- If the heat addition into the system is due to EM heating of the ceramic, i.e., when $Q(T) > 0$, the right hand side of (5.48) is positive for $\bar{M}_0^2 < \frac{1}{\gamma}$. The outlet temperature monotonically increases with the applied EM power, $\bar{P}$. Since we operate in Stage I shown in Figure 5.10, we can see that the outlet $\bar{M}^2$ also increases with $T$ (and also with $\bar{P}$).

- Maximum temperature that can be achieved in the system is $T = T_{\max}$ which occurs when $\bar{M}^2 = \frac{1}{\gamma}$ as seen in Figure 5.10. From (5.53) we can find out expression for $T_{\max}$ as

$$T_{\max} = \frac{T_0(1 + \gamma\bar{M}_0^2)^2}{4\gamma\bar{M}_0^2}. \tag{5.55}$$

  Note that the maximum temperature that can be achieved in the system is not dependent on the applied power, but is a function of $\bar{M}_0^2$.

- With some algebraic manipulations on (5.48) and (5.52) it is possible to show that

$$m\frac{d(\bar{M}^2)}{dx} = \bar{M}^2\left[\frac{1 + \gamma\bar{M}^2}{\gamma(1 - \bar{M}^2)}\right]\frac{Q(T)}{T}. \tag{5.56}$$

  The right hand side of this equation is always positive when $\bar{M}^2 < 1$. We can then conclude that if the flow is subsonic at the inlet, the heat addition results in increase of the Mach number at the outlet until $\bar{M}^2 = 1$ (i.e., $\bar{M}^2$ at the outlet monotonically increases with $\bar{P}$

until we reach $\bar{M}^2 = 1$). When $\bar{M}^2 > 1$ at the inlet (i.e., the flow is supersonic), heat addition results into drop in the Mach number. Moreover, shock waves are expected to occur when heat is added into a supersonic flow [57]. For this reason, subsonic flows are heated to achieve desired gas velocity in typical aerospace applications. Therefore, in this chapter, we only consider cases when the flow is subsonic at the inlet.

- When $\bar{P}$ is such that $Q(T) > 0$ and $\frac{1}{\gamma} < \bar{M}^2 < 1$ within a computational domain defined as $x_{\text{crit}} < x < 1$, the right hand side of (5.48) is negative for $x > x_{\text{crit}}$. This means that the gas experiences cooling effect in the region $x > x_{\text{crit}}$ when heat is added into the system. The relation between $\bar{M}^2$ and $T$ for this scenario is described by Stage II in Figure 5.10.

- When $P$ is increased even further, and $Q(T)$ is such that $\bar{M}^2 = 1$ within the computational domain, the RHS of (5.48) becomes $-\infty$, and a further increase in $\bar{M}^2$ is not possible. This phenomenon is known as *thermal choking* in the classical Rayleigh flows [56, 57]. Theoretically, it means that when the flow is initially subsonic, no matter how much heat we add into the system, it is not possible to reach a supersonic state (i.e., $\bar{M}^2 > 1$) at the outlet. Experimentally, if we keep adding heat into the system even further, outlet $\bar{M}^2$ remains the same (sonic state), but the inlet properties, such as gas temperature or pressure, change to accommodate further heat addition [56,57]. The model presented here does not consider the impact of heat addition into a thermally choked flow (this is the limit on the Rayleigh flow approximation). In the Results section below, we consider cases when thermal choking is absent. We discuss this phenomenon in more details in the upcoming subsections.

### 5.2.1 Results

We now numerically solve the model given by (5.48) and (5.53) using `ode15s` function in MATLAB for inlet conditions of $\bar{M}_0^2 = 0.0298$ and $T_0 = 1$ (i.e., gas enters at 60 m/s and 300 K in the channel). The model is solved numerically for increasing values of $\bar{P}$, keeping rest of the parameters constant with $\bar{B}i = 0.4$ and $\bar{R} = 0.1$. Results from this model are organized as follows:

- We first explain the thermal energy balance taking place in the EM HX when we operate in

Stage I shown in Figure 5.10, i.e., at the outlet we have $\bar{M}^2 \leq \frac{1}{\gamma}$ and $T \leq T_{\max}$. In this Stage I, it is expected that both $T$ and $\bar{M}^2$ at the outlet increase monotonically with $\bar{P}$.

- We then consider the operation of the EM HX in Stage II shown in Figure 5.10, i.e., at the outlet we have $\frac{1}{\gamma} < \bar{M}^2_{\text{outlet}} < 1$ and $T_{\text{outlet}}$ drops with increase in $\bar{P}$ (also $T_{\text{outlet}} < T_{\max}$). By carrying out a linear stability analysis, we show that the Stage II is unstable such that infinitesimal fluctuations in the applied EM power lead to rapid rise of $\bar{M}^2$ resulting in a thermally choked flow.

- Finally, we explain thermal choking phenomenon and discuss possible approaches to avoid choking experimentally.

**Operation in Stage I**

Results from the solution of (5.48) and (5.52) for $\bar{P} = 10$ and $\bar{P} = 50$ are plotted in Figure 5.11. When $\bar{P} = 10$, we operate on the lower branch of the response curve (as seen from the temperature values), and the kinetic energy (KE) of the gas per unit volume at the outlet, i.e., KE $= \frac{1}{2}\rho u^2$, turns out to be 1.5 times the KE at the inlet. However, when $\bar{P} = 50$, we observe onset of thermal runaway in the ceramic region as seen from the jump in temperature values. As a result, we observe a jump in KE about 9 times the initial value.

For this scenario, the competition between thermal runaway and the skin effect can be seen from Figure 5.12. When the EM heat source is large, onset of thermal runaway takes place, but as a result of increased $\epsilon_2''$, we observe skin effect, i.e., most of the incident EM energy is absorbed at the interface between the fluid channel and the ceramic. Since there is less EM power available for heating, $q_{\text{dot}}$ drops down and is balanced by net heat losses to the environment, i.e., $Q(T) = 0$. Since heat is not being added into the ceramic, both $T$ and $u$ become uniform in space until the outlet at $x = 1$. The power response equation that gives us $Q(T) = 0$ can be written as

$$\bar{P} = \frac{\bar{B}i(T-1) + \bar{R}(T^4 - 1)}{k||E_2||^2(T)\epsilon''(T)}. \tag{5.57}$$

In Figure 5.13, we plot outlet temperature as a function of $\bar{P}$ given by numerical model of (5.48)

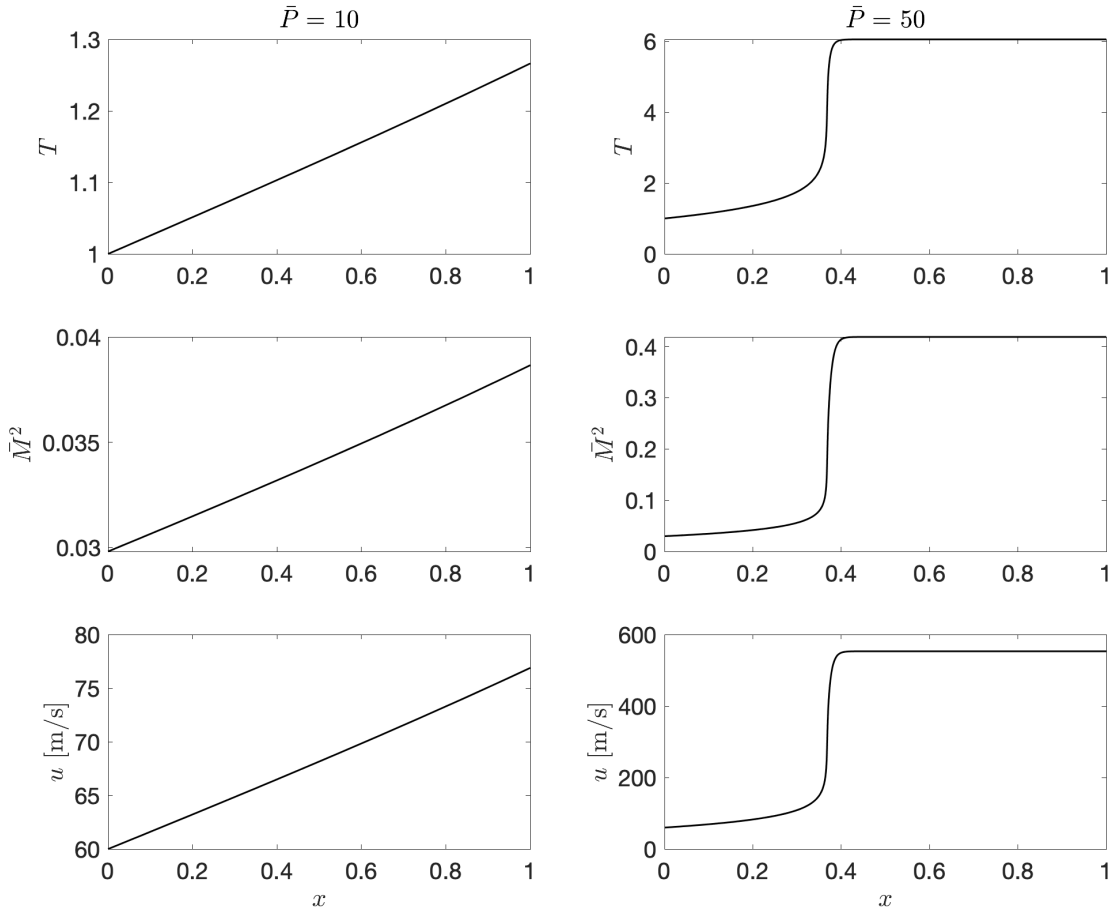


Figure 5.11: Results from the solution of (5.48) and (5.52) when $\bar{P} = 10$ (a) and $\bar{P} = 50$ (b). Common parameters in these models are $\bar{B}i = 0.4$, $\bar{R} = 0.1$, and inlet velocity and temperature are $u_{\text{in}} = 60$ m/s and $T_{\text{in}} = 1$, respectively. Increase in $\bar{P}$ is due to increase in the applied EM power.

and (5.53), and analytical solution of (5.57). As expected, both the models agree with each other when operated on the upper branch as the skin effect causes $Q(T) = 0$. When thermal runway initiates within in the ceramic, the phenomena of skin effect promotes the balance between EM heat source and environmental heat losses. This stabilized the temperature growth and the energy balance is then given by (5.57) (i.e., $Q(T) = 0$). But, when we operate on the lower branch, the temperature is not uniform at the outlet as seen from Figure 5.11 (a). This explains why both the response curves do not agree on the lower branch.

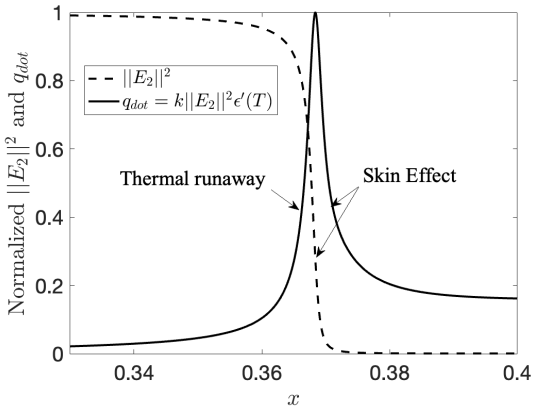


Figure 5.12: Normalized electric field strength, $||E_2||^2$, and $q_{\text{dot}} = k||E_2||^2\epsilon''(T)$ as a function of $x$ in the region where thermal runway takes place when $\bar{P} = 50$. Values are normalized by dividing the respective local maximum. Temperature profile for this scenario is shown in Figure 5.11 (b).

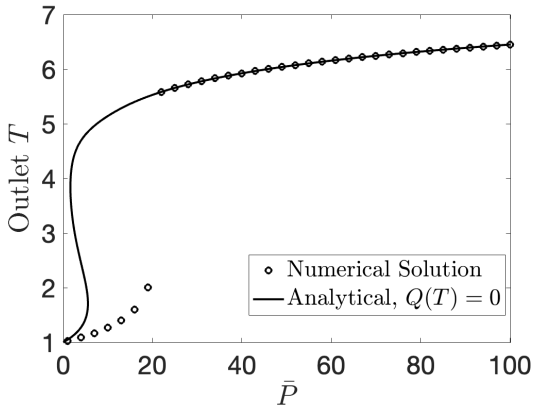


Figure 5.13: Comparison of power response curves given by the numerical solution of (5.48) and (5.53) and analytical solution of (5.57). The model of (5.57) assumes that temperature is uniform in space.

From this comparison shown in Figure 5.13, we show that the outlet conditions ($T_{\text{outlet}}$ and $\bar{M}^2_{\text{outlet}}$) in Stage I can be determined by simultaneously solving two nonlinear equations (5.57) and (5.47). This simplification is valid only when thermal runaway takes place in the ceramic, and the EM HX is operated on the upper branch of the response curve. Until otherwise noted, we will use this simplification to determine the outlet conditions of the EM HX when operated in Stage I.

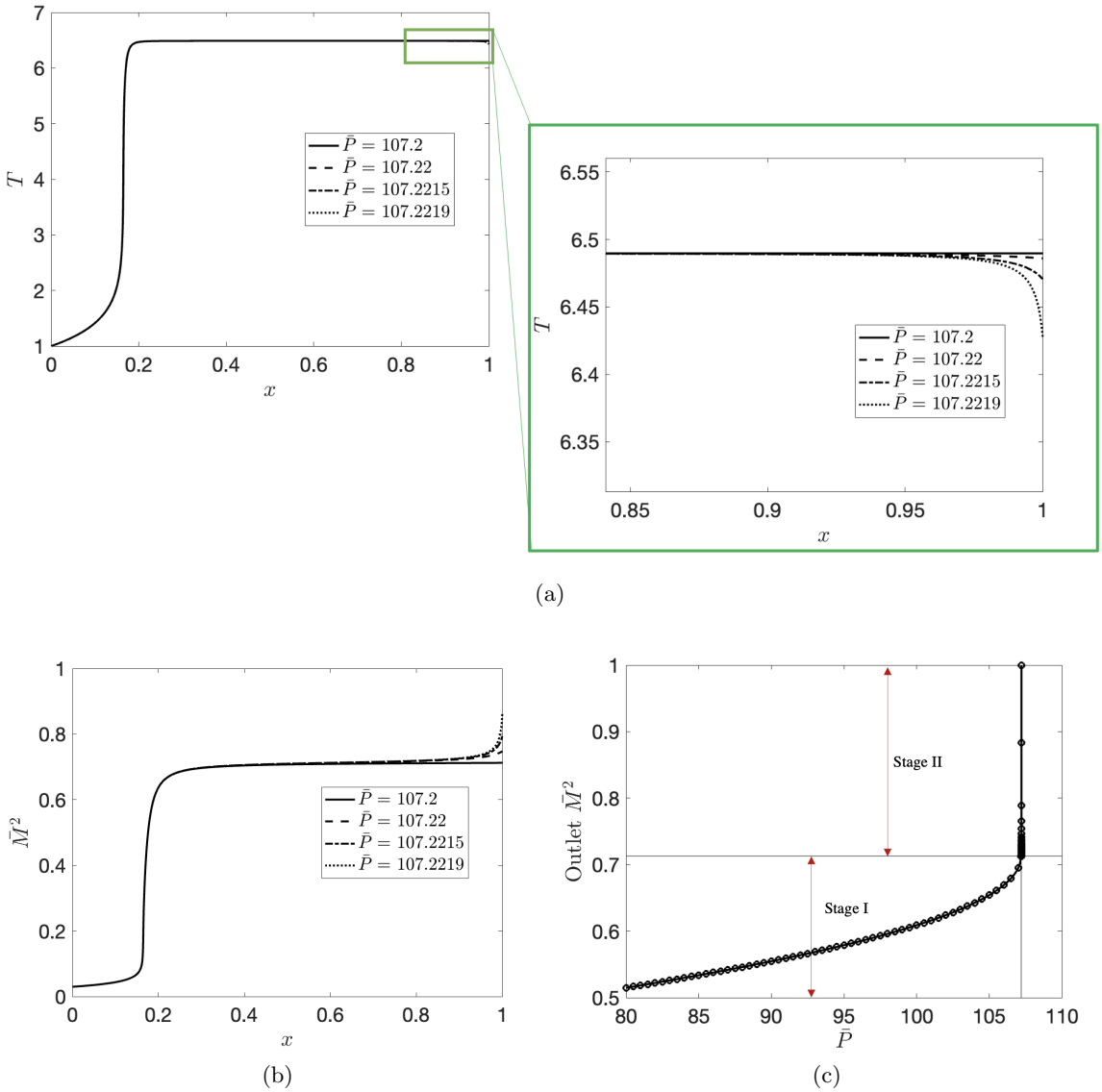


Figure 5.14: Temperature profiles (a) and $\bar{M}^2$ (b) as a function $x$ with increasing applied EM power, $\bar{P}$ when operated in Stage II shown in Figure 5.10. $\bar{M}^2_{\text{outlet}}$ as a function of $\bar{P}$ (c) when operated in Stages I and II. Parameters that are kept constant in these simulations are $\bar{M}^2_0 = 0.0298$, $T_0 = 1$, $\bar{B}i = 0.4$, and $\bar{R} = 0.1$.

### Operation in Stage II and Thermal Choking

We now set $\bar{P}$ such that we have $\bar{M}^2_{\text{outlet}} > \frac{1}{\gamma}$ at the outlet (i.e., the EM HX operates in the Stage II shown in Figure 5.10) when $\bar{M}^2_0 = 0.0298$ (i.e., inlet velocity of 60 m/s), $T_0 = 1$, $\bar{B}i = 0.4$ and $\bar{R} = 0.1$. Results from the numerical model when the EM HX operates in the Stage II are shown in Figure 5.14. As seen in Figures 5.14 (a) and (b), gas experiences cooling effect when $\bar{M}^2 > \frac{1}{\gamma}$

(as the RHS of (5.48) becomes negative for $\bar{M}^2 > \frac{1}{\gamma}$ ) and $\bar{M}^2$ monotonically increases with $\bar{P}$ (as the RHS of (5.56) is always positive for $\bar{M}^2 < 1$). In Figure 5.14 (c), we plot $\bar{M}^2_{\text{outlet}}$ as a function of $\bar{P}$ when the EM HX operates in Stages I and II. We see that the increase in $\bar{M}^2$ with $\bar{P}$ is very drastic in Stage II in comparison with Stage I (i.e., $\bar{M}^2$ is very sensitive to the applied power in Stage II). To understand why this occurs, we carry out a linear stability analysis on uniform and constant solutions at steady-state (i.e., outlet conditions when thermal runway occurs). We assume that $T_{\text{ss}}$ and $\bar{M}^2_{\text{ss}}$ are the uniform base-state solutions that satisfy the algebraic constraint (5.53). Now introducing infinitesimal perturbations in the base-state solution as

$$T = T_{\text{ss}} + \tilde{T},$$
$$\bar{M}^2 = \bar{M}^2_{\text{ss}} + \tilde{\bar{M}}^2,$$

and linearizing (5.48) and (5.53) about the uniform base-state solution, we get

$$m\gamma(1-\bar{M}^2_{\text{ss}})\frac{d\tilde{T}}{dx} = \left[m\gamma\frac{dT_{\text{ss}}}{dx} - Q(T_{\text{ss}})\gamma\right]\tilde{\bar{M}}^2 + \left[(1-\gamma\bar{M}^2_{\text{ss}})\left(\frac{dQ}{dT}\right)_{T_{\text{ss}}}\right]\tilde{T}, \tag{5.58a}$$

$$\tilde{T} = \left[\left(\frac{1+\gamma\bar{M}^2_0}{1+\gamma\bar{M}^2_{\text{ss}}}\right)^2 - \frac{2\gamma T_{\text{ss}}}{1+\gamma\bar{M}^2_{\text{ss}}}\right]\tilde{\bar{M}}^2. \tag{5.58b}$$

We can further simplify the linearized system of equations (5.58) by utilizing that we have $\frac{dT_{\text{ss}}}{dx} = 0$ and $Q(T_{\text{ss}}) = 0$ (this is true when thermal runaway occurs in the ceramic). Finally we assume that $\tilde{T} = Ae^{sx}$, where $A$ and $s$ are amplitude and growth rate of infinitesimal perturbations. Substituting $\tilde{T} = Ae^{sx}$ in (5.58), and solving for $s$, we get

$$s = \frac{(1-\gamma\bar{M}^2_{\text{ss}})\left(\frac{dQ}{dT}\right)_{T_{\text{ss}}}}{m\gamma(1-\bar{M}^2)},$$

where $\left(\frac{dQ}{dT}\right) = k\bar{P}\left[\frac{d(||E_2||^2)}{dT}\epsilon''(T) + ||E_2||^2\frac{d\epsilon''}{dT}\right] - \bar{B}i - 4\bar{R}T^3$. As the uniform base-state solution is assumed to be on the upper branch, we can look at Figure 5.12 and conclude that $\frac{d(||E_2||^2)}{dT} < 0$ and $||E_2||^2 \to 0$ and $\left(\frac{dQ}{dT}\right)_{T_{\text{ss}}} < 0$ on the upper branch near the outlet (this observation is consistent with [26, 28, 29]). We can then conclude that when $\bar{M}^2_{\text{ss}} < \frac{1}{\gamma}$, $s$ is negative, which means that

the outlet solution is linearly stable against infinitesimal perturbations. However, when $\bar{M}^2_{\text{ss}} > \frac{1}{\gamma}$, $s$ becomes positive. This means that infinitesimal disturbances introduced in the temperature solution at the outlet are growing exponentially in space. As a result of this instability, $\bar{M}^2$ increases rapidly until it reaches 1 (i.e., sonic state), and we achieve thermal choking within the channel.

The Rayleigh flow becomes thermally choked when $\bar{M}^2 = 1$. The linear stability analysis shows that the Stage II is very sensitive to disturbances in the applied power (i.e., disturbances in $T$ and $\bar{M}^2$). For instance, if we let $\bar{P}_{\text{choked}} = \bar{P}_{\text{crit}} + \Delta\bar{P}$, where $\bar{P}_{\text{crit}}$ and $\bar{P}_{\text{choked}}$ are the applied powers, when $\bar{M}^2_{\text{outlet}} = \frac{1}{\gamma}$ and $\bar{M}^2_{\text{outlet}} = 1$, respectively. From Figure 5.14 (c) we get $\Delta\bar{P} = 0.02$ for $\bar{M}^2_0 = 0.0298$, $T_0 = 1$, $\bar{B}i = 0.4$ and $\bar{R} = 0.1$. When this instability is promoted, small changes in the applied power lead to rapid growth of $T$ and $\bar{M}^2$ leading to a thermally choked flow. Although operating an EM HX in Stage II suggests generation of maximum possible KE of the gas, these states may not be possible without the thermally choked channel flow.

In many aerospace application, such as aircraft engines or external combustion engines, heat is added into a subsonic flow of a gas to achieve the desired gas velocity. We show that the gain in the gas flow velocity is proportional to how much heat is being added into the gas by the engine. But, theoretically, when the flow reaches the sonic state, further heat addition is not possible without altering the inlet condition due to thermal choking. Experimentally, alternations in the inlet condition due to thermal choking lead to drop in mechanical power output of the engine [56]. If the heat is added into the flow which is supersonic at the inlet, shock waves can occur as a result of thermal choking, and again performance of the engine drops down [57]. Therefore, in typical aircraft engines, heat is added into a subsonic flow to achieve $\bar{M}^2 < 1$ and different types nozzle assemblies are used to reach supersonic states at the outlet. In this chapter, however, we focus only on gas acceleration due to heat addition and leave the consideration of nozzle systems for future developments.

The EM HX discussed here is also limited by thermal choking. When $\bar{M}^2 = 1$, right hand side of (5.48) becomes $-\infty$ indicating thermal choking, i.e., conservation laws can no longer be described by Rayleigh flow approximation. This motivates another research question:

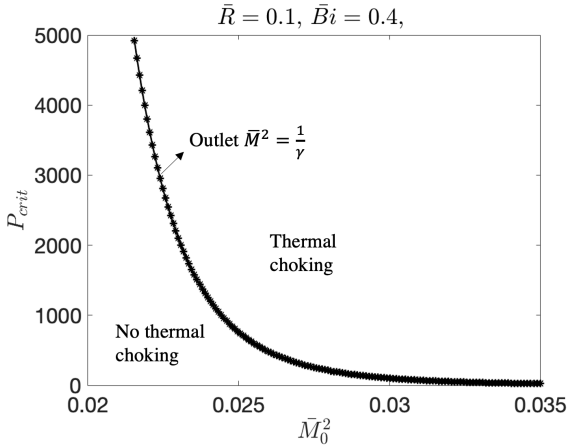


Figure 5.15: Critical power, $\bar{P}_{\text{crit}}$, as a function of inlet mach number $\bar{M}_0^2$. When $\bar{P} = \bar{P}_{\text{crit}}$, $\bar{M}^2_{\text{outlet}} = \frac{1}{\gamma}$ and $T_{\text{outlet}} = T_{\max}$ as given by (5.55).

- *What is the critical powers, $P_{crit}$, at which thermal choking occurs? The answer to this question then gives us the region of validity of the model described in this section.*

In the previous subsection, we identified that the Stage II (which is defined when $\frac{1}{\gamma} < \bar{M}^2 < 1$) is unstable such that infinitesimal fluctuations in $T$ or $\bar{M}^2$ make the flow to become thermally choked. But, when the EM HX is operated in the Stage I, we achieve a stable operation. The maximum possible $\bar{M}^2$ and $T$ in the Stage I are $\bar{M}^2_{\max} = \frac{1}{\gamma}$ and $T_{\max}$ given by (5.55), respectively. If we let $P_{\text{crit}}$ to be the applied EM power when at the outlet we have $\bar{M}^2_{\text{outlet}} = \frac{1}{\gamma}$ and $T_{\text{outlet}} = T_{\max}$, then thermal choking is absent when $\bar{P} < \bar{P}_{\text{crit}}$. Since this state lies in Stage I, we can utilize the simplification we discussed earlier that the balance between thermal runaway and skin effect causes $Q(T) = 0$ and outlet conditions can be determined by simultaneously solving two nonlinear equations (5.57) and (5.53). Since our goal is to determine $\bar{P}_{\text{crit}}$ such that $T_{\text{out}} = T_{\max}$ and $\bar{M}^2_{\text{outlet}} = \frac{1}{\gamma}$, we can solve (5.57) for a given $T_{\max}$ as

$$\bar{P}_{\text{crit}} = \frac{\bar{B}i(T_{\max} - 1) + \bar{R}(T^4_{\max} - 1)}{k||E_2||^2(T_{\max})\epsilon''(T_{\max})}. \tag{5.59}$$

Looking at (5.55), $T_{\max}$ increases nonlinearly as $\bar{M}_0^2$ decreases. This suggests that $\bar{P}_{\text{crit}}$ also increases as $\bar{M}_0^2$ decreases. We now solve (5.55) and (5.59) for different values of $\bar{M}_0^2$, and this result is plotted in Figure 5.15. This plot is siginificant from the experimental design point of view. From this curve,

it is possible to choose inlet flow speeds depending on the incident power levels such that thermal choking can be avoided.

**Effectiveness Calculations**

To determine the efficiency of the EM HX, we define mechanical efficiency of energy conversion based on the net mechanical power output and the total energy transferred to the fluid. The mechanical efficiency, $\chi_{\text{mech}}$, is defined as

$$\chi_{\text{mech}} = \frac{\text{Mechanical Power Gained}}{\text{Applied EM Power}} \times 100.$$

The total thermal efficiency of the device, $\chi_{\text{total}}$ is defined as

$$\chi_{\text{total}} = \frac{\text{Mechanical Power Gained + Increase in the Internal Energy}}{\text{Applied EM Power}} \times 100$$

Mechanical power density per unit cross-sectional area of the channel at any location (in W/m$^2$) is expressed by

$$P_{\text{mech}} = \dot{M}\bar{V}^2,$$

where $\bar{V}$ is the flow velocity (in m/s), $\dot{M} = \rho_f \bar{V}$ is the mass flow rate per unit cross-sectional area (in kg/m$^2$s), $\rho_f$ is the fluid density (in kg/m$^3$). Similarly, the internal energy density of the gas per unit cross-sectional area is given by

$$P_{\text{internal}} = \dot{M} c_{v_f} \bar{T},$$

where $c_{v_f}$ is the specific heat of the gas at constant volume (in J/kgK) and $\bar{T}$ is the gas temperature (in K). With these expressions we can write

$$\chi_{\text{mech}} = \eta \dot{M} \left[ \frac{\bar{V}^2_{(\text{at } x=1)} - \bar{V}^2_{(\text{at } x=0)}}{P_{av}} \right] \times 100,$$

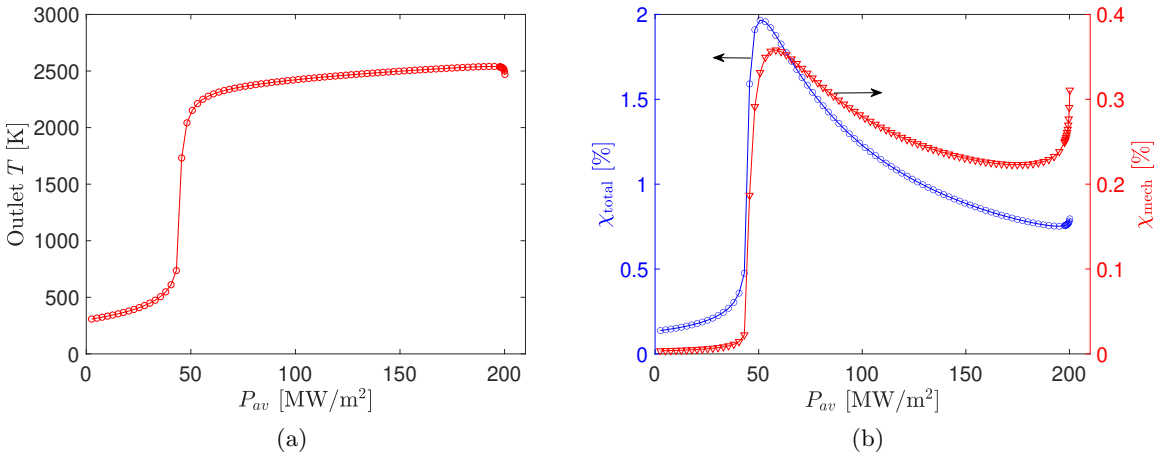


Figure 5.16: Dimensional outlet temperature as a function of $P_{av}$ (a), and $\chi_{\text{total}}$ and $\chi_{\text{mech}}$ as a function of $P_{av}$ (b). In this simulation $l_1 = l_2 = 0.01$ m, $L = 1$ m, heat transfer coefficient and radiation emissivity at $z = 0$ are 13 W/m$^2$K and 0.7, respectively. Maximum $\chi$ is observed as soon as thermal runaway initiates in the ceramic.

where $P_{av}$ is the dimensional applied EM power density given by (5.2). Similarly,

$$\chi_{\text{total}} = \eta \dot{M} \left\{ \frac{\left[\bar{V}^2_{(\text{at } x=1)} - \bar{V}^2_{(\text{at } x=0)}\right] + c_{v_f}\left[\bar{T}_{(\text{at } x=1)} - \bar{T}_{(\text{at } x=0)}\right]}{P_{av}} \right\} \times 100, \tag{5.60}$$

For effectiveness calculations shown below we use air as a working fluid and zirconia as the ceramic (properties of zirconia are taken from [17]). All the material properties except the ceramic loss factor and the gas density are assumed constant. We keep $\epsilon_{r_1} = 1$, $\epsilon_{r_2} = 6.69$, $c_{p_1} = 1,000$ J/kgK, $R = 287$ J/kgK, $c_{p_2} = 219$ J/kgK, $k_1 = 0.02$ W/mK, $k_2 = 0.2$ W/mK, $\rho_2 = 2,848$ Kg/m$^3$, heat transfer coefficient and radiation emissivity between the fluid channel wall and the environment are 13 W/m$^2$K and 0.7, respectively. At the inlet the gas enters with flow velocity is 52 m/s and temperature of 300 K. The ambient is assumed to be at constant temperature of 300 K and at constant pressure of 1 atm.

For material properties discussed above we plot the power response curve based on the outlet temperature in Figure 5.16(a), and $\chi_{\text{total}}$ and $\chi_{\text{mech}}$ are plotted in Figure 5.16(b). We observe that thermal choking occurs when $P_{av} = 200.1$ MW/m$^2$. Although, both $\chi_{\text{mech}}$ and $\chi_{\text{total}}$ improve when choking occurs, the maximum efficiency is achieved when we achieve high ceramic temperature

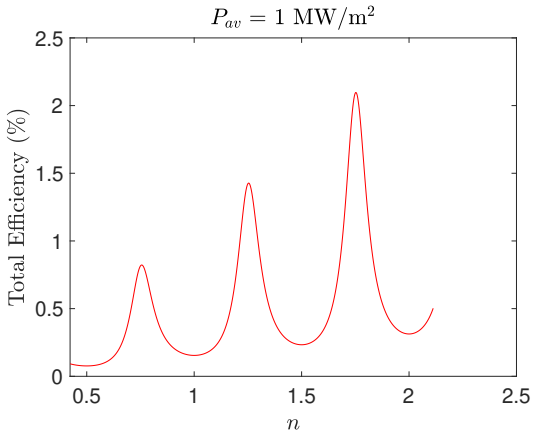


Figure 5.17: $\chi_{\text{total}}$ as a function of ceramic layer thickness, $l_2 = n\lambda_2$. Variations in $l_2$ are achieved by changing the value of $n$. Peak values $\chi_{\text{total}}$ are observed when $n = \frac{1}{4}, \frac{3}{4}, \frac{5}{4}, \ldots$. This indicate that electric field resonance takes place between the incident wave and the reflected wave from the grounded end.

(onset of thermal runaway) at low applied EM powers. This observation is consistent with what we found in chapter 3. Regardless of whether a fluid is compressible or incompressible, the most efficient operation may occur when high temperatures are achieved at lower applied powers. For instance, the leftmost turning point on the double S-curve may lead to the most efficient operation of the EM HX as discussed in chapter 3 (see Figure 3.6). But, as shown in chapter 2, a double S-curve is not possible for the considered EM HX when we have air as the working fluid. This motivates another question: can we achieve the onset of thermal runaway at lower applied powers? One possible way is to increase the ceramic thickness.

In Figure 5.17, we keep the applied power to be 1 MW/m$^2$ and plot $\chi_{\text{total}}$ as a function of ceramic channel thickness, $l_2$. Here we increase $l_2$ by changing $n$ such that $l_2 = n\lambda_2$, where $\lambda_2$ is the wavelength of EM waves in the ceramic region. The spikes in the values of $\chi_{\text{total}}$ occur when $n = \frac{1}{4}, \frac{3}{4}, \frac{5}{4}, \ldots$. Such behavior of $\chi_{\text{total}}$ suggests that electric field resonance occurs between the incident wave and the reflected wave from the grounded end when ceramic channel thickness are such that $l_2 = n\frac{\lambda_2}{4}$, where $n$ can be an odd integer. As a result, ceramic heats up efficiently as compared to the non-resonating cases, and lead to the efficient operation.

In Figure 5.18 we plot power response curves and $\chi_{\text{total}}$ as a function of $P_{av}$ with $n$. We observe that the maximum $\chi_{\text{total}}$ increases with $n$. This can be explained by looking at the power response

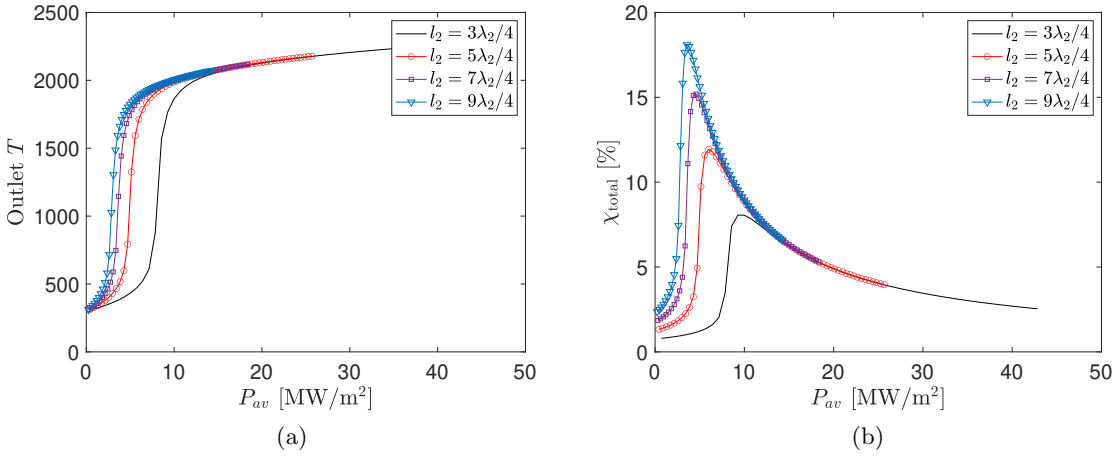


Figure 5.18: Power response curves (a) and $\chi_{\text{total}}$ as a function of $P_{av}$ (b) when ceramic thickness is increased. In these simulations $l_1 = 0.01$ m.

curves shown in Figure 5.18(a). The applied EM power required to achieve the onset of thermal runaway in the ceramic drops down as we increase $n$; as high temperatures are achieved at lower applied powers, maximum $\chi_{\text{total}}$ improves with $n$. Due to EM field attenuation in the ceramic region, the amplitude of the reflected wave from the grounded end is smaller compared to the incident EM field intensity. When ceramic thickness is large enough (i.e., $n \to \infty$), amplitude of the reflected wave becomes negligible. Since the electric field resonance is expected to become weaker as ceramic thickness increases, the maximum efficiencies may asymptotically reach to a constant value as $n \to \infty$. In this EM HX, maximum theoretical total efficiency strongly depends on how much EM power is reflected at the incident boundary. The work of [60] considers EM heating of AlN:Mo susceptors without any fluid flow. They report that about 45-70% of incident power is reflected back to the atmosphere at high temperatures (around 1100 K) leading to total efficiency of EM heat generation on the order of 30-55%. In the considered EM HX, some of the heat is lost to the environment through convection and radiation. Theoretically, the maximum possible efficiencies that can be achieved in this EM HX are expected to be less than 55%.

Another possible way of improving $\chi_{\text{total}}$ is to increase the fluid channel thicknesses, $l_1$. As $\epsilon_{r_1} = 1$ which is the same as the dielectric constant of the surroundings, increasing size of the fluid domain does not alter the EM characteristics of the problem. But the cross-sectional area of

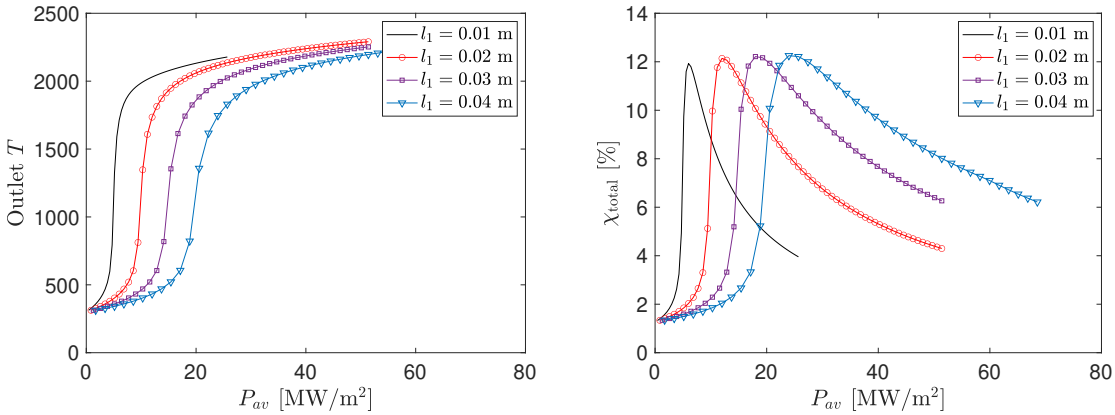


Figure 5.19: Power response curves (a) and $\chi_{\text{total}}$ as a function of $P_{av}$ (b) when fluid channel thickness is increased. In these simulations, $l_2 = 5\lambda_2/4$.

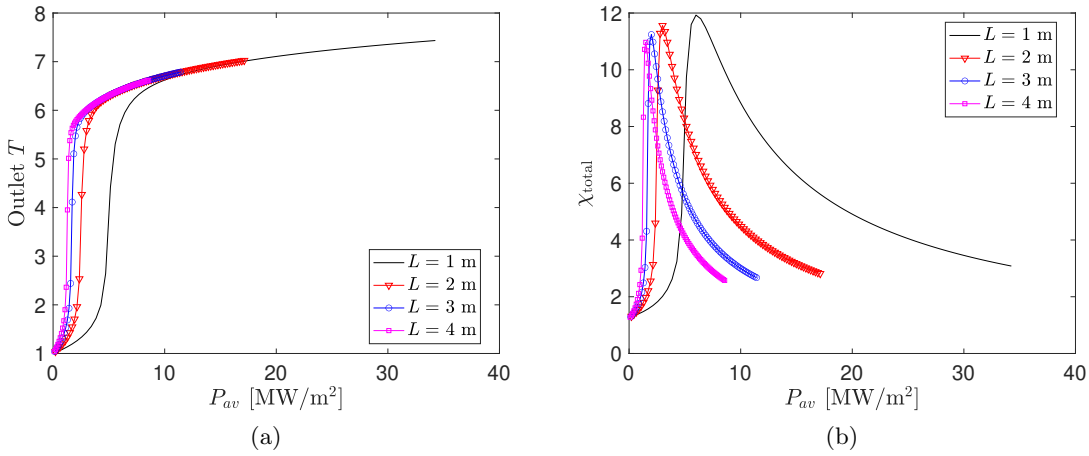


Figure 5.20: Power response curves (a) and $\chi_{\text{total}}$ as a function of $P_{av}$ (b) when the fetch length of the EM HX is increased. In these simulations, $l_1 = 0.01$ m and $l_2 = 5\lambda_2/4$.

the fluid channel increases linearly with $l_1$. By keeping the inlet flow velocity to be 52 m/s, we increase the total mass flow rate of the gas. In Figure 5.19, we plot power response curves and $\chi_{\text{total}}$ as a function of $P_{av}$. We see that the maximum $\chi_{\text{total}}$ does not significantly improve with $l_1$. This can be explained by looking at power response curves shown in Figure 5.19(a). As the total mass flow rate of the gas increases with $l_1$, total heat transferred by convection and work of thermal expansion also increases. As expected, the power required to achieve thermal runaway in the ceramic increase with $l_1$ and the maximum $\chi_{\text{total}}$ does not increase significantly. Again, this observation is consistent with what we found in chapter 3.

Another factor that may affect EM heating of the ceramic, is the fetch length, $L$, of the EM HX. With increase in $L$, the total heat added into the ceramic increases. As a result, $P_{av}$ required to achieve the onset of thermal runaway decreases with $L$ as seen in Figure 5.20(a). But, $\chi_{\text{total}}$ is directly proportional to the aspect ratio, $\eta$, as seen in (5.60). With increase in $L$ keeping $l_1$ and $l_2$ the same, we decrease $\eta$ of the EM HX. Although $P_{av}$ needed for thermal runaway to occur drops as seen in Figure 5.20(a), reduction in $\eta$ causes $\chi_{\text{total}}$ to drop down with increase in $L$ as seen in Figure 5.20(b).

## 5.3 Conclusions

In this chapter, we have developed analytical models that can capture thermal energy transport mechanisms occurring at the pore-scale of an EM HX which consists of a porous lossy ceramic (heated by EM waves) and compressible gas is flowing through the pores. To model the pore-scale gas dynamics, we have considered a 2D thin and long double-layer EM HX such that a channel carrying a compressible flow of an ideal gas is in perfect thermal contact with a thin ceramic layer.

The impact of coupling between compressible gas-dynamics and thermal runaway depends on the values of $\Lambda$ and $\bar{M}^2$. When channel thickness is small ($\sim 100$ $\mu$m) such that $\Lambda$ is of $o(1)$, both $Re$ and $\bar{M}^2$ are small and viscous stresses are dominating compared to the flow inertia. For this scenario we apply lubrication theory to develop analytical model which describes cross-sectional averaged mass, momentum, and thermal energy conservation laws along with equations governing the electric field amplitude. Resulting system of ODE is solved numerically using MATLAB's ODE

solvers. From this lubrication model, we have found that when the work of expansion dominates the net heat added into the system, gas begins to cool down locally (this is known as JT cooling). By carrying out parametric studies, we have determined critical conditions under which onset of JT cooling takes place within the fluid. By investigating the local competition between JT cooling and thermal runaway, we have found that work of expansion has a little impact on temperatures during thermal runaway, but it causes outlet temperatures to drop down.

Because of slow flow speeds, the lubrication model is not a viable design of an EM HX because of low mechanical power output. To address this we have considered a high-speed compressible flow through the channel such that $Re \gg 1$ and $\bar{M}^2$ is of $o(1)$. This allows us ignore the contribution due to viscous stresses within the fluid, and assume that the flow is frictionless, i.e., the gas-dynamics in the channel is described by the law of Rayleigh flow. By applying the thin domain asymptotic theory, we derive a system of ODEs that governs the cross sectional averaged conservation laws, which is then solved numerically in MATLAB. We consider the inlet conditions such that the flow is subsonic, but due to heat addition, gas does work of thermal expansion and accelerates as it moves from inlet to outlet. The model of Rayleigh flow coupled with EM heating of ceramics is limited by the phenomenon of thermal choking. When flow velocity and temperatures are such that we reach sonic state ($\bar{M}^2 = 1$) within the channel, thermal choking occur and further heat addition is not possible without altering the inlet flow conditions. By carrying out linear stability analysis, we find that when we have $\frac{1}{\gamma} < \bar{M}^2 < 1$ inside the computational domain, infinitesimal fluctuations in temperatures (or the applied EM power) lead to rapid rise of flow mach numbers resulting in to a thermally choked flow. Through this stability analysis, we have determined the critical applied EM power, $\bar{P}_{\text{crit}}$ such that when $\bar{P} > \bar{P}_{\text{crit}}$, small fluctuations $\bar{P}$ lead to thermal choking in the channel. By carrying out a parametric study, we have then determined how $\bar{P}_{\text{crit}}$ is affected by the inlet flow conditions. This result is significant from the practical application point of view as it allows us to design experiments by avoiding thermal choking within the fluid region. Maximum practical Mach number that can be achieved is $\frac{1}{\gamma}$, and expression governing the maximum possible temperature within the channel is derived.

To determine the effectiveness of the EM HX, total thermal and mechanical efficiencies of the

device are calculated. It is found that the most efficient operation occurs when high temperatures are achieved at the low applied power when thermal runaway initiates. By carrying out parametric studies on $l_2$, we find that the electric field resonance occurs in the ceramic layer if $l_2 = \frac{n\lambda_2}{4}$, where $n$ can by any odd integer. As a result, thermal runaway occurs at low applied powers when we increase the value of $n$, and this causes maximum efficiency of the energy conservation to increase with $n$.

# 6 COMPRESSIBLE FLOW THROUGH LOSSY POROUS CERAMIC LAYER

One possible design of an EM HX consists of a porous ceramic material heated by incident EM waves and a compressible gas passing through the pores transfers heat from the ceramic and delivers mechanical power at the outlet. Because of increased contact area between the fluid and the ceramic, heat transfer improvements are expected in such EM HX. For example, the NASA's MTLS [54] rocket, which converts incident EM energy to thrust, consists of an array of thin and long ceramic tubes which are heated by EM. This structure may be idealized as a simple porous medium which obeys the capillary tube model of permeability and porosity [32]. Designing such an EM HX with porous ceramic material requires understanding of the dominant gas dynamics effects and their coupling with thermal runaway at the pore-scale. In the previous chapter, we idealized the microscale structure with a long and thin double layer EM HX which consists of a fluid channel maintaining thermal contact with a lossy ceramic. Since this simple model is aimed towards uncovering dominant multiphysics at the pore-scale, the thicknesses of the fluid and the ceramic layers are comparable to the size of the pores.

The compressible dynamics taking place at the pore-scale depends of the values of Bearing number, $\Lambda$, which is the ratio of viscous pressure scale to ambient atmospheric pressure, and the Mach number, $\bar{M}^2$, which is the ratio of flow velocity to the speed of sound in the gas. When pore-scale lengths are small such that $\Lambda$ is of $o(1)$ and $\bar{M}^2 \ll 1$, mechanical power output is small due to slow flow speeds, however we found in the previous chapter that the Joule-Thompson (JT) cooling occurs when work of expansion dominates the net heat added into the ceramic. This motivates following research questions:

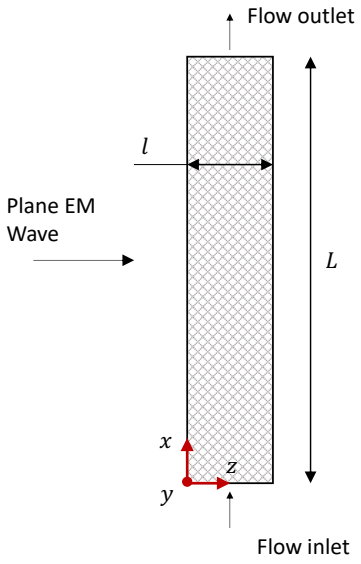


Figure 6.1: Structure of the considered EM HX with a lossy porous media. We keep $l = 0.05$ m and $L = 0.5$ m. Plane EM wave polarized in the $y$-direction and propagating in the $z$-direction is irradiated normally on the porous structure.

- *How does microscale JT cooling affect the energy transfer mechanisms at the macroscale? How does JT cooling compete with thermal runaway at the macroscale?*

To answer these question, we consider an EM HX which consists of a lossy porous ceramic heated by EM waves, and a compressible gas is flowing through the pores. The geometry of the EM HX is shown in Figure 6.1. The pore-scale lengths are such that $\Lambda$ is of $o(1)$, $\bar{M}^2 \ll 1$, and the pore-scale Reynolds number, $Re$, which gives us relative importance of the flow inertia compared to the viscous stresses, is small due to slow flow speeds. Since $Re < 10$ for this scenario, the macroscale fluid mass and momentum conservation equations can be described by the Darcy's law applied to compressible gases [32], which says that the average flow rate of the gas through the pores is directly proportional to pressure gradient within the fluid. On the other hand, when flow speeds are high and $\Lambda \ll 1$ (i.e, $Re \gg 1$ and the flow inertia is dominating compared to the viscous stresses at the pore-scale), the compressible gas-dynamics is mainly governed by $\bar{M}^2$. In the previous chapter, we found that when $\bar{M}^2 = 1$ at the pore-scale, thermal choking occurs, and it is not possible to add heat into the gas without altering the inlet conditions. For such values of $\bar{M}^2$, we have $Re \gg 1$, which suggests that the macroscale fluid momentum conservation may be better described by the

Forchheimer's law [32]

$$-\nabla p = \alpha \mathbf{u} + \beta |\mathbf{u}| \mathbf{u},$$

where $p$ is the fluid gauge pressure, $\mathbf{u}$ is the volume averaged flow velocity, and $\alpha$ and $\beta$ are proportionality constants which depend on the microscopic structure of the porous medium. In the works of [61, 62], values of $\alpha$ and $\beta$ are determined for nonisothermal compressible flows, but velocity and temperature ranges in their experiment are $o(1)$ m/s and $o(10^2)$ K. But, in our problem, gas-dynamics is coupled with thermal runaway phenomena, and experimental determination of proportionality constants at such high temperature conditions is still unexplored. It is possible to derive macroscale mass and momentum conservation laws using the method of homogenization. But, we leave consideration of such analytical effort for the future development and focus on investigating the impact of coupling between JT cooling and thermal runaway at the macroscale.

## 6.1 Development of the Macroscale Model

The compressible Darcy's law which describes macroscale fluid mass and momentum conservation is

$$\phi \frac{\partial \rho_f}{\partial t} + \nabla \cdot (\rho_f \mathbf{u}) = 0, \tag{6.1a}$$

$$\mathbf{u} = -\frac{\kappa}{\mu} \nabla p, \tag{6.1b}$$

where $\phi$ is the porosity (or void fraction) of the porous media which is assumed to be a constant value for simplicity, $\rho_f$ is the gas density, $\mathbf{u}$ is the Darcy velocity vector, $\kappa$ is the permeability of the porous media, $\mu$ is the dynamic viscosity of the gas, and $p$ is the fluid gauge pressure. The relation between the porosity, $\phi$, and $\kappa$ is dependent on the microscopic structure of the porous media. For example, if a porous region is assumed to consist of a bundle of straight, long and thin tubes, then the capillary tube model can describe the relation between $\phi$ and $\kappa$ [32]. Another possible way of approximating microscopic structure of the porous media is to assume that the medium is a packed bed of solid sphere of uniform diameter. The relation between $\phi$ and $\kappa$ for this scenario is given by

the Konzey-Carman relations as

$$\kappa = \frac{d_p}{180}\frac{\phi^3}{(1-\phi)^2} \tag{6.2}$$

where $d_p$ is mean diameter of the solid spheres. Analytical derivation of (6.2), and other similar empirical relations between $\phi$ and $\kappa$ are described in chapter 6 of [63]. Since it is known that the Konzey-Carman empirical model agrees well with experimental results compared to other relations [32,63], we use (6.2) in our model by setting $\phi = 0.1$ and $d_p$ to be of $1\times10^{-4}$ m to get $\kappa = 6.85\times10^{-14}$ $\mathrm{m}^2$.

We assume that EM waves polarized in the $y$-direction and propagating in the $z$-direction with frequency of $f = 2.45$ GHz are incident normally on the porous ceramic. Since the wavelength of EM waves is larger than the pore-scale lengths, effective medium Maxwell's equations can describe the electric field strength in the porous region. Since EM field is polarized in the $y$-direction and permittivity gradients are in the $xz$-plane, electric field becomes divergence free (from the Gauss' law), such that $\mathbf{E} = E(x,z)\hat{y}$, where $E(x,z)$ is the amplitude of the electric field vector which obeys

$$\nabla^2 E + k_0^2\left(\epsilon_{r_{\text{eff}}} + i\epsilon''_{\text{eff}}\right)E = 0, \tag{6.3}$$

where $k_0$ is the wavenumber of EM waves in the free space, $\epsilon_{r_{\text{eff}}} = \phi\epsilon_{r_f} + (1-\phi)\epsilon_{r_s}$ is the effective dielectric constant, $\epsilon_{r_f}$ and $\epsilon_{r_s}$ are the dielectric constants of fluid and solid regions, respectively, $\epsilon''_{\text{eff}} = \phi\epsilon''_f + (1-\phi)\epsilon''_s$ is the effective dielectric loss factor, $\epsilon''_f$ and $\epsilon''_s$ are the loss factors of the fluid and the solid regions, respectively. Since the fluid region is lossless and the solid region is ceramic, we have $\epsilon''_f = 0$ and $\epsilon''_s$ increases exponentially with temperature.

The power density of the applied EM field is given by

$$P_{av} = \frac{E_0^2}{2\Upsilon}, \tag{6.4}$$

where $E_0$ is the strength of incident electric field and $\Upsilon$ is the impedance of the free space.

The energy conservation equation at the macroscale is given by

$$(\rho c_v)_{\text{eff}}\frac{\partial T}{\partial t} + (\rho c_v)_f \mathbf{u}\cdot\nabla T + (p_{\text{atm}} + p)\nabla\cdot\mathbf{u} = k_{\text{eff}}\nabla^2 T + \frac{1}{2}|E|^2\epsilon''_{\text{eff}}(T), \tag{6.5}$$

where $(\rho c_v)_{eff} = \phi(\rho c_v)_f + (1-\phi)(\rho c_p)_s$ is the effective heat capacity of the porous region, $\rho_f$ and $\rho_s$ are the densities of the gas and the ceramic, $c_{v_f}$ is the heat capacity of the gas at constant volume, $p_{\text{atm}}$ is the ambient atmospheric pressure, and $c_{p_s}$ is specific heat capacity of the ceramic region, and $k_{\text{eff}}$ is the effective thermal conductivity the porous media. This model of the energy conservation is derived by assuming that local thermal equilibrium always exists between the gas and the ceramic region, i.e., we always have equal temperature of the gas and the ceramic at the pore-scale. By applying the method of volume averaging [64], it is possible to derive (6.5); at the microscale, energy conservation laws in the fluid and ceramic regions are integrated over a representative element volume (REV), and the deviation of the properties from their volume averaged values is ignored. Derivation of (6.5) using the volume averaging method (without the EM heat source term) can be found in [64, 65] (description of the method can be found in [64], and derivation of (6.5) for incompressible case can be found in [65]). Expression for $k_{\text{eff}}$ depends on the microscopic geometry of the porous media. If we approximate the porous laminate by a packed bed of uniform spheres, i.e., the Konzey-Carman model, $k_{\text{eff}}$ simply becomes the volume averaged thermal conductivity [32], i.e., $k_{\text{eff}} = \phi k_f + (1-\phi)k_s$, where $k_f$ and $k_s$ are the thermal conductivity of fluid and the solid medium.

Finally, the equation of state that gives the relation between $p$, $\rho_f$, and $T$ is given by

$$p_{\text{atm}} + p = \rho_f R_g T, \tag{6.6}$$

where $p_{\text{atm}}$ is the ambient pressure which is 1 atm in our model, and $R_g = 287$ J/kgK is the gas constant.

Boundary conditions at $z = 0$ are given by

$$\frac{\partial E}{\partial z} + ik_0 E = 2ik_0 E_0, \tag{6.7a}$$

$$\frac{\partial T}{\partial z} = h(T - T_A) + \xi s_r (T^4 - T_A^4), \tag{6.7b}$$

$$\mathbf{u} \cdot \hat{n} = 0 \text{ (no penetration condition)}, \tag{6.7c}$$

where $E_0$ is the strength of the incident EM wave, $h$ is the heat transfer coefficient which has

constant value of 5 W/m$^2$k, $\xi$ is the emissivity of the surface which we set up as a constant value of 0.2, $s_r$ is the Stefan-Boltzmann radiation constant, and $\hat{n}$ is the outward unit normal vector.

Boundary conditions at $z = l$ are

$$E = 0, \text{ (grounded end)} \tag{6.8a}$$

$$\frac{\partial T}{\partial z} = 0, \tag{6.8b}$$

$$\mathbf{u} \cdot \hat{n} = 0 \text{ (no penetration condition).} \tag{6.8c}$$

Boundary conditions at $x = 0$ are

$$\frac{\partial E}{\partial z} = 0, \tag{6.9a}$$

$$T = 300 \text{ K}, \tag{6.9b}$$

$$p = p_{\text{in}}, \tag{6.9c}$$

where $p_{\text{in}}$ is the gauge pressure at the inlet.

Finally the conditions on the top boundary at $x = L$ are

$$\frac{\partial E}{\partial z} = 0, \tag{6.10a}$$

$$\frac{\partial T}{\partial z} = 0, , \tag{6.10b}$$

$$p = 0. \tag{6.10c}$$

We solve the system equations (6.1)-(6.10) numerically using COMSOL Multiphysics package. Since the compressible gas dynamics is coupled to thermal runaway in the ceramic, this model is nonlinear. Steady-state solver, which uses Newton-Raphson method, may not converge if the initial guess is not close to the true solution. To address this, we use a two-step solution approach. In the first step we use a time-dependent solver for a given range of time steps. Second step utilizes the steady-state solver; the initial guess for this step is extracted from the final solution from the time-dependent solver. This approach takes about 2 hours to get the solution when

thermal runaway is expected to occur. But the total solution time required for parametric studies is reduced significantly if we reuse solution form the previous parameter as initial guess for the next parameter. The time-dependent solver utilizes the second-order backward difference method to discretize the time derivatives in conjunction with adaptive time-stepping algorithm. To capture nonlinear dynamics in the model, the adaptive time-stepping algorithm chooses step size according to the values of temporal gradients. The advantage of this solution approach is that we can capture nonlinear dynamics along with steady-state operation of the EM HX. As done in previous chapters, we use quadratic Lagrange triangular elements to discretize the system of equations. We carry out converge tests on the COMSOL model and choose maximum size of the element such that we have at least 80 element per wavelength in the porous region.

In the simulations presented below we set $\epsilon_f = 1$, $\mu_f = 1 \times 10^{-5}$ Ns/m$^2$, $k_f = 0.02$ W/mK, $c_{v_f} = 717$ J/kgK, $\phi = 0.1$, $\kappa = 6.85 \times 10^{-14}$ m$^2$, $p_{\text{atm}} = 1$ atm, $\epsilon_s = 6.69$, $\rho_s = 2,848$ J/kgK, $c_{p_s} = 219$ J/kgK, and $\epsilon_s'' = 0.0004e^{2.32\left[\frac{T-T_A}{T_A}\right]}$. The solid porous matrix consists of zirconia and its properties are taken from [17].

## 6.2 Results

To identify how JT cooling affects the macroscale energy transfer we define the Bearing number as $\Lambda = \frac{p_{\text{in}}}{p_{\text{atm}}}$, where $p_{\text{in}}$ is the gauge pressure at the inlet which is a specified inlet condition in the COMSOL Model. As $\Lambda$ increases, gas expands from high pressure inlet to low pressure outlet though a thin and restricted area (the porous ceramic); when work of expansion is larger than the total heat added to the system, JT cooling is expected.

We first look at the operation of the EM HX on the lower stable branch. Steady-state results from the COMSOL simulation are shown in Figure 6.2 for increasing values of $\Lambda$ when the EM HX operates on the lower stable branch (this can be understood by looking at temperature ranges seen in Figure 6.2(a)-(d)). The applied EM power is kept at 60 kW/m$^2$ and the initial temperature is maintained at 300 K. The steady-state $T$ patterns shown in Figure 6.2(a)-(d) show that the gas experiences JT cooling effect near the outlet. Since we have zero gauge pressure condition at the outlet, density of the gas (which is directly proportional to the absolute pressure), drops near the

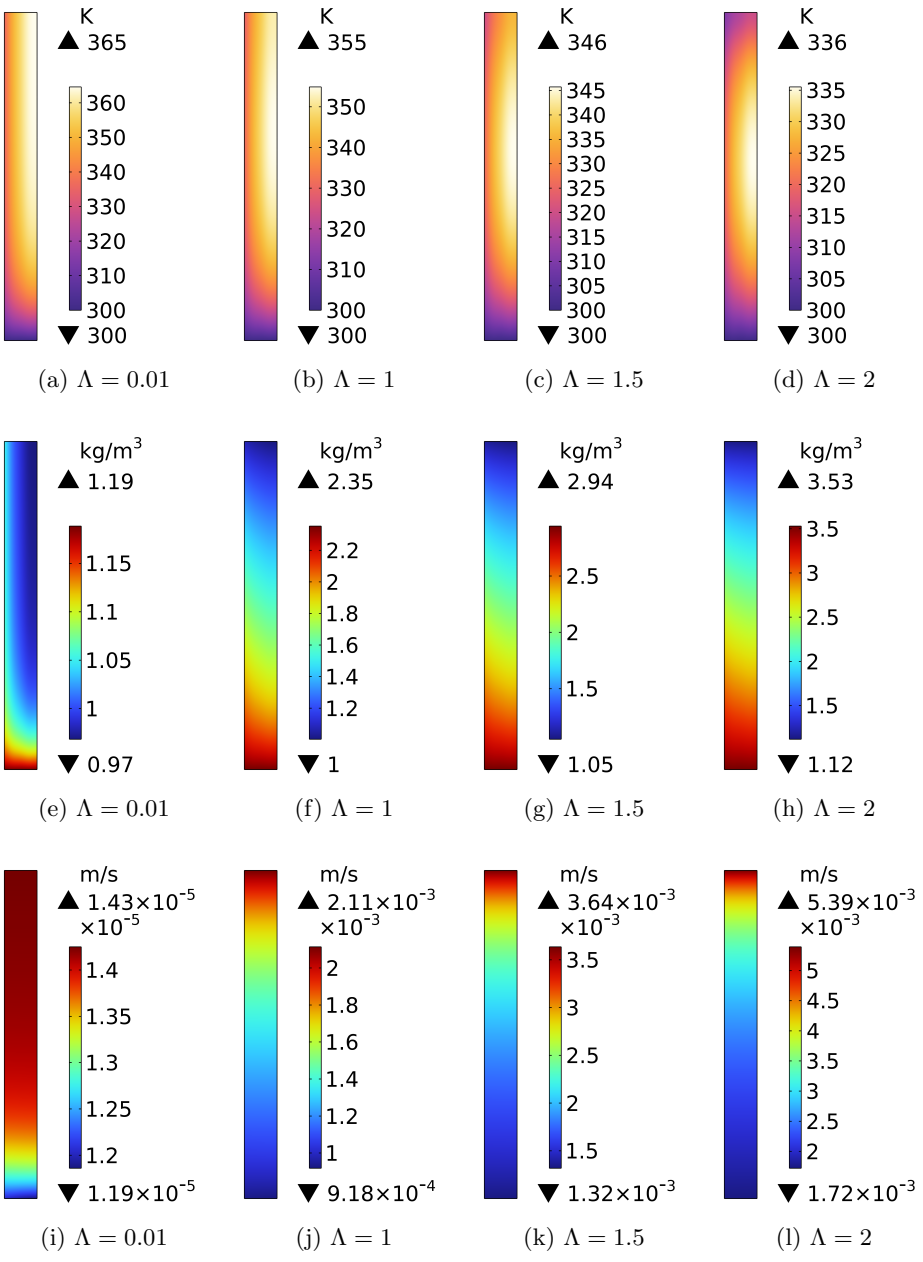


(a) $\Lambda = 0.01$ (b) $\Lambda = 1$ (c) $\Lambda = 1.5$ (d) $\Lambda = 2$

(e) $\Lambda = 0.01$ (f) $\Lambda = 1$ (g) $\Lambda = 1.5$ (h) $\Lambda = 2$

(i) $\Lambda = 0.01$ (j) $\Lambda = 1$ (k) $\Lambda = 1.5$ (l) $\Lambda = 2$

Figure 6.2: Results from the COMSOL model at the steady-state for respective values of $\Lambda$, where $\Lambda = \frac{p_{\text{in}}}{p_{\text{atm}}}$.Steady-state $T$ patterns are shown in (a)-(d), $\rho_f$ patterns are shown in (e)-(h), and $|\mathbf{u}|$ profiles are shown in (i)-(l). The applied EM power, $P_{av} = 60$ kW/m$^2$ lower branch operation shown here is achieved when initial temperature is set to 300 K.

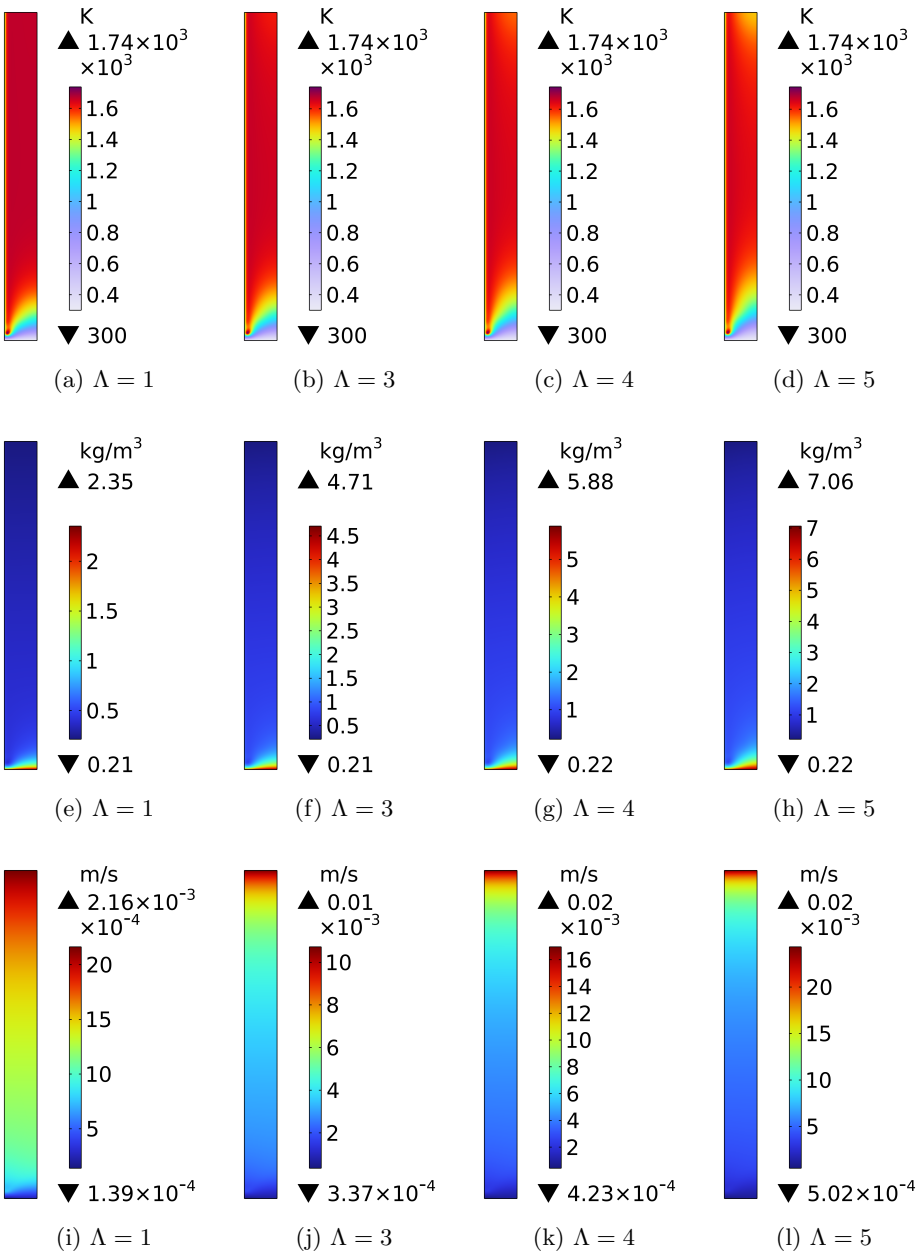


(a) $\Lambda = 1$ (b) $\Lambda = 3$ (c) $\Lambda = 4$ (d) $\Lambda = 5$

(e) $\Lambda = 1$ (f) $\Lambda = 3$ (g) $\Lambda = 4$ (h) $\Lambda = 5$

(i) $\Lambda = 1$ (j) $\Lambda = 3$ (k) $\Lambda = 4$ (l) $\Lambda = 5$

Figure 6.3: Results from the COMSOL model at the steady-state for respective values of $\Lambda$, where $\Lambda = \frac{p_{\text{in}}}{p_{\text{atm}}}$.Steady-state $T$ patterns are shown in (a)-(d), $\rho_f$ patterns are shown in (e)-(h), and $|\mathbf{u}|$ profiles are shown in (i)-(l). The applied EM power, $P_{av} = 60$ kW/m$^2$ lower branch operation shown here is achieved when initial temperature is set to 2,000 K.

outlet to satisfy the equation of state; this can be seen in Figure 6.2(e)-(h). Because of the density drop near the outlet, gas accelerates to satisfy the mass conservation law as seen in Figure 6.2(i)-(l). Therefore, The work of thermal expansion has a stronger impact near the outlet and causes cooling of the gas.

We now look at operation of the EM HX on the upper stable branch. To achieve this, we keep the same $P_{av} = 60$ kW/m$^2$ but now maintain the initial temperature to be 2,500 K, and run the COMSOL simulation for increasing values of $\Lambda$. Steady-state results from this scenario are plotted in Figure 6.3. Looking at $T$, $\rho_f$, and $|\mathbf{u}|$ patterns shown in Figure 6.3, the observation is consistent that JT cooling phenomena persist even during thermal runaway, and has a stronger impact near the outlet.

## 6.3 Conclusions

In this chapter, we have developed a macroscale model of an EM HX which consists of a lossy ceramic material heated by EM waves, and a gaseous flow through the pores delivers power at the outlet. As shown in the previous chapter, there are two new heat transfer mechanisms occur at the pore scale: JT cooling and thermal choking. Motivation behind this chapter is to investigate whether these mechanisms persist at the macroscale and how they affect energy conversion at the macroscale. Since JT cooling occurs at the low Reynolds number, we use compressible Darcy's law to describe macroscale mass and momentum conservation coupled with effective medium energy and Helmholtz equations. This model is then solved numerically using COMSOL Multiphysics. Results presented here show that the JT cooling persist at the macroscale and has a stronger impact near the outlet, even when thermal runaway occurs within the ceramic. Although, the EM HX considered here is not a viable design for mechanical power generation due to slow flow speeds, the results suggests that when high speed gaseous flow through a lossy porous ceramic is considered, macroscale models must be developed by capturing microscale thermal choking. This can be a future extension of the work presented in this chapter.

# 7 IMPACT AND CONCLUSIONS

This work is motivated by applications of ground-to-ground power beaming where energy is transferred from one location to another through the atmosphere with the help of high-power and high-frequency EM radiations. Such technologies consist of a transmitter that converts the input energy into EM radiation, and at the receiving end, the incident EM power is converted into any other energy form. In this work, we have attempted to determine viability of EM HXs that may act as receivers in power beaming applications and convert the EM energy into heat or mechanical power.

The designs of EM HXs we consider in this research consist of a ceramic region, heated by high-power EM waves, and a fluid flow maintaining thermal contact with the heated ceramic then delivers power at the outlet. A nonlinear phenomenon that is inherent during EM processing of lossy ceramics, such as silicon carbide and zirconia, is thermal runaway; a rapid temperature rise (up 2,500 K for silicon carbide) as a result of small change in the applied EM power. Such a strong heating mechanism in the ceramic motivates us to explore possibilities of achieving efficient energy conversion by coupling a fluid flow with the phenomenon of thermal runaway in the ceramic. Experimentally, it is challenging to maintain the continuous operation of an EM HX without mechanical failure of ceramics through melting or cracking during thermal runaway. For this reasons, in chapter 2 of this dissertation we have extended the approach of [28, 29] by considering heating of a two-layer (lossless-lossy) structure due to asymmetric irradiation of plane EM waves. One end of the ceramic maintains perfect thermal contact with the lossless dielectric layer, and the other end of the ceramic is grounded (i.e., electric field vanishes at this boundary). As the EM waves reflect from the grounded end, we show that a constructive interference between the incident and the reflected waves occurs within the ceramic region, which is represented by an additional

stable branch of the power response curve at moderate temperatures. This additional family of solutions is significant for the development of EM HX as we have demonstrated a practical way of achieving resonance based control over thermal runaway from asymmetric irradiation by EM waves. The middle stable branch allows EM HXs to operate at elevated temperatures such that a safe and efficient operation may be possible, but numerical models that simulate coupled interaction between a fluid flow and thermal runaway are required to determine viability of this energy harnessing approach.

When an incompressible fluid flow is coupled with thermal runaway within the ceramic, heat is transferred by conduction, convection, phase-change due to boiling heat transfer, and work of expansion in the vapor phase of the fluid. Modeling this complete problem is challenging due to nonlinear nature of heat transfer mechanisms involved. For this reason, we break down the full problem into more tractable scenarios, and individually study the impact of each heat transfer mechanisms within the fluid and their coupling with the phenomenon of thermal runaway in the ceramic.

In chapter 3 of this dissertation, we study how convective heat transfer affects the onset of thermal runaway within the ceramic, and vice versa. To do that, we have considered a triple layer EM HX (fluid-ceramic-fluid) such that two fluid channels carrying a pressure-drive Poiseuille-flow maintain perfect thermal contact with the ceramic. Layer thicknesses are chosen according to [28, 29] such that a double S-curve is possible at the steady-state. We have found that the EM HX operating near the leftmost turning points on the middle stable branch are the most efficient compared to operation on lower or upper branches. As a result of electric field resonance, the ceramic heats up efficiently and high temperatures are possible at low applied powers making this region of the middle-stable branch the most efficient. We have also found out that thermal runaway initiates locally when the maximum temperature within the ceramic reaches a critical value, and local hotspot is generated within the ceramic. Finally, by carrying out a parametric study on fluid's dielectric constant, we have shown that the double S-curve is possible if permittivity variation of the fluid region is within 10%. Although the EM HX considered in this chapter does not replicate practical scenario (due to single-phase approximation), these findings are applicable regardless of

whether a fluid flow is compressible or incompressible.

From practical point of view, it is of experimental interest to consider EM HXs that involve coupling between a compressible fluid flow and EM heating of the ceramic. In addition to conduction and convection, we have another mode of heat transfer which is the result of thermal expansion. From fluid density variations, RB convection occurs when buoyancy dominates the viscous stresses within the fluid. Additionally, the gas accelerates to satisfy the mass conservation constraint in the presence of fluid density variations.

As a first step towards considering compressible gas dynamics, in chapter 4, we focus on identifying the impact of coupling between the onset of RB convection and EM heating of the ceramic, and chapter 5 is aimed towards investigating the coupling between gas acceleration and the phenomenon of thermal runaway. Before we can identify how RB convection affects the performance of the device, we first need to determine onset characteristics of the RB convection within the fluid. To do that, we have considered a laminar fluid flow of a lossless fluid, which obeys Boussinesq approximation, situated on top of a lossy ceramic heated by EM waves in the presence of gravity acting downward. Plane EM waves, polarized in the direction of the flow, are irradiated normally on the fluid layer. Because of heat transfer from the ceramic, fluid near the interface is less dense compared to fluid at the opposite boundary. RB convection occurs when buoyancy dominates viscous stresses within the fluid. Through a linear stability analysis, we have found that infinitesimal temperature perturbations introduced in the base-state solution give rise to a fringe field (i.e., electric field perturbation). Since the heat source is dependent on the electric field amplitude, the fringe field feeds back into the system and affects the stability of the EM HX.

A normal-mode analysis reveals that we have three distinct mechanisms of primary instabilities in the EM HX. Firstly, the thermal runaway instability in the ceramic which is inherent due to nonlinear nature of EM heating. Secondly, the fringe field instability occurs as a result of the coupling between the fringe field and temperature perturbations. Both thermal runaway and fringe field instabilities are independent of buoyancy. However, the fringe field instability is dependent on the electric field resonance that is required to achieve a double S-curve. Thirdly, the last instability mechanism is the RB convection; when both thermal runaway and fringe field instabilities are

absent, onset of RB convection takes place when the Rayleigh number is above some critical value. Through a parametric study, we have determined values of the critical Rayleigh number on stable regions of the power response curve. Due to these three modes of primary instability, performance of the EM HX depends on the nonlinear interactions between them. For this reason, future extension of this chapter would be to develop 3D numerical models that can evaluate the performance of the EM HXs.

Another possible design of an EM HX consists of a lossy porous ceramic heated by EM waves and a compressible gas flowing through the pores then delivers the power at the outlet. We showed in chapter 3 that thermal runaway is a local phenomenon, and is expected to occur at the pore-scale. Before we can design such EM HX with porous ceramics, we first need to address the impact of coupling between pore-scale compressible gas-dynamics and thermal runaway in the ceramic. To do that, we make an idealization and assume that the pore-scale energy transport is represented by a long thin double-layer EM HX such that a fluid carrying channel maintains a perfect thermal contact with a ceramic layer. Plane EM waves are normally irradiated on the structure, and only the ceramic is heated by the EM waves. The compressible gas in the fluid channel transfers heat from the ceramic and does work of thermal expansion.

The impact of coupling between compressible gas dynamics and thermal runaway depends on the values of the Bearing number, $\Lambda$, and the Mach number, $\bar{M}^2$. We first consider the cases of $\Lambda$ to be of $o(1)$. For this scenario, channel thicknesses are $o(10^{-6})$ m and the flow speeds are such that $\bar{M}^2 \ll 1$ and the Reynolds number, $Re \ll 1$. We apply lubrication theory and derive a system of ordinary differential equations that describes the cross-sectional averaged mass, momentum, and energy conservation laws at the leading-order. For this scenario of $\Lambda \sim o(1)$, the gas flows from a high-pressure inlet to a low pressure outlet through a very thin and long channel (restricted and confined space); when work of thermal expansion dominates the heat added to the ceramic, the gas experiences cooling effect which is known as JT cooling. By looking at local competition between different modes of heat transfer during thermal runaway, we found that JT cooling has negligible impact during thermal runaway, but causes outlet temperatures to drop down.

Apart from the JT cooling phenomenon, the lubrication model is not a practical choice for

mechanical power generation from EM waves due to such slow flow speeds. To address this, we couple a high-speed Rayleigh flow of an ideal gas (frictionless and nonadiabatic compressible flow) such that $\bar{M}^2$ is of $o(1)$, $Re \gg 1$, and $\Lambda = 0$. We found that when the flow reaches a sonic state, i.e., $\bar{M}^2 = 1$, thermal choking occurs, and further heat addition is not possible without altering the inlet flow conditions. Through a linear stability analysis, we have then determined critical EM power at which thermal choking occurs, and how we can choose inlet flow speeds to avoid thermal choking. Although the maximum possible $\bar{M}^2$ is 1, the most efficient operation of EM HX is found to be when thermal runaway initiates within the ceramic. Finally, by carrying out parametric studies on layer thicknesses, we have found that electric field resonance occurs in the ceramic when its thickness is $l_2 = n\frac{\lambda_2}{4}$, where $n$ can be any odd integer, $\lambda_2$ is the wavelength of EM waves in the ceramic. The electric field resonance causes efficient heating of the ceramic and leads to improvements in the effectiveness of energy conversion from the EM HX.

In chapter 6 of the thesis, we develop a numerical model of an EM HX which has a lossy porous ceramic heated by EM waves and a compressible gas which is flowing through the pores transfers heat from the ceramic. As shown in chapter 5, the compressible gas dynamics taking place at the pore-scale depends on the values of $\Lambda$ and $\bar{M}^2$. In this chapter, we focus on cases when $\Lambda$ is of $o(1)$, and leave the consideration of high $\bar{M}^2$ for future development. For these values of $\Lambda$, when work of expansion dominates the net heat added to the system, JT cooling is expected to occur. Motivation behind this chapter is to identify how JT cooling affects the onset of thermal runaway at the macroscale. Since flow speeds are slow, $Re$ is small. This allows us to use compressible Darcy's law to describe fluid mass and momentum conservation at the macroscale. In addition, we couple effective medium energy conservation and Helmholtz equations with the Darcy law, and solve the resulting 2D system of equations in COMSOL Multiphysics.

We find that the JT cooling has stronger impact near the outlet even during the thermal runaway. Results from this model confirm that the mechanisms found in chapter 5 persist at the macroscale; this motivates another research question: how does the phenomenon of thermal choking affect the macroscale energy transfer? Future extension of this chapter may be focused on deriving macroscale conservation laws that capture thermal choking at the pore-scale.

The models presented here reveal some of the key design parameters of EM HX such as electric field resonance producing a double S-curve, the fringe field instability and its interaction with the convective heat transfer mechanisms, JT cooling and thermal choking that occur when compressible gas dynamics is coupled with the phenomenon of thermal runaway. But we have made several assumptions while developing these models.

In chapter 2, the temperature dependence of dielectric constants is ignored. Wavelengths of EM waves in respective medium change when permittivities vary with temperature, i.e., electric field resonance criteria for the double S-curve changes with temperature. In chapter 3, it is shown that the middle branch exists when these variations are within 10% of the reference value, but larger deviations may be expected in ceramic materials. One way of addressing this challenge would be to dynamically adapt the frequency of incident EM waves so that the wavelength of EM waves in respective regions remains the same when dielectric constants change with temperature. Analytical model described in chapter 2 can be extended to determine the viability of this adaptive approach.

In chapter 5, the considered double layer EM HX results into an S-shaped power response curve at the steady-state. Experimentally, when thermal runaway occurs within the ceramic, melting or mechanical failure of materials is expected to occur due to such high temperature. One possible way of achieving a double S-curve with gaseous coolants is to consider a triple layer EM HX such that an air channel is attached to a lossless dielectric which maintains perfect thermal contact with a ceramic layer (air-lossless-lossy structure). Thicknesses of lossless and lossy layers can be chosen such that electric field resonance occurs in the lossy region promoting efficient heating at low applied powers. Asymptotic models described in chapter 5 can certainly be extended to different geometries.

In all of the models presented here, for simplicity, it is assumed that thermophysical material properties are constant and do not vary with temperature (except in chapter 5 where density of the gas is a function of fluid pressure and temperature). The volumetric heat capacity ($\rho c_p$) of a material has stronger impact on the rate at which temperature is evolving with time and how long it would take to reach the steady-state. Similarly, the thermal conductivity of the ceramic material has dominant impact how quickly the material can dissipate heat during thermal runaway.

Typically for zirconia, the both volumetric heat capacity and thermal conductivity increase with temperature [17], competition between drop in transient temperature growth rate and improved heat diffusion then dictates temperature response during thermal runaway. Similarly in the fluid region, the equation of state is assumed to be given by the ideal gas law. But this assumption may not hold true at higher pressure. The NASA MTLS experiment [54], where propulsion is achieved by expanding high-pressure liquid hydrogen gas, highlights the usefulness of real gases in generating mechanical power. But understanding the impact of non-ideal behavior of the gas on JT cooling requires a separate study.

Efficiency plots from chapters 3 and 5 highlight a practical way of achieving higher energy conversion efficiencies; reach high ceramic temperatures at lower applied powers. It is shown that the electric field resonance causes efficient heating of the ceramic leading to a double S-curve at the steady-state. But an experimental verification of this mechanism is yet to be carried out. In addition, the highest possible conversion efficiencies are limited due to reflection of incident EM power back to atmosphere. It may be possible to explore techniques such as impedance matching (typically used in microwave circuit design) to minimize the losses due to reflection. But a separate investigation is required to understand how such techniques can be applied to open systems such as EM HXs. As shown in chapter 5, the mechanical power output from an EM HX is proportional to the gain in the gas velocity and temperature. But when the flow velocity increases, heat losses through convection and work of expansion also increase. To compensate for increased heat removal rate from the ceramic, applied EM power required to achieve thermal runaway increases with flow velocity. Clearly there exists a trade-off between how much mechanical power can be obtained and the required EM power to achieve sufficient heating of the ceramic. As a future extension, optimization studies may be carried out to determine ideal operating conditions based on the maximum possible energy conversion efficiencies.

# A COMPARISON BETWEEN THE COMSOL AND FINITE DIFFERENCE MODELS

Here we compare the steady-state temperature and electric field profiles produced by both COMSOL Multiphysics and IMEX models. Both of the models solve the system of equations given by (3.3)-(3.17), and the solution methodology is discussed in chapter 3. The comparison is made for two cases: one with no fluid flow and another with fluid flow. As both models use different discretization schemes, the results from the COMSOL model are interpolated onto the grid used in the IMEX model using MATLAB's Delaunay triangulation technique [66]. We quantify the differences seen in the profiles using

$$E_r = \left| \frac{\phi_{IMEX} - \phi_{COMSOL}}{\phi_{IMEX}} \right|, \tag{A.1}$$

where $E_r$ is the absolute relative error which also includes interpolation error, and $\phi$ can be $T$ or $|E|$.

We set $Pe = 0$ and solve the system (3.3)-(3.7) along with the boundary conditions (3.10)-(3.17) in COMSOL Multiphysics and with the IMEX scheme. For this case, the steady-state is achieved when EM losses are balanced by thermal losses to the surroundings. Figure A.1 shows the comparison of steady-state temperature and electric field profiles in regions 2 and 3 for incident power of $P_{av} = 3,000\ W/m^2$. Power response curves for different $Pe$ are shown in Figure 3.3. Stable branches shown in this plot are produced by performing parametric sweep on incident powers with different initial temperatures, and average steady-state temperatures are plotted against the incident power. It is seen that lower, middle, and upper branches are achieved when initial temperatures are maintained at 300 $K$, 1,000 $K$ and 2,500 $K$, respectively. For $P_{av} = 3,000\ W/m^2$, the

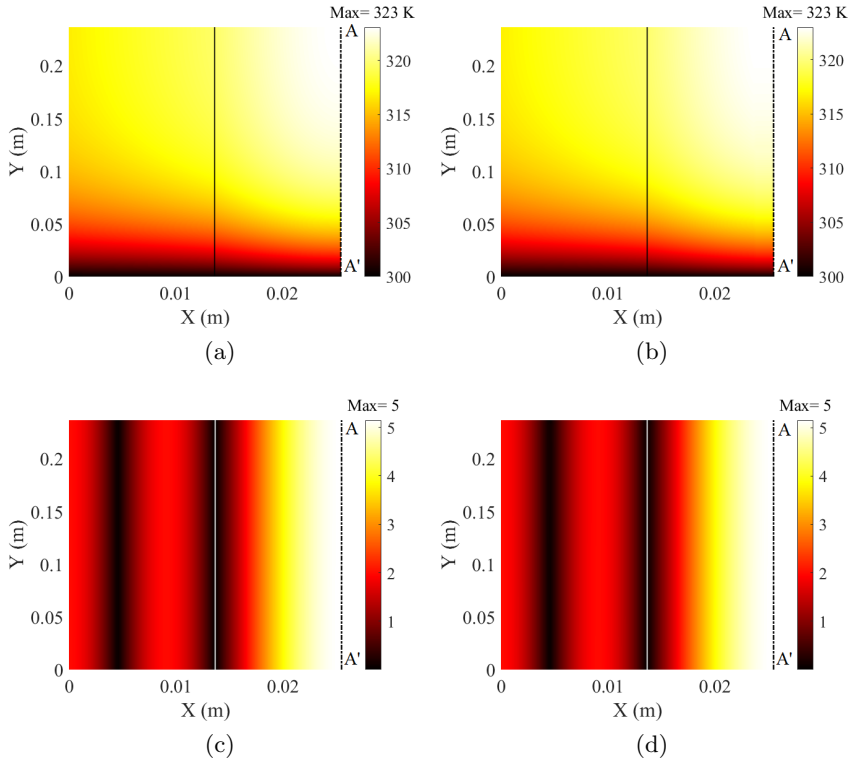


Figure A.1: Steady-state dimensional $T$ profiles produced by IMEX (a) and COMSOL (b), dimensionless $|E|$ profiles given by IMEX (c) and COMSOL (d) models for power $P_{av} = 3,000\ W/m^2$ with no flow case $Pe = 0$. The solid line represents the interface between regions 2 and 3 and AA' is the axis of symmetry. Maximum and average $E_r$ in comparison of (a) and (b) is 0.005 and $6.57 \times 10^{-4}$, and between (c) and (d) is 0.24 and 0.004, respectively.

steady-state temperatures are low (Figure A.1) and EM HX operates on the lower branch which can be seen from Figure 3.3. In Figure A.2, as we increase the $P_{av}$ to $8,000\ W/m^2$, we observe significant rise in temperature: maximum value in ceramic region increases from 323 $K$ to $1,400\ K$, and solution is found to be on the middle branch (see Figure 3.3). As a result of this transition from lower to middle branch, a hot spot is observed in the lossy region which indicates localized heating. We discuss this phenomenon in following section.

As soon as we achieve transition between lower and the middle branch, we observe nonuniform distribution of electric field amplitude as seen in Figure A.1 and Figure A.2. When the device operates on the lower branch for $P_{av} = 3,000\ W/m^2$ and $Pe = 0$, temperatures are low (maximum of 323 $K$) and $\sigma_3 \sim 0.0004\ S/m$, therefore, attenuation of electric field amplitude in ceramic region is small as seen in Figure A.1 (c) and (d). On the other hand, when $P_{av} = 8,000\ W/m^2$ for $Pe = 0$, we

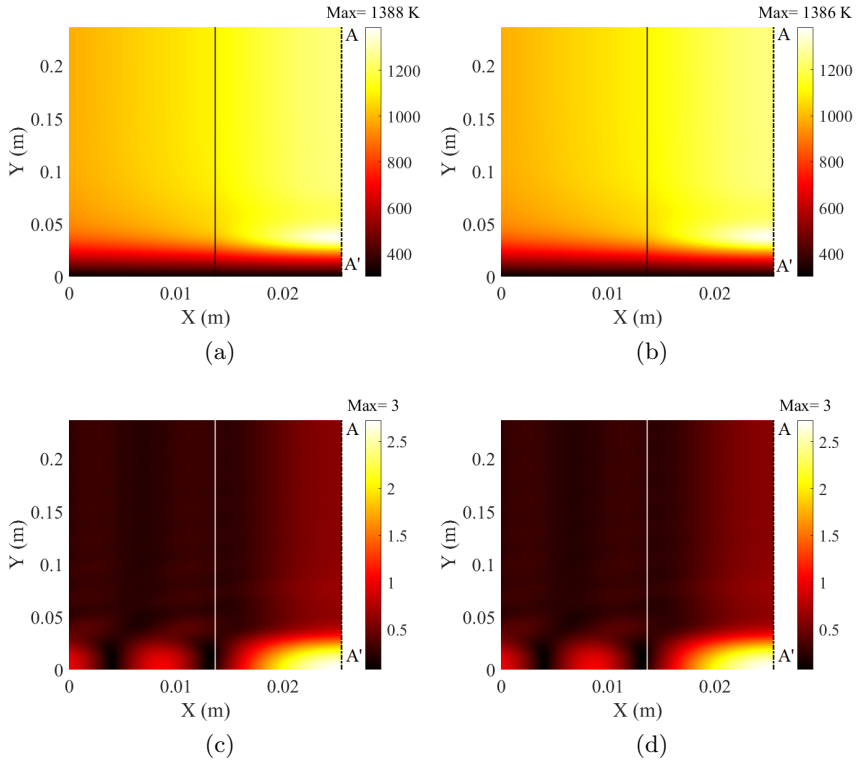


Figure A.2: Steady-state dimensional $T$ profiles produced by IMEX (a) and COMSOL (b), dimensionless $|E|$ profiles given by IMEX (c) and COMSOL (d) models for power $P_{av} = 8,000\ W/m^2$ with no flow case $Pe = 0$. The solid line represents the interface between regions 2 and 3 and AA' is the axis of symmetry. Maximum and average $E_r$ in comparison of (a) and (b) is 0.01 and $5.3 \times 10^{-4}$, and between (c) and (d) is 0.14 and 0.01, respectively.

operate on the middle branch and average temperatures are high (maximum of $1,400\ K$). Dirichlet condition maintained at the bottom boundary causes a nonuniform temperature distribution and, $\sigma_3$ is maximum (or minimum) where temperature is maximum (or minimum), therefore, it is expected to see attenuation of field amplitude in high temperature regions, which is seen in Figure A.2 (c) and (d) where maximum field amplitude is observed near the bottom boundary where the temperature is minimum.

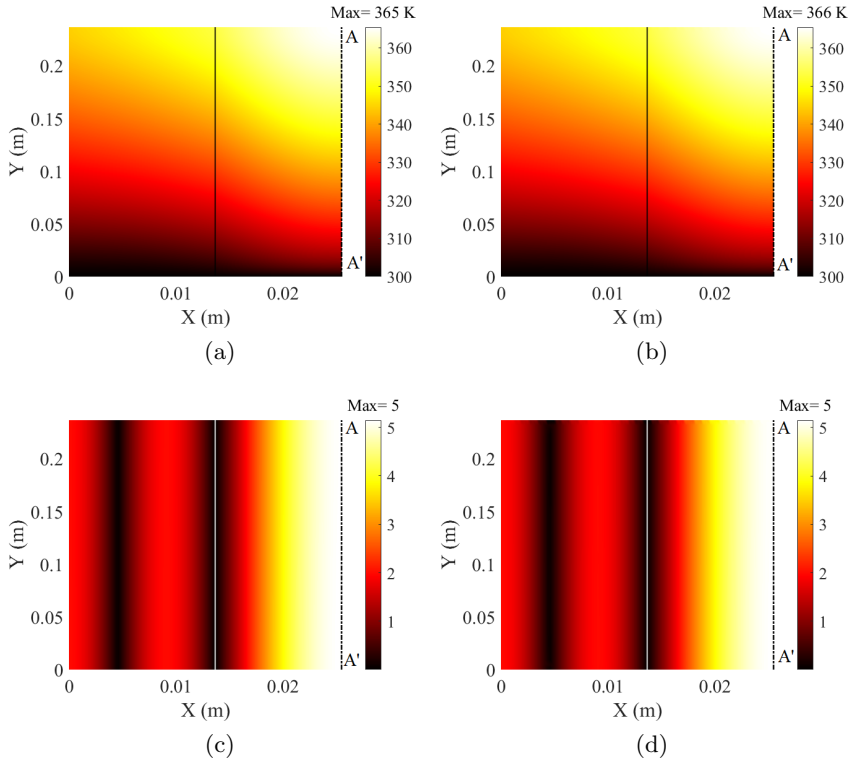


Figure A.3: Steady-state dimensional $T$ profiles produced by IMEX (a) and COMSOL (b), dimensionless $|E|$ profiles given by IMEX (c) and COMSOL (d) models for power $P_{av} = 8,000\ W/m^2$ with flow case $Pe = 8.6$ and $\eta = 0.06$. The solid line represents the interface between regions 2 and 3 and AA' is the axis of symmetry. Maximum and average $E_r$ in comparison of (a) and (b) is 0.003 and $1.42 \times 10^{-4}$, and between (c) and (d) is 0.24 and 0.004, respectively.

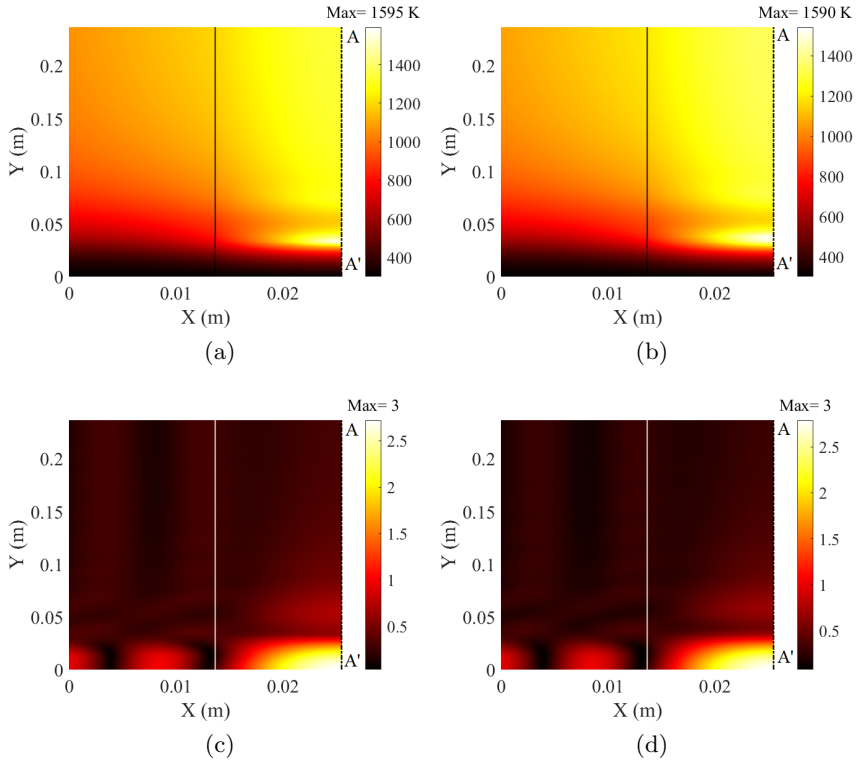


Figure A.4: Steady-state dimensional $T$ profiles produced by IMEX (a) and COMSOL (b), dimensionless $|E|$ profiles given by IMEX (c) and COMSOL (d) models for power $P_{av} = 15,000\ W/m^2$ with flow case $Pe = 8.6$ and $\eta = 0.06$. The solid line represents the interface between regions 2 and 3 and AA' is the axis of symmetry. Maximum and average $E_r$ in comparison of (a) and (b) is 0.09 and $2.5 \times 10^{-3}$, and between (c) and (d) is 0.5 and 0.03, respectively.

# B VERIFICATION OF THE LINEAR STABILITY THEORY

Here we provide a verification of the linear stability theory discussed in chapter 4 of the thesis. We compare growth rates from linear stability model with a transient model solved in COMSOL Multiphysics. The COMSOL model solves the linearized system of equation (4.16)-(4.21), but, for EM-thermal scenario we have no flow (i.e., $\tilde{\mathbf{u}}, \tilde{p}, Ra^2 = 0$). When $a = 0$ is considered, perturbations become independent of $x$ and $y$, and the linearized COMSOL model reduces 1D. As it is expected that perturbations to grow exponentially in time, transients from the COMSOL model can be represented by

$$\tilde{T} = Ae^{s_c t},$$

where $A$ is a constant, and $s_c$ represents growth rate from COMSOL. If we take natural log on the both sides we get,

$$\log \tilde{T} = \log A + s_c t,$$

which means that when $\log \tilde{T}$ is plotted against the time coordinate $t$, slope of the line give us the growth rate from the COMSOL simulation. In Figure B.1 we evaluate growth rates from the 1D transient COMSOL model for unstable base-states at $P = 0.6$ and $P = 1$ and we find a very good agreement between growth rates given by both COMSOL and linear stability models.

We now introduce $xz$-dependent perturbations in the base state when $Ra^2 = 0$, and linearized COMSOL is now 2D. Growth rates given by both COMSOL and linear stability models for this 2D scenario are compared in Figure B.2. Again, we observe a very good agreement between these two models.

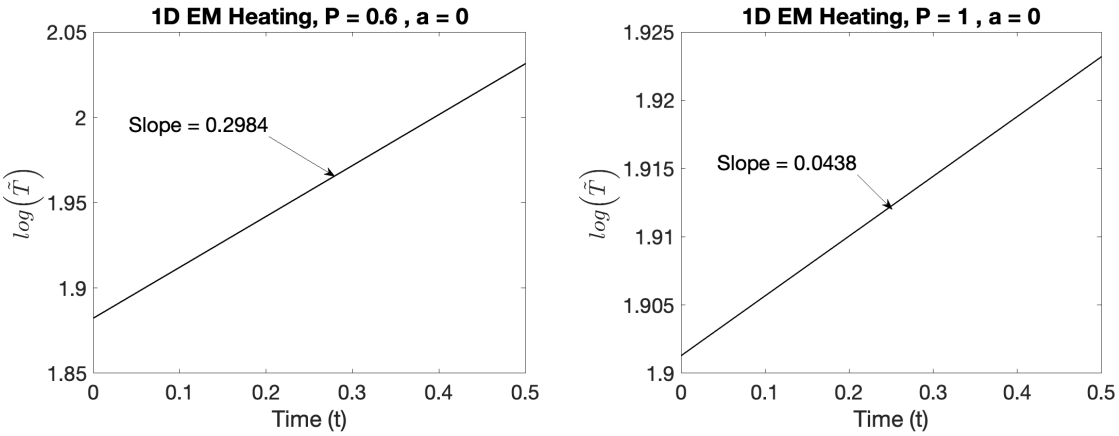


(a) (b)

Figure B.1: Growth rate of the unstable solutions from a linearized transient COMSOL model for $P = 0.6$ (a) and $P = 1$ (b). Axes data is scaled on natural logarithm so that slope of the plot represent exponential growth rate. Growth rates from linear stability analysis are 0.2986 and 0.0436 for $P = 0.6$ and $P = 1$, respectively.

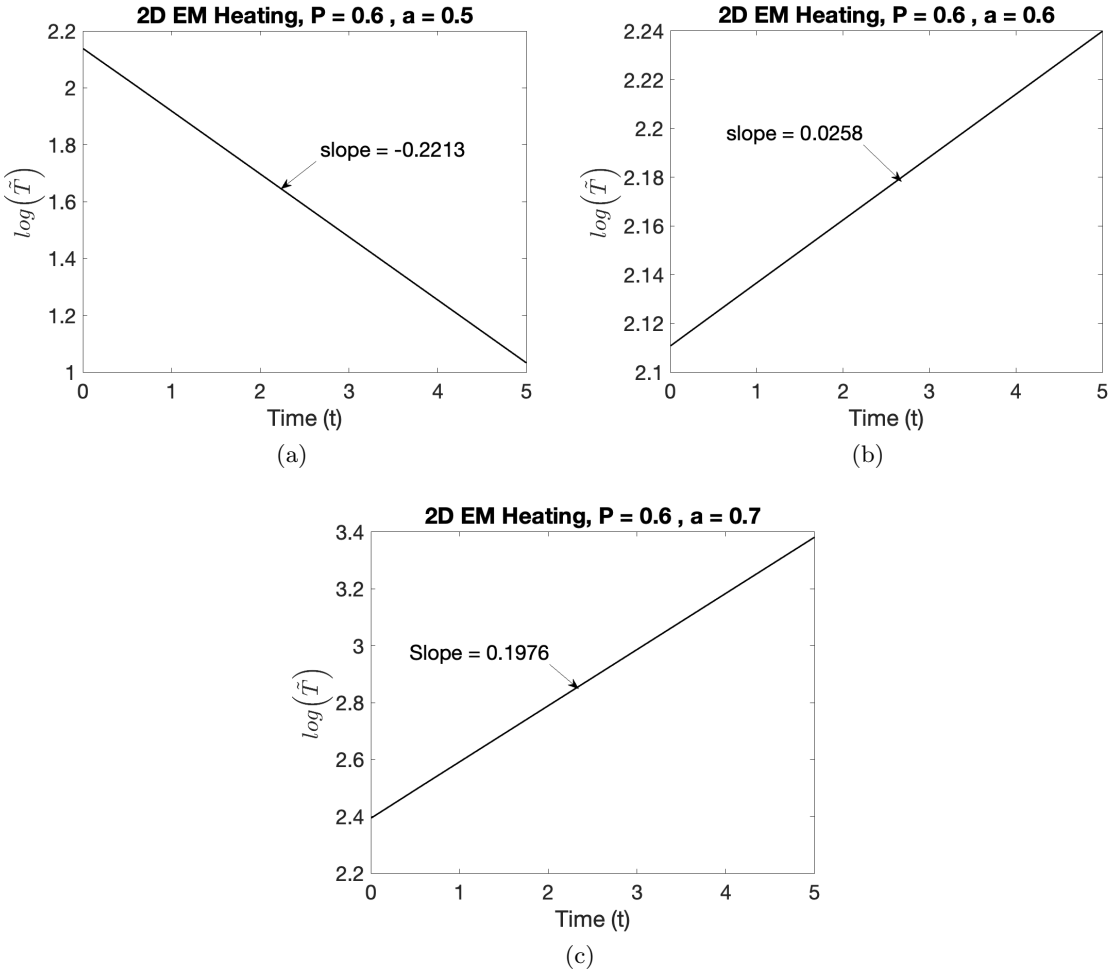


Figure B.2: Growth rates of the unstable solutions from a linearized transient COMSOL model for $P = 0.6$ when $a = 0.5$ (a), $b = 0.6$ (b), and $c = 0.7$ (c). Axes data is scaled on natural logarithm so that slope of the plot represent exponential growth rate from the COMSOL model. Growth rates from linear stability analysis for $a = 0.5$, $a = 0.6$, and $a = 0.7$ are $-0.2237$, 0.0240 and 0.1965, respectively.

# C COMPARISON OF LUBRICATION MODEL WITH EXACT SOLUTIONS

Here we show an agreement between the numerical solution of the lubrication model and an exact solution of the model for a limiting case with $\Lambda = 0$ (i.e., $\rho_1$ is independent of $p$) and $\epsilon_2'' = \frac{0.0004}{\omega\epsilon_0}$. With these values, we can solve for $E$ independently, $p$ is decoupled from $T$, $q$ turns out to be a constant, and nonlinear terms in (5.23a) and (5.25) drop out. Equation (5.23a) reduces to

$$m\gamma Pe\frac{dT}{dx} + BiT = (Bi + q), \tag{C.1}$$

and (5.25) becomes

$$-\eta(1 + kl)\frac{d^2T}{dx^2} + m\gamma Pe\frac{dT}{dx} + BiT = (Bi + q). \tag{C.2}$$

Both (C.1) and (C.2) can be solved exactly given $m$ and the boundary conditions (5.24) and (5.26). As $p$ is decoupled from $T$ when $\Lambda = 0$, once we solve for $T$ for a given $m$, we can then back out $p$ by solving

$$\frac{dp}{dx} = -mT. \tag{C.3}$$

Noting that (C.3) only requires one boundary condition for the complete solution of $p$ for a given $m$, and the appropriate $m$ is determined by using the secant root finding method such that $p$ satisfies the both boundary conditions. These exact solutions are used as a reference for verification of numerical codes discussed in the previous section.

Numerical solution to (5.25), i.e., MATLAB's BVP solver coupled with the secant method, is 4th order accurate in space so we can expect that the relative errors between the exact and

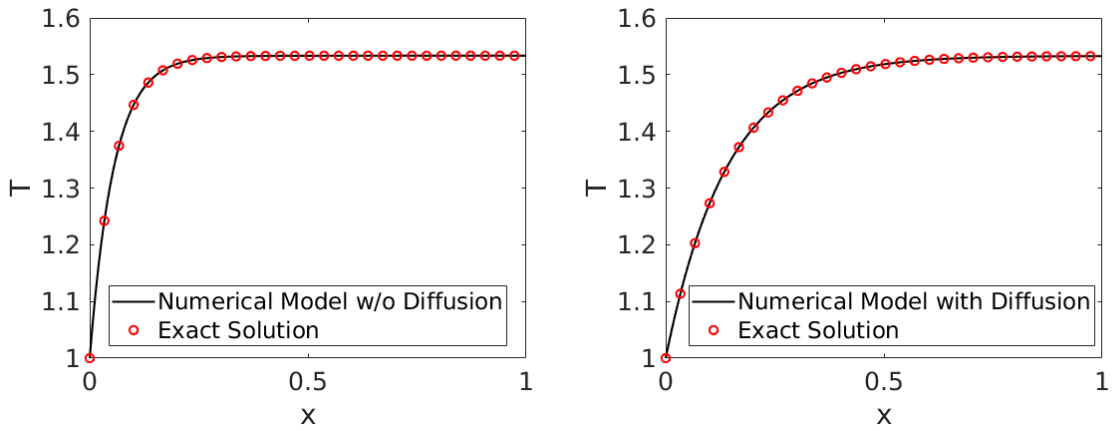


Figure C.1: Comparison temperature of profiles produced by the model without (a) and with (b) thermal diffusion with respective exact solutions for $\Lambda = 0$, $\epsilon_2'' = \frac{0.0004}{\omega\epsilon_0}$, $l_1 = 0.01$ m $l_2 = 0.02$ m, $L = 3$ m and incident EM power $P_{av} = 5,000$ W/m$^2$. Average relative errors seen in (a) and (b) are $7.8 \times 10^{-10}$ and $1.25 \times 10^{-8}$, respectively.

numerical solutions to be within $O(\Delta x^4)$, where $\Delta x$ is the step size of the cell. Similarly, numerical solution of (5.23) is 5th order accurate in space, so the expected errors are $O(\Delta x^5)$. In both of these comparisons, we used uniform spatial step size of 0.01 (i.e., discretized the region of solution $0 < x < 1$ into 100 mesh points). Looking at Figure C.1, we see that errors seen in $T$ in comparison of both the numerical approaches are within the expected tolerances.

# Bibliography


[1] A. Jamar, Z. Majid, W. Azmi, M. Norhafana, and A. Razak, "A review of water heating system for solar energy applications," *Int. Commun. in Heat and Mass Transfer*, vol. 76, pp. 178–187, 2016.

[2] W. C. Brown and E. E. Eves, "Beamed microwave power transmission and its application to space," *IEEE transactions on Microwave Theory and Techniques*, vol. 40, no. 6, pp. 1239–1250, 1992.

[3] J. N. Benford and R. Dickinson, "Space propulsion and power beaming using millimeter systems," in *Intense Microwave Pulses III*, vol. 2557, pp. 179–192, International Society for Optics and Photonics, 1995.

[4] J. Benford, "Space applications of high-power microwaves," *IEEE Transactions on Plasma Science*, vol. 36, no. 3, pp. 569–581, 2008.

[5] B. Jawdat, B. Hoff, M. Hilario, A. Baros, P. Pelletier, T. Sabo, and F. Dynys, "Composite ceramics for power beaming," in *IEEE Wireless Power Transfer Conference (WPTC), 978-1-5090-4595-3/17*, pp. 1–4, 2017.

[6] B. Hoff, M. Hilario, B. Jawdat, A. Baros, F. Dynys, J. Mackey, V. Yakovlev, C. Andraka, K. Armijo, E. Savrun, *et al.*, "Millimeter wave interactions with high temperature materials and their applications to power beaming," in *Proc. 52nd IMPI Microwave Power Symp*, pp. 82–83, 2018.

[7] A. A. Mohekar, J. M. Gaone, B. S. Tilley, and V. V. Yakovlev, "A 2D coupled electromagnetic, thermal and fluid flow model: application to layered microwave heat exchangers," in *IEEE/MTT-S International Microwave Symposium-IMS*, pp. 1389–1392, 2018.

[8] A. Mohekar, B. Tilley, and V. Yakovlev, "Plane wave irradiation of a layered system: resonance-based control over thermal runaway," in *AMPERE 2019. 17th International Conference on Microwave and High Frequency Heating*, pp. 292–300, Editorial Universitat Politècnica de València, 2019.

[9] P. Kumi, S. A. Martin, V. V. Yakovlev, M. S. Hilario, B. W. Hoff, and I. M. Rittersdorf, "Electromagnetic-thermal model of a millimeter-wave heat exchanger based on an AlN: Mo susceptor," *COMPEL-The Intern. J. for Comp. and Math. in Electrical and Electronic Eng.*, vol. 39, no. 2, pp. 481–496, 2020.

[10] G. A. Landis, "Beamed energy propulsion for practical interstellar flight," *Journal of the British Interplanetary Society*, vol. 52, pp. 420–423, 1999.

[11] K. L. Parkin, L. D. DiDomenico, and F. E. Culick, "The microwave thermal thruster concept," in *2nd Intern. Symp. on Beamed Energy Propulsion*, pp. 418–429, 2004.

[12] D. J. Griffiths, *Introduction to Electrodynamics*. American Association of Physics Teachers, 2005.

[13] H. Ockendon and J. R. Ockendon, *Waves and Compressible Flow*. Springer, 2004.

[14] D. M. Pozar, *Microwave Engineering*. John wiley & sons, 2011.

[15] T. L. Bergman, F. P. Incropera, D. P. DeWitt, and A. S. Lavine, *Fundamentals of Heat and Mass Transfer*. John Wiley & Sons, 2011.

[16] J. M. Hill and M. J. Jennings, "Formulation of model equations for heating by microwave radiation," *Applied Mathematical Modelling*, vol. 17, no. 7, pp. 369–379, 1993.

[17] V. V. Yakovlev, S. M. Allan, M. L. Fall, and H. S. Shulman, "Computational study of thermal runaway in microwave processing of zirconia," *Microwave and RF Power Applications,* J. Tao, Ed., Cépaduès Éditions, pp. 303–306, 2011.

[18] X. Wu, *Experimental and Theoretical Study of Microwave Heating of Thermal Runaway Materials*. PhD thesis, Virginia Polytechnic Institute, 2002.

[19] X. Wu, J. Thomas Jr, and W. A. Davis, "Control of thermal runaway in microwave resonant cavities," *Journal of Applied Physics*, vol. 92, no. 6, pp. 3374–3380, 2002.

[20] Z. Peng and J.-Y. Hwang, "Microwave-assisted metallurgy," *International Materials Reviews*, vol. 60, no. 1, pp. 30–63, 2015.

[21] K. I. Rybakov, E. A. Olevsky, and E. V. Krikun, "Microwave sintering: fundamentals and modeling," *Journal of the American Ceramic Society*, vol. 96, no. 4, pp. 1003–1020, 2013.

[22] J. Binner, M. Porter, B. Baker, J. Zou, V. Venkatachalam, V. R. Diaz, A. D'Angio, P. Ramanujam, T. Zhang, and T. Murthy, "Selection, processing, properties and applications of ultra-high temperature ceramic matrix composites, uhtcmcs–a review," *International Materials Reviews*, vol. 65, no. 7, pp. 389–444, 2020.

[23] H. Jiang, K.-s. Moon, Z. Zhang, S. Pothukuchi, and C. Wong, "Variable frequency microwave synthesis of silver nanoparticles," *Journal of Nanoparticle Research*, vol. 8, no. 1, pp. 117–124, 2006.

[24] G. O. Beale and M. Li, "Robust temperature control for microwave heating of ceramics," *IEEE Transactions on Industrial Electronics*, vol. 44, no. 1, pp. 124–131, 1997.

[25] G. Kriegsmann, M. Brodwin, and D. Watters, "Microwave heating of a ceramic halfspace," *SIAM Journal on Applied Mathematics*, vol. 50, no. 4, pp. 1088–1098, 1990.

[26] G. A. Kriegsmann, "Thermal runaway in microwave heated ceramics: A one-dimensional model," *Journal of Applied Physics*, vol. 71, no. 4, pp. 1960–1966, 1992.

[27] J. A. Pelesko and G. A. Kriegsmann, "Microwave heating of ceramic laminates," *Journal of Engineering Mathematics*, vol. 32, no. 1, pp. 1–18, 1997.

[28] J. M. Gaone, B. S. Tilley, and V. V. Yakovlev, "Permittivity-based control of thermal runaway in a triple-layer laminate," in *IEEE MTT-S Intern. Microwave Symp. Dig. (Honolulu, HI, June 2017)*, pp. 459–462.

[29] J. Gaone, B. Tilley, and V. Yakovlev, "Electromagnetic heating control via high-frequencyresonance of a triple-layer laminate," *Journal of Engineering Mathematics*, vol. 114, no. 1, pp. 65–86, 2019.

[30] S. Chandrasekhar, *Hydrodynamic and Hydromagnetic Stability*. Courier Corporation, 2013.

[31] P. G. Drazin and W. H. Reid, *Hydrodynamic Stability*. Cambridge university press, 2004.

[32] J. Bear, *Dynamics of Fluids in Porous Media*. Courier Corporation, 2013.

[33] D. Salvi, D. Boldor, G. Aita, and C. Sabliov, "COMSOL Multiphysics model for continuous flow microwave heating of liquids," *Journal of Food Engineering*, vol. 104, no. 3, pp. 422–429, 2011.

[34] D. Salvi, D. Boldor, J. Ortego, G. Aita, and C. Sabliov, "Numerical modeling of continuous flow microwave heating: a critical comparison of COMSOL and ANSYS," *Journal of Microwave Power and Electromagnetic Energy*, vol. 44, no. 4, pp. 187–197, 2010.

[35] W. B. Westphal and A. Sils, *Dielectric Constant and Loss Data*. Massachusetts Institute of Technogy Cambridge Lab for Insulation Research, 1972.

[36] X. He, Y. Li, L. Wang, Y. Sun, and S. Zhang, "High emissivity coatings for high temperature application: Progress and prospect," *Thin Solid Films*, vol. 517, no. 17, pp. 5120–5129, 2009.

[37] D. Mahadik, S. Gujjar, G. M. Gouda, and H. C. Barshilia, "Double layer sio2/al2o3 high emissivity coatings on stainless steel substrates using simple spray deposition system," *Applied surface science*, vol. 299, pp. 6–11, 2014.

[38] Z. Khattak and H. M. Ali, "Air cooled heat sink geometries subjected to forced flow: A critical review," *International Journal of Heat and Mass Transfer*, vol. 130, pp. 141–161, 2019.

[39] P. M. Meaney, C. J. Fox, S. D. Geimer, and K. D. Paulsen, "Electrical characterization of glycerin: Water mixtures: Implications for use as a coupling medium in microwave tomography," *IEEE transactions on microwave theory and techniques*, vol. 65, no. 5, pp. 1471–1478, 2017.

[40] G. P. Association, *Physical Properties of Glycerine and its Solutions*. Glycerine Producers' Association, 1963.

[41] G. I. Taylor, "Dispersion of soluble matter in solvent flowing slowly through a tube," *Proceedings of the Royal Society of London. Series A. Mathematical and Physical Sciences*, vol. 219, no. 1137, pp. 186–203, 1953.

[42] Y. Saad, *Iterative Methods for Sparse Linear Systems*. SIAM, 2003.

[43] S. J. Ruuth, "Implicit-explicit methods for reaction-diffusion problems in pattern formation," *Journal of Mathematical Biology*, vol. 34, no. 2, pp. 148–176, 1995.

[44] W. H. Press, S. A. Teukolsky, W. T. Vetterling, and B. P. Flannery, *Numerical Recipes 3rd Edition: The Art of Scientific Computing*. Cambridge university press, 2007.

[45] S. Mazumder, *Numerical Methods for Partial Differential Equations: Finite Difference and Finite Volume Methods*. Academic Press, 2015.

[46] M. N. Sadiku, *Numerical Techniques in Electromagnetics with MATLAB*. CRC Press, 2011.

[47] Y. S. Wong and G. Li, "Exact finite difference schemes for solving helmholtz equation at any wavenumber," *International Journal of Numerical Analysis and Modeling, Series B*, vol. 2, no. 1, pp. 91–108, 2011.

[48] A. A. Mohekar, B. S. Tilley, and V. V. Yakovlev, "A triple-layer electromagnetic heat exchanger with plane poiseuille flow: Control and local onset of thermal runaway," *IEEE Journal on Multiscale and Multiphysics Computational Techniques*, vol. 5, pp. 119–131, 2020.

[49] H. B. Squire, "On the stability for three-dimensional disturbances of viscous fluid flow between parallel walls," *Proceedings of the Royal Society of London. Series A, Containing Papers of a Mathematical and Physical Character*, vol. 142, no. 847, pp. 621–628, 1933.

[50] K. Gage and W. Reid, "The stability of thermally stratified plane poiseuille flow," *Journal of Fluid Mechanics*, vol. 33, no. 1, pp. 21–32, 1968.

[51] J. Gilchrist, G. A. Kriegsmann, and D. T. Papageorgiou, "Stability of a microwave heated fluid layer," *IMA journal of applied mathematics*, vol. 60, no. 1, pp. 73–89, 1998.

[52] M. Bhattacharya and T. Basak, "Analysis on the onset of microwave induced convection within a horizontal water layer," *Journal of Physics D: Applied Physics*, vol. 41, no. 15, p. 155505, 2008.

[53] M. Bhattacharya and T. Basak, "Linear stability analysis for the onset of convection during microwave heating of oil confined within horizontal plates," *Journal of Applied Physics*, vol. 105, no. 2, p. 024906, 2009.

[54] D. Murakami and K. Parkin, "An overview of the nasa ames millimeter-wave thermal launch system," in *48th AIAA/ASME/SAE/ASEE Joint Propulsion Conference & Exhibit*, p. 3741, 2012.

[55] D. V. Schroeder, *An Introduction to Thermal Physics*. American Association of Physics Teachers, 1999.

[56] R. D. Zucker and O. Biblarz, *Fundamentals of Gas Dynamics*. John Wiley & Sons, 2019.

[57] V. Babu, *Fundamentals of Gas Dynamics*. Springer, 2008.

[58] L. F. Shampine, J. Kierzenka, and M. W. Reichelt, "Solving boundary value problems for ordinary differential equations in matlab with bvp4c," *Tutorial notes*, vol. 2000, pp. 1–27, 2000.

[59] L. F. Shampine and M. W. Reichelt, "The matlab ODE suite," *SIAM journal on scientific computing*, vol. 18, no. 1, pp. 1–22, 1997.

[60] C. M. Hogan, B. W. Hoff, I. M. Rittersdorf, and V. V. Yakovlev, "Computational characterization of millimetre-wave heat exchangers with an aln: Mo susceptor of multiple cylindrical elements," *Journal of Microwave Power and Electromagnetic Energy*, vol. 56, no. 1, pp. 18–36, 2022.

[61] B. I. Pavel and A. A. Mohamad, "An experimental and numerical study on heat transfer enhancement for gas heat exchangers fitted with porous media," *International Journal of Heat and Mass Transfer*, vol. 47, no. 23, pp. 4939–4952, 2004.

[62] A. Mohamad, "Heat transfer enhancements in heat exchangers fitted with porous media part i: constant wall temperature," *International Journal of Thermal Sciences*, vol. 42, no. 4, pp. 385–395, 2003.

[63] A. E. Scheidegger, *The Physics of Flow Through Porous Media*. University of Toronto press, 2020.

[64] S. Whitaker, *The Method of Volume Averaging*. Springer Science and Business Media, 2013.

[65] L. Wang, L.-P. Wang, Z. Guo, and J. Mi, "Volume-averaged macroscopic equation for fluid flow in moving porous media," *International Journal of Heat and Mass Transfer*, vol. 82, pp. 357–368, 2015.

[66] P. Persson and G. Strang, "A simple mesh generator in MATLAB," *SIAM review*, vol. 46, no. 2, pp. 329–345, 2004.